Ultrafast Laser Technologies and Applications

Femto-UP 2020

Edited by
Jérémie Léonard & Charles Hirlimann

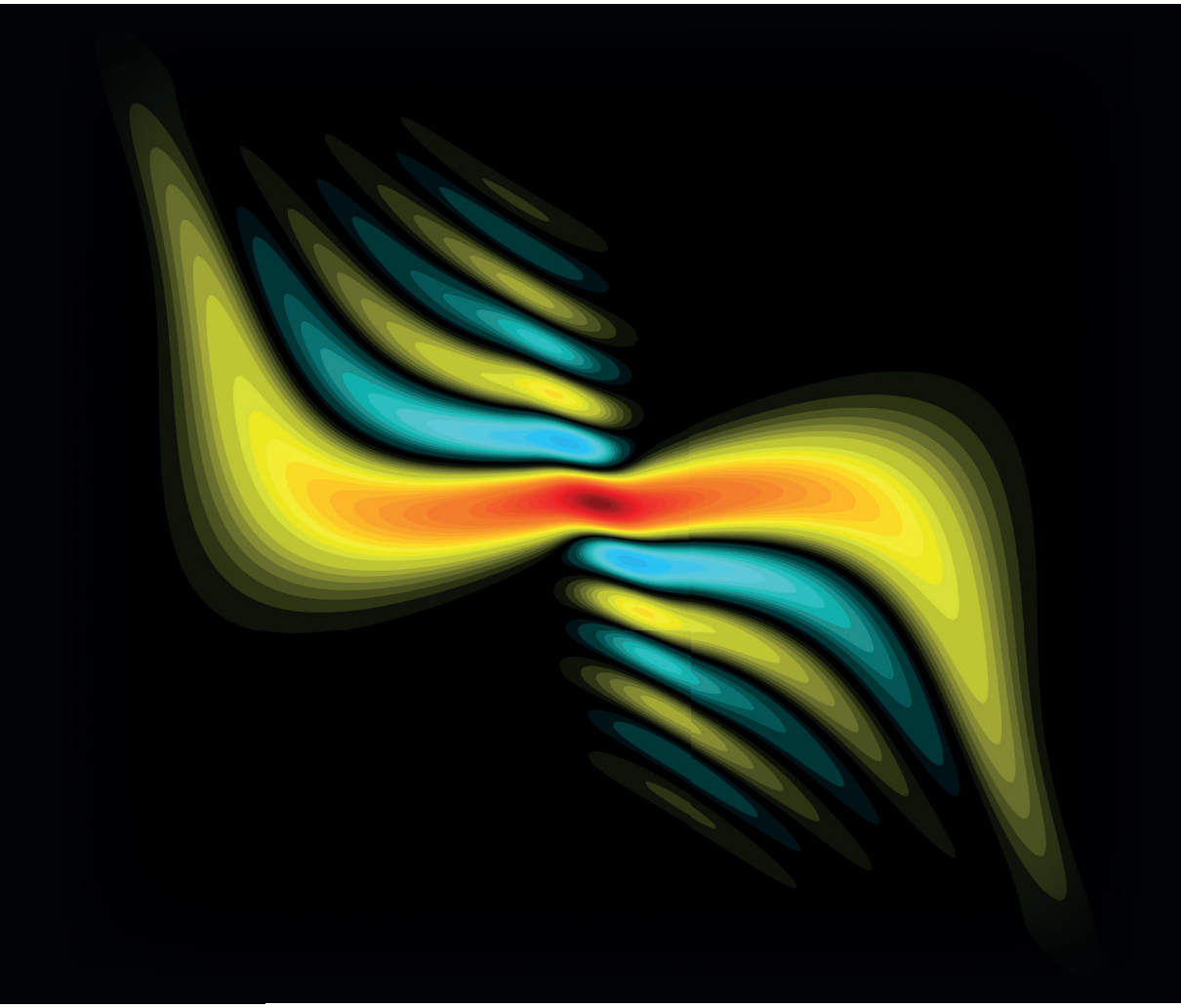

edp sciences PRESSES UNIVERSITAIRES DE STRASBOURG

Ultrafast Laser Technologies and Applications
Femto-UP 2020

Edited by
Jérémie Léonard & Charles Hirlimann

This Book gathers original tutorials delivered as lectures by the authors at the international Femto-UP 2020 School, which took place online from 8th to 29th of March 2021 and gathered 600 participants worldwide. Like the previous occurrences of the Femto-UP School, the 2020 edition and this Book do target a multidisciplinary public of scientists at various points of their carrier from undergraduate and graduate students to senior researchers and technical staff. The aim is to provide generic scientific knowledge on ultrafast laser technologies including, generation, amplification, manipulation and characterization of ultrashort laser pulses, and pedagogical accounts of a selection of state-of-the-art applications of ultrashort laser pulses. The Femto-UP 2020 School comprised numerical practical sessions using original pedagogical or technical numerical tools (based on the Python programming language) also included to this Book as supplementary electronic material.

Jérémie LÉONARD is CNRS directeur de recherche at IPCMS (Strasbourg, France). He chaired the Femto-UP 2020 School.

Charles HIRLIMANN is CNRS directeur de recherche émérite at IPCMS (Strasbourg, France).

edp sciences

Université de Strasbourg

ISBN : 978-2-7598-2719-0
979-10-344-0145-1

Jérémie LÉONARD
and Charles HIRLIMANN, Eds

Ultrafast Lasers Technologies and Applications

The Femto-UP 2020 School

The electronic version of the book is available online with free access at the following address: https://doi.org/10.1051/978-2-7598-2719-0

Printed in France

EDP Sciences – ISBN(print): 978-2-7598-2719-0 – ISBN(ebook): 978-2-7598-2720-6
DOI: 10.1051/978-2-7598-2719-0

PUS – ISBN(print): 979-10-344-0145-1 – ISBN(ebook): 979-10-344-0365-3

Foreword

The Femto-UP School

Since the year 2000, the Femto-UP School has been organized every third or fourth year in France, by members of the French scientific community belonging to the networks "Réseau femto" and "GDR UP". Initiated in 1997 by François Salin and Gérard Charton, the "Réseau femto"[i] belongs to the CNRS MITI ("Mission pour les Initiatives Transverses et Interdisciplinaires"). The "Réseau femto" network aims largely at spreading femtosecond technologies including all techniques related to the development, characterization, and use of femtosecond laser sources throughout the French scientific community. The CNRS "Groupement de Recherche (GDR) UP"[ii] is a National research network on Ultrafast Phenomena (UP) created on January 2016, by Franck Lépine (CNRS, ILM) and Lionel Poisson (CNRS, LIDYL). GDR UP brings together the French community of experimenters and theorists (from over 50 laboratories) developing scientific activities in the field of ultrafast science (*i.e.*, on the Attosecond, Femtosecond, and Picosecond time scales) and investigating all states of matter: diluted, solid, nanometric, liquid, plasma, and biological. GDR UP aims at creating new links between the communities and promoting new opportunities offered by emerging light sources, spectroscopic techniques, and theoretical approaches.

The School is intended to train the attendees on generic knowledge about ultrafast laser physics and give insights into the latest developments in the field of "ultrafast laser technologies and applications". It targets a multidisciplinary public of scientists at any level of their research career (from master's or PhD beginners up to senior technical staff and researchers) with a series of lectures covering (i) basic concepts of ultrafast laser technologies (laser pulse generation, propagation, amplification, and characterization) as well as (ii) a selection of more specialized topics and applications of these technologies.

[i] http://reseau-femto.cnrs.fr/.

[ii] http://gdrupilm.univ-lyon1.fr/index.html.

DOI: 10.1051/978-2-7598-2719-0.c901

The 2020 Edition of the Femto-UP School (the 6th occurrence) was proposed and organized by members of the Department of Ultrafast Optics and Nanophotonics of the Institut de Physique et Chimie des Matériaux de Strasbourg (IPCMS-DON). Initially planned to take place in Alsace (France) in the form of an on-site "École Thématique du CNRS" in November 2020, it had to be cancelled due to the Covid-19 pandemic. It was then organized in 2021, in a very different and unprecedented, online format, in the form of typically 2-hour-long video-conferences, two to four times a week, from March 8th to March 29th. In total, the online event[iii] included 20 h of Lectures and 6 h of Numerical Practical sessions, including a preliminary 2-hour-long Python "crash" tutorial organized one week before the School.

Unlike previous editions where 70–90 participants physically gathered in some remote, beautiful location in France, for the 2020 edition up to 600 participants registered from all over the world (see figure 1), and 200–400 people attended each online session. Several factors have contributed to the strong increase in the audience of Femto-UP this year. First, the international attractiveness of our laboratories has literally imposed the use of English language as a course support to include/involve young doctoral and post-doctoral students of various non-French-speaking origins. This also enabled inviting experts from abroad, thus broadening the scope and diversity of the topics, techniques, and ways of introducing concepts. Secondly, keeping the school in a remote mode has greatly encouraged the enrollment of listeners from all over Europe and even beyond (see figure 1). In addition, the absence of school preparation and operation costs enabled a free-of-charge registration. Third, for the first time in the Femto-UP School, three sessions were organized in the form of Numerical Practical encountering a great success, allowing participants to discover or practice numerical tools and illustrate fundamental concepts used during their day-to-day manipulations of femtosecond laser pulses. All these points constituted a scientific experiment in itself, the consequences of which should be discussed and deepened for the preparation of the next occurrence of the Femto-UP school.

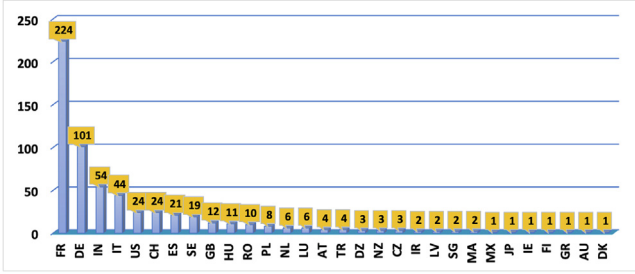

Fig. 1 – Distribution of the countries of the 600 participants to the Femto-UP 2020 School. (30 countries in total).

[iii] https://femto-up2020.sciencesconf.org/resource/page/id/2.

This Book

The Chapters of this Book are independent, original Tutorials, written by the Lecturers of the School, closely following the corresponding Lectures delivered online during the School. The first part of the Book includes chapters 1–5 and focuses on general physical concepts and technical implementations of ultrafast laser pulses, with a historical testimony about the genesis of femtosecond laser pulses (chapter 1), followed by tutorials on generation (chapter 2), amplification (chapter 3), propagation (chapter 4), and characterization (chapter 5) of femtosecond laser pulses. Original, supplementary electronic materials, are likely becoming generic pedagogical material to illustrate femtosecond pulse propagation (Jupyter notebook, see chapter 4) or a generic technical tool to characterize femtosecond pulse durations (PyMoDAQ-femto module, see chapter 5). The second part of the Book (chapters 6–9) gathers tutorials introducing to a selection of state-of-the-art applications of ultrafast lasers and the underlying physical concepts, including high-order harmonic generation (chapter 6), the development of the European Extreme Light Infrastructure in Bucharest (chapter 7), multidimensional coherent spectroscopies (chapter 8) and nonlinear optical imaging at the nanoscale (chapter 9).

Acknowledgements

The School organizing committee was composed of IPCMS members including Jérémie Léonard (chair), Alberto Barsella, Alex Boeglin, Marie Barthélémy, François Fras, Stefan Haacke, Valérie Halté-Filippi, Paul-Antoine Hervieux, Charles Hirlimann, Giovanni Manfredi, Mircea Vomir, with the technical assistance of Christine Tugène and Thien Ho Minh.

The scientific advisory committee was composed of members of the "réseau Femto" and "GDR UP" boards including Marie Barthélémy (IPCMS), Catherine Le Blanc (LULI), Véronique Boutou (Inst. Néel), Christian Bordas (ILM), Pascale Changenet (LOB), Olivier Faucher (ICB), Franck Lépine (ILM), Lionel Poisson (LIDYL), Valérie Halté-Filippi (IPCMS), Jean-François Hergott (LIDYL), and Vincent de Waele (LASIR).

For this online edition of the School, a FemtoUP chat was implemented to enable interactions between participants, organizers, and lecturers. In particular, a team of "moderators" including Alberto Barsella (IPMCS), Leila Ben Mahfoud (Uni. Saint-Etienne), Johanna Brazard (Uni. Genève), François Fras (IPCMS), Amira Gharbi (IPCMS), Deeksha Gupta (IPCMS), Samiul Islam (IPCMS), Bogdan Marekha (IPCMS), Debobrata Rajak (Uni. Bordeaux), Thomas Roland (Uni. Lille), Oscar Urquidi Gandarillas (Uni. Genève), and Shannon Whitlock (Uni. Strasbourg), was extremely efficient at maintaining a "hot line" to assist all participants during the Numerical Practical.

We acknowledge financial support for the organization of the School and the Edition of the present Book (partnership between Presses Universitaires de Strasbourg and EDP Science) from the Université de Strasbourg, Réseau Femto, and GDR UP.

For the Femto-UP 2020 organizing committee,
Jérémie Léonard & Charles Hirlimann, editors,
Strasbourg, 2021.

Authors List

Contents

CHAPTER 4

CHAPTER 5

CHAPTER 8

CHAPTER 9

Chapter 1

Around the Genesis of Femto-Lasers

Charles Hirlimann*

Institut de Physique et Chimie des Matériaux de Strasbourg (IPCMS), UMR 7504 CNRS – Université de Strasbourg, 23 Rue du Lœss, F-67034 Strasbourg cedex 2, France

In the last century, the decade of the 80s saw the birth of lasers producing really short light pulses, less than 100 fs. The collision of pulses in a ring laser was at the origin of this advance, then came the compression of out- and intra-cavity pulses which completed the abrupt descent in duration. In this text, I propose guiding you in a memorial walk in this wonderful decade that goes from the era of a "dirty" dye laser, (the so-called CPM), to the era of "clean, easy-to-use" solid-state lasers (Ti:Sa). I will mention some of the major players in this epic, and I will attempt to evoke the bubbling of ideas that accompanies such an era.

First of all, I would like to stress that this contribution is by no way objective. It is only my partial vision of the beginning of the femtosecond adventure. Having spent part of the 1980s working in Bell Labs, the AT&T research laboratories based in Holmdel, New-Jersey, where the femto-adventure did start, I do report here on the very first steps of studies in the field of ultrafast phenomena in matter based on my memories.

The very beginning

Since the very beginning of the laser adventure, researchers in Bell Labs, Murray Hill were deeply involved in laser physics following the invention of the first continuous He–Ne gas laser, by Ali Javan, as early as December 1960[1]. The excitement was sustained by the frustration generated by the feeling of having let the competitors, specially T. H. Maiman, prevail in the race toward the invention of the laser. The feeling at the place was such that every young researcher dreamed he would be the inventor of a new transistor or a new laser.

*charles.hirlimann@ipcms.unistra.fr

DOI: 10.1051/978-2-7598-2719-0.c001

The 1970s saw the development of dye lasers, the successful model of which was that of active media made up of laminar jets of ethylene glycol dissolving organic molecules placed inside the optical cavity. A laser cavity initially contained a jet acting as a gain medium; Rhodamine 6G was the most popular dye for that purpose. Due to its Fabry–Pérot interferometer nature, any linear laser cavity only accepts a discrete series of frequencies, the so-called modes of the cavity, the frequency spacing of which is determined by the cavity length and their number by the width of the gain available (more details can be found in[2] and references herein). This was the starting basic tool towards producing femtosecond pulses.

If one adds a device inside the cavity of a laser that modulates its quality factor (Q-factor) by introducing periodic losses at the spacing frequency of its modes, then it ensures that the modes are synchronized with each other. In addition, the synchronous superposition of several equi-spaced light frequencies leads, by constructive interference, to the formation of a light pulse! Which is exactly what one is looking for in the field of light pulse production. The key is: the larger the range of frequencies additively superimposed, the shorter the resulting light pulse. This synchronization of the modes is named mode-locking.

Passive mode-locking. Many ways have been explored for modulating one or the other of the optical properties of a laser cavity in order to synchronize the modes. The most widespread technique was at first the active modulation of the refractive index of a prism using an acoustic wave. Placed inside the cavity of gas lasers, such a prism induced periodical losses insuring the synchronization of the modes and allowing the routine production of light pulses in the picosecond regime. Spectroscopy's need for tunable light sources has led to the development of gas-lasers-pumped, wide-gain dye lasers allowing for the selection of an intracavity frequency band. Then it was discovered that adding inside the laser cavity another dye jet that would vehiculate a saturable absorber would produce a Q-factor modulation at the frequency of the cavity and, therefore, induce "passive mode-locking", achieving tunable picosecond pulses. The quality of the "mode-locking" is dependent on the relative position inside the cavity of the gain medium and the saturable absorber (see figure 1.1 and more details in reference[3]). The two pulses counter-propagating in the cavity do automatically collide inside the saturable absorber for this corresponds to a maximum induced transparency and therefore to a minimum in the losses. The saturation process of the absorption is more efficient, the depth of the modulation is higher, and the efficiency of the mode-locking process improves. At the time of pulse collision a transient "standing-wave" is created inside the saturable jet that interacts with the Fabry–Pérot cavity standing-wave.

Using such a scheme Jean-Claude Diels was the very first researcher to use the word femtosecond[4] to characterize sub-picosecond optical pulses. Since the spatial extension of a 100 fs light pulse is approximately 30 μm, for producing light pulses with this duration, the thickness of the gain and saturable jets had to be of the same order of magnitude. The inevitable variations of the operating conditions of a laser do induce instabilities in the Fabry–Pérot behavior of the cavity and make such a system inherently unstable.

Therefore the origin of femto lasers may rather be traced down to an article published in 1981[5].

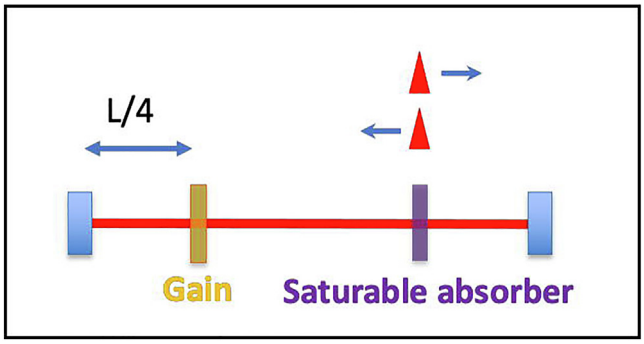

FIG. 1.1 – Linear laser cavity with both a gain medium and a medium which absorption can saturate for high enough light intensities. In such a configuration the transparency of the cavity is modulated at its exact frequency: $\vartheta = \frac{c}{2L}$, with c the light velocity, L the cavity length. When running, the cavity admits two counter-propagating pulses that do collide inside the saturable absorber, increasing the Q-factor modulation contrast as compared to the saturation by unique propagating pulses and therefore insuring a high-quality mode-locking process. In this arrangement it is necessary to adjust the position of the saturable absorber to insure the collision of the pulses.

Generation of optical pulses shorter than 0.1 psec by colliding pulse mode locking

Appl. Phys. Lett. **38**, 671 (1981)
R.L. Fork, B.I. Greene, and C.V. Shank

This paper described a ring dye laser in which mode-locking was achieved through the automatic collision of the counter-propagating pulses of the cavity inside a saturable absorber (see figure 1.2). This configuration was called "CPM" for colliding pulsed mode-locked dye laser; it allowed, in a very simple manner, to get rid of the spectrometer nature of the laser cavity and to highly improve the stability of the device.

Charles Shank[6] was heading the Quantum Physics and Electronic Research Department at Bell Labs, Holmdel New-Jersey, and he had a large experience in the physics of dye lasers. He was best known for his design of distributed feedback dye lasers[7]. He was pushing forwards to achieving the shortest possible light pulses. Richard Fork[8] was granted a PhD in Physics at MIT and at the time was the only permanent member of Shank's team and he was well known for his studies of active mode-locking in gas lasers[9].

Benjamin Greene, was a post-doc in Bell Labs @ Murray Hill, New-Jersey, and he spent time learning the physics of short pulses generating dye lasers in Shank's group. He is the one who suggested the ring design of the CPM.

The original CPM was made available during the year 1980 (figures 1.3 and 1.4). The very original machine was a tricky one. The nozzle flowing the saturable absorber jet had to be squeezed down as to produce laminar jets having a thickness of the order of 50 μm, and one of the folding mirrors of the cavity had to admit a few % losses in the yellow part of the visible spectrum for pushing the operating wavelength to the

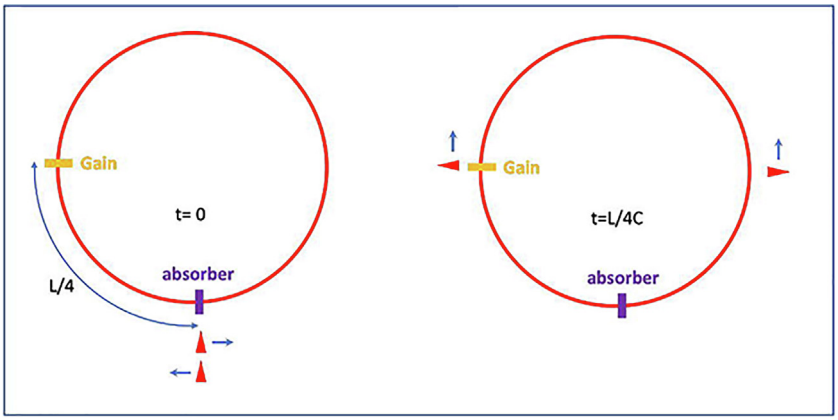

FIG. 1.2 – Schematics of the pulse timing in the colliding pulse mode-locked ring dye laser CPM. Gain and absorber jets are set apart at a distance that is of the order of ¼ of the full length of the ring. The design is equivalent to the one in figure 1.1, the difference being that the cavity is not any more a Fabry–Pérot interferometer inducing instabilities. No position adjustement of the saturable absorber is anymore necessary. This resulted in a better stability and shorter pulses. The gain recovery time is short enough as to insure symmetrical saturated amplification to the counter-propagating pulses.

"magic" value of 620 nm (2 eV). This highly non-linear apparatus had a spontaneous chaotic behavior, following a Feigenbaum route to chaos as a function of the pumping laser power[i,10]. With fast reacting dyes, when increasing the pumping power, the increased amount of energy stored in the gain medium first allows for the apparition of a couple of counter-propagating pulses; further pumping increase induces further doubling of the number of pulses in a way that is controlled by the non-linearity of both the gain and the absorber saturation. With only small uncontrolled power changes of the pumping laser (a CW Ar^+ gas laser running @ 514 nm) the CPM running rep-rate would quite often jump from 100 to 200 MHz meaning a doubling of the pulses. Performing experiments needed one operator in charge of the experiment and another one in charge of the proper functioning of the laser.

Last but not least, the specific aspect of the new "femtosecond" regime was the absolute need to care about the phase of the various components of the wide spectra of the pulses that covers almost the full range of the visible frequencies. Because of the frequency dispersion of the optical index in matter when a light pulse travels through some transparent material, the blue components of the spectrum are more delayed than the red ones and the net result is a time spreading of the pulse (see figure 1.5 and in this book: chapters 2 and 4). Curiously, this problem of frequency dispersion had an "on-the-shelf" solution available since 1964 that was not yet applied: the Gires–Tournois interferometer[11] (GTI). François Gires and Pierre Tournois demonstrated the possibility to construct an optical device inducing an

[i]Personal observation, never published.

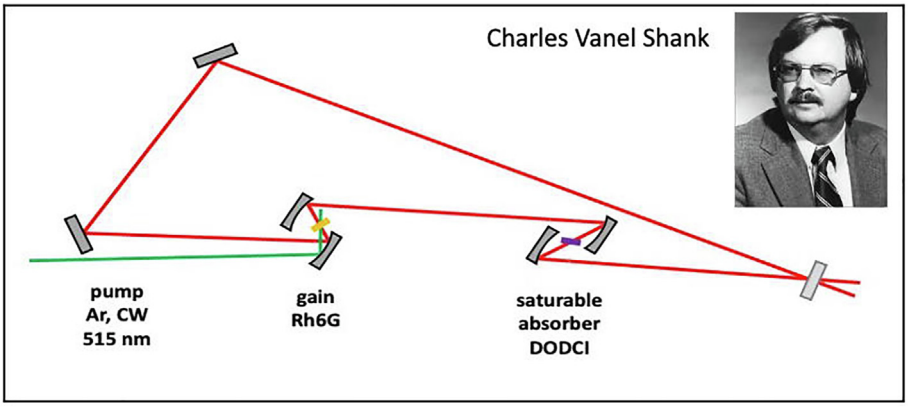

FIG. 1.3 – Sketch of the CPM laser. The gain jet and the absorber jet are separated by a distance close to a quarter of the perimeter of the "ring" cavity (not a critical parameter). The upper mirror of the cavity admits losses in the yellow part of the gain spectrum in order to force the central lasing wavelength to 620 nm that is imposed by the gain and absorber spectra. One of the two exiting red beams is used for characterizations: pulse duration, repetition rate, peak intensity, wavelength. The total number of adjustments degrees of freedom in such a set-up is around 50.

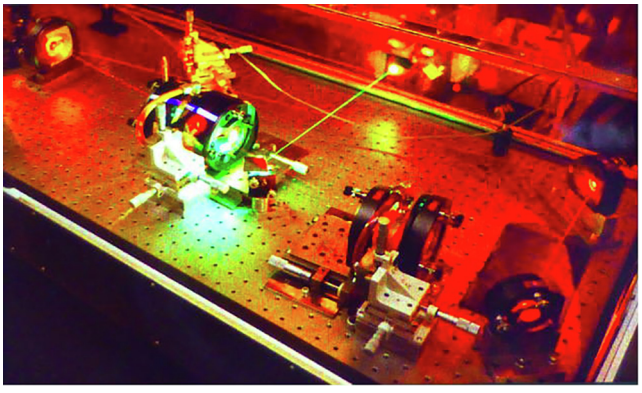

FIG. 1.4 – Photograph of the first CPM built in Bell labs, Holmdel, N-J.

opposite (*i.e.* negative) frequency dispersion that could be used to "compress" positively chirped optical pulses[ii]. Treacy[12] transposed the GTI into a dual pair of gratings that allowed for the adjustment of the frequency chirp of a light pulse. The two pairs of gratings do disperse the frequencies of a light pulse, collimate the beam, and counter disperse the frequencies in such a way that red frequencies traveling in air do experience a shorter pass and could catch up with the blue frequencies. For a 10 fs pulse at 620 nm the spectrum full width at half maximum (FWHM) is 62 nm, *i.e.* 15% of the visible spectrum. Taking into account the wings of the spectrum, the pulse actually covers most of the visible window[13].

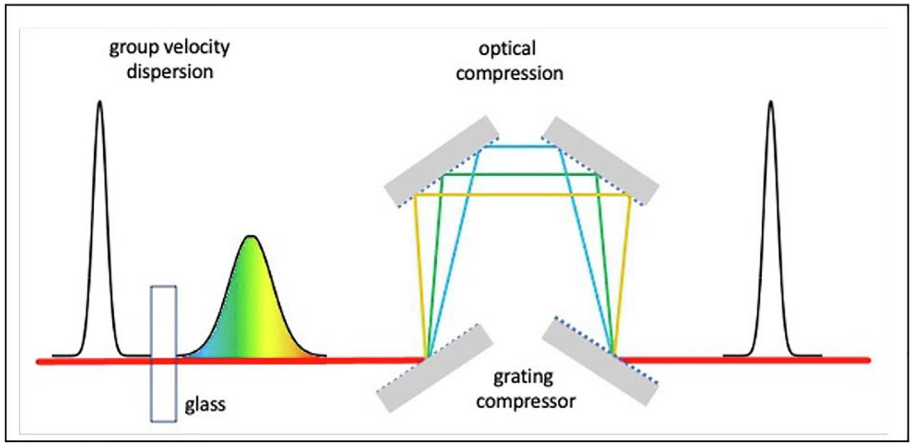

FIG. 1.5 – Schematics of a gratings pulse compression device (Treacy compressor). A short light pulse (left) crosses a plate of glass thereby undergoing positive group velocity dispersion and thus time broadening. The red light wavelength components do travel faster in glass than the blue ones. A set of two pairs of diffraction gratings is arranged in such a way that the optical path in air of the redder wavelengths is longer than that of the bluest ones, thus allowing the recovering of the original duration of the pulse.

Up to the end of the year 1981, a dye amplifier was developed that raised the energy of the light pulses up to 350 μJ (see figure 1.6). It was designed as a set of dye cells pumped by the green light of a frequency-doubled Nd:YAG laser operating @ 10 Hz rep-rate, separated by saturable dye jets. The energy was large enough to

[ii]Pierre Tournois and François Gires were both employees of the C. S. F. company (Compagnie générale de télégraphie sans fil) that had based a large research facility in Corbeville near Orsay, France. This company had a large experience in chirped pulse amplification (CPA), spreading and compressing microwave pulses used in radars. On a Sunday, they went to their boss's home for a party and just for the fun of it they decided to calculate a device that could be operated in the optical frequency domain. The article, presenting their results, ends with the premonitory sentence: "La compression d'impulsion laser apportera peut-être une solution au problème des très hautes puissances". Perhaps will laser pulse compression provide a solution to the problem of very high pulse powers.

allow for continuum generation in an optical fiber. 0.3 to 3 GW peak powers were reached with pulse duration ranging from 70 to 90 fs[14,iii].

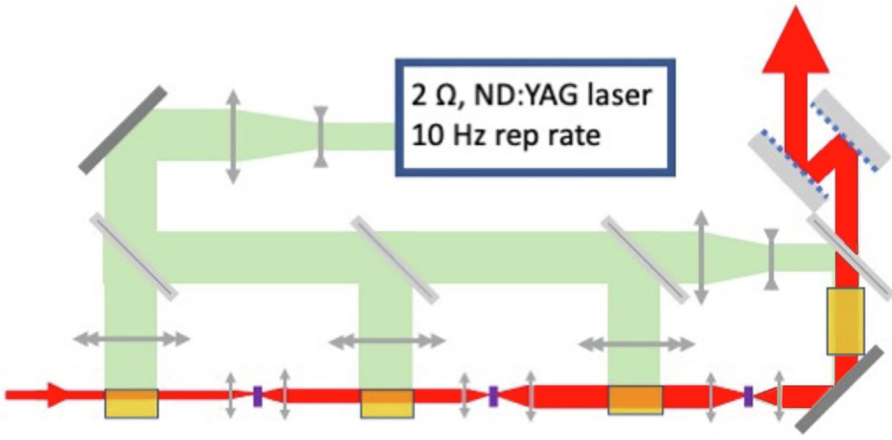

FIG. 1.6 – Sketch of the four-stage amplifier developed for the femtosecond pulses.

Time to do experiments

It is one thing to carry out, in a short period of time, a laser physics experiment to demonstrate some desired property; it is another one to use this property to perform an experiment requiring a long recording duration.

Despite its intrinsic instability, at the end of the year 1981, the full system, oscillator + amplifier, was ready for experiments. In addition, the first experiment addressed the question: "how long does it take for silicon to melt when suddenly illuminated with a powerful femtosecond light pulse?"

Two experiments were performed to answer the question.

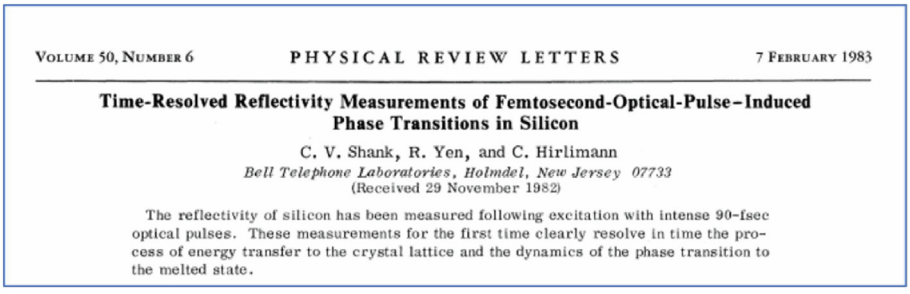

VOLUME 50, NUMBER 6 PHYSICAL REVIEW LETTERS 7 FEBRUARY 1983

Time-Resolved Reflectivity Measurements of Femtosecond-Optical-Pulse–Induced Phase Transitions in Silicon

C. V. Shank, R. Yen, and C. Hirlimann
Bell Telephone Laboratories, Holmdel, New Jersey 07733
(Received 29 November 1982)

The reflectivity of silicon has been measured following excitation with intense 90-fsec optical pulses. These measurements for the first time clearly resolve in time the process of energy transfer to the crystal lattice and the dynamics of the phase transition to the melted state.

[iii] Arnold Migus, one of the former directors of the French CNRS (Centre National de la Recherche Scientifique), was an invited Professor in Shank's lab at the time the amplifier was being set-up.

In the first one[15], the reflection of a weak probe-pulse on silicon was measured as a function of time after the surface of a (111) oriented silicon wafer was hit by a powerful pump-pulse (0.1 μJ max – 90 fs) with central photon energy @ 2 eV[iv]. Three probing wavelengths ranging from blue to near infra-red were used and the pump intensity was varied with a full amplitude of 4. It was first established that the pump pulse, by breaking the covalent bond binding the silicon atoms, creates a dense electron-hole plasma that slowly decays ($\sim$ 10 ps) through diffusion in the bulk crystal. The picture is: at the end of the pump pulse, the energy of the light pulse is transferred to the electronic system inside the focal volume. Due to simple inertia[v], silicon atoms are still arranged as a crystal network with a large excess of energy (2 eV exciting photons compared to the silicon band gap 1.12 eV). The surface of the Si wafer is a perturbative symmetry breaker where melting (in the sense of a disordered distribution of atoms) starts creating a melting front that rapidly propagates inwards the high-density plasma crystal. At the lowest pump intensities, the reflectivity change from the reflectivity of still silicon is negative being governed by the electronic system, while at higher intensities and long (10 ps) pump-probe delay times, the reflectivity change is positive being the one of silicon in its molten phase. A modeling of the dynamical reflection curves was performed balancing the negative contribution of the plasma and the positive contribution of the molten volume in which the front velocity was used as a fitting parameter. For a pump intensity strong enough for melting to first occur, a melt-front propagation velocity of 6.2 10^5 cm/s was found, comparable to the velocity of sound in silicon crystals. For the highest pump intensities, 2.5 times larger, the melting-front velocity was 25 10^5 cm/s. These velocities were independent from the probe wavelength. It is worth noticing that the photo-melting process described here is pretty much different from the usual thermal melting of silicon. When heating a piece of silicon, the energy is transferred to the atoms and melting is considered to have taken place when the root mean square displacement of each atom is a fraction $x = 0.2$–0.25 of the dimension of the unit cell of the crystal (Lindemann's criterium). The phase transition goes through an increasing number of covalent bonds breaking down along with the increasing agitation of the atoms. On the contrary, in the photo-fusion process, the bonds are broken at first by the impinging photons and it takes some time for the atoms to disorder down to the molten phase.

This experiment gave a good inside view of the photo-melting process of silicon, but unfortunately one could only say that the melting of silicon lasts for a fraction of a picosecond.

[iv]Strangely enough the white light continuum needed for the reflectivity spectroscopy experiment was generated through a cell containing heavy water D_2O, which was supposed to be more efficient in the near infrared. Contrary to what's written in the article, the automatic generation of the raster pattern needed for ensuring the access of each impinging pulse (rep-rate 10 Hz) to a fresh silicon surface was not ready in time. So that the two in-charge post-docs, Richard Yen and myself, had to alternately relay to make the laser run smoothly and to hand-push the buttons of the stepping motors controllers, moving the silicon wafer. This took place in three sessions of 15 h, in one week. In the course of the experiments, at times the laser was running quietly, we could observe the Fabry–Pérot interference inside the molten volume, but the laser intensity fluctuations avoided reproducibility.

[v]The mass of a silicon atom is 75 000 times larger than the mass of an electron.

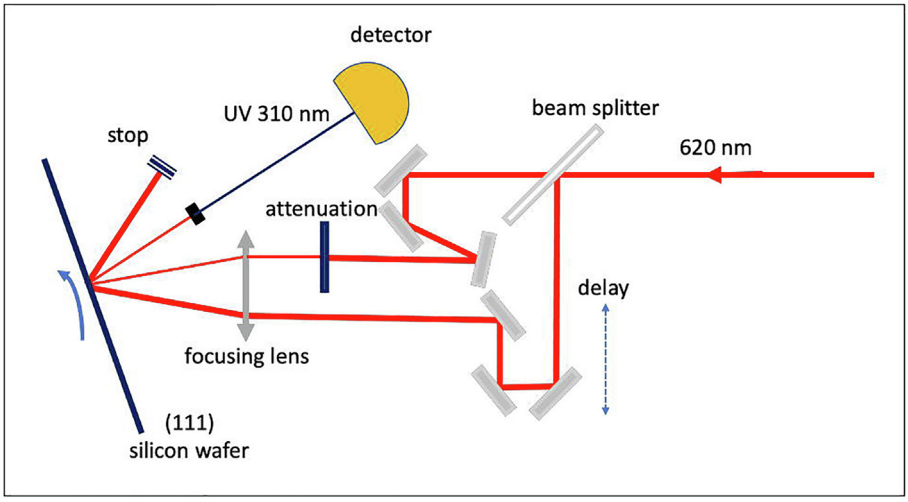

FIG. 1.7 – Experimental set-up for measuring the dynamics of the second harmonic generation at the silicon surface under the effect of an intense light pulse. The amplified 620 nm pulse train (10 Hz rep-rate) is split into an intense pump beam that passes through a delay line and a weak probe beam that reflects on the molten silicon. The very weak second harmonic signal generated by the probe on the surface of the excited spot is measured. The silicon wafer is moved in a spiraling way to ensure that a new surface is presented in front of each of the pump pulses.

In a second very clear experiment[16], the symmetry of the excited silicon was measured (see figure 1.7). Being central-symmetric silicon only generates second harmonic light from its surface where this symmetry is broken. The experiment consisted in measuring the second harmonic generated by a weak probe-pulse as a function of the delay with the strong excitation-pulse, the same as in the previous experiment. With no exciting pulse (−10 ps), the second harmonic intensity as a function of the angular position of the crystal fully exhibits the ternary symmetry of the (111) axis in silicon (figure 1.8a @ −10 ps), while 3 ps after the excitation-pulse the emission is fully isotropic demonstrating the molten nature of the material (see figure 1.8a @ 3 ps). Figure 1.8b shows the time evolution of the probe second harmonic generation in the 120° direction of the wafer. From these results, the photo-induced solid–liquid phase transition has been estimated to be 300 fs[vi]!

[vi]In this experiment, the 10 Hz rotation-translation of the Silicon wafer was fully computer controlled. There was no need for white light generation, making life easier. The difficulty was in distinguishing the very weak second harmonic light generated by the weak probe (10% of the pump intensity) from the strong signal generated by the pump.

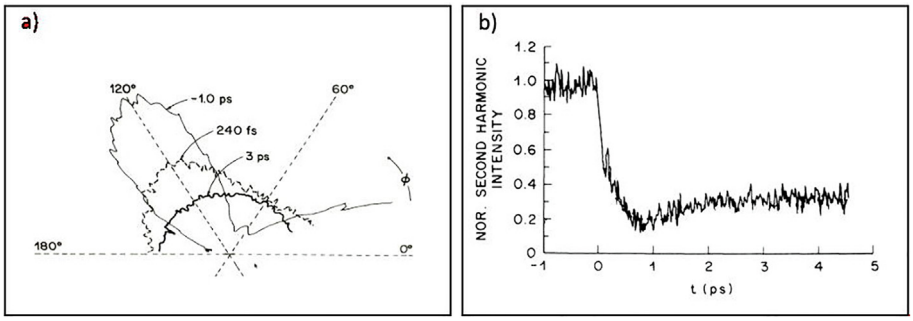

FIG. 1.8 – (a) Second harmonic intensity as a function of time and angular position of the silicon crystal. (b) Dynamics of the second harmonic intensity in the 120° direction. © With permission of Optica Publishing Group.

Let's stabilize the CPM[vii]

Despite numerous successful experiments performed using a CPM dye laser, there was clearly a strong need for some way to dramatically decrease the intensity fluctuations of the laser.

In the course of the year 1982, Shank's group received a preprint from Jean-Claude Diels' group at North Texas State University[viii] in which these authors stated that having the CPM laser pulses crossing a plate of glass outside the cavity did shorten them, demonstrating that negative chirp was taking place inside the cavity. This negative chirp was understood as being due to the excitation of the saturable absorber below its energy resonance and its value was shown to depend on the saturation intensity and therefore it could be "controlled" through the dye concentration in the absorber jet. In order to optimize the group velocity dispersion (GVD) experienced by the light pulses, the authors did introduced a prism on the beam way inside the ring cavity so as to allow for the variation of the length of glass the pulses had to cross, therefore introducing a "controlled" amount of positive GVD to compensate for the negative GVD induced by the saturable absorber. Playing around with the absorber dye concentration and the position of the prism, they succeeded in producing 60 fs pulses, thereby breaking down the previous 90 fs record[17].

At the time, some thinking was going along as to replace the gratings in a pulse compressor by prisms because Brewster prisms do not introduce optical losses. In the absence of any theoretical support, there was no reason to believe that there could be some configuration of a set of prisms that could produce net negative dispersion due to their intrinsic positive dispersion.

[vii] In a first attempt towards stabilization, in year 1984, the squeezed metal tubes used for producing the laminar thin jets were replaced with expensive polished sapphire nozzles that smoothed down the jets. The real purpose of these nozzles was to slow down competitors who couldn't afford their buying.

[viii] This work was co-authored by our colleague Joël Fontaine of Strasbourg who was at the time a post-doc in Diels's group.

Janis Valdmanis worked at Bell Labs, in Murray Hill, N-J, on ultra-fast electro-optical effects in semiconductors. To further push his research, he joined forces with Richard Fork in Bell Labs Holmdel and together, they empirically developed a new CPM in which they introduced four intra-cavity prisms[18] for controlling the group velocity dispersion of the pulses (see figure 1.9), and it worked! At the time John Gordon was "Mister soliton" in the team having demonstrated the solitonic propagation of light in mono-mode optical fibers[19]. He argued that with this design, the femtosecond laser had gone from a purely passively mode-locked cavity to a soliton-like mode-locked one. Indeed, the new laser contained the same kind of ingredients that are found in the one-dimensional soliton propagation of a wave: the exact compensation of a non-linear negative group velocity dispersion (laser cavity components) by a positive group-velocity dispersion (prisms). This compensation effect leads to a stabilization of the mode-locking in the cavity and therefore to a very marked improvement in the stability of the intensity of the produced laser pulses. However, since this compensation does not occur continuously during the propagation, but alternately by passing through the prisms and then through the other components of the cavity, it is not possible to speak of soliton propagation. Moreover, during their propagation along the cavity, the light pulses do suffer compensating gain and losses which is not the case for real solitons. The terms soliton-like and quasi-soliton have therefore been used to describe the new mode of operation of the laser. The new record for a laser pulse duration was then 30 fs[ix]!

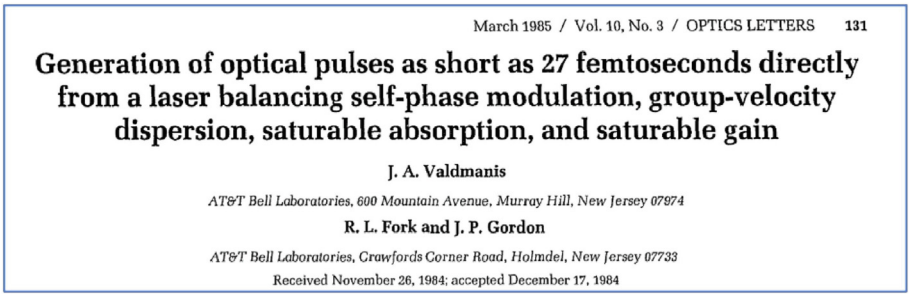

March 1985 / Vol. 10, No. 3 / OPTICS LETTERS 131

Generation of optical pulses as short as 27 femtoseconds directly from a laser balancing self-phase modulation, group-velocity dispersion, saturable absorption, and saturable gain

J. A. Valdmanis

AT&T Bell Laboratories, 600 Mountain Avenue, Murray Hill, New Jersey 07974

R. L. Fork and J. P. Gordon

AT&T Bell Laboratories, Crawfords Corner Road, Holmdel, New Jersey 07733

Received November 26, 1984; accepted December 17, 1984

Oscar Martinez was a member of the Argentinian Scientific and Technical Research Council at the time he visited Shank's team as a post-doc. He is the one who triggered the quantitative understanding of the prism optical compressor[20]. He, and coworkers, gave the theoretical ground to prism compressor, showing that despite their intrinsic positive group velocity dispersive behavior, ad hoc geometries can be designed to engineer a net negative dispersion. Brewster prisms had to be used at their minimum deviation angle so that no distortion was added to the beams crossing

[ix]Fred Beisser, who worked as technical support in Shank's team, once told me that the very short pulses duration was only available right after the renewal of the dyes. It was especially true for Rhodamine 6G that only had a half-an-hour lifetime at 30 fs. Fred died november 1, 2021 in East Brunswick, NJ, at age 79.

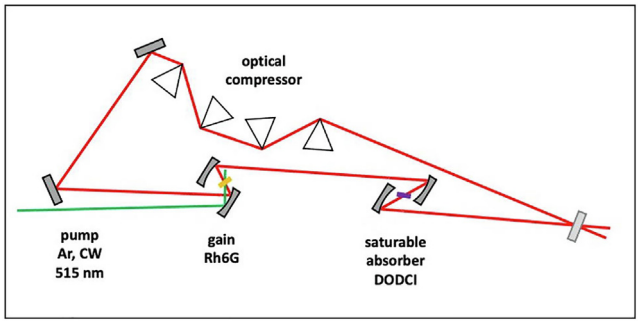

FIG. 1.9 – Sketch of a compensated CPM. In an analogy with the 4-gratings compressor, 4 prisms were empirically set-up inside the cavity of the laser. Silica Brewster prisms have been used in which when at the minimum deflection the light beams reflect at the Brewster angle on the inlet and outlet faces. In this way, light polarized in the plane of incidence does not suffer any loss by reflection. Polarization in the plane of incidence is obtained by setting the gain and saturable absorber jets also at the Brewster angle, with the vertical light polarization of the gas laser being set horizontal with a periscope.

the prisms and no reflection did occur on the eight interfaces when the light polarization was set to be in the plane of incidence (P polarization). The polarization in the cavity was controlled by setting the gain and saturable jets at the Brewster angle.

Then came the experimental demonstration by François Salin and co-workers[21] at the Institut d'Optique at Orsay, France, of the very soliton-like nature of the CPM behavior. They experimentally demonstrated that the quasi-soliton propagation was central in the operation of the dispersion compensated CPM.[x] Solitons of order one to three were observed using clever stroboscopic-like techniques allowing for the observation of the pulse shape (through autocorrelation measurements) and the spectrum (multichannel analysis) of the pulse train of a compensated CPM laser at varying time delays along the full period of solitons. The various soliton regimes were selected through defocusing of the laser beam onto the saturable absorber jet and a minute adjustment of the four prism compensator.

VOLUME 60, NUMBER 7 PHYSICAL REVIEW LETTERS 15 FEBRUARY 1988

Experimental Observation of Nonsymmetrical $N = 2$ Solitons in a Femtosecond Laser

F. Salin, P. Grangier, G. Roger, and A. Brun
Institut d'Optique Théorique et Appliquée, Université Paris-Sud, 91406 Orsay Cédex, France
(Received 29 September 1987)

[x]Remarkably, during his thesis defense, in response to a question, François Salin affirmed that once started, the compensated CPM would continue functioning even if the dye was removed from the saturable absorber jet because it is the self-phase modulation in the solvent which is the central element of the quasi-soliton operation.

Here comes in the "magic mode-locking"

The recognition that the quasi-soliton behavior of the CPM was mainly due to the spectrum broadening associated to the self-phase modulation non-linear effect in the dyes' solvent in the cavity naturally lead to the main evolution of the femtosecond lasers.

During the year 1990, Wilson Sibbett a Professor at St Andrews University, Scotland, designed a new, much simpler cavity for generating ultrashort light pulses[22] (see figure 1.10).

42 OPTICS LETTERS / Vol. 16, No. 1 / January 1, 1991

60-fsec pulse generation from a self-mode-locked Ti:sapphire laser

D. E. Spence, P. N. Kean, and W. Sibbett

J. F. Allen Physics Research Laboratories, Department of Physics and Astronomy, University of St. Andrews, North Haugh, St. Andrews,

Received July 20, 1990; accepted November 2, 1990

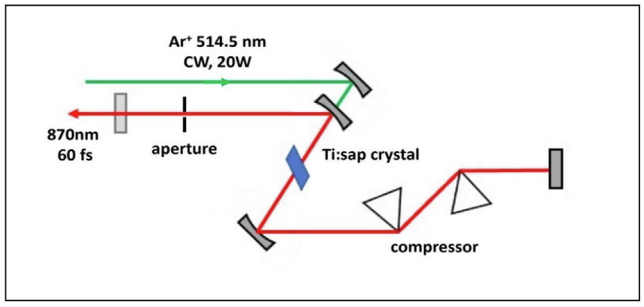

FIG. 1.10 – Wilson Sibbett's first Titanium doped Sapphire crystal laser. The collision of pulses being unnecessary, the cavity has been set back to a linear one therefore reducing the number of prisms in the optical compressor to only two. A strong self-phase modulation process does take place in the gain crystal that insures passive mode-locking of a large frequency spectrum and a quasi-soliton propagation mode is set into action by the optical compressor.

Wilson was working at the time on solid state gain materials having a large emission spectrum. In the field of research of tunable lasers, the Holy Grail of the time was to get rid of all those tedious-maintenance dye jets that were the source of so many stains. The dynamic nature of the jets made them primarily important sources of instabilities in laser cavities, and solid gain media were highly desired. Wilson was focusing on the study of sapphire crystals doped with titanium having a very large emission spectrum in the deep red part of the visible spectrum. For that purpose, he had replaced the dye jet of a commercially available tunable picosecond laser with a Ti:Sapphire crystal. In the course of his experiments, he noticed that the

laser would randomly start running mode-locked, emitting a train of short pulses. He then discovered that applying a small perturbation to the laser cavity did start the mode-locking behavior. Noticing a strong group velocity dispersion of the pulses he thought of placing a pair of Brewster prisms with a high refractive index in the path of the beam. Fortunately, there was enough room in the cavity of his laser! The light pulses he produced that way were 60 fs wide! Bingo, no more jet.

At first, the interplay between the group velocity dispersion produced by the self-phase modulation and the prism compressor described by François Salin had not yet sufficiently diffused in the field of laser physics: one used the words "magic mode-locking" for describing the functioning of the Ti:Sapphire laser. The new laser design was much simpler: no more ring cavity, no more saturable absorber, only one medium insuring both a large bandwidth gain and self-phase modulation mode-locking, and only two prisms to compensate for the frequency chirp induced by both the propagation of the pulses inside the gain crystal and the self-phase modulation process.

The year 1990 clearly marks the maturity of the femtosecond pulse generation techniques.

A few words on the interplay between research and industry

Very early in the decade of the 1980s, the major producers of ionized argon lasers were interested in new emerging techniques for producing ultrashort pulses. With the help of Patrick Georges at the "Institut d'Optique" in Orsay, France, the Photonetics/Coherent company, developed a table-top compensated dye CPM laser[xi]. It was no commercial hit, but nevertheless it helped spread the new paradigms among the laser community, seeding the perspective of new pertinent experiments in the minds of physicists, chemists, and biologists. At the time Sibbett discovered the "magic mode-locking", the Coherent company was exploring a Kerr lens mode-locking device (the self-phase modulation process taking place in a Kerr medium, outside the gain medium) that further helped develop their own Ti:Sa laser.

As soon as the year 1991[xii], the two major laser companies launched their long-lasting competition in the field of solid-state femto-lasers: Tsunami, Mira…

The occurrence on the market of the Ti:sapphire laser was an essential turning point in the democratization of ultra-fast optics. This laser, simple in its use and maintenance, could therefore be put into all hands and became the source of a multitude of new fields of knowledge in physics, chemistry and biology.

[xi]The enthusiasm of the company's representative, Jean-Luc Tapié, a former student of Gérard Mourou in Rochester, presenting the CPM dye laser on scientific fairs always was a great pleasure.

[xii]During the fall of the year 1991, I visited Jim Kafka, CTO for Spectra-Physics in Palo-Alto, CA. He showed me both the huge hangar they had been built to house a large power laser diode factory, but more strikingly, I could take a look at the new mechanical design of their passively mode-locked picosecond dye laser. Jim was very proud explaining that they had just decided to change lanes and follow Wilson Sibbett in his design of a Ti:Sapphire femto-laser.

This interaction between research and industry in the field of femto-lasers is an excellent and edifying counter-example of the "death-valley" deadly separating basic research from innovation, separating transfer of new concepts from the academic world to industries, that funding agencies are, still, always complaining about. In this field, there has always been strong dialectic exchanges between basic researchers and companies' engineers. There are two main reasons for this state of affairs. The first one is the permanent proximity of laser manufacturers to their consumers, and staff in both of them had gone through the same type of higher education degrees and could relate to each other. There is maybe another reason, more subtle: at the time of the development of the CPM the telephone company AT&T, owner of the Bell Labs, was still a regulated company which inventions had to go "open access".

Ever shorter light pulses

The possibilities of producing really short pulses from a laser cavity had come to an end. Diving further towards shorter pulses then needed external treatments (See figure 1.11).

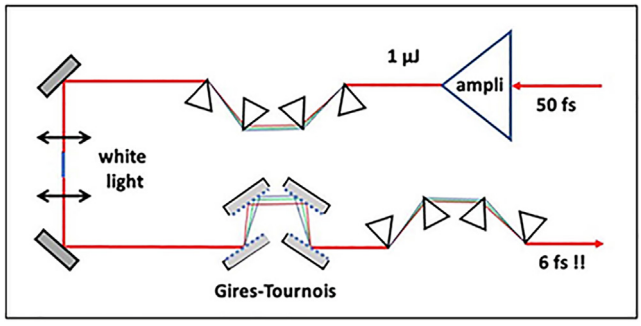

FIG. 1.11 – Designs of a very short optical pulse generator. 50 fs amplified pulses with an energy of 1 μJ are first set to their Fourier transform limit through a prism optical compressor. Producing pulses 10 times shorter means widening the light spectrum by the same amount; this is achieved by self-phase modulation inside a short single-mode optical fiber 1 cm long. The resulting white light pulse is then recompressed to third-order dispersion via a grating + double prism optical compressor resulting in ultra-short light pulses of 6 fs.

This was performed in Shank's team at Bell Labs, by Carlos Henrique de Brito Cruz from the University of Campinas in Brazil; at the time he was working as an invited professor[23]. Compressed 50 fs pulses were focused into a short mono-mode optical fiber in such conditions as to favor self-phase modulation, spectrum broadening against stimulated Brillouin and Raman scattering (see in this book chapter 4). The real difficulty in generating ultrashort pulses is to properly compensate the phase distortion in the broadened spectrum. It had already been recognized that compensation of the dispersion up to the cubic phase distortion is a key ingredient for

taking full advantage of the full spectral width. The solution to this problem came from the discovery that the cubic phase distortion generated by a prism compressor can be made negative, while the equivalent distortion in a grating compressor remains positive. This change in sign indicates that the use of both types of optical compressors allows one to properly compensate for phase distortion up to the third order. The resulting 6 fs light pulses at 620 nm do correspond to only three oscillations of the electromagnetic field at half intensity maximum. This technique, Ti:Sa + post-compression, is nowadays routinely used for the production of intense, few-cycle Vis-IR pulses needed for producing XUV, electron bursts, high-order harmonic generation (HHG), attosecond pulses, and more (see in this book chapters 4 and 6).

So, over a period of 40 years, the duration of light pulses in the visible spectrum decreased by twelve orders of magnitude! This, of course, is not the end of the story as we know that the attosecond regime was reached in 2001[24].

References

[1] Javan A., Bennett W.R., Jr., Herriott D.R. (1961, February 1) Population inversion and continuous optical maser oscillation in a gas discharge containing a He–Ne mixture, *Phys. Rev. Lett.* **6**, 106.

[2] Rullière C. (Ed.). (2003) *Femtosecond laser pulses*. Springer.

[3] Fork R.L., Shank C.V., Yen R., Hirlimann C.A. (1983) Femtosecond optical pulses, *IEEE J. Quantum Electron. QE* **19**.

[4] Diels J.-C., Van Stryland E., Benedict G. (1978, April) Generation and measurement of 200 femtosecond optical pulses, *Opt. Commun.* **25**, 93.

[5] Fork R.L., Greene B.I., Shank C.V. (1981) Generation of optical pulses shorter than 0.1 psec by colliding pulse mode locking, *Appl. Phys. Lett.* **38**, 671.

[6] https://en.wikipedia.org/wiki/Charles_V._Shank.

[7] Shank C.V., Njorkholm J.E., Kogelnick H. (1971) *Appl. Phys. Lett.* **18**, 306.

[8] Richard Fork est décédé le 16 mai 2018 à Huntsville, Alabama.

[9] Hargrove E., Fork R.L., Pollack M.A. (1964) Locking of He–Ne laser modes induced by synchronous intracavity modulation, *Appl. Phys. Lett.* **5**, 4.

[10] Locquet A. (2020) Routes to chaos of a semiconductor laser subjected to external optical feedback: A review, *Photonics* **7**, 22.

[11] Gires F., Tournois P. (1964, June 22) Interféromètre utilisable pour la compression d'impulsions lumineuses modulées en fréquence, *C. R. Hebd. Séance Acad. Sci.* **258**, 6112.

[12] Treacy E.B. (1969) Optical pulse compression with diffraction gratings, *IEEE J. Quantum Electron.* **5**, 454.

[13] Rullière C. (Ed.). (2003) *Femtosecond laser pulses*. Springer, p. 31.

[14] Fork R.L., Shank C.V., Yen R., Hirlimann C.A. (1983) Femtosecond optical pulses, *IEEE J. Quantum Electron. QE* **19**.

[15] Shank C.V., Yen R., Hirlimann C. (1983, February 7) Time-resolved reflectivity measurements of femtosecond-optical-pulse-induced phase transitions in silicon, *Phys. Rev. Lett.* **50,** 454.

[16] Shank C.V., Yen R., Hirlimann C. (1983, September 5) Femtosecond-time-resolved surface structural dynamics of optically excited silicon, *Phys. Rev. Lett.* **51**, 900.

[17] Dietel W., Fontaine J.J., Diels J.-C. (1983, January) Intracavity pulse compression with glass: A new method of generating pulses shorter than 60 fsec, *Opt. Lett.* **8**, 4.

[18] Valdmanis J.A., Fork R.L., Gordon J.P. (1985) Generation of optical pulses as short as 27 femtoseconds directly from a laser balancing self-phase modulation, group-velocity dispersion, saturable absorption, and saturable gain, *Opt. Lett.*, **10**, 131.

[19] Mollenauer L.F., Stolen R.H., Gordon J.P. (1980) Experimental observation of picosecond pulse narrowing and solitons in optical fibers, *Phys. Rev. Lett.* **45**, 1095.

[20] Fork R.L., Martinez O.E., Gordon J.P. (1984) Negative dispersion using pairs of prisms, *Opt. Lett.* **9**, 150.

[21] Salin F., Grangier P., Roger G., Brun A. (1988) Experimental observation of non-symmetrical $N = 2$ solitons in a femtosecond laser, *Phys. Rev. Lett.* **60**, 569.

[22] Spence D.E., Kean P.N., Sibbett W. (1991) 60-fsec pulse generation from a self-mode-locked Ti:sapphire laser, *Opt. Lett.* **16**, 42.

[23] Fork R.L., Brito Cruz C.H., Becker P.C., Shank C.V. (1987) Compression of optical pulses to six femtoseconds by using cubic phase compensation, *Opt. Lett.* **12**, 483.

[24] Paul P.M., Toma E.S., Breger P., Mullot G., Augé F., Balcou Ph., Muller H.G., Agostini P. (2001) Observation of a train of attosecond pulses from high harmonic generation, *Science* **292**, 1689.

Chapter 2

Generation of Femtosecond Pulses

Adeline Bonvalet*

Laboratoire d'Optique et Biosciences
CNRS, INSERM, École Polytechnique, I.P. Paris, Palaiseau, France

2.1 Introduction

Femtosecond lasers that appeared in the 1980s have since undergone numerous developments, while the scope of their applications has broadened. The first applications mainly exploited the duration of femtosecond pulses to improve the temporal resolution of spectroscopic experiments seeking to observe the very first steps of physical or biological processes. Since then, a wide range of applications have emerged, taking advantage of the remarkable properties of femtosecond pulses. The concentration of the energy, in space and time, has led to many scientific and industrial developments from material processing to new imaging techniques to name a few. The very particular characteristics of the spectrum of these pulses, equivalent to a frequency comb, have also revolutionized metrology. In this document, we present the properties of femtosecond pulses and provide some tools to describe them. We briefly present the central concept of spectral phase and discuss the key elements of a femtosecond laser cavity, namely modelocking and group velocity management. Some basic oscillator architectures are presented, keeping in mind that the world of femtosecond lasers is today extremely vast.

2.2 Description of Ultrashort Light Pulses

2.2.1 Real and Complex Electric Fields

Optical pulses can be fully described by a real electric field $E(t)$ whereas a harmonic wave is multiplied with an envelope function. However, a description in the spectral

*adeline.bonvalet@polytechnique.edu

DOI: 10.1051/978-2-7598-2719-0.c002

domain is necessary to have a complete understanding of the structure and properties of femtosecond pulses. The electric field can indeed be seen as the superposition of monochromatic waves, and the Fourier decomposition is used to describe it at a fixed point in space

$$E(t) = \int E(\omega) \exp(-i\omega t) \frac{d\omega}{2\pi} \tag{2.1}$$

with

$$E(\omega) = \int E(t) \exp(i\omega t)\, dt \tag{2.2}$$

$E(\omega)$ is the inverse Fourier transform of $E(t)$ and is a complex quantity. Since the field $E(t)$ is a real value, it verifies

$$\begin{aligned} E^*(t) &= E(t) \\ E^*(\omega) &= E(-\omega) \end{aligned} \tag{2.3}$$

Hence knowledge of the spectrum for positive frequencies is sufficient for a full characterization of the light field. We can define a complex field containing only the positive part of the spectrum

$$\mathcal{E}(\omega) = 2\Theta(\omega) E(\omega) \tag{2.4}$$

where $\Theta(\omega)$ is the Heaviside function.

The Fourier transform of this field is termed the analytic field

$$\mathcal{E}(t) = FT(\mathcal{E}(\omega)) \tag{2.5}$$

The steps leading to this complex representation of the pulse are represented in figure 2.1.

These temporal and spectral fields are complex and can thus be expressed in terms of their amplitude and phase

$$\begin{aligned} \mathcal{E}(t) &= |\mathcal{E}(t)| \exp(i\phi(t)) \\ \mathcal{E}(\omega) &= |\mathcal{E}(\omega)| \exp(i\varphi(\omega)) \end{aligned} \tag{2.6}$$

$|\mathcal{E}(t)|$, $|\mathcal{E}(\omega)|$, $\phi(t)$, $\varphi(\omega)$ are, respectively, the temporal and spectral amplitudes, and the temporal and spectral phases. The real electric fields can be retrieved by the relations

$$\begin{aligned} E(\omega) &= \frac{1}{2}(\mathcal{E}(\omega) + \mathcal{E}^*(-\omega)) \\ E(t) &= \frac{1}{2}(\mathcal{E}(t) + \mathcal{E}^*(t)) = Re(\mathcal{E}(t)) \end{aligned} \tag{2.7}$$

However, in practice it is often easier to manipulate the complex valued electric fields than the real valued ones, as it simplifies Fourier analysis. In particular, we will see below that the spectral phase $\varphi(\omega)$ is a central quantity in the description of

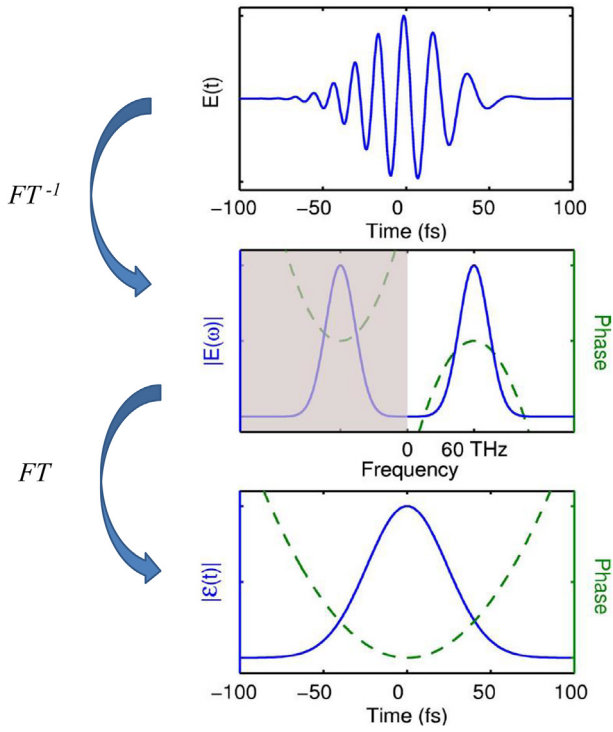

FIG. 2.1 – Real and complex fields: The spectral field is the inverse Fourier transform of the real temporal field, the analytical field is obtained by Fourier transform of the frequency-positive part of the spectral field.

ultrashort pulse properties, as it allows to describe the relative temporal delay of the spectral components.

2.2.2 Intensity

The temporal and spectral intensity functions are defined by

$$\begin{aligned} I(t) &= \frac{1}{2}\epsilon_0 cn|\mathcal{E}(t)|^2 \\ I(\omega) &= \frac{1}{2}\epsilon_0 cn|\mathcal{E}(\omega)|^2 \end{aligned} \tag{2.8}$$

with ϵ_0 being the vacuum permittivity, c the speed of light, and n the refractive index. Since the shape and not the absolute magnitude of the envelope functions is the quantity of interest, all the prefactors are commonly omitted.

2.2.3 Temporal and Spectral Widths

The duration of a pulse can be defined through root mean square (RMS) values, using the temporal intensity as a weight distribution. If t_0 is the center of the intensity profile then the duration is

$$\Delta t = \sqrt{\langle (t - t_0)^2 \rangle} \tag{2.9}$$

Similarly, if ω_0 is the center of the spectrum, the spectral width can be defined by

$$\Delta\omega = \sqrt{\langle (\omega - \omega_0)^2 \rangle} \tag{2.10}$$

These two values are linked by the relationship $\Delta t \Delta\omega \geq 1/2$, which constrains spectral and temporal widths: the shorter the pulse duration the larger the spectral width. It can be demonstrated that for a given intensity, the duration is minimum when the spectral phase varies linearly with the frequency[1,2]. This special case corresponds to pulses named 'Fourier transform limited'. A pulse with a spectral phase varying non linearly with the frequency will necessarily be temporally broadened.

It is important to note that for simple envelope functions the pulse duration is most often defined by the full width at half maximum (FWHM) $\Delta t_{1/2}$ of the temporal intensity, instead of the root mean square Δt. Similarly the spectral width can be defined by the full width at half maximum of the spectral intensity.

2.2.4 Case of a Gaussian Pulse

As an illustration, we will focus on a Gaussian laser pulse mathematically described by

$$\mathcal{E}(t) = \exp\left(-\frac{t^2}{2a^2}\right) \exp(-i\omega_0 t) \tag{2.11}$$

where ω_0 is the carrier frequency and a a non-zero parameter. The spectral field is deduced by Fourier transformation

$$\mathcal{E}(\omega) = a\sqrt{2\pi} \exp\left(-\frac{a^2}{2}(\omega - \omega_0)^2\right) \tag{2.12}$$

and corresponds to a Gaussian spectrum centered on the carrying frequency ω_0 as represented on figure 2.2. The temporal intensity is the square modulus of the temporal field

$$I(t) = \exp\left(-\frac{t^2}{a^2}\right) \tag{2.13}$$

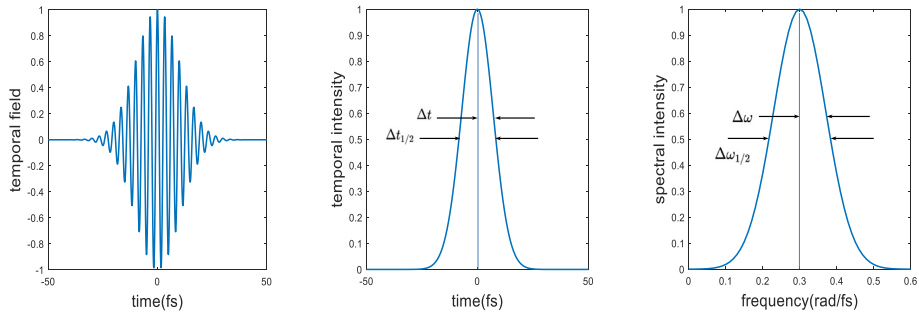

FIG. 2.2 – Temporal field, temporal and spectral intensities of a Gaussian pulse.

The RMS width is given by $\Delta t = a/\sqrt{2}$, while the FWHM $\Delta t_{1/2}$ is

$$\Delta t_{1/2} = \sqrt{8\ln 2}\Delta t = 2.355\Delta t \tag{2.14}$$

In the spectral domain, the spectral intensity is the squared modulus of the spectral field

$$I(\omega) = \exp(-a^2(\omega - \omega_0)^2) \tag{2.15}$$

and the RMS width is $\Delta\omega = 1/a\sqrt{2}$.

Time and spectral bandwidths are thus related by $\Delta t\Delta\omega = 1/2$. This equality is only reached with Gaussian pulses, which means that for a given spectral width, the Gaussian pulse has the shortest possible duration. This relationship known as the time-bandwidth product can be written with the FWHM values

$$\Delta t_{1/2}\Delta\omega_{1/2} = 4\ln 2 \tag{2.16}$$

or also in terms of frequencies ν rather than angular frequencies ω

$$\Delta t\Delta\nu = 0.441 \tag{2.17}$$

This equality is only reached when the Gaussian pulse is Fourier transform limited. Adding nonlinear phase terms leads to the inequality

$$\Delta t\Delta\nu > 0.441 \tag{2.18}$$

For other pulse shapes, a similar time bandwidth inequality can be derived

$$\Delta t\Delta\nu \geq \kappa \tag{2.19}$$

with different values of κ for different pulse shapes[2,3], like for instance 0.315 for bandwidth-limited sech^2 shaped pulses often found in femtosecond lasers.

2.2.5 Spectral Phase

The spectral phase $\varphi(\omega)$ that has been introduced in equation (2.6) is a very important quantity since it determines, for a given spectrum, the shape of a pulse.

For a better understanding, we can look at the effects of the different terms of a polynomial spectral phase distributed around a central frequency ω_0

$$\varphi(\omega) = \varphi(\omega_0) + \varphi'(\omega_0)(\omega - \omega_0) + \frac{1}{2}\varphi''(\omega_0)(\omega - \omega_0)^2 + \frac{1}{6}\varphi'''(\omega_0)(\omega - \omega_0)^3 + \cdots \tag{2.20}$$

and define the group delay $\tau_g(\omega)$ that describes the relative temporal delay of a given spectral component

$$\tau_g(\omega) = \varphi'(\omega) \tag{2.21}$$

The zeroth order of the spectral phase is a constant that does not change the temporal envelope of the pulse. The first-order term leads to a temporal translation of the envelope in the time domain, in other words, a constant group delay, but does not have any impact on the temporal structure either. Considering only these two terms, all the spectral components are propagating at the same speed and the pulse is Fourier transform limited. On the contrary, higher orders of the phase lead to a non-constant group delay and modify the temporal pulse shape.

For instance, the second-order term corresponds to a quadratic spectral phase

$$\varphi(\omega) = \frac{1}{2}\varphi''(\omega_0)(\omega - \omega_0)^2 \tag{2.22}$$

and the corresponding group delay

$$\tau_g(\omega) = \varphi''(\omega_0)(\omega - \omega_0) \tag{2.23}$$

τ_g varies linearly with the frequency. Two spectral components of the pulse are thus separated by a time delay proportional to their frequency difference, and the temporal shape is broadened. The pulse is said to be linearly chirped, or to present a chirp. Chirped pulses are very useful in ultrafast science and technology and in particular in pulse amplification where they have allowed to increase considerably the peak power of ultrashort pulses[4].

In figure 2.3 is represented the temporal electric field of three pulses with an identical spectrum but different spectral phases: linear or quadratic with positive or negative curvature. In the middle of the figure, the shortest pulse corresponds to a linear spectral phase, and a constant group delay. On the left, the group delay increases with the frequency, so that the higher frequency components do arrive after the lower ones. The pulse presents a positive chirp, or is up-chirped. On the right, the chirp is negative and the higher frequency components do travel faster, the pulse is down-chirped.

Spectral phase coefficients of third order, *i.e.* a contribution to the phase function of the form $\varphi(\omega) = \frac{1}{2}\varphi'''(\omega_0)(\omega - \omega_0)^3$, are referred to as third-order dispersion (TOD). In contrast with lower order terms, they can lead to an asymmetric shape of the temporal envelope[3,5].

In summary, the constant and linear terms of the spectral phase do not change the temporal envelope and are often omitted, but the multiple order terms have to be taken into account carefully when manipulating femtosecond pulses.

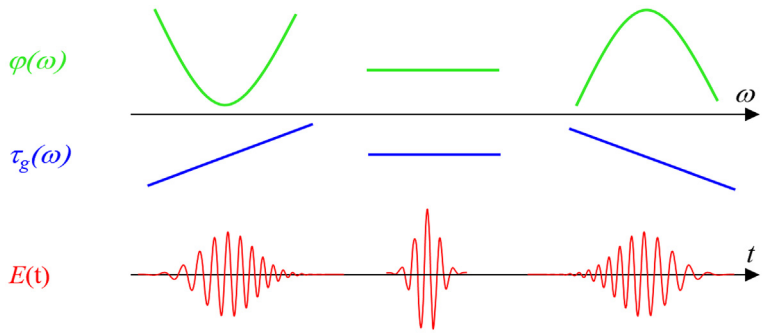

FIG. 2.3 – Effect of a positive, constant, or negative second-order spectral phase on the pulse temporal electric field.

2.2.6 Propagation

A pulse travelling a distance z through a medium with index of refraction $n(\omega)$ accumulates the following spectral phase

$$\varphi(z,\omega) = \varphi(0,\omega) + k(\omega)z \tag{2.24}$$

where $k(\omega) = n(\omega)\omega/c$ is the wave vector amplitude in the medium of index $n(\omega)$. The group delay is then

$$\tau_g(z,\omega) = \frac{\partial\varphi(z,\omega)}{\partial\omega} = \tau_g(0,\omega) + \frac{z}{V_g(\omega)} \tag{2.25}$$

with $V_g(\omega) = 1/k'(\omega)$ the group velocity, that describes the velocity of the envelope, and $V_\phi(\omega) = \omega/k(\omega)$ the phase velocity (the velocity of the carrier). If we develop the wave vector in Taylor's series, then the group delay is

$$\tau_g(z,\omega) = \tau_g(0,\omega) + k'(\omega_0)z + (\omega-\omega_0)k''(\omega_0)z + \cdots \tag{2.26}$$

The constant and linear terms do not change the temporal envelope of the pulse. Considering the second-order term, we observe that if $k''(\omega_0) \neq 0$, the group delay is linear in frequency and the different spectral components of the pulse do not propagate at the same speed in the material. The pulse presents a chirp induced by the propagation in the dispersive medium.

$k''(\omega_0)$ characterizes the group velocity dispersion (GVD), or the group delay dispersion (GDD) accumulated over a propagation along z.

In summary, a pulse propagating in a dispersive medium accumulates a spectral phase that broadens the temporal envelope. This elongation is all the more important as the spectrum is broad and the material dispersive.

In the visible range, most optical glasses do present a normal dispersion, (*i.e.* a positive GVD): smaller frequency components traveling faster than those of higher frequency through the medium are found at the front of the pulse.

In the infrared both positive and negative GVD in materials are encountered, and different glasses can be ingeniously used to compensate for the chirp induced by the propagation in a medium.

2.3 Generation of Femtosecond Pulses

Femtosecond pulses can be generated with different kind of lasers often named femtosecond oscillators that deliver moderate pulse energies (nJ) and high pulse repetition rate (mainly MHz to tens of GHz) for different wavelengths (mainly red and infrared). Higher pulse energies can be obtained with amplification systems at lower repetition rates, and a large variety of wavelengths are accessible when using nonlinear effects.

Basically, a femtosecond oscillator is a laser cavity composed of an end mirror and an output coupler separated by a distance L, between which are inserted components that ensure three functions:

- amplification in a gain medium,
- compensation of the group velocity dispersion,
- mode-locking, a technique to ensure the pulsed regime and that is described below.

A single pulse travels back and forth between the two mirrors, and is partially transmitted by the output coupler at each roundtrip. The output beam is then constituted of a train of pulses separated by a time period equal to $2L/c$.

We will first present the concepts of mode-locking and dispersion management, and then some basic femtosecond resonators.

2.3.1 Fundamental of Mode-Locking

The generation of ultrashort pulses relies on a technique termed mode-locking that allows an impulsive regime in place of a continuous one.

A femtosecond oscillator is a laser, and thus presents longitudinal modes ω_n separated by a frequency $\delta\omega$ inversely proportional to the laser cavity length L

$$\begin{aligned} \omega_n &= 2\pi n \frac{c}{2L} \\ \delta\omega &= 2\pi \frac{c}{2L} \end{aligned} \tag{2.27}$$

The laser spectrum includes the modes that experience more gain than loss and are therefore above the laser threshold. The total electric field is thus given by the sum of all the lasing modes (typically more than 10 000)

$$E(t) = \sum_{n=0}^{N-1} E_n \sin(\omega_n t + \phi_n(t)) \tag{2.28}$$

with $\omega_n = 2\pi\nu_n$, $\phi_n(t)$ the phase of the nth mode, and N the number of oscillating modes.

In a continuous regime, the phase between the modes varies randomly in time and the generated output beam is continuous. If the phases are fixed with respect to each other, the modes can interfere constructively into a single pulse. To simplify we consider $\phi_n(t) = 0$ and $E_n = E_0$ to find

$$E(t) = E_0 \sum_{n=0}^{N-1} \sin(\omega_n t) \tag{2.29}$$

The intensity is the squared modulus of the field and is then given by

$$I(t) = I_0 \left[\frac{\sin(N\delta\omega t/2)}{\sin(\delta\omega t/2)}\right]^2 \tag{2.30}$$

with I_0 being the average intensity of one wave. The energy is then concentrated in a short pulse whose synthesis can be seen as the superposition of monochromatic waves. The mode locking consists in enforcing a constant phase relationship between these waves (see figure 2.4) so that they can interfere constructively into short pulses. This equation underlines that a higher number of oscillating modes N yields a higher intensity and a shorter pulse duration, which is simply another way to express the fact that a gain medium with a large spectral bandwidth is required to generate ultrashort pulses.

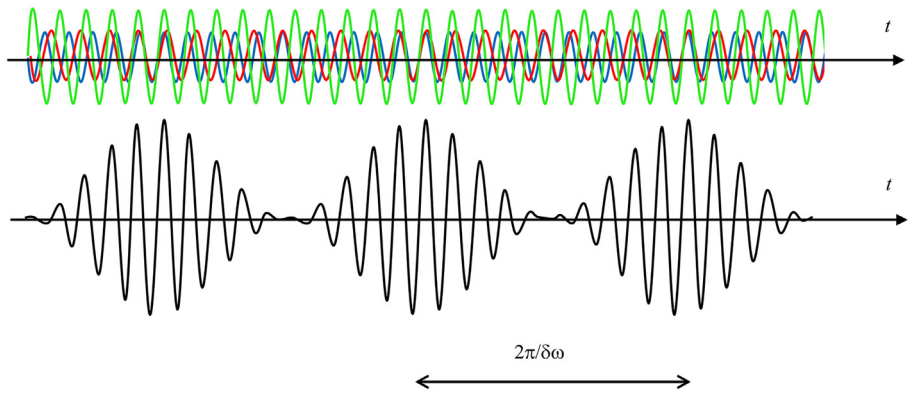

FIG. 2.4 – Temporal superposition of monochromatic waves locked in phase (up), giving rise to pulses (down).

Mode-locking can be achieved by passive or active techniques, and consists in favoring pulsed regime over continuous regime by applying periodic losses. In the time domain, it can be interpreted as a 'time window' opened at each round trip, providing

a higher gain/loss ratio for the photons concentrated in a pulse. Active techniques use acousto-optic or electro-optic modulators inserted into the cavity and synchronized with the cavity round trip[6]. Passive techniques are more widespread in ultrashort oscillators and rely on saturable absorption/gain or self-phase modulation: the pulse itself induces a loss modulation inherently synchronized to the cavity round trip frequency. Two major techniques, named Kerr-lens mode locking and SESAM, are described below.

2.3.1.1 Kerr-Lens Mode-Locking

The Kerr effect is a nonlinear process where the refractive index of a material is modified by the electric field of an electromagnetic wave[1]. This effect can be described by the equation

$$n(r) = n_0 + n_2 I(r) \tag{2.31}$$

where n_0 is the linear index of refraction while n_2 is the coefficient of the nonlinear index, and $I(r)$ the intensity as a function of a radial coordinate r. As the beam intensity has a Gaussian shape, the induced index presents a Gaussian variation across the beam profile, leading to an intensity-dependent lens into the medium. This process called self-focusing generates different propagation paths for continuous or pulsed beams. Therefore one can design a cavity stable for pulsed operation, while unstable for continuous operation, which is equivalent to a loss modulation that favors the pulsed regime over the continuous one. As the Kerr effect is a non-resonant nonlinearity, it acts as a very fast (few fs) and very broadband saturable absorber. This technique of nonlinear self-focusing in the gain medium is named Kerr-lens Mode-locking (KLM)[7,8]. A disadvantage is that despite pulsed regime is favored, it needs to be initiated by a mechanical perturbation (generally the vibration of an optical component of the cavity). Moreover, it cannot be implemented in all kinds of lasers, like fiber ones for instance, and other techniques of saturable absorption have been developed.

2.3.1.2 SESAM: Semiconductor Saturable Absorber Mirror

A saturable absorber has decreasing light absorption with increasing light fluence[9], the fluence being the optical energy by unit area. A SESAM is a semiconductor saturable absorber device made out of a quantum well structure grown on a Bragg mirror[10]. The photon absorption in the quantum well transfers the electrons from the valence band to the conduction band where they can accumulate, lowering the absorption. Thanks to the Bragg mirror, a SESAM operates in reflection. It absorbs photons as long as the optical fluence is low, but becomes a mirror for high optical density pulses, which creates the condition for a pulsed regime. The key parameters of a saturable absorber are the wavelength range, the dynamics response (how fast it recovers), the saturation fluence (level where the device saturates), the modulation depth (fully saturated nonlinear reflectivity change), and the nonsaturable loss (loss of a saturated absorber). These last parameters are represented in figure 2.5.

A great advantage of using SESAM components is that they allow for a self-starting pulsed regime with no need of additional perturbation in the cavity.

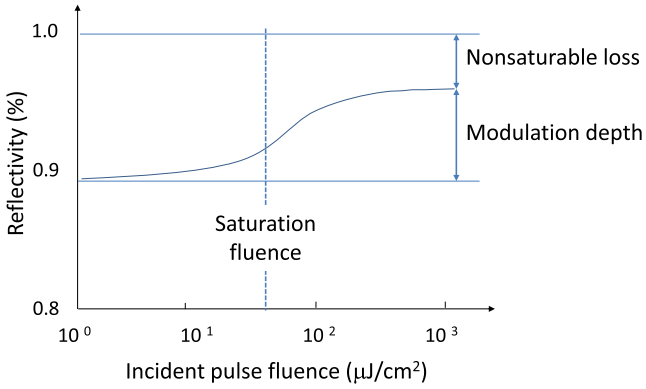

FIG. 2.5 – Saturable absorption parameters: Saturation fluence, Modulation depth, Non-saturable loss.

2.3.2 Group Velocity Dispersion Management

As seen previously, a pulse propagating through dispersive media undergoes a group delay dispersion resulting in a chirped pulse. Inside a laser cavity, in order to maintain an identical pulse after each round-trip, we need to compensate for the dispersion induced mainly not only by the gain medium but also by optics or air. This is achieved by introducing optical components that deliver an adjusted group velocity dispersion. Different solutions are possible with the use of prisms, gratings, or specially designed mirrors.

2.3.2.1 Prisms

A frequently used device is based on angular dispersion delivered by prisms that allow to spatially separate the spectral components. A sequence of two prisms permits to adjust a group delay dispersion while maintaining the collimation of the beam[11]. The obtained dispersion depends on the distance separating the two prisms and the amount of crossed glass. It is therefore possible to slightly tune the group delay dispersion by translating one of the prisms along its axis of symmetry. Using two pairs of prisms allows to cancel out the lateral displacement (called spatial chirp) of the spectral components (see figure 2.6).

Two prisms can only be used associated with a mirror in a double pass configuration. Outside a cavity, the mirror would be slightly offset to translate the output beam in the vertical plane so that it can be picked up (see figure 2.7).

2.3.2.2 Gratings

Diffraction gratings do also provide group delay dispersion through angular dispersion (see figure 2.8), in simple or double pass configuration[12]. Gratings are much more dispersive than prisms, but they do introduce higher losses, so they are mainly

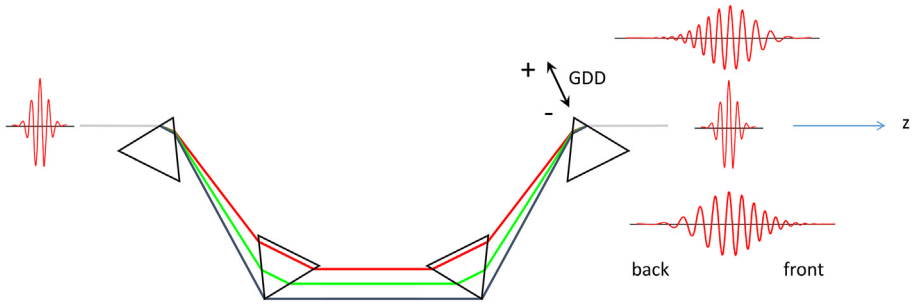

FIG. 2.6 – 4-prism sequence for adjustable group delay dispersion.

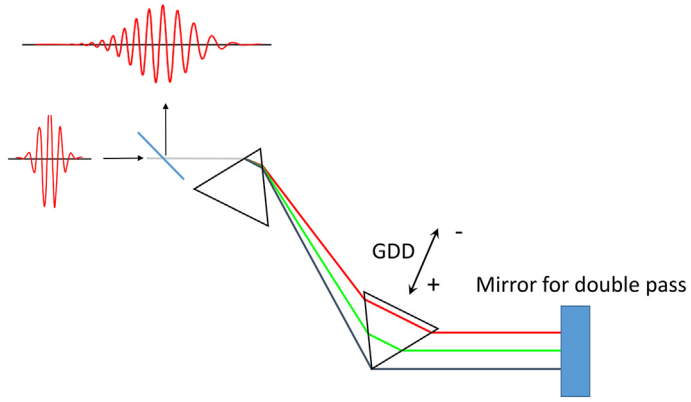

FIG. 2.7 – 2-prism sequence in double pass for adjustable group delay dispersion.

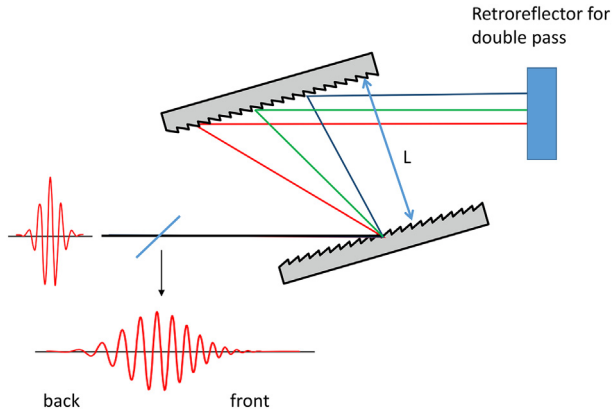

FIG. 2.8 – Grating pair for adjustable delay dispersion changing the separation distance.

used outside the laser cavity, except for fiber lasers where they can compensate large amounts of dispersion.

2.3.2.3 Chirped Mirrors

Another solution consists in using specially designed dielectric multilayer mirrors where the different wavelengths do experience different optical paths. The basic concept relies on Bragg mirrors, made of alternating low and high index layers with variable layer thickness values (see figure 2.9). The introduced dispersion can be tuned by using several mirrors to multiply the reflections[13,14].

Another kind of dispersive mirrors are Gires-Tournois interferometers (GTI)[15]. They rely on a Fabry–Perot configuration made of a highly reflective back mirror and a partially reflective one to introduce chromatic chirp. Compared to prisms or gratings pulse compression systems, GTI mirrors exhibit lower losses and sensitivity

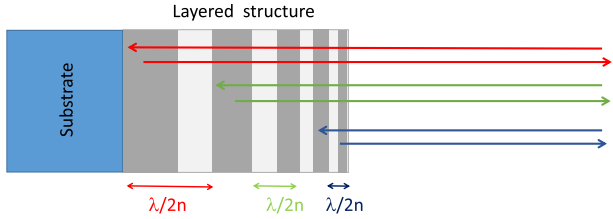

FIG. 2.9 – Basic concept of a chirped mirror. Due to the layered structure, each wavelength is reflected at a different position and the pulse acquires negative chirp.

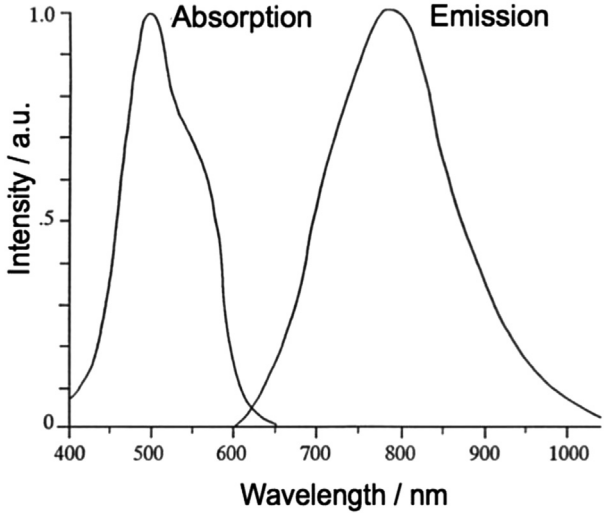

FIG. 2.10 – Ti:Sa absorption and emission spectra.

to mechanical misalignment errors, thus enabling higher output power and stability of laser systems, but their spectral bandwidth is limited, preventing their use for the shortest pulses.

2.3.3 Oscillator Technologies

2.3.3.1 Titanium-Sapphire Oscillator

Oscillators based on Titanium-doped Sapphire (Ti:Sapphire) crystals can deliver very short pulses from a few femtoseconds to a hundred femtoseconds typically. The Ti:Sapphire gain medium offers an extremely broad gain bandwidth and a large emission cross section. It can be lased over the entire band from 660 to 1100 nm, and needs to be pumped with green light (see figure 2.10). Its fluorescence time is low ($3\,\mu$s) and its thermal conduction high ($35\,\mathrm{W.K^{-1}.m^{-1}}$)[16].

The pulsed regime is obtained by Kerr-lens modelocking in the Ti:Sapphire crystal, and can be initiated by a mechanical vibration or a saturable absorber. Dispersion is generally managed by prisms and/or chirped mirrors. Figure 2.11 represents a basic Ti:Sapphire cavity including a crystal longitudinally-pumped by a diode-pumped solid-state laser, and a pair of prisms. Typical performances of this scheme are output pulse energy of a few nJs at 80 MHz repetition rate and 15 fs duration.

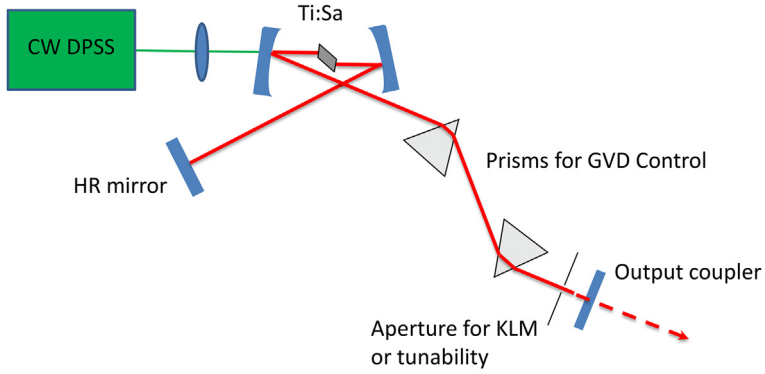

FIG. 2.11 – A standard Ti:Sapphire oscillator cavity.

The Kerr effect induced in the Ti:Sapphire crystal is not only responsible for a spatial filtering but also for a spectral broadening by self-phase modulation[17] that favors the generation of extremely short pulses[18]. Ti:Sapphire oscillators offer the shortest pulse duration on a wide spectral range, and have been extensively developed, for direct application or to seed high peak power laser chains. Their main drawback is that they need a green pump laser (usually a frequency-doubled diode-pumped Nd:YVO_4) that leads to complex, expensive and inefficient systems.

2.3.3.2 Ytterbium-Doped Bulk Oscillator

Other widespread oscillators are based on crystals or glasses doped with Yb^{3+} ions. Many different hosts are available (YAG, glass, KYW, CALGO…), giving lots of different characteristics[19,20]. Their huge advantage over Ti:Sapphire oscillators is that they can be pumped directly by diode lasers at 980 nm, which matches well with the emission bands of high power diode lasers. They present a small quantum defect allowing for high power efficiency and reducing thermal effects. They can thus deliver very high average power and energy levels[21] but the pulse duration generally remains in the range of 100–800 fs. Most of them use a SESAM to ensure mode-locking, and prisms or chirped mirrors to manage the group velocity dispersion. An example of a typical cavity is shown in figure 2.12.

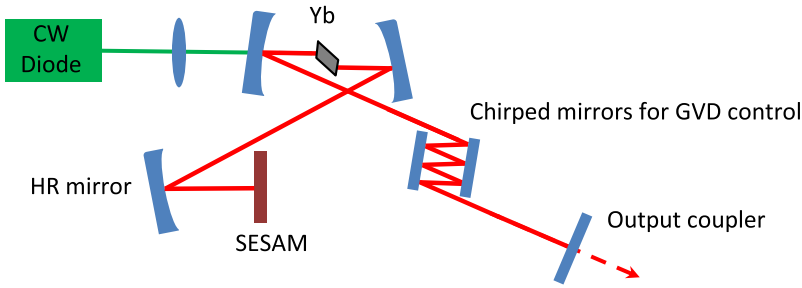

FIG. 2.12 – An example of Yb:doped bulk oscillator cavity.

Typical performances for basic oscillators are tens of nJ pulse energy at 50 MHz repetition rate. The emission wavelength is in the near infrared (around 1030 nm).

2.3.3.3 Fiber-Based Oscillators

Fiber lasers are based on glass fibers doped with rare-earth ions, most often Ytterbium and Erbium, but also other doping elements like Thulium or Holmium. These active fibers constitute gain media with high gain efficiency and a large gain bandwidth, typically tens of nanometers. Fiber lasers have many qualities: they can be very compact and rugged, especially if free space optics are not used, and they can take advantage of low-cost and reliable components developed for telecommunications. The laser output is naturally fiber-coupled and the guiding effect provides excellent beam quality and high spatial stability. Moreover, the low thermal properties of glasses are mitigated by the propagation on long distances which lowers the heating due to pump absorption. The drawbacks of these long propagation distances in confined medium are of course the dispersion and the high nonlinear effects that are much stronger than in bulk lasers. Dispersion is managed by different means. For Erbium lasers, it is possible to use fibers with dispersion of the opposite sign (in the infrared) but higher orders of dispersion are not easy to compensate for.

Bulk gratings can be used but also fibered components like for example chirped Bragg mirror fibers[22] or hollow-core photonic bandgap fibers[23]. A typical cavity is represented on figure 2.13.

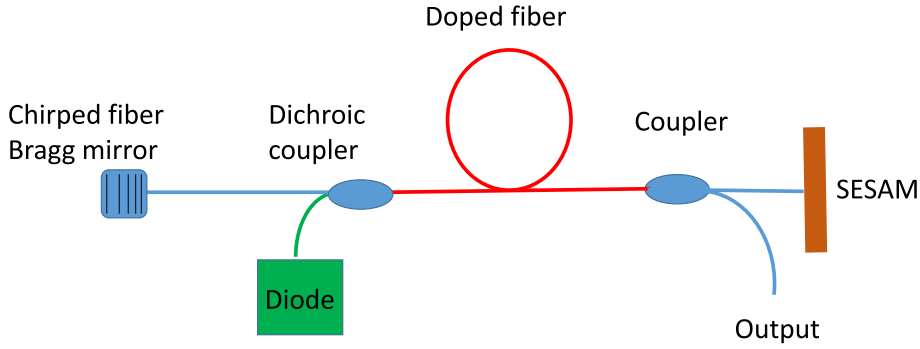

FIG. 2.13 – Example of fiber-based oscillator cavity.

Mode-locking in fiber lasers is often obtained by the use of saturable absorber like SESAM, but other techniques that exploit nonlinear polarization rotation (where a power-dependent polarization change is converted into a power-dependent transmission through a polarizing optical element) are also popular[24]. The main drawback of fiber oscillators is that they are limited in terms of energy and power by the confinement of the beam in a small fiber core, but they can easily be coupled with high power fiber-based amplifiers.

2.4 Conclusions

In this lecture, we have presented the principles allowing the generation of femtosecond pulses and described some basic architectures of oscillators. Despite their moderate energy, pulses generated by femtosecond oscillators find many applications by themselves in fields as diverse as bio-imaging, metrology, or spectroscopy. They are also frequently seeding amplifiers when high peak power or energy is required. Almost all the amplifiers rely on a technique called chirped pulse amplification (CPA)[4] that includes three steps: the pulses are first chirped so that the peak power is lowered enough to avoid optical damage, they are then amplified, and eventually compressed to retrieve their initial duration. The amplification can provide intense pulses for highly non-linear processes, thus allowing to generate photons in the whole electromagnetic spectrum and considerably broadening the fields of application of femtosecond pulses.

Acknowledgements

The author wishes to thank her colleagues from the Laboratoire d'Optique et Biosciences, and is very grateful to Manuel Joffre for his invaluable help in this work.

More detailed information on femtosecond pulses can be found in the textbooks referenced in the bibliography, and the first sections of this document are largely inspired by courses dispensed by Manuel Joffre and available on https://cel.archives-ouvertes.fr/cel-00092964v4.

I also recommend the courses of the previous Ecole Femto with special thanks to Frédéric Druon, Marc Hanna, and Ammar Hideur.

References

[1] Joffre M., "Optique non-linéaire en régimes continu et femtoseconde", Master, Lecture, 2010. This Lecture was taught at the Master "Concepts fondamentaux de la Physique" (ENS - Ecole Polytechnique - Paris VI–Paris XI) between 2000 and 2012.
[2] Rulliere C., et al. (2005) *Femtosecond laser pulses.* Springer.
[3] Wollenhaupt M., Assion A., Baumert T. (2007) Femtosecond laser pulses: linear properties, manipulation, generation and measurement, in: *Springer handbook of lasers and optics*, (F. Träger, Ed.) Springer, New York, New York, NY, 937.
[4] Strickland D., Mourou G. (1985) Compression of amplified chirped optical pulses, *Opt. Commun.* **56**, 219.
[5] Monmayrant A., Weber S.J., Chatel B. (2010) A newcomer's guide to ultrashort pulse shaping and characterization, *J. Phys. B: At. Mol. Opt. Phys.* **43**, 103001.
[6] Fermann M.E., Galvanauskas A., Sucha G. (2002) *Ultrafast lasers: technology and applications.* CRC Press, **80**.
[7] Spence D.E., Kean P.N., Sibbett W. (1991) 60-fsec pulse generation from a self-mode-locked Ti:Sapphire laser, *Opt. Lett.* **16**, 42.
[8] Brabec T., Spielmann C., Curley P.F., Krausz F. (1992) Kerr lens mode locking, *Opt. Lett.* **17**, 1292.
[9] DeMaria A.J., Stetser D.A., Heynau H. (1966) Self mode-locking of lasers with saturable absorbers, *Appl. Phys. Lett.* **8**, 174.
[10] Keller U., Weingarten K., Kärtner F., Kopf D., Braun B., Jung I., Fluck R., Hönninger C., Matuschek N., Aus-der-Au J. (1996) Semiconductor saturable absorber mirrors (sesam's) for femtosecond to nanosecond pulse generation in solid-state lasers, *IEEE J. Sel. Top. Quantum Electron.* **2**, 435.
[11] Fork R.L., Martinez O.E., Gordon J.P. (1984) Negative dispersion using pairs of prisms, *Opt. Lett.* **9**, 150.
[12] Treacy E. (1969) Optical pulse compression with diffraction gratings, *IEEE J. Quantum Electron.* **5**, 454.
[13] Szipöcs R., Ferencz K., Spielmann C., Krausz F. (1994) Chirped multilayer coatings for broadband dispersion control in femtosecond lasers, *Opt. Lett.* **19**, 201.
[14] Steinmeyer G. (2006) Femtosecond dispersion compensation with multilayer coatings: toward the optical octave, *Appl. Opt.* **45**, 1484.
[15] Akhmanov S.A., Vysloukh V.A., Chirkin A.S., Atanov Y. (1992) *Optics of femtosecond pulses.* American Institute of Physics, N.Y.
[16] Moulton P.F. (1986) Spectroscopic and laser characteristics of Ti:Al_2O_3, *JOSA B.* **3**, 125.
[17] Shen Y.R., Yang G.-Z. (1989) Theory of self-phase modulation and spectral broadening, in: *The supercontinuum laser source*, (R.R. Alfano, Ed.) Springer, New York, New York, NY, 1.

[18] Sutter D.H., Steinmeyer G., Gallmann L., Matuschek N., Morier-Genoud F., Keller U., Scheuer V., Angelow G., Tschudi T. (1999) Semiconductor saturable-absorber mirror–assisted kerrlens mode-locked ti:sapphire laser producing pulses in the two-cycle regime, *Opt. Lett.* **24**, 631.

[19] Krupke W.F. (2000) Ytterbium solid-state lasers the first decade, *IEEE J. Sel. Top. Quantum Electron.* **6**, 1287.

[20] Druon F., Ricaud S., Papadopoulos D.N., Pellegrina A., Camy P., Doualan J.L., Moncorgé R., Courjaud A., Mottay E., Georges P. (2011) On Yb: CaF_2 and Yb: SrF_2: review of spectroscopic and thermal properties and their impact on femtosecond and high power laser performance, *Opt. Mater. Express* **1**, 489.

[21] Hönninger C., Paschotta R., Graf M., Morier-Genoud F., Zhang G., Moser M., Biswal S., Nees J., Braun A., Mourou G., Johannsen I., Giesen A., Seeber W., Keller U. (1999) Ultrafast ytterbium-doped bulk lasers and laser amplifiers, *Appl. Phy. B Lasers Opt.* **69**, 3.

[22] Gumenyuk R., Vartiainen I., Tuovinen H., Kivistö S., Chamorovskiy Y., Okhotnikov O.G. (2011) Dispersion compensation technologies for femtosecond fiber system, *Appl. Opt.* **50**, 797.

[23] Lim H., Wise F.W. (2004) Control of dispersion in a femtosecond ytterbium laser by use of hollow-core photonic bandgap fiber, *Opt. Express* **12**, 2231.

[24] Fermann M.E., Andrejco M.J., Silberberg Y., Stock M.L. (1993) Passive mode locking by using nonlinear polarization evolution in a polarization-maintaining erbium-doped fiber, *Opt. Lett.* **18**, 894.

Chapter 3

Trends, Challenges and Applications of High-Average Power Ultrafast Lasers

Clara J. Saraceno*

Ruhr University Bochum – Germany

3.1 Introduction

Ultrafast lasers have been at the forefront of many breakthroughs in physics, chemistry, biology, as well as mechanical and electrical engineering – including several Nobel Prizes – since their invention in the 1980s. They have moved from specialized laboratory tools to commercial equipment extensively used in both laboratories and industries. In this progress line, those who were at the forefront of laser technology could access unique regimes of light-matter interaction and push science forward. To give one specific example of an area where progress in ultrafast laser technology has been fundamental in enabling breakthroughs is ultrafast spectroscopy. Techniques such as pump-probe spectroscopy have become ubiquitous to study the dynamics of atomic and molecular systems from the attosecond to the picosecond regime, with light pulses spanning the entire electromagnetic spectrum (XUV to THz). Nowadays, ultrafast spectroscopy continues to expand, supported by immense improvement of ultrafast technologies.

In fact, ultrafast lasers with GW peak power, few tens of fs and hundreds of nm wide spectral bandwidths have become widespread tools for this and other applications. Pushing the performance of ultrafast laser systems represents an entire area of research aiming at ever-improvement of laser parameters.

In this manuscript, we focus our attention on one important parameter of ultrafast lasers, which has seen immense improvement in the last decade, namely the average power available from these sources. We start by giving a short reminder on

*clara.saraceno@ruhr-uni-bochum.de

DOI: 10.1051/978-2-7598-2719-0.c003

the most important parameters of such ultrashort pulse laser systems. We then discuss laser geometries suitable for high-power, and the latest state-of-the-art of these technologies, as well as the ongoing challenges in high-power ultrafast lasers.

3.2 Summary of Important Ultrashort Pulse Parameters

As introduced in chapter 2, ultrashort pulses can be characterized by their electric field in the time domain (figure 3.1) (electric-field amplitude and phase) or equivalently in the frequency domain (spectral amplitude and phase). In both the time- and frequency domains, several relevant metrics can be extracted that give us practical information about the pulses at hand, relevant to the targeted application. It is important to notice that certain pulse parameters refer to the properties of a *single pulse* whereas others refer to the repetitive aspect of these pulses in the form of a *pulse train*.

FIG. 3.1 – Schematic illustration of the electric-field structure of a linearly polarized ultrashort pulse train. © MS, Martin Saraceno, 2021.

In table 3.1, are summarized some of the most important parameters used by the ultrafast community to characterize ultrashort pulses. Please note that here we omit some important parameters related to the phase properties of the electric field of a pulse train, *i.e.*, the carrier–envelope phase properties, which become increasingly relevant when discussing pulses with few-cycle pulse durations, such as the ones shown in figure 3.1. In the discussion section of this manuscript, we will not cover these aspects, but only focus on parameters relevant to the *(complex) pulse envelope*, *i.e.*, the pulse envelope amplitude and phase in the time domain (and the corresponding equivalent in the frequency domain, the *complex spectral amplitude shifted to zero frequency*). It is important to keep in mind that most parameters commonly used to describe ultrashort pulses are extracted using approximations. The limits of these approximations are important to keep in mind in extreme cases, such as few-cycle pulses or extremely broad bandwidths.

In the time domain, the most important *single pulse* parameters are the pulse energy in Joules and duration in seconds. Whereas the pulse energy is easy to define as the integral of the instantaneous power over time, the pulse duration can be defined in different ways. The most usual definition is the full-width at half maximum (FWHM) of the temporal intensity profile τ_p. For most pulses, this is an appropriate measure of the timescale over which the energy is concentrated. However, with complex pulse shapes, for example, the ones exiting from nonlinear compression setups, which often do contain wings as described below, this metric can be misleading and other metrics (such as the root-mean-square definition) can better represent the pulse duration. From the pulse energy and duration, it is possible to calculate the peak power of the pulse *i.e.*, the maximum instantaneous power of the pulse in Watts. The link between peak power, pulse energy and pulse duration depends on the exact instantaneous power profile of the pulse.

A common approximation made in the community is to approximate the peak power by:

$$P_{\mathrm{pk}} \approx E_p/\tau_p \tag{3.1}$$

which is only strictly true for rectangle-shaped pulses. For well-known pulse shapes, one can calculate a proportionality factor that allows us to exactly calculate the peak power; the most common example used is the Gaussian-shaped pulse yielding:

$$P_{\mathrm{pk}} = 0.94 \cdot E_p/\tau_p \tag{3.2}$$

For unknown, complex pulse shapes, the peak power remains ambiguous.

A similar ambiguity occurs when considering another critical parameter of ultrafast laser science, peak intensity I_{pk} in units of $\mathrm{W/m^2}$, which is often approximated by:

$$I_{\mathrm{pk}} = P_{\mathrm{pk}}/A \tag{3.3}$$

with A being the area of the beam.

With the same argumentation as for the peak power, the exact maximum of the intensity across a spatial distribution requires the knowledge of the exact beam profile. In ultrafast science, we often deal with lasers that operate in the single-fundamental mode, therefore the beam profile is Gaussian and we can therefore calculate the peak intensity using:

$$I_{\mathrm{pk}} = 2 \cdot P_{\mathrm{pk}}/\pi\omega_0^2 \tag{3.4}$$

In the spectral domain, the most important parameters characterizing an ultrashort pulse are the carrier wavelength λ_0 (or frequency ν_0) and the spectral bandwidth $\Delta\lambda_p$ (resp. $\Delta\nu_p$). Most commonly, the carrier frequency is defined as the central frequency, where, for simple spectra, lies the bulk of the spectral energy, and the spectral bandwidth is the FWHM of the intensity spectrum of the pulse. Following a discussion similar to the one for the pulse width in the time domain, these definitions become increasingly flawed for very broad bandwidths and complex shaped spectra; therefore, they should be used with caution. Please note that we do not discuss here the relevant parameters of the frequency representation of a *train of pulses*, which is not a continuous spectrum but a *frequency comb* under a continuous envelope, characterized by the above-mentioned parameters.

The frequency and time domain description of ultrashort pulses being linked by a Fourier transformation, the so-called time-bandwidth product (TBP, no unit), defined by the product of the FWHM duration of the intensity profile τ_p and the FWHM width of the frequency intensity spectrum $\Delta\nu_p$ gives us information on the shortest possible pulses achievable with a given spectral width. The value of this product depends on the shape of the pulse. Furthermore, it is clear from the above-mentioned discussion on the ambiguity of the FWHM definitions that this parameter is to be considered with care.

TAB. 3.1 – Most important laser parameters and some subtleties in their definition.

Notation	Everyday parameters	How are they linked together?	Comments/Subtleties
E_p	Pulse energy (J)		
τ_p	Pulse duration (fs)		Definition often FWHM – becomes ambiguous for complex pulses RMS pulse duration better suited for complex pulse shapes
P_{pk}	Peak power (W)	*Can be calculated from* E_p and τ_p	Exact value requires knowledge about pulse shape Simple for well-known pulse shapes (for example Gaussian)
I_{pk}	Peak intensity ($\mathrm{W/m^2}$)	*Can be calculated from* P_{pk} and *beam area* A	Requires knowledge about transverse beam profile
f_{rep}	Repetition rate (Hz)		
P_{av}	Average power (W)	$P_{\mathrm{av}} = f_{\mathrm{rep}} E_p$	Usually technology limited
λ_0, ν_0	Carrier wavelength (nm), carrier frequency (Hz)		Ambiguous for very broad, complex shaped spectra
$\Delta\lambda_{\mathrm{p}}$, $\Delta\nu_p$	Spectral bandwidth (nm, Hz)		Often defined by FWHM width of spectral intensity in nm, ambiguous for very broad complex shaped spectra
TBP	Time-bandwidth product (no unit)	TBP $= \tau_p \Delta\nu_p$	Defined with intensity FWHM Reaches a minimum that gives information about the shortest pulses reachable with a given spectral width Can be flawed for complex, very short pulses

Another important parameter of particular relevance for the topics which we will cover here is the repetition rate of the pulses in Hz, f_{rep}, *i.e.* how many pulses per unit time are available for an experiment. Knowledge of the repetition rate and the single pulse energy E_p then allows one to calculate the average power or *energy per unit time* of an ultrafast laser or average power in Watts

$$P_{\text{av}} = E_p f_{\text{rep}} \tag{3.5}$$

In the following paragraph we discuss technologies designed for reaching high average power, *i.e.* laser systems that allow for a combination of high pulse energy and high repetition rate, as desired in an experimental setup.

3.3 High Average Power Lasers

3.3.1 Introduction

Reaching high average powers is an important goal in ultrafast laser technology. The relevance of reaching higher average powers for experiments using ultrashort pulse trains is illustrated in figure 3.2. Usually, a certain experimental setup calls for a given peak power and pulse duration combination that depends on the phenomena to be studied. This usually means that a minimum amount of *pulse energy* is fixed by experimental constraints. Given that $P_{\text{av}} = E_p f_{\text{rep}}$, a larger average power means that a higher repetition rate can be reached at a given pulse energy. A larger repetition rate pulse train is beneficial for shortening measurement durations (we measure more events/s) or at a given measurement duration to improve the signal-to-noise ratio (SNR), because we can integrate over a larger number of pulses.

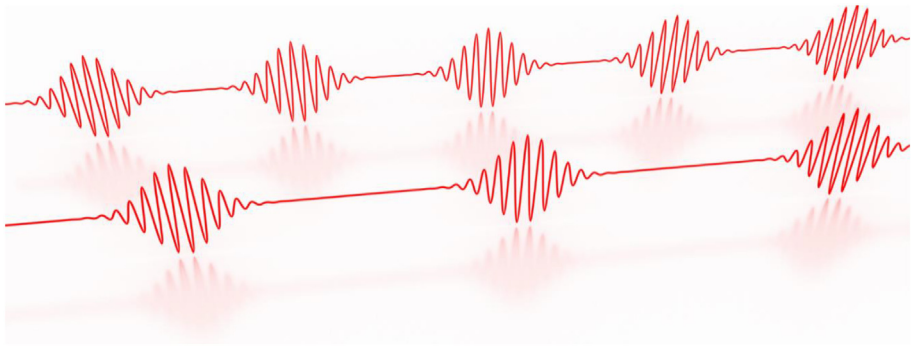

FIG. 3.2 – Two ultrashort pulse trains with fixed pulse duration and pulse energy but different repetition rates. The pulse train on top has a higher average power than the one underneath, illustrating the relevance of high-average power scaling for shorter measurement durations and better signal-to-noise ratio. © MS, Martin Saraceno, 2021.

The biggest difficulty in achieving high average powers is heat management in the laser gain media used in oscillators and amplifiers. The most commonly used technology for ultrafast lasers is based on Titanium-doped Sapphire (Ti:Sa) systems: Ti:Sa offers several advantages for ultrafast oscillators and amplifiers, the most crucial one being an extremely broad emission bandwidth, allowing to routinely generate sub-30 fs pulses directly from multi-mJ amplifiers and even few-cycle pulses from carefully dispersion tailored oscillators. However, Ti:Sa lasers are strongly limited in average power by thermal aberrations inherent to their bulk laser geometry. Several disadvantageous laser properties do limit power scaling: a large quantum defect, a small upper-level lifetime, and a strong degradation of crystal quality when increasing doping concentration. Typical commercially available Ti:Sa lasers only reach up to a few watts of average power (or up to some tens of watts in complex cryogenic systems). These limitations in average power result in unwanted compromises to be made in the pulse repetition rate, *i.e.*, a high pulse energy can only be reached at few kHz repetition rates with amplifiers; and higher repetition rates in the MHz regime are only reached with nJ pulse energies from oscillators. This leads to strong limitations on the experiments that can be performed and the samples that can be studied.

The emergence of new laser technologies based on Yb^{3+} (further simplified to Yb-)-doped gain materials in geometries that are more advantageous for heat extraction than the bulk laser geometry (fibers, slabs, thin-disks, see figure 3.3) has resulted in spectacular advances in high-average power ultrafast laser systems in the last decade. Yb- as an active ion has inherent advantages for power scaling – a long upper-state lifetime combined with large emission cross-sections, a very small quantum defect (for example for Yb:YAG a pumping wavelength at 940 nm or 969 nm and emission wavelength at 1030 nm) and pumping wavelengths accessible to high power diode pumps. These spectroscopic advantages allow for geometries with better cooling properties than the traditionally used rods, making use of a better surface-to-volume ratio.

Based on these architectures, lab-based ultrafast lasers have now long surpassed the kilowatt average power level and even very recently the 10 kW milestone[1–3], see figure 3.4. Commercially available systems are following this trend and nowadays multi-hundred-watt level systems are becoming increasingly common in ultrafast laboratories and in industrial scenarios. In the following, we focus on one example of a technology that has made particularly fast progress in the last decade that is thin-disk lasers (TDLs).

3.3.2 Example: The Thin-Disk Geometry

The TDL concept dates back to 1994 and was invented by *A.* Giesen and coworkers[4] at the Institut für Strahlwerkzeuge (IFSW) at the University of Stuttgart, Germany. In a TDL, the gain medium is shaped like a very thin (typically in the range of 100–300 μm) disk with a large diameter in comparison to its thickness (figure 3.5). The back side of the disk is coated with a highly reflecting mirror for both the pump and laser wavelengths and contacted on an appropriate heatsink (in the latest

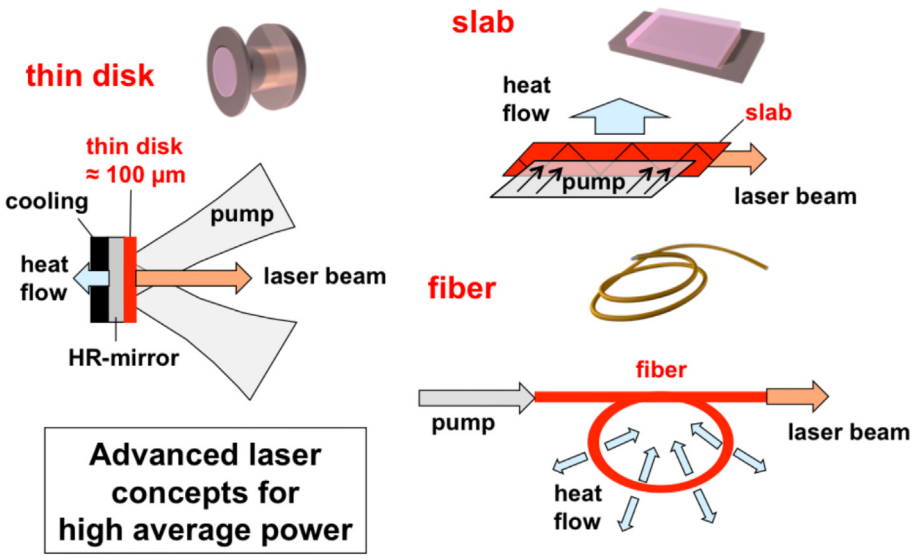

FIG. 3.3 – Concepts for high average power lasers.

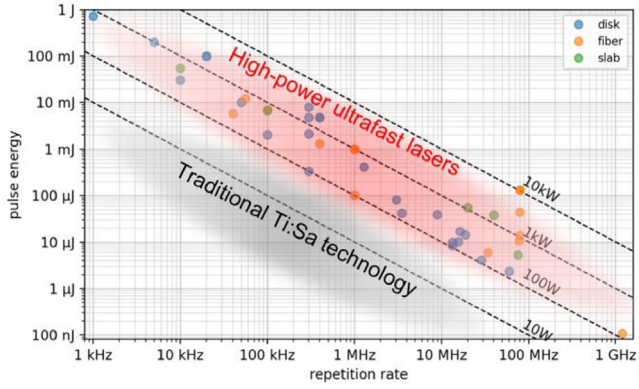

FIG. 3.4 – State-of-the-art high-power ultrafast lasers illustrating latest advances reached with Yb-doped ultrafast laser systems in the fiber, slab and disk geometries. © MS, Martin Saraceno, 2021.

results most commonly diamond). The front side is anti-reflection coated for the same wavelengths. In this way, the gain medium can be very efficiently water-cooled through the backside and used in a resonator or amplifier in reflection (as an "active mirror"). If the pump and laser spot sizes applied are correspondingly large (typically one to two orders of magnitude larger than the thickness), a one-dimensional heat-flow is obtained, and the scaling of the average output power can simply be achieved by increasing the pumped area and pump power by the same factor.

Because of the short length of the gain medium, a correspondingly small single-pass absorption and gain are typically achieved in this geometry: both efficient pumping of solid-state laser media and amplification with significant gain in this geometry, therefore, do require multiple-passes through the gain medium. For pumping, this is achieved by implementing an optical system composed of a parabolic mirror and prism-retro-reflectors that allow re-imaging of the pump beam on the thin-disk as many times as required to obtain sufficient pump-light absorption. Commercially available industrial pumping modules with up to 72 pump-light passes do provide the necessary platform for efficient pumping in this geometry. For efficient amplification, multiple passes are achieved either in a resonator (oscillator or regenerative amplifier) or by geometric multiplexing (like the pump pass arrangement depicted in figure 3.5a) or a combination of both.

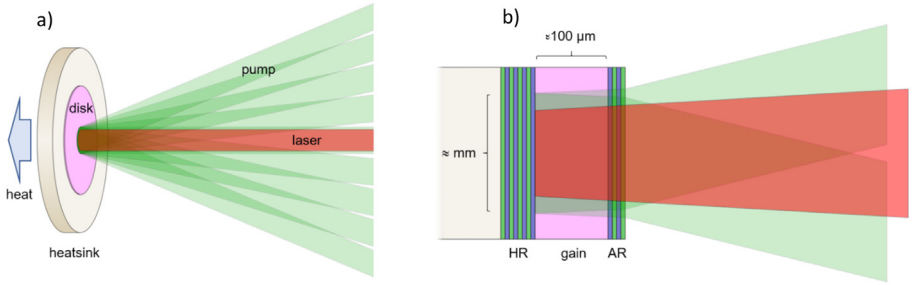

FIG. 3.5 – TDL concept (a) Schematic illustration of one of the most typically used arrangements (to scale of a typical Yb:YAG TDL): multi-pass pumping and single-pass gain. The re-imaged pump beam after each disk pass can be thought of as multiple beams impingent on the disk with decreasing intensity at each bounce. A similar multi-pass arrangement can be made for the laser beam (b) schematic side view of the disk (not to scale). Image from[5].

In figure 3.6, we schematically present the different concepts used nowadays for the generation and amplification of ultrashort pulses in the thin-disk geometry, with an average power in the range of hundreds of watts to kilowatts. Most state-of-the-art results have been achieved using Yb:doped garnets, due to their small difference between pump and laser wavelength, resulting in small residual heat *production via* non-radiative processes. Besides these garnets do possess excellent thermo-mechanical properties, large enough gain bandwidth for femtosecond operation, and well-established manufacturing processes in the TDL geometry.

In a thin-disk multi-pass amplifier, the core components are the thin disk itself and the array of mirrors that do allow for the geometrical folding of the seed beam though the disk. Figure 3.6a, shows a schematic of such an amplifier. The amplifier medium consists of an anti-reflection coated thin disk typically set on a diamond heat sink. The beam path is folded over the disk by an array of 40–80 plane typically inch-sized mirrors, allowing for a total gain of one-to-two orders of magnitude.

In a thin-disk regenerative amplifier, multiple passes through the gain medium are achieved by placing the disk in a resonator with a Pockels cell, which controls the number of roundtrips and ejects strongly amplified pulses after many roundtrips (figure 3.6b). For particularly high-energy, chirped-pulse amplification (CPA) may be employed, *i.e.*, the seed pulses may be temporally stretched to ns durations, typically in a fiber Bragg grating, and a larger beam-diameter pulse compressor can be used for the amplified beam, allowing for multi-GW peak powers. However, in contrast to fiber (*i.e.*, waveguide-confined) lasers, intra-cavity nonlinearities can be avoided by scaling the transverse beam size at many orders of magnitude higher peak powers, such that CPA can often be avoided in thin-disk regenerative amplifiers.

In mode-locked thin-disk oscillators (figure 3.6c), a single-transverse mode, high-power laser oscillator is mode locked to generate ultrashort pulses. These systems are attractive for applications calling for very high repetition rates: they provide energetic pulses at MHz repetition rates from a compact, single oscillator, and they may even give access to increased intra-cavity peak powers. Most commonly, Semiconductor Saturable Absorber Mirror (SESAM)[6] soliton-mode-locking[7], or Kerr–Lens mode-locking[8] are used for pulse formation. In both these mode-locking mechanisms, nonlinearity in the form of self-phase modulation (which will be discussed below in more detail) and dispersion must balance each other at each roundtrip of the pulses throughout the resonator, and stable pulse formation requires that these effects remain moderate per roundtrip. Therefore, one critical challenge of this technology is to achieve stable mode-locked pulses at extremely high intracavity average and peak powers, free of damage of intracavity optics.

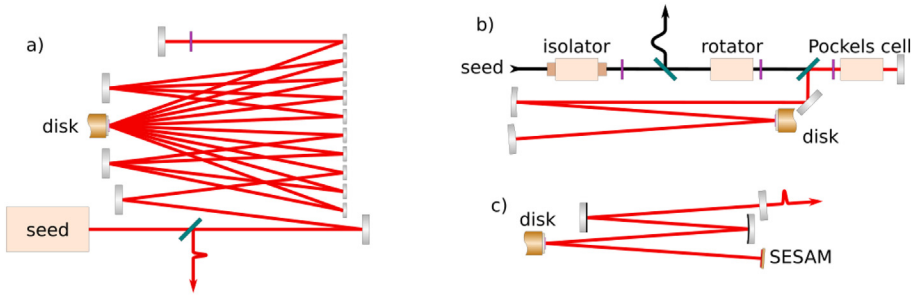

FIG. 3.6 – Schematic illustration of the different schemes for the generation of ultrashort pulses with hundreds of watts to kilowatts with thin-disk lasers. (a) multi-pass amplifier, (b) regenerative amplifier, and (c) mode-locked oscillator (here illustrated is the case of SESAM mode-locking). Image from[5].

3.3.3 State of the Art of the Technology

In addition to an excellent heat extraction capability, the thin-disk geometry offers significant advantages for ultrafast operation. The large mode areas on the gain medium and the short propagation distance of the pulses through this gain medium make it inherently advantageous for generating only small nonlinearities at very

high pulse energies. TDL regenerative and multi-pass amplifiers have proven to be extremely successful to scale up energy and average output power of ultrafast laser systems to new frontiers, exceeding the kilowatt average power with pulse energies ranging from the multi-millijoule to the multi-hundreds of millijoule level[2,9]. These extremely high pulse energies and high power are achievable from a single-gain unit. With kilowatt-class chirped fiber amplifiers (FCPA), a coherent combination is required to reach these levels. However, FCPA do reach at the moment the highest average power from any ultrafast laser system – albeit so far at more moderate pulse energies[3]. Most recent results of CPA-based thin-disk regenerative amplifiers have demonstrated 200 mJ of pulse energy at 1 kW of average power in 1 ps long pulses (*i.e.* approaching TW peak powers) at 5 kHz repetition rate[2]. Thin-disk multi-pass amplifiers used as booster amplifiers have also shown spectacular progresses reaching the kW level amplifiers with large parameter flexibility. The latest experiments led to the demonstration of ps pulses with 720 mJ pulse energy at kHz repetition rate[10] and of up to 2.45 kW at a repetition rate of 300 kHz, corresponding to a pulse energy of more than 8 mJ, and a pulse duration below 8 ps[11].

One unique advantage of the TDL geometry compared to other high-power geometries is that it offers the possibility of direct mode-locking of oscillators with very high average power operating in the multi-MHz repetition rate with tens of microjoules of pulse energy. The possibility of achieving one-box high-power and high-energy mode-locked oscillators again stands in strong contrast with other geometries, such as fibers and slabs, where high-power oscillators are difficult to scale up, both in power and energy, due to the long interaction length between the pulses and the gain medium.

Since their first demonstration in the year 2000[12], mode-locked thin-disk oscillators have consistently achieved orders of magnitude higher average power and pulse energy than any other ultrafast oscillator technology, reaching comparable levels to advanced high-power amplifiers operating at MHz repetition rate. Average power up to 350 W with 900 fs pulses[13], and pulse energy up to 80 μJ with 1 ps pulses (66 MW of peak power)[14] has been demonstrated with SESAM mode-locking. Comparable average powers and peak powers have also been demonstrated with Kerr-lens mode-locking, where 270 W with 330 fs pulse duration (38 MW peak power) have been reached[15]. Most of these results were achieved by operating the oscillator in vacuum chambers[16] in order to avoid that the roundtrip nonlinearity (self-phase modulation) becomes too high due to the air nonlinear response, which affects mode-locking stability at highest intracavity peak powers. Alternately, the intracavity power can be reduced by multiplying the number of gain passes inside the mode-locked resonator. This approach (also referred to as "active multi-pass cell") was demonstrated early on using SESAM mode-locking, and impressive results were achieved[17], reaching 40 μJ pulse energy without the need for vacuum.

3.3.4 Applications Driving These Advances

Much of the progress achieved in the development of high-power ultrafast laser systems has been driven by the growing industrial market of ultrafast lasers for high-precision material processing. Cold ablation of a large variety of materials can

be driven at higher speeds with high repetition rate, high energy ultrafast lasers. In fact, many of the state-of-the-art laser systems have been demonstrated in an industrial R&D environment. In this field, the advantages of kW ultrafast lasers are starting to be demonstrated: for example, efficient processing of carbon fiber reinforced polymer (CFRP) with negligible thermal damage was demonstrated. This was enabled by the application of a thin-disk multi-pass amplifier system generating ps pulses at an average output power exceeding 1 kW[18]. Additionally, new findings appear to show that glass cutting can benefit from this technology[19].

In scientific research, many efforts pursued to increase the average power of near infrared (NIR) ultrafast TDLs aimed at increasing the flux of XUV pulses obtained *via* high harmonic generation. Large progress in this area has been achieved with high-power ultrafast fiber amplifiers[20]. TDL driving sources, in particular at much higher energy levels, are also expected to provide advances in this area as shorter pulses become available. This will benefit a large number of time-resolved experimental methods using XUV pulses, which could be dramatically improved with a higher flux. One example is the study of ionization dynamics using coincidence measurements, where long recording durations are necessary to reach reasonable statistics. In this case, a higher repetition rate allows to significantly reduce measurement durations and/or to improve signal-to-noise ratio. Another example is the study of photoemission dynamics from surfaces, where space charge effects do limit the applicable pulse intensity; therefore, a high repetition rate is desired to reach sufficiently high signal-to-noise ratio at lower excitation intensity[21].

In parallel to the large progress achieved in the above-mentioned areas, other application areas are nowadays emerging that do benefit from the availability of ultrafast laser sources with ever-increasing average power. Several large research consortia have been established in the last years aiming at exploring the new possibilities offered by these laser systems: the laser lightning rod project that aims at using filaments to divert lightning, the FemtoSurf project for exploring multi-beam processing, the kW-Flexiburst project for exploring the next generation processing tool at kW average power and GHz repetition rates, the LAMPAS project aiming a exploring the large scale surface functionalization, and the Hiperdias project for exploring processing of Si and Diamond with kW class femtosecond laser pulses, to cite only a few examples.

3.4 Ongoing Challenge for High-Power Ultrafast Laser Technology: Pulse Duration

Despite the spectacular advances mentioned above, these high-average power systems (both oscillators and amplifiers) have been rather slow in replacing Ti:Sa technology. The main reason is the rather long pulse durations achieved directly from the laser systems (typically >300 fs), due to the limited bandwidth available in Yb-doped gain media, making Ti:Sapphire in many cases still the main choice for application fields in particular in scientific research.

However, external pulse compression techniques have also made large leaps forward in the last years, making it possible nowadays to reach the realm of pulse durations and peak powers available from Ti:Sa systems with a significantly higher repetition rate. We start here by giving some reminders of the basic nonlinear mechanisms involved in pulse compression: self-phase modulation and self-focusing, then we summarize most recent efforts for pushing high-average power ultrafast lasers along the way below 100 fs.

In addition to external pulse compression, many efforts are also being dedicated to find other host materials that could broaden the available gain bandwidth of Yb- without sacrificing thermal/or other spectroscopic properties that might degrade average power scaling[22]. However, advances along this line compared to efficient external compression methods has been comparatively slow; therefore, we restrict our discussion here to external pulse compression techniques based on spectral broadening *via* self-phase modulation, which have seen particularly spectacular progress at high average powers. Nevertheless, other techniques do exist that are also making progress in this direction which will not be discussed here but should be mentioned: the most relevant one being optical parametric chirped pulse amplification (OPCPA)[23] pumped by the above-mentioned kilowatt-class, ps pulse duration systems.

3.4.1 Self-Phase Modulation and Self-Focusing

Propagation of an intense pulse in common media such as dielectrics, gives rise to nonlinear optical effects – *i.e.*, effects that scale with the input intensity and not the amplitude as for linear effects. These effects are of utmost importance, because they can result in alterations of the pulses – both in the temporal and spectral domains. Here we focus on one effect that is of utmost relevance for ultrafast laser technology: **self-phase modulation (SPM).** SPM originates in the intensity dependence of the refractive index and results in changes on the temporal phase, the spectral phase and the spectral intensity of an ultrashort pulse.

Kerr-effect and SPM

The Kerr-effect is the first-order intensity-dependent refractive index and can be written:

$$n(I) = n_0 + n_2 I \tag{3.6}$$

where n is the total refractive index, n_0 is the refractive index at low intensity, I is the intensity and $n_2 I$ is therefore the Kerr nonlinear contribution to the refractive index. In the literature n_2 is usually called *nonlinear refractive index*, but, as mentioned before, it needs to be multiplied by the intensity to give the relevant contribution to the refractive index. Reasonably, n_2 is most typically given in units of an inverse intensity, *i.e.* in cm^2/W. When an ultrashort pulsed laser beam with constant peak intensity propagates through a Kerr-medium of length L_k, this time-dependent refractive index changes across the pulse and this results in a nonlinear phase shift that follows the intensity profile of the pulse:

$$\varphi(t) = -kn(I)L_K = -k[n + n_2 I(t)]L_K \tag{3.7}$$

the nonlinear phase shift $\varphi_2(t)$ is given by

$$\varphi_2(t) = -kn_2 I(t) L_K \tag{3.8}$$

and δ is the self-phase-modulation coefficient, *i.e.*, SPM-coefficient:

$$\delta \equiv \frac{\partial \varphi_2}{\partial I} = kn_2 L_K \tag{3.9}$$

In the situation where the intensity cannot be considered constant along the propagation direction, the so-called *B-integral* gives a value of the spatially integrated nonlinear shift (along the propagation direction) and is given by:

$$B \equiv \int_0^{L_k} \varphi_2(t,z)\,dz = \frac{2\pi}{\lambda} \int_0^{L_k} n_2 I(t,z)\,dz \tag{3.10}$$

SPM alone broadens the bandwidth of a pulse for most materials, because the frequency is given by:

$$\omega_2(t) = \frac{d\varphi_2(t)}{dt} = -\delta \frac{dI(t)}{dt} \tag{3.11}$$

This causes a *frequency excursion* across the pulse that is strongest at the flanks of the pulse (figure 3.7) where the derivative of the intensity is maximum. For a transform-limited pulse, SPM produces in the leading edge of the pulse (*i.e.* $\frac{dI(t)}{dt} > 0$) a reduction of the frequency (*i.e.* $\omega_2(t) < 0$ according to equation 3.11) and in the trailing edge of the pulse (*i.e.* $\frac{dI(t)}{dt} < 0$) an increase in the frequency (*i.e.* $\omega_2(t) > 0$ according to equation 3.11).

SPM contributes to the creation of new frequency components that can add constructively or destructively to the existing broadband frequency components of the pulse: under certain circumstances (for example in the case of an input transform-limited pulse, a positive n_2, and the simple scenario where only SPM is present), this results in significant spectral broadening as illustrated in figure 3.8, the pulse temporal envelope remains unchanged, and the accumulated spectral phase is nearly parabolic and positive. In practice, this spectral braodening can therefore be used for temporal pulse compression, for example using spectral braodening in fibers and subsequent dispersion compensation using prism pairs or grating compressors (See chapters 1 and 4).

One should note that the simple case described above is the case where only SPM is present and no dispersion. In this case, the amplitude of the pulse in the time domain is not affected. This is however rather unrealistic, as dispersion is usually present, which affects the temporal intensity profile and in turn affects SPM. To study the effects of dispersion and SPM simultaneously, numerical pulse propagation simulations are required to evaluate the pulse temporal and spectral shapes (See *e.g.* chapter 4).

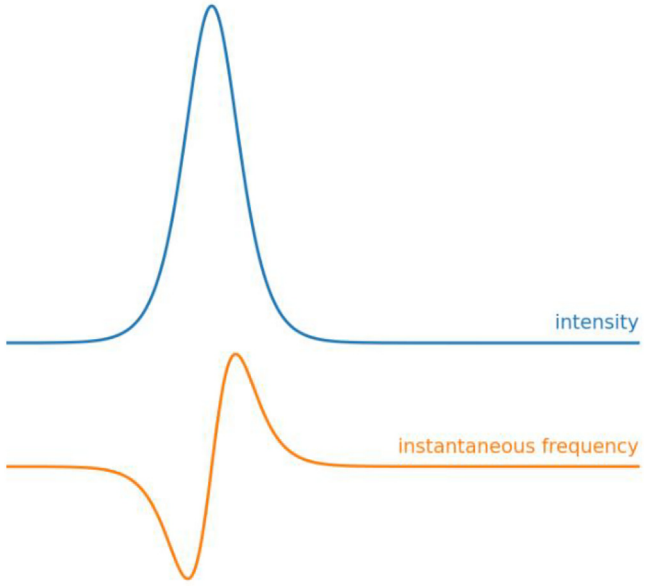

FIG. 3.7 – Effect of SPM on the instantaneous frequency of a pulse, assuming $n_2 > 0$: Top: time-dependent intensity with the leading and trailing edge of the pulse. Bottom: instantaneous frequency. Materials with $n_2 > 0$ will produce a spectral broadening generating lower frequencies (*i.e.*, "red" frequency components) in the leading edge of the pulse and higher frequencies (*i.e.*, "blue" frequency components) in the trailing edge of the pulse, which can be partly compensated by second-order negative dispersion. © MS, Martin Saraceno, 2021.

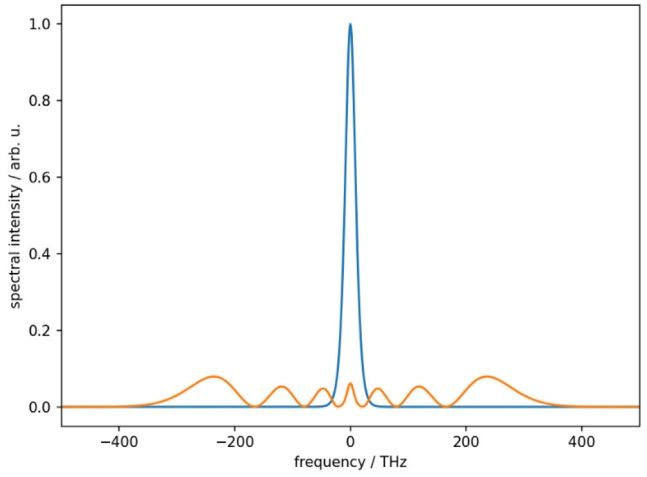

FIG. 3.8 – Spectral broadening of narrowband transform-limited pulses (blue) due to SPM. The oscillatory structure of the SPM broadened spectra (illustrated here in orange) originates from constructive and destructive interferences between the newly generated frequencies and the existing frequencies of the pulses. © MS, Martin Saraceno, 2021.

Self-focusing

Following the same discussion as above, the intensity dependence of the refractive index has an influence on the spatial properties of the beam for any beam that is not spatially homogeneous. Typical ultrashort lasers do exhibit a Gaussian transverse beam, which causes a spatial Kerr-effect resulting in a focusing lens effect (figure 3.9).

For a sufficiently thin Kerr-material compared to the Rayleigh range of the beam with length L_K one can assume that the beam radius w is constant and that one can make a parabolic approximation for the Gaussian beam profile:

$$I(x,y) = I_p \exp\left(-2\frac{x^2+y^2}{w^2}\right) \overset{(x^2+y^2)<<w^2}{\longrightarrow} \approx I_p\left(1-2\frac{x^2+y^2}{w^2}\right) \tag{3.12}$$

Under this approximation, we obtain a parabolic refractive index variation:

$$\begin{aligned} n(x,y) &= n_0 + n_2 I(x,y) \\ &\cong n_0 + n_2 I_p - 2n_2 I_p \tfrac{x^2+y^2}{w^2} \\ &\cong n_p - 2\Delta n_p \tfrac{x^2+y^2}{w^2}\, n(x,y) \end{aligned} \tag{3.13}$$

where $\Delta n_p = n_2 I_p$ and $n_p = n + \Delta n_p$. This parabolic refractive index variation corresponds to a focusing lens with a **focal length** f given by in the thin lens approximation:

$$f = \frac{w^2}{4\Delta n_p L_K} \tag{3.14}$$

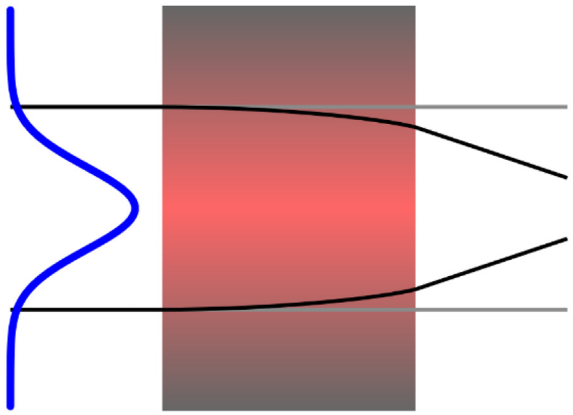

FIG. 3.9 – Self-focusing through the Kerr-effect; the incoming beam profile which is typically Gaussian causes spatial refractive index modulation following the beam profile. This acts like a lens and the beam emerges focused from the Kerr medium. This effect is used, for example, in combination with an appropriate aperture as an artificial saturable absorber for Kerr-lens mode-locking. © MS, Martin Saraceno, 2021.

The most important parameter to characterize self-focusing strength is the critical peak power P_{cr} which is defined by the peak power over which the self-focusing effect overcomes the effect of diffraction and thus can lead to the beam collapse:

$$P_{cr} \equiv 3.72\lambda_0^2/8\pi n_0 n_2 \tag{3.15}$$

It is rather straightforward to understand that self-focusing can result in material damage by acting as a self-amplifier for the intensity inside the material. Before this damage occurs, self-focusing can also lead to significant beam degradation. To understand this, one can consider the modulation observed in the spectral domain as also occurring in the spatial-coordinates – *i.e.*, in the spatial frequency k_x, k_y space – thus coupling energy into higher order modes and degrading the beam.

In general, the propagation of beams in the presence of both SPM, self-focusing and diffraction leads to complex propagation with spatio-temporal couplings that can only be correctly captured by sophisticated simulation tools. The picture becomes even more complex when considering ionization that can occur at high intensities – opening the possibility of a filamentation regime.

3.4.2 State-of-the-Art Pulse Compression of High-Average Power Ultrafast Lasers

The above-mentioned spectral broadening *via* SPM has been extensively used as a technique to increase the bandwidth of narrowband pulses for temporal compression. We focus here on techniques compatible with high average power levels. For low pulse energy levels (*i.e.* systems with high repetition rate), large-mode area solid-core fibers areas were used early on[24]. However, these systems are inherently limited to input peak powers below the critical self-focusing limit (for example 4 MW for linearly polarized pulses in fused silica), and fibers with very large mode areas (as required to avoid surface damage) suffer from high alignment and bending loss sensitivity.

For high-energy lasers, the most traditionally used technology is SPM in gas-filled hollow-capillaries[25]. These make use of propagation *via* grazing incidence creating selective losses for high-order modes. This technique has been extremely successfully when applied to mJ pulses at high average power[26] – also with high average power lasers, and benefits from the flexibility of applying different gases at varying pressures for tuning self-phase modulation for different energy levels. The limiting factor at very high pulse peak powers is ionization of the gas in the capillary. Another difficulty is that losses become increasingly large at moderate core diameters, and typically used large cores do require long, very straight capillaries that become cumbersome in practice.

For intermediate pulse energies and peak powers, hollow-core fibers, such as for example Kagome-type fibers[27], are an attractive alternative as they offer the same flexibility than hollow-core capillaries in terms of gas nature and pressure, but with waveguiding, making them less lossy and sensitive. These have also been investigated at the 100 W level and beyond[28].

However, all these pulse compression techniques did either exhibit rather high-loss and/or made it difficult to handle the high-average powers due to damage issues and they therefore struggled to bring the state-of-the-art level to the pulse durations available from Ti:Sa systems. This has however significantly changed in the last few years, with the introduction of better-suited pulse compression techniques which will likely accelerate the introduction of these high average power systems in an increasing number of fields. An example of this is the recent demonstration and deployment of Herriott-type multi-pass cells (MPCs) for spectral broadening at high-average power.

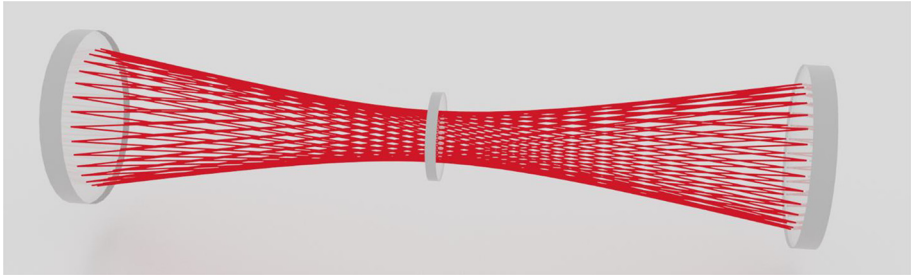

FIG. 3.10 – Schematic illustration of a Herriott-type MPC with a nonlinear medium (in this case a glass plate) placed at the focus. The two mirrors forming the MPC are curved and define a specific mode in the cell. For high pulse energies, the air or another gas inside the cell can be also used as a nonlinear medium. © MS, Martin Saraceno, 2021.

In such MPCs (figure 3.10) the pulses do undergo many roundtrips through a nonlinear medium (depending on the available pulse energy, the nonlinear medium can be a plate or simply a gaseous medium placed at the focus), causing them to undergo small amounts of self-phase modulation (SPM) on each pass, but enough overall to achieve significant spectral broadening. This allows for a smoothing of the spatiotemporal couplings and beam degradation due to self-focusing, allowing for an overall large spectral broadening without beam degradation. MPCs do allow for compact and robust setups that are very insensitive to alignment errors, unlike fiber-based setups that are cumbersome to operate at high average power. In the very first demonstration in 2016[29], an Yb:YAG slab laser system (10 MHz repetition rate, 850 fs pulse duration) was spectrally broadened from 1.6 to >13.5 nm bandwidth at an input power >400 W. The pulses were compressed down to pulse durations of 170 fs with an output power of 375 W reaching an overall transmission of >90%, clearly demonstrating the immense potential of this technique. Since then, ultrafast laser systems with average powers of several hundred watts up to the kilowatt level[30–33] and pulse energies in a wide range from the few μJ to the multi-mJ have been compressed to less than 100 fs, with high efficiency.

3.5 Conclusion and Outlook Towards Future Directions

Ultrafast lasers with ever-increasing average power are an active topic of investigation in the laser community that has made impressive progress in the last ten years. Record average powers up to 10 kW, and *J*-class systems with kHz repetition rates are among many of the recent achievements that pave the way to new areas of research. It can be expected that this progress will continue in the next decade toward the 100 kW level. Many of the bottlenecks delaying the adoption of these technologies for demanding scientific applications are currently being overcome, the most prominent example being about the pulse duration which is now reaching that of Ti:Sa laser systems. Applications making use of the available average power are starting to become easier to perform, in particular given that 100 W class ultrafast laser systems become more widely commercially available. Many new areas will also emerge as these laser systems are explored as driving sources for further nonlinear conversion. In general, there is a clear trend towards extending high-power operation to a wide spectral range spanning all the way from the XUV[20] to the terahertz (THz) regime[34,35], going through the deep-UV and the mid and far-IR ranges. This will be supported by ongoing research in materials for these frequency ranges, and corresponding studies to explore and improve their thermal properties.

References

[1] Russbueldt P., Mans T., Weitenberg J., Hoffmann H.D., Poprawe R. (Dec. 2010) Compact diode-pumped 1.1 kW Yb:YAG Innoslab femtosecond amplifier, *Opt. Lett.* **35**, 4169, https://doi.org/10.1364/OL.35.004169.

[2] Nubbemeyer T. *et al.* (Apr. 2017) 1 kW, 200 mJ picosecond thin-disk laser system, *Opt. Lett.* **42**, 1381, https://doi.org/10.1364/OL.42.001381.

[3] Müller M. *et al.* (Jun. 2020) 10.4 kW coherently combined ultrafast fiber laser, *Opt. Lett.* **45**, 3083, https://doi.org/10.1364/OL.392843.

[4] Giesen A., Hügel H., Voss A., Wittig K., Brauch U., Opower H., Scalable concept for diode-pumped high-power solid-state lasers, *Appl. Phys. B* **58**, 1994, https://doi.org/10.1007/BF01081875.

[5] Saraceno C.J., Sutter D., Metzger T., Abdou Ahmed M. (Dec. 2019) The amazing progress of high-power ultrafast thin-disk lasers, *J. Eur. Opt. Soc.-Rapid Publ.* **15**, 15, https://doi.org/10.1186/s41476-019-0108-1.

[6] Keller U. *et al.* (Sep. 1996) Semiconductor saturable absorber mirrors (SESAM's) for femtosecond to nanosecond pulse generation in solid-state lasers, *IEEE J. Select. Topics Quantum Electron.* **2**, 435, https://doi.org/10.1109/2944.571743.

[7] Kartner F.X., Jung I.D., Keller U. (Sep. 1996) Soliton mode-locking with saturable absorbers, *IEEE J. Select. Topics Quantum Electron.* **2**, 540, https://doi.org/10.1109/2944.571754.

[8] Brabec T., Spielmann C., Curley P.F., Krausz F. (Sep. 1992) Kerr lens mode locking, *Opt. Lett. OL* **17**, 1292, https://doi.org/10.1364/OL.17.001292.

[9] Negel J.-P. *et al.* (Aug. 2015) Ultrafast thin-disk multipass laser amplifier delivering 14 kW (47 mJ, 1030 nm) average power converted to 820 W at 515 nm and 234 W at 343 nm, *Opt. Express* **23**, 21064, https://doi.org/10.1364/OE.23.021064.

[10] Herkommer C. *et al.* (Sep. 2020) "Ultrafast thin-disk multipass amplifier with 720 mJ operating at kHz repetition rate for applications in atmospheric research," *Opt. Express, OE* **28**, 30164, https://doi.org/10.1364/OE.404185.

[11] Abdou-Ahmed M. (2017) *Development of high-power thin-disk lasers: status and perspectives, presented at the JNPLI.* Strasbourg, France.
[12] der Au J.A. *et al.* (Jun. 2000) 16.2 W average power from a diode-pumped femtosecond Yb: YAG thin disk laser, *Opt. Lett. OL* **25**, 859, https://doi.org/10.1364/OL.25.000859.
[13] Saltarelli F., Graumann I.J., Lang L., Bauer D., Phillips C.R., Keller U. (Oct. 2019) Power scaling of ultrafast oscillators: 350 W average-power sub-picosecond thin-disk laser, *Opt. Express, OE* **27**, 31465, https://doi.org/10.1364/OE.27.031465.
[14] Saraceno C.J. *et al.* (Jan. 2014) Ultrafast thin-disk laser with 80 μJ pulse energy and 242 W of average power, *Opt. Lett.* **39**, 9, https://doi.org/10.1364/OL.39.000009.
[15] Brons J. *et al.* (Nov. 2014) "Energy scaling of Kerr-lens mode-locked thin-disk oscillators, *Opt. Lett.* **39**, 6442, https://doi.org/10.1364/OL.39.006442.
[16] Saraceno C.J. *et al.* (Oct. 2012) 275 W average output power from a femtosecond thin disk oscillator operated in a vacuum environment, *Opt. Express* **20**, 23535, https://doi.org/10.1364/OE.20.023535.
[17] Bauer D., Zawischa I., Sutter D.H., Killi A., Dekorsy T. (Apr. 2012) Mode-locked Yb:YAG thin-disk oscillator with 41 μJ pulse energy at 145 W average infrared power and high power frequency conversion, *Opt. Express* **20**, 9698, https://doi.org/10.1364/OE.20.009698.
[18] Graf T., Weber R., Abdou-Ahmed M., Onuseit V., Freitag C., Weidenman M. (2015) Efficient High-quality Processing of CFRP with a kW Ultrafast Thin-disk Laser, presented at the Advanced Solid State Lasers.
[19] Dietz T. *et al.* (Apr. 2020) Ultrafast thin-disk multi-pass amplifier system providing 1.9 kW of average output power and pulse energies in the 10 mJ range at 1 ps of pulse duration for glass-cleaving applications, *Opt. Express, OE* **28**, 11415, https://doi.org/10.1364/OE.383926.
[20] Hädrich S. *et al.* (Oct. 2014) High photon flux table-top coherent extreme-ultraviolet source, *Nature Photonics* **8**, 779, https://doi.org/10.1038/nphoton.2014.214.
[21] Chiang C.-T. *et al.* (Jan. 2015) Boosting laboratory photoelectron spectroscopy by megahertz high-order harmonics, *New J. Phys.* **17**, 013035, https://doi.org/10.1088/1367-2630/17/1/013035.
[22] K. Beil *et al.* (Oct. 2013) Yb-doped mixed sesquioxides for ultrashort pulse generation in the thin disk laser setup, *Appl. Phys. B* **113**, 13, https://doi.org/10.1007/s00340-013-5433-2.
[23] Mecseki K. *et al.* (Mar. 2019) High average power 88 W OPCPA system for high-repetition-rate experiments at the LCLS x-ray free-electron laser, *Opt. Lett. OL*, **44**, 1257, https://doi.org/10.1364/OL.44.001257.
[24] Südmeyer T. *et al.* (Oct. 2003) Nonlinear femtosecond pulse compression at high average power levels by use of a large-mode-area holey fiber, *Opt. Lett. OL* **28**, 1951, https://doi.org/10.1364/OL.28.001951.
[25] Nisoli M. *et al.* (Apr. 1997) Compression of high-energy laser pulses below 5 fs, *Opt. Lett. OL* **22**, 522, https://doi.org/10.1364/OL.22.000522.
[26] Hädrich S. *et al.* (Sep. 2016) Energetic sub-2-cycle laser with 216 W average power, *Opt. Lett. OL* **41**, 4332, https://doi.org/10.1364/OL.41.004332.
[27] Benabid F., Knight J.C., Antonopoulos G., Russell P.S.J. (Oct. 2002) Stimulated raman scattering in hydrogen-filled hollow-core photonic crystal fiber, *Science*, **298**, 399, https://doi.org/10.1126/science.1076408.
[28] Emaury F. *et al.* (Dec. 2014) Efficient spectral broadening in the 100 W average power regime using gas-filled kagome HC-PCF and pulse compression, *Opt. Lett. OL* **39**, 6843, https://doi.org/10.1364/OL.39.006843.
[29] Schulte J., Sartorius T., Weitenberg J., Vernaleken A., Russbueldt P. (Oct. 2016) Nonlinear pulse compression in a multi-pass cell," *Optics Lett.* **41**, 4511, https://doi.org/10.1364/OL.41.004511.
[30] Weitenberg J. *et al.* (Aug. 2017) Multi-pass-cell-based nonlinear pulse compression to 115 fs at 75 μJ pulse energy and 300 W average power, *Opt. Express* **25**, 20502, https://doi.org/10.1364/OE.25.020502.
[31] Kaumanns M. *et al.* (Dec. 2018) Multipass spectral broadening of 18 mJ pulses compressible from 13 ps to 41 fs, *Opt. Lett.* **43**, 5877, https://doi.org/10.1364/OL.43.005877.

[32] Grebing C. *et al.* (Nov. 2020) Kilowatt-average-power compression of millijoule pulses in a gas-filled multi-pass cell, *Opt. Lett. OL* **45**, 6250, https://doi.org/10.1364/OL.408998.

[33] Tsai C.-L. *et al.* (Sep. 2019) Efficient nonlinear compression of a mode-locked thin-disk oscillator to 27 fs at 98 W average power, *Opt. Lett.* **44**, 4115, https://doi.org/10.1364/OL.44.004115.

[34] Kramer P.L., Windeler M.K.R., Mecseki K., Champenois E.G., Hoffmann M.C., Tavella F. (May 2020) Enabling high repetition rate nonlinear THz science with a kilowatt-class sub-100 fs laser source, *Opt. Express* **28**, 16951, https://doi.org/10.1364/OE.389653.

[35] Meyer F., Vogel T., Ahmed S., Saraceno C. (Mar. 2020) Single-cycle, MHz-repetition rate THz source with 66 mW of average power, *Opt. Lett.* **45**, 2494, https://doi.org/10.1364/OL.386305.

Chapter 4

Basics of Femtosecond Pulse Manipulation: Simple Numerical Tools*

Baptiste Fabre and Yann Mairesse*****

Université de Bordeaux – CNRS – CEA, CELIA, UMR5107, F33405 Talence, France

Many detailed courses already exist on the generation and characterization of femtosecond pulses[1–3]. The goal of this chapter is not to provide an extensive review, but rather to give a few practical tools to develop an intuition on how simple effects can be at play in a femtosecond laboratory. This chapter is accompanied by a Jupyterlab Notebook containing the python code necessary to generate all presented examples. All "Let us practice" sections are detailed in the Notebook. To get Jupyterlab, the easiest way is to install *Anaconda Individual Edition*[i], which is available for Windows, Linux and MacOs.

We will start from the output of a femtosecond laser system. What happens to femtosecond pulses as they propagate along in the laboratory? They can travel through air, glass, birefringent media… They can be reflected on mirrors, focused by lenses… All optical elements placed on the path of a femtosecond pulse are susceptible to modify its temporal profile. In general, experimentalists tend not to measure things as long as there is no issue in their experiment. Of course this is bad, but why bother measuring the temporal profile of the pulses if the cross-correlation in the pump-probe scans is short? Why worry about space–time couplings if the experiment works? How could the pulse be elliptical if no birefringent medium is used? Advanced techniques do exist to accurately tackle all these questions in the laboratory, yet there are many situations where they are not used, and sometimes it is ok. Indeed, if your

*Supplementary electronic material available at: https://hal.archives-ouvertes.fr/hal-03624701.

**baptiste.fabre@u-bordeaux.fr

***yann.mairesse@u-bordeaux.fr

[i]https://www.anaconda.com/products/individual.

DOI: 10.1051/978-2-7598-2719-0.c004

laser delivers 300 fs Fourier limited pulses with a few hundreds microjoules in a 2 mm beam, we will see that it is very unlikely that their temporal profile will be distorted by propagation. On the other hand, if you deal with 20 fs pulses with a multi mJ energy in a 10 mm beam, you should start to worry. In the worst case scenario, the pulses can be stretched by linear dispersion, spectrally broadened by self-phase modulation in air and transmissive optics, which causes the beam to be spatially inhomogeneous and self-focused, and the initially linear polarization state can be elliptical or circular because of simple bounces on misaligned mirrors.

In the first part, we present the basic functions used throughout the paper, from Fourier transform to time–frequency representations. Next, we describe the influence of the spectral phase of a femtosecond pulse on its temporal profile. In the third part, we investigate the linear propagation in different media and provide a few examples of dispersion. Section 4.4 deals with the influence of self-phase modulation on the temporal profile of femtosecond pulses, and its applications for post-compression. Section 4.5 discusses the role of reflections on mirrors, in particular their influence on the polarization state of light.

4.1 Presentation of Useful Functions

Throughout the paper we will introduce some functions and show the output of code which is available in the Supplementary Material. All coding relies on `Python 3.8`, but should work with all `Python 3.X` versions. Let us first import the classical libraries `numpy` and `matplotlib.pyplot`. In general, python libraries, and in particular `numpy`, should be imported using an alias (for example `np` in the case of `numpy`), but in order to lighten the writing and make it easier for beginners, we will omit this alias. This means that for instance to use the exponential function, we will type `exp()` instead of `np.exp()`. We can do this here because we do not import many libraries. This could be a problem if one function was defined in two different libraries.

```
from numpy import *
from matplotlib.pyplot import *

#Control size of figures
rcParams ['figure.figsize'] = [12, 8]
```

In this section, useful functions for the manipulation of electric fields in the time and frequency domains will be presented. All these functions, and the ones that will be presented in the next sections, could be grouped in a same file, which would constitute your own library.

4.1.1 Travelling Between Time and Frequency

4.1.1.1 Definitions

To move from the time to the frequency domain, and *vice versa*, we will use the Fast-Fourier Transform (FFT) function. Let us for instance start from an electric field defined in the time domain, and evenly sampled along a time window extending over Δt, by steps of δt, and with a number of samples N: $t = [-\frac{\Delta t}{2} : \delta t : \frac{\Delta t}{2}]$. The angular frequency window over which the FFT will be calculated is $\omega = [-\frac{\Delta\omega}{2} : \delta\omega : \frac{\Delta\omega}{2}]$, where:

$$\begin{aligned} \delta t &= t[1] - t[0] \\ \Delta t &= N \times \delta t \\ \delta\omega &= \frac{2\pi}{\Delta t} \\ \Delta\omega &= \delta\omega \times N = \frac{2\pi}{\delta t} \end{aligned}$$

The overall extent of the angular frequency window is thus determined by the sampling rate in the time domain, which is quite intuitive: it is necessary to use a small value of δt, *i.e.* a fine sampling of the time axis, to be able to access to high frequencies. On the other hand, the sampling of the angular frequency axis, $\delta\omega$, is determined by the overall extent of the time window Δt.

4.1.1.2 Zero Padding

Starting from a given time window, the angular frequency sampling may be insufficient to properly resolve the spectrum. In that case, it is possible to increase the extent of the temporal window in the FFT calculation, using *zero padding*, *i.e.* by adding zeros to the function before Fourier transforming it. The time window now has a size of N_{zp}:

$$t = \left[-\frac{\Delta t}{2} : \delta t : -\frac{\Delta t}{2} + (N_{zp} - 1) \times \delta t\right]$$

The time sampling rate δt being unchanged, the extent of the angular frequency window remains unchanged too:

$$\Delta\omega = \frac{2\pi}{\delta t}$$

However, the angular frequency sampling rate is smaller:

$$\delta\omega = \frac{2\pi}{N_{zp}\delta t}$$

This enables a finer sampling of the spectrum.

The two following functions enable switching easily from time to frequency and *vice versa*:

- `time2freq(t,Nbw)` takes as an argument an array of times with sampling rate δt and returns an array of `Nbw` angular frequencies ω (rad.s^{-1}).
- `freq2time(w,Nbt)` takes as an argument an array of angular frequencies and returns an array of `Nbt` times t (s).

R One remark, even if it is absolutely not mandatory, we will work in general with symmetrical frequency and time domain (same number of points, and zero time and zero frequency at the center of the window). This makes switching back and forth between the two domains easier.

4.1.2 Fourier Transform and Inverse Fourier Transform

In python, the `fft` and `ifft` functions which perform the fast Fourier transform (FFT) and its inverse (IFFT) can be imported from `numpy.fft` library:

```
from numpy.fft import fft, ifft
```

4.1.2.1 Centering of the Fourier Transform with Respect to Time or Frequency

From a numerical point of view, these functions should be applied to signal where the zero frequency (resp. the zero time) corresponds to the first element of the array, positive frequency (time) runs from 0 to half the array, and negative frequency (time) runs from half the array to its end. In our case, as we use time and frequency axis whose zero is at the center of the window, it is thus necessary to shift the arrays to bring the central frequency, located at `NbPoints/2` (where `NbPoints` is `Nbw` or `Nbt`) to the first position. This is done using the function `fftshift` from `numpy.fft library` (see figure 4.1).

Lets see how this works:

```
from numpy.fft import fftshift
```

```
datatest=3+cos (2.356e15*t)
plot(abs(fft(datatest)))
plot(fftshift(abs(fft(datatest))), 'r')
legend(['Zero frequency at origin, positive frequencies until␣
↪half xscale, then negative frequencies', 'fftshift->Zero␣
↪frequency at the center of the xscale'])
```

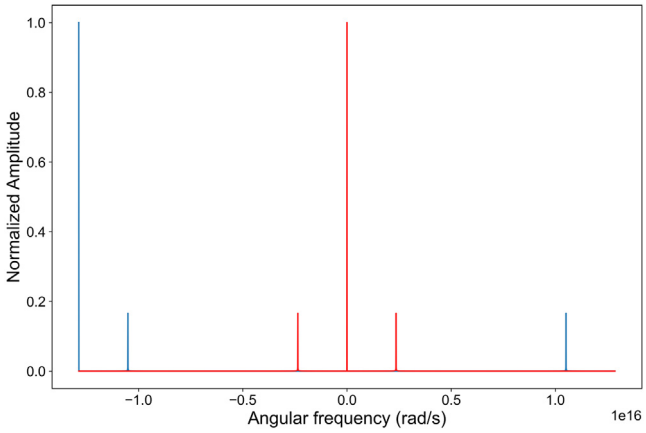

FIG. 4.1 – Illustration of the shift of the central frequency using `fftshift` function. Blue plain line: zero frequency at origin, positive frequencies until half xscale, then negative frequencies. Red plain line: zero frequency at the center of the xscale.

We chose here to work with symmetrical time or frequency domains, *i.e.* with the zero time and zero frequency at the center of the x-scale.

Since this is not the original scale of the fft, we need to *fftshift* the data, then Fourier transform it, then *fftshift* it again.

We can then define two new functions, called `FT` and `IFT` in order to perform Fourier Transform and Inverse Fourier Transform following this sequence:

```
# Perform the FFT for symetric space (time or frequency)
def FT(data,NbPoints):
    return fftshift(fft(fftshift(data),NbPoints))

# Perform the IFFT for symetric space (time or frequency)
def IFT(data,NbPoints):
    return fftshift(ifft(fftshift(data),NbPoints))
```

4.1.2.2 Example

In the following example, we combine fftshift and zero-padding.

```
Nbt = 2048,Nbw=Nbt
t=linspace(-500e-15,500e-15,Nbt)
datatest=3+cos(2.356e15*t)
w=time2freq(t,Nbw)
plot(w,fftshift(abs(fft(datatest,Nbw)))/
```

```
 ↪amax(abs(fft(datatest,Nbw))),'r')
Nbw=16384,w=time2freq(t,Nbw)
plot(w,fftshift(abs(fft(datatest,Nbw)))/
 ↪amax(abs(fft(datatest,Nbw))),'tab:blue')
xlim((2.2e15,2.5e15)),ylim((0,0.2))
Legend=legend(['2048 points','16384 points'],
       handlelength=2, handleheight=3,bbox_to_anchor=(0.9, 0.9))
xlabel('Angular frequency (rad/s)'),ylabel('Normalized Amplitude')
frame = Legend.get_frame()
Legend.get_frame().set_linewidth(2)
```

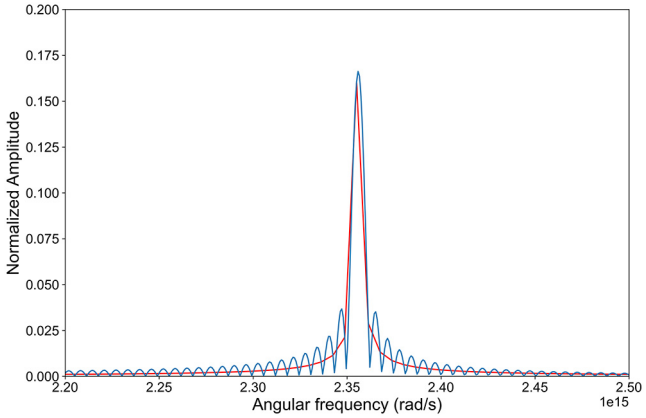

FIG. 4.2 – Illustration of zero-padding of the temporal function with 2048 points (red line) and 16 384 points (blue line).

In figure 4.2, the spectrum obtained by zero-padding shows multiple bounces around the main frequency component. What is the origin of these bounces? The zero-padded function is a cosine function on the first 2048 points, followed by a set of zeros on the next 14 336 points. In other words, this function is the product of a cosine, whose Fourier transform is a set of Dirac peaks, and a rectangular function, whose Fourier transform is a sinc. The Fourier transform of the product of two functions is the convolution of the Fourier transforms of the two functions. The bounces are thus those of the sinc function.

4.1.3 Definition of Electric Fields

In order to avoid sign problems, one has to define a convention for the definition of electric field in time and frequency domains. The following convention will be used here:

4.1.3.1 In the Time Domain

$$E(t) = |E(t)|e^{-i\phi(t)} \tag{4.1}$$

where $|E(t)|$ is the amplitude and $\phi(t)$ the temporal phase of the field.

The intensity profile (pulse envelope) is then given by: $I(t) = |E(t)|^2$. In other words, the electric field can be defined as:

$$E(t) = \sqrt{I(t)}e^{-i\phi(t)} \tag{4.2}$$

In this lecture, we will describe the initial pulse shape using a Gaussian shape. This is done thanks to the following function which takes as arguments:

- `t`: the array of times.
- `fwhm_t`: the pulse duration, defined as full width at half maximum of the intensity profile.

```
def calc_I_t(t, fwhm_t):
    return exp(-4*log(2)*(t)**2/fwhm_t**2)
```

4.1.3.2 In the Angular Frequency Domain

We can similarly define the electric field in the frequency domain:

$$E(\omega) = |E(\omega)|e^{+i\phi(\omega)} \tag{4.3}$$

where $|E(\omega)|$ is the amplitude and $\phi(\omega)$ the spectral phase of the field.

The spectrum is then given by: $I(\omega) = |E(\omega)|^2$. In other words, the electric field can be defined as:

$$E(\omega) = \sqrt{I(\omega)}e^{i\phi(\omega)} \tag{4.4}$$

```
def calc_I_w(w, w0, fwhm_w):
    return exp(-4*log(2)*(w-w0)**2/fwhm_w**2)
```

4.1.3.3 Fourier Transforms

Within these conventions:

- The electric field $E(\omega)$ in the angular frequency domain is the inverse Fourier transform of $E(t)$: use `IFT(E_t,Nbw)`.

- Electric field $E(t)$ in the time domain is the Fourier transform of $E(\omega)$: use `FT(E_w,Nbt)`.

Let us practice !

(1) Define a spectrum with a gaussian shape and a central frequency $\omega_0 = 0$ and a width equal to 20×10^{14} rad.s^{-1} (This is a non physical example). In order to simplify interpretations, we will use the same number of points for time and angular frequencies. In principle, it is possible to use different sizes for arrays, but it implies some modifications in the code, in particular when comparing phases.
(2) Define the electric field in the angular frequency domain with a constant zero phase.
(3) Compute the electric field in the time domain and its phase.
(4) Plot on the spectrum, intensity and phases.
(5) What happens if we consider a more realistic electric field describing, for example, a pulse at $\lambda_0 = 800$ nm with a 40 nm full half maximum bandwidth?
(6) Define the spectrum associated with this pulse.
(7) Then, compute the electric field in the angular frequency domain, still with a constant phase equal to 0.
(8) Finally, we can obtain the electric field in time domain applying Fourier transform on $E(\omega)$. Compare the spectrum, intensity and phases.

4.1.3.4 Conclusion: Removing of a Linear Temporal Phase

As shown in the previous subsection, shifting the spectrum by a quantity ω_0, induces a linear temporal phase $-\omega_0 t$. This is a well known property of the Fourier transform. In practice, this linear component can make it difficult to study variations of the temporal phase. It is thus often convenient to remove it, for instance using the following function:

```
def RemoveLinearPhase(phi_t,t):
    ind_min=int(len(t)/2-len(t)/10)
    ind_max=int(len(t)/2+len(t)/10)
    phi_t=phi_t-polyval(polyfit(t[ind_min:ind_max],phi_t[ind_min:
 ↪ind_max],1),t)
    return phi_t
```

4.1.4 Pulse Duration

4.1.4.1 Full Width Half Maximum

One way to measure the duration of a pulse is to use the full width half maximum (FWHM). This can be done using the following function, defined for any function Y of X:

```
def calcFWHM(X,Y):
    ind_max=Y.argmax()
    ind_inf_half_max=abs(Y[0:ind_max]-Y[ind_max]/2).argmin()
    ind_sup_half_max=abs(Y[ind_max:]-Y[ind_max]/2).
 ↪argmin()+ind_max

    return X[ind_sup_half_max] - X[ind_inf_half_max]
```

Using the electric field defined previously, we find a duration of:

```
print('The FWHM duration of a Fourier Limited pulse at {:.1f} nm␣
 ↪with a wavelength bandwidth (FWHM) of {:.1f} nm is equal to {:.
 ↪1f} fs'\
      .format(lambda0*1e9,fwhm_lambda*1e9,calcFWHM(t,abs(E_t)**2.
 ↪0)*1e15))
```

```
The FWHM duration of a Fourier Limited pulse at 800.0 nm with a␣
 ↪wavelength
bandwidth (FWHM) of 40.0 nm is equal to 23.4 fs
```

4.1.4.2 RMS Duration

If the pulse shape is structured (*i.e.* if the shape is not a nice Gaussian), the FWHM may not reflect this structuring and thus gives a poor estimation of the real duration. In this case, it is possible to use another metric which takes into account the full temporal distribution of the pulse. The **Root Mean Square** half-width duration is defined as:

$$\tau_{\mathrm{RMS}} = \sqrt{\frac{\int t^2 I(t)\,dt}{\int I(t)\,dt}} \tag{4.5}$$

and can be calculated using the following function:

```
def calcRMS(X,Y):
    from scipy.integrate import simps
    Y=roll(Y,int(len(Y)/2)-argmax(abs(Y)))
    num=simps(X**2*Y,X)
    den=simps(Y,X)
    return sqrt(num/den) #return the RMS duration
```

which gives for the previously defined pulse:

```
print('The RMS half width duration of a Fourier Limited pulse at␣
 ↪{:.1f} nm with a wavelength bandwidth (FWHM) of {:.1f} nm is␣
 ↪equal to {:.1f} fs'\
      .format(lambda0*1e9,fwhm_lambda*1e9,calcRMS(t,abs(E_t)**2.
 ↪0)*1e15))
```

```
The RMS half-width duration of a Fourier Limited pulse at 800.0 nm␣
 ↪ with a wavelength
bandwidth (FWHM) of 40.0 nm is equal to 10.0 fs
```

4.1.5 Time–Frequency Representations

The temporal profile of a light pulse is obtained by Fourier transforming its complex spectrum. The intensity profile $I(t)$ is definitely an important quantity but it does not contain all information about the pulse. For example, a Fourier-limited Gaussian narrowband pulse and a chirped broadband Gaussian pulse can have the same intensity profile. As we will see later, these two pulses have a different spectral phase, constant for the former, quadratic for the latter. However the spectral phase may not be the most intuitive representation. Here, we introduce two frequently used time–frequency distributions: the **Gabor analysis** and the **Wigner distribution**. Time–frequency distributions are in fact very common and intuitive[4]. They show the temporal evolution of the instantaneous frequency of a pulse, exactly like a music score where different notes (*i.e.* frequency components) are depicted as a function of time.

4.1.5.1 Gabor Transform (Spectrogram)

A straightforward way to obtain a time–frequency distribution is to cut a temporal slice of the signal of interest around a given time, calculate the spectrum of the slice, and repeat this operation for different temporal positions of the slice. The resulting quantity is a 2D function of time and frequency. From a mathematical point of view, the **Gabor transform** of a field $E(t)$ can be defined as the FFT of the product of the signal with a gate $G(t-\tau)$:

$$\mathcal{G}(\omega,\tau) = \mathrm{FFT}[E(t)G(t-\tau)] \tag{4.6}$$

In the following, we will define the gate as a Gaussian whose width is related to a parameter α. Other types of gate functions could be used (rectangular, supergaussian…).

```
def gabor(t,E_t,Nbw,alpha):
    def gaussian(t,alpha):
        return 1./2*sqrt(pi*alpha)*exp(-t**2/(alpha)**2)
    E_w=zeros((len(t),Nbw),dtype=complex)
    for i,tau in enumerate(t):
        E_w[i,:]=FT(E_t*gaussian(t-tau,alpha),Nbw)
    return flipud(transpose(E_w))
# flipud is used to flip upside-down the matrix, in order to use␣
↪pcolormesh for the plotting. If you prefer to use imshow, do␣
↪not forget to remove this flipud command.
```

We can study the effect of α on the temporal and frequency resolution. For that purpose we define a function to plot the Gabor distribution:

```
def plot_gabor(G,t,w,tmin,tmax,wmin,wmax,name):
```

where *tmin*,*tmax*,*wmin*,*wmax* are the limits of the axis on the plot, and *name* is the title.

Let us apply this Gabor transform to the previous pulse, with $\alpha = 10 \times 10^{-15}$ s (see figure 4.3):

```
#Define the limits for the plots
alpha=10.0e-15
G=gabor(t,E_t,Nbw,alpha)
tmin,tmax=-50e-15,50e-15
wmin,wmax=2e15,2.8e15
plot_gabor(G,t,w,tmin,tmax,wmin,wmax,'Gabor transform for␣
↪$\\alpha =${:.1e}'.format(alpha))
```

The white line at the bottom of the plot in figure 4.3 is the temporal marginal, obtained by summing the Gabor distribution over all frequencies.

Let us practice !

(1) Change the spectral bandwidth of the pulse and look at the influence on the duration.
(2) Change the value of α to see how it affects temporal and spectral resolution of the Gabor analysis.

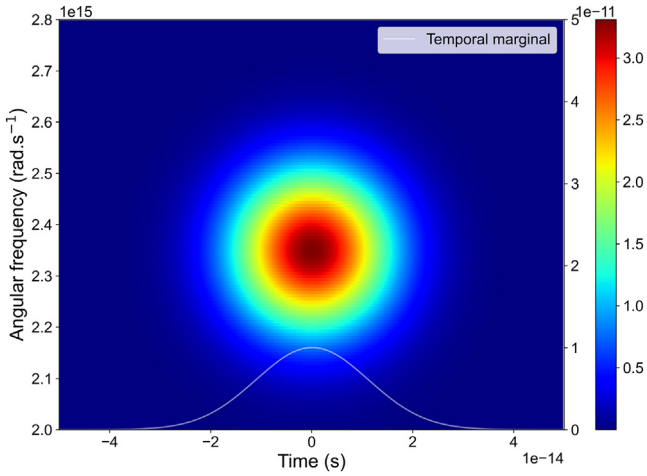

FIG. 4.3 – Gabor transform of a 23.4 fs FWHM duration pulse for $\alpha = 10$ fs, where α is a parameter related to the width of the Gaussian gate function. White line: temporal marginal.

Conclusion: Using a small value of α increases the temporal resolution of the Gabor analysis but degrades the frequency distribution.

4.1.5.2 Wigner Distribution

An alternative time–frequency representation can be obtained by calculating the Wigner distribution of the field $E(t)$, defined as:

$$\mathcal{W}(t,w) = \mathrm{FFT}\left(E\left(t+\frac{\tau}{2}\right)E^*\left(t-\frac{\tau}{2}\right)\right) \tag{4.7}$$

In order to get the signal at $t+\frac{\tau}{2}$ and $t-\frac{\tau}{2}$ we use the Fourier Transform shift theorem (see figure 4.4):

```
N=len(E_t)
E_t_plus_tau_2␣
 ↪=flipud(ifft(outer(fftshift(fft(E_t)),ones(N))*exp(␣
 ↪-1j*outer(w,t)/2 ),axis=0))
E_t_minus_tau_2 =␣
 ↪flipud(ifft(outer(fftshift(fft(E_t)),ones(N))*exp(␣
 ↪1j*outer(w,t)/2 ),axis=0))
T,W=meshgrid(t,w)
fig=figure()
subplot(1,2,1),pcolormesh(T,W,E_t_plus_tau_2.
 ↪real,cmap='jet',shading='auto')
xlabel('Time (s)'),ylabel('Angular frequency (rad.s$^{-1}$)')
subplot(1,2,2),pcolormesh(T,W,E_t_minus_tau_2.
 ↪real,cmap='jet',shading='auto')
xlabel('Time (s)'),ylabel('Angular frequency (rad.s$^{-1}$)')
```

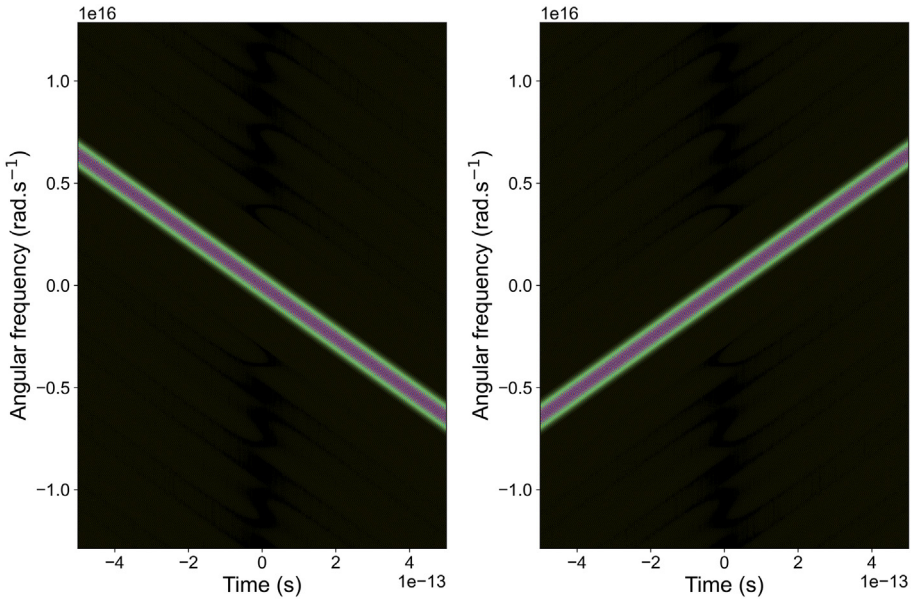

FIG. 4.4 – Illustration of the Fourier Transform shift theorem.

Finally, the complete function that computes the Wigner distribution can be defined as:

```
def wigner(Ex,t,w):
    N=len(Ex)
    EX1 =ifft(outer(fftshift(fft(Ex)),ones(N))*exp(␣
↪-1j*outer(w,t)/2 ),axis=0)
    EX2 = ifft(outer(fftshift(fft(Ex)),ones(N))*exp(␣
↪1j*outer(w,t)/2 ),axis=0)
    W=real(fftshift(fft(fftshift(EX1*conj(EX2),axes=1)
    ,axis=1),axes=1))
    return transpose(W)
```

We can also define a function to plot the Wigner distribution using `pcolormesh`

```
def plot_wigner(WIG,t,w,tmin,tmax,wmin,wmax,name):
```

The Wigner distribution of the pulse, presented in figure 4.5, is calculated by:

```
WIG=wigner(E_t,t,w)
```

and plotted by:

```
#define the limits for plotting
tmin,tmax=-50e-15,50e-15
wmin,wmax=2e15,2.8e15
plot_wigner(WIG,t,w,tmin,tmax,wmin,wmax,'Wigner distribution')
```

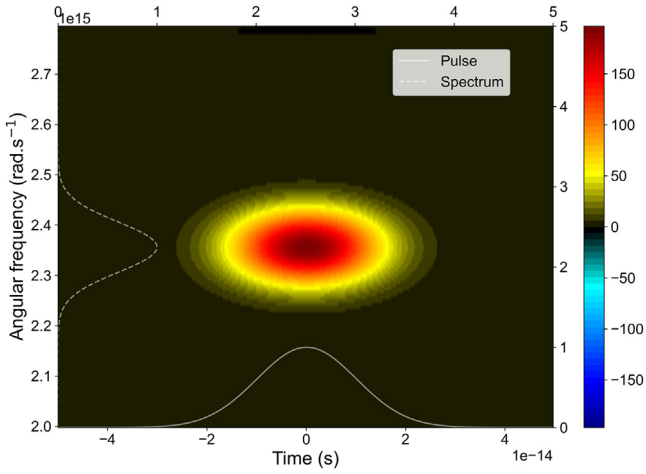

FIG. 4.5 – Wigner distribution of a 23.4 fs FWHM duration pulse. Plain white line: temporal marginal. Dashed white line: spectral marginal.

Unlike the Gabor transform, the Wigner distribution can take negative values. We will see later what this means. The white lines on the above figure show the two marginals, computed by summing the Wigner distribution along the frequency and time axis. The temporal marginal is equal to the intensity profile of the light pulse. The spectral marginal of the Wigner distribution is the pulse spectrum. This is an interesting property of the Wigner distribution: its projections are the intensity and the spectrum.

4.2 Influence of the Spectral Phase

In this part, we use the basic tools presented above to investigate the influence of various spectral phases on the temporal profile of a femtosecond pulse. The initial pulse is defined as being a Gaussian spectrum centered at 800 nm, with a 40 nm FWHM bandwidth and a flat spectral phase presented in figure 4.6 (see the corresponding code in the Jupyter Notebook).

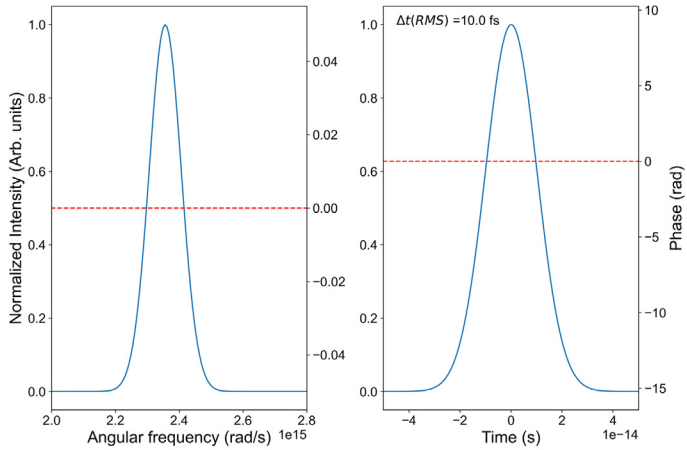

FIG. 4.6 – Spectral (left) and temporal (right) intensity profile of the initial pulse at 800 nm with 23.4 fs FWHM duration and 40 nm FWHM spectral width. Red dashed line: spectral phase.

The pulse is centered around $\omega_0 = 2.356 \times 10^{15}$ rad/s. Its temporal profile is Gaussian, with a 23.4 fs duration (FWHM). The temporal phase is flat, once the linear component associated with the non-zero central frequency is removed. This pulse is the shortest pulse that can be achieved with the given spectrum. It is said to be Fourier-limited. In the following, we establish the influence of the spectral phase on the temporal profile, by adding polynomial phases of increasing order.

4.2.1 Effect of a Linear Spectral Phase

The lowest order phase variation we can add to the pulse is a linear spectral phase (see figure 4.7), defined as:

$$\phi_{\text{lin}}(\omega) = -(\omega - \omega_0)\tau$$

where $\tau = -50$ fs is the slope of the phase.

```
# parameter tau
tau=-50e-15 #fs
# Linear phase
phi_w_lin = -(w-w0)*tau

# Electric field in the angular frequency domain
E_w_lin=sqrt(calc_I_w(w,w0,fwhm_w))*exp(phi_w_lin*1j)
phi_w_lin=unwrap(angle(E_w_lin))

# Electric field in the time domain
E_t_lin=FT(E_w_lin,Nbt)
phi_t_lin=unwrap(angle(E_t_lin))
```

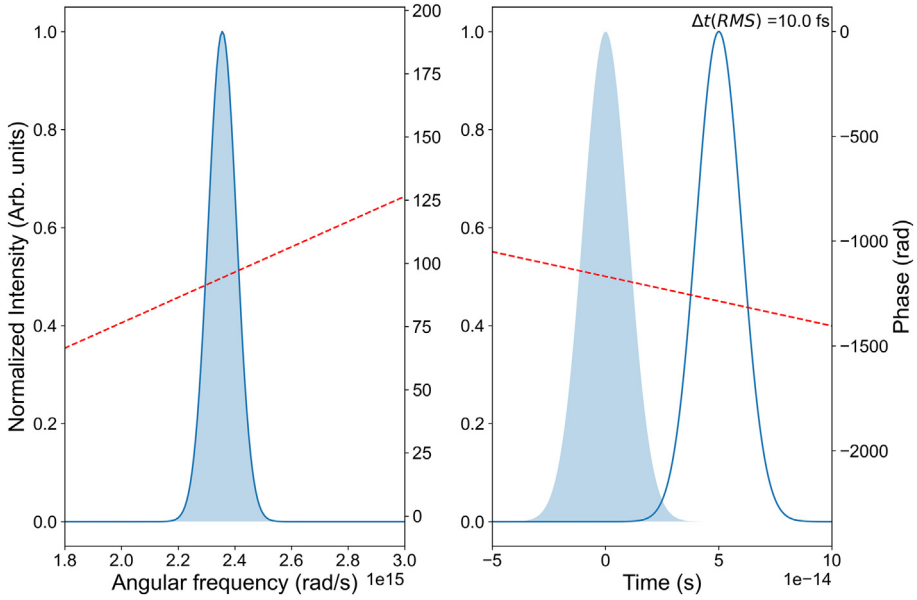

FIG. 4.7 – Effect of a linear phase on the spectrum (left) and temporal intensity (right) of an initial pulse at 800 nm with 23.4 fs FWHM duration and 40 nm FWHM spectral width. Light blue shaded areas do correspond to the zero spectral phase case. Red dashed line: spectral (left) and temporal (right) phases.

The above figure shows the initial pulse (shaded area), and the pulse resulting from the addition of the linear spectral phase. The pulse is centered around $t = 50$ fs, which corresponds to the slope of the linear spectral phase, and its duration is unchanged. This illustrates the definition of the group delay:

$$\tau_g(\omega) = \frac{\partial \phi(\omega)}{\partial \omega} \tag{4.8}$$

Conclusion: A linear spectral phase induces a time shift of the pulse. This is an illustration of the Fourier Transform shift theorem, used above to compute the Wigner transforms.

4.2.2 Quadratic Spectral Phase

We now define a second-order spectral phase as:

$$\phi_{\text{quad}} = \phi_2(\omega - \omega_0)^2$$

where $\phi_2 = 300$ fs^2 (see figure 4.8).

```
#parameter phi2
phi2=300*(1e-15)**2.0 #fs^2
#quadratic spectral phase
phi_w_quad = phi2*(w-w0)**2
#Electric field in the angular frequency domain
E_w_quad=sqrt(calc_I_w(w,w0,fwhm_w))*exp(0.5*phi_w_quad*1j)
phi_w_quad=unwrap(angle(E_w_quad))
#Electric field in the time domain
E_t_quad=FT(E_w_quad,Nbt)
phi_t_quad=unwrap(angle(E_t_quad))
```

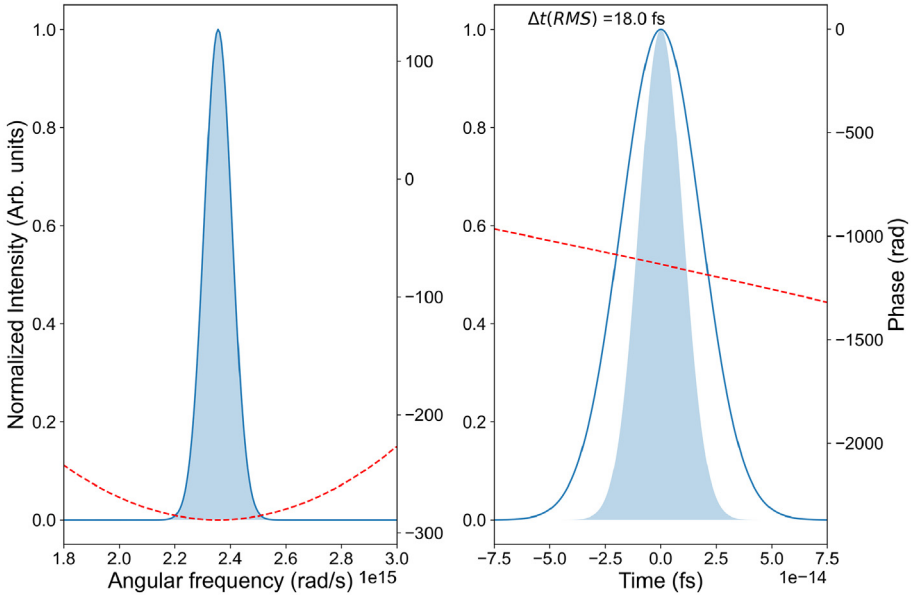

FIG. 4.8 – Effect of a quadratic phase on the spectrum (left) and temporal intensity (right) of an initial pulse at 800 nm with 23.4 fs FWHM duration and 40 nm FWHM spectral width. Light blue shaded areas do correspond to the zero spectral phase case. Red dashed line: spectral (left) and temporal (right) phases.

The pulse profile remains Gaussian, but the duration increases to 42.5 fs. Note that the linear component of the temporal phase has not been removed here, hiding the quadratic temporal phase.

Conclusion: A quadratic spectral phase induces a temporal broadening of the pulse.

Gabor transform

More information on the influence of the quadratic phase can be obtained by plotting a spectrogram (Gabor distribution) of the pulse (see figure 4.9).

```
alpha=10.0e-15
G_quad=gabor(t,E_t_quad,Nbw,alpha)
plot_gabor(G_quad,t,w,tmin,tmax,wmin,wmax,'Gabor transform for␣
↪quadratic spectral phase with $\\alpha =${:.1e}'.format(alpha))
```

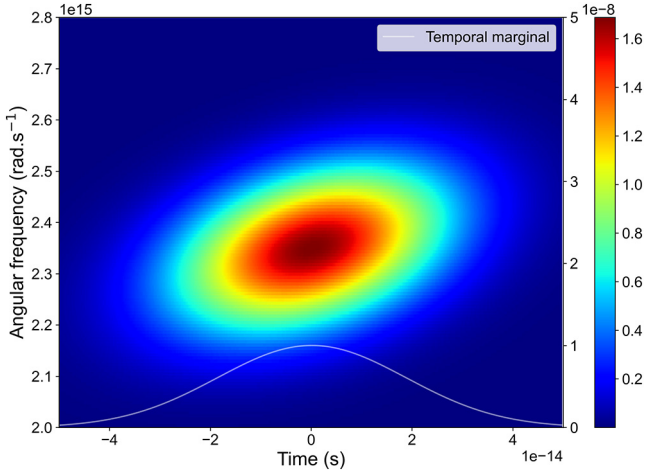

FIG. 4.9 – Gabor distribution ($\alpha = 10$ fs) of a pulse at 800 nm with 23.4 fs FWHM duration and 40 nm FWHM spectral width with a quadratic spectral phase.

The distribution shows a clear tilt. The angular frequency of the pulse increases with time. Such a pulse is called "positively chirped", by analogy with the song of a bird. This chirp can also be quantified by calculating the group delay $\tau_g(\omega) = \frac{\partial\phi(\omega)}{\partial\omega} = 2\phi_2(\omega - \omega_0)$, which increases linearly with frequency.

Wigner distribution

```
W_quad=wigner(E_t_quad,t,w),plot_wigner(W_quad,t,w,tmin,tmax,
wmin,
wmax,'Wigner distribution for a quadratic spectral phase')
```

The Wigner distribution provides a direct visualization, as presented in figure 4.10, of the linear chirp of the pulse, *i.e.* the linear increase of the group delay with time. Compared with the Gabor analysis, the Wigner distribution is spectrally narrower, offering a better resolution.

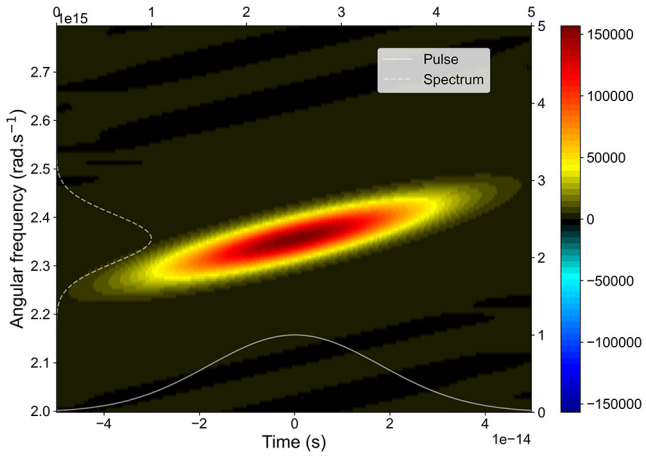

FIG. 4.10 – Wigner distribution of a pulse at 800 nm with 23.4 fs FWHM duration and 40 nm FWHM spectral width with a quadratic spectral phase.

4.2.3 Cubic Spectral Phase

The cubic spectral phase (see figure 4.11) is defined as

$$\phi_{\text{cub}} = \phi_3(\omega - \omega_0)^3$$

with $\phi_3 = 2000$ fs^3.

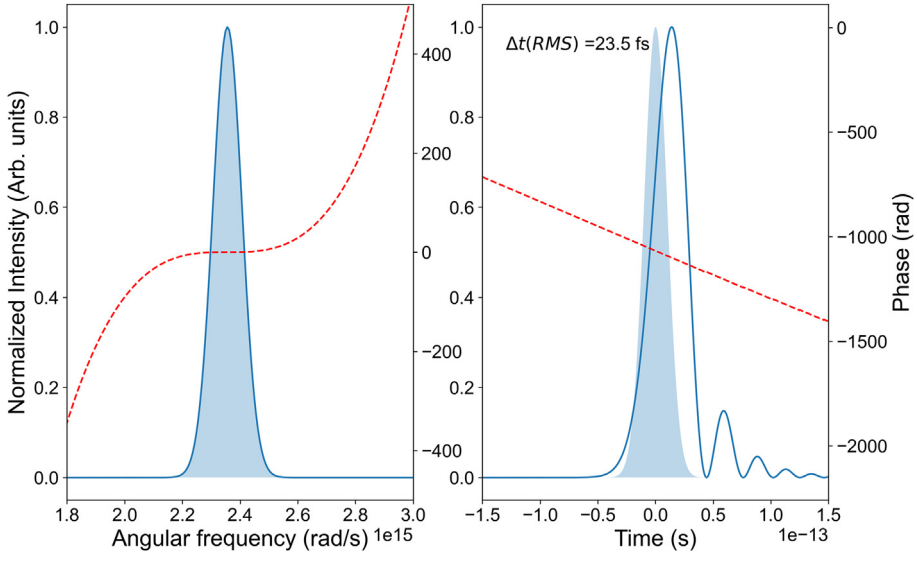

FIG. 4.11 – Effect of a cubic phase on the spectrum (left) and temporal intensity (right) of an initial pulse at 800 nm with 23.4 fs FWHM duration and 40 nm FWHM spectral width. Light blue shaded areas correspond to the zero spectral phase case. Red dashed line: spectral (left) and temporal (right) phases.

The cubic spectral phase introduces an asymmetry in the temporal profile of the pulse. The main pulse is elongated, with a 34.2 fs FWHM, and post pulses do appear. Changing the sign of ϕ_3 would reverse the pulse temporally.

Conclusion: A cubic spectral phase induces a non gaussian pulse, with pre or post pulses.

Gabor transform

The Gabor transform, see figure 4.12, is not particularly helpful in understanding the temporal shape of the pulse. It shows a main component associated with the main peak, followed by a series of wiggles corresponding to the postpulses.

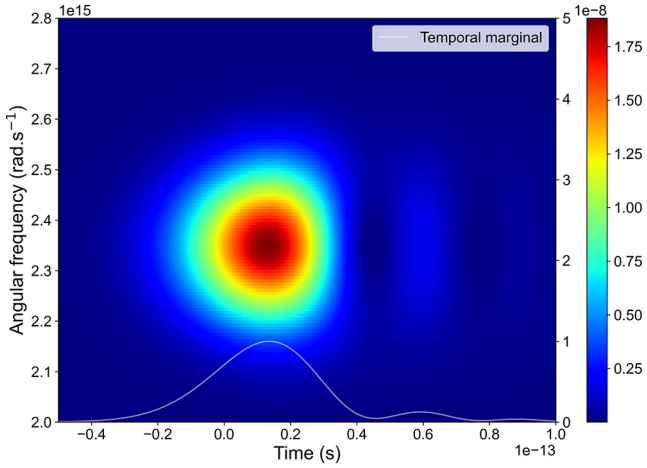

FIG. 4.12 – Gabor distribution ($\alpha = 10$ fs) of a pulse at 800 nm with 23.4 fs FWHM duration and 40 nm FWHM spectral width with a cubic spectral phase.

Wigner distribution

The component of the Wigner distribution (see figure 4.13) follows a bow shape. It reflects the quadratic shape of the group delay: $\tau_g(\omega) = \frac{\partial\phi(\omega)}{\partial\omega} = 3\phi_3(\omega - \omega_0)^2$. Interestingly, the Wigner distribution shows positive and negative lobes. These are caused by the beating between the lower and higher frequencies in the spectrum. In a similar manner, as two spectrally overlapping delayed pulses produce a spectral interference pattern, two spectrally shifted components overlapping temporally do produce a temporal interference pattern (beating). The Wigner distribution thus reveals the interference which causes the post-pulses in the temporal profile.

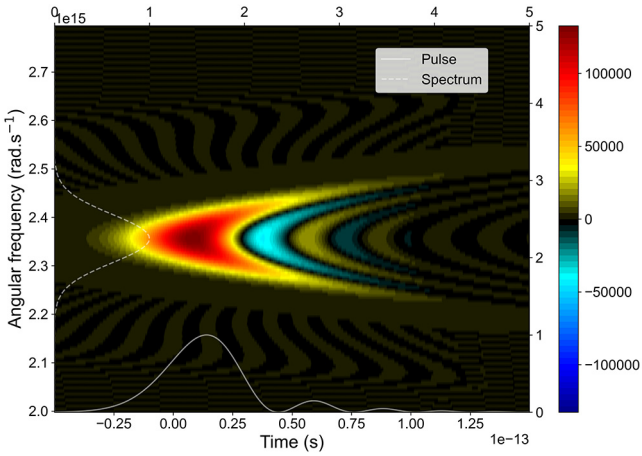

FIG. 4.13 – Wigner distribution of a pulse at 800 nm with 23.4 fs FWHM duration and 40 nm FWHM spectral width with a a cubic phase.

Let us practice !

Send the pulse with cubic phase into a Mach–Zehnder interferometer, which creates two replicas, delayed by a 150 fs delay.

(1) Define the resulting electric field and calculate its Gabor and Wigner distributions. See how they depend on the delay.
(2) What is the main difference between these two representations?
(3) What happens to the spectrum?

4.3 Linear Dispersion in Different Media

We have investigated numerically the influence of various spectral phases on a femtosecond pulse, and have seen that time–frequency representations could provide interesting insight into the influence of these phases. We now turn to a more realistic situation in which a femtosecond pulse propagates in the laboratory. The propagation of electromagnetic fields is determined by Maxwell's equations and is a four dimensional problem (space and time). Here, we will assume that the beam has a homogeneous spatial profile, and that the only influence of propagation is linear dispersion. We will treat the non-linear dispersion case in the next section.

4.3.1 Refractive Index

When a femtosecond pulse propagates in a medium, the different frequency components do not see the same index of refraction. In air, this dependence can be represented by dispersion formula:

$$n(\lambda) = 1 + \frac{B_1}{C_1 - \lambda^{-2}} + \frac{B_2}{C_2 - \lambda^{-2}}$$

where λ is given in m and:

- $B_1 = 0.05792105$
- $C_1 = 238.0185$
- $B_2 = 0.00167917$
- $C_2 = 57.362$

For other media, the refractive index can be represented by Sellmeier's formula:

$$n^2 = 1 + \frac{B_1\lambda^2}{\lambda^2 - C_1} + \frac{B_2\lambda^2}{\lambda^2 - C_2} + \frac{B_3\lambda^2}{\lambda^2 - C_3} \tag{4.9}$$

where the B_i and C_i coefficients can be obtained from various sources, *e.g.* the website refractiveindex.info.

The following function returns the refractive index for common media (air, SiO_2, BK7)

```
def refractive_index(Lambda,medium):
```

4.3.2 Propagation

In order to take into account the influence of the dependence of the refractive index with the wavelength, we calculate the accumulated spectral phase as:

$$\begin{aligned}\phi(\omega) &= k(\omega)z \\ &= \frac{\omega n}{c}z\end{aligned}$$

where z is the coordinate along the direction of propagation (the input face of the medium corresponds to $z = 0$), ω the array of angular frequencies and n the refractive index (which depends on λ and as a consequence on ω).

We can then define the following function `propagation` which returns the electric field (in time) as a function of z, and `FWHM`, an array which contains the pulse duration during propagation.

```
def propagation(t,w,E_w,length,Nbz,tmin,tmax,medium='air',
plot1D=False, plot2D=True):
```

4.3.3 Definition of Input Pulse

Throughout the following, we will be using three different pulses to illustrate the influence of different media:

- a 300 fs pulse at 1030 nm from a Yb amplifier;
- a 25 fs pulse at 800 nm from a Ti:Sa amplifier;
- a 5 fs pulse at 700 nm from a postcompression scheme.

The spectra and temporal profiles are defined through the following commands, here for the 25 fs pulse (see figure 4.14) – the other cases are defined in the Jupyter Notebook.

```
lambda0_25fs=800e-9 #nm,w0_25fs=2*pi*3e8/lambda0_25fs
duration_25fs=25e-15
I_t_25fs=calc_I_t(t,duration_25fs)
# Field at z=0
E_t_25fs_in=sqrt(I_t_25fs)*exp(-1j*w0_25fs*t)
E_w_25fs_in=IFT(E_t_25fs_in,Nbw)
```

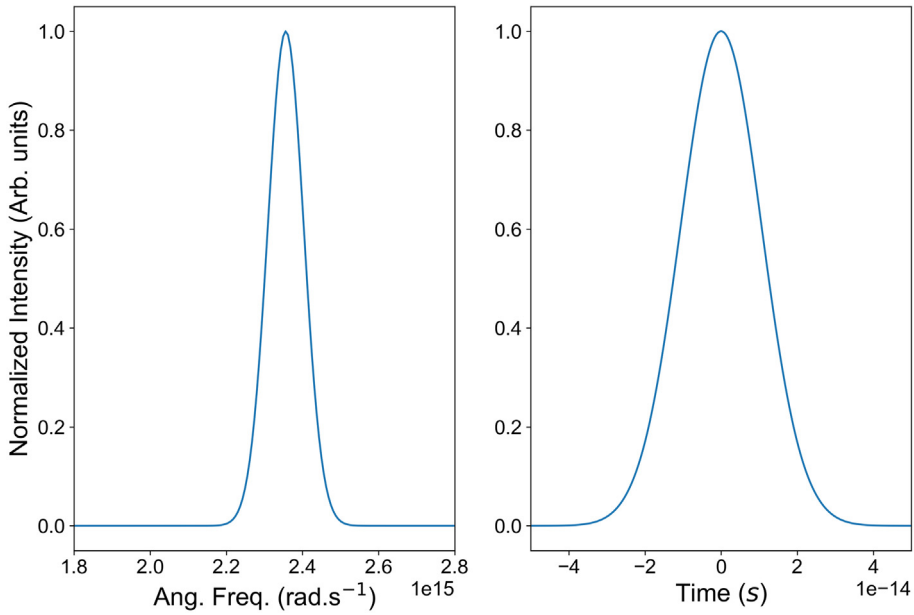

FIG. 4.14 – Spectrum (left) and temporal intensity (right) of an initial pulse at 800 nm with 25 fs FWHM duration.

4.3.4 Propagation in Air

We now propagate the different pulses in various thicknesses of air. In each case, we calculate the Gabor transform at the exit point of the medium, the Wigner distribution at the exit point, as well as the evolution of the pulse duration during the propagation in the medium.

Propagation in 100 m of air of the 300 fs pulse

```
# Length of the medium
L=100
medium='air'
NbPoints=10

FWHM,Z,E_t_z_air_300fs=propagation(t,w,E_w_300fs_in,L,NbPoints,
tmin,tmax,medium, plot1D=False,plot2D=True)

# alpha parameter for Gabor transform
alpha=50e-15
# E_t_z_air[:,-1] corresponds to the last point i.e. the output␣
↪of the medium
# Gabor transform
G=gabor(t,E_t_z_air_300fs[:,-1],Nbw,alpha)
plot_gabor(G,t,w,tmin,tmax,wmin,wmax,'Gabor at exit point')
# Wigner distribution
WIG=wigner(E_t_z_air_300fs[:,-1],t,w)
plot_wigner(WIG,t,w,tmin,tmax,wmin,wmax,'Wigner at exit point')

#Plot of the duration along z
figure()
plot(Z,FWHM*1e15)
title('Duration for {:.0f} fs - Propagation in {:.0f} m of {}'.
↪format(duration_300fs*1e15,L,medium))
xlabel('Distance $z$ (m)')
ylabel('Duration (fs)')
ylim((290,310))
```

We start by plotting in figure 4.15 the evolution of the temporal profile of the pulse as it propagates through the medium. No change is visible. The second plot (right panel of figure 4.15) confirms that the FWHM duration of the pulse remains constant throughout propagation in 100 m of air.

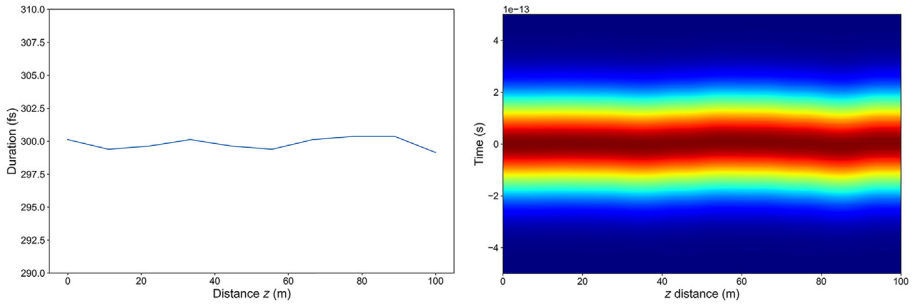

FIG. 4.15 – Left panel: Evolution of the pulse duration for an initial pulse at 1030 nm and 300 fs FWHM duration propagating through 100 m of air. Right panel: Evolution of the temporal intensity profile.

Next, we plot the Gabor and Wigner distributions (see figure 4.16) of the pulse at the exit of the medium. They show no sign of dispersion.

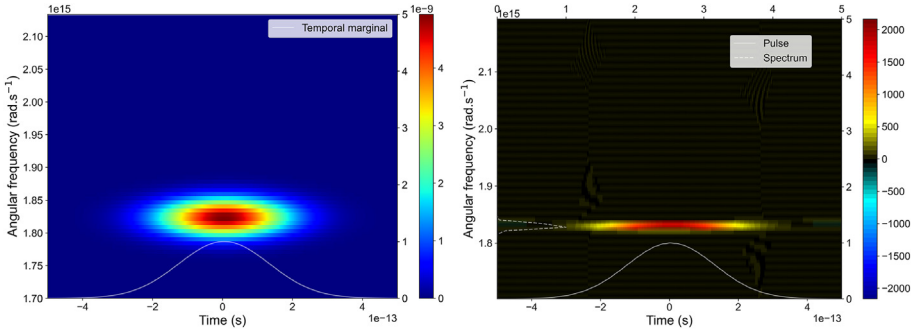

FIG. 4.16 – Left panel: Gabor transform for an initial pulse at 1030 nm and 300 fs FWHM duration after propagation through 100 m of air. Right panel: Wigner distribution.

Conclusion: Linear dispersion from air is never an issue for 300 fs pulses at 1030 nm.

Propagation in 100 m of air of the 25 fs pulse

The evolution of the temporal profile of the pulse as it propagates in air shows apparent oscillations (see right panel of figure 4.17). These are visual artifacts of the 2D interpolation in the plot. To check this, you can redo the calculation by increasing the number of points `NbPoints`, and see how this modifies the appearance of the results.

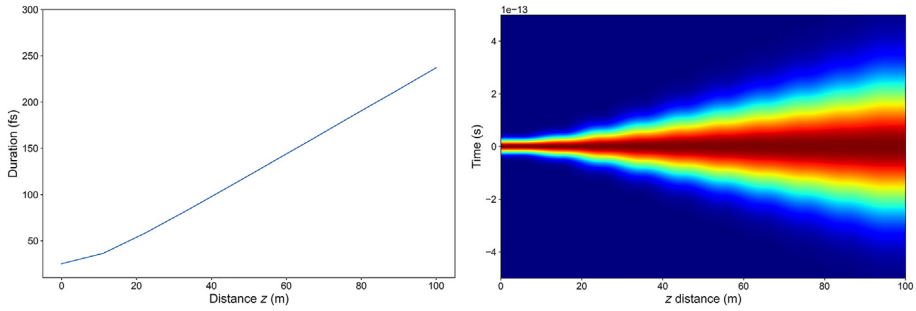

FIG. 4.17 – Left panel: Evolution of the pulse duration for an initial pulse at 800 nm and 25 fs FWHM duration propagating through 100 m of air. Right panel: Evolution of the temporal intensity profile.

The temporal profile of the pulse clearly broadens during propagation. This can be quantified by monitoring the evolution of the pulse duration as a function of the propagation distance as shown in the left panel of figure 4.17. After 100 m of propagation, the pulse duration reaches almost 250 fs, *i.e.* the pulse is temporally stretched by one order of magnitude.

The Gabor and Wigner distributions enable visualizing the influence of propagation in the time–frequency domain (see figure 4.18).

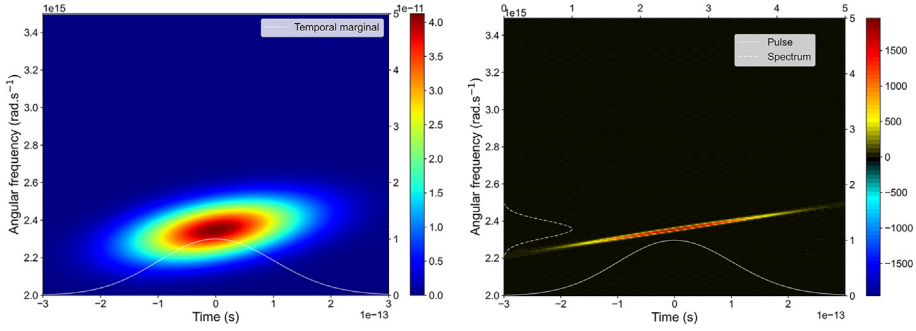

FIG. 4.18 – Left panel: Gabor transform for an initial pulse at 800 nm and 25 fs FWHM duration after propagation through 100 m of air. Right panel: Wigner distribution.

Conclusion: After a few meters of propagation, the pulse starts to be stretched by the linear dispersion of air. The time–frequency distributions of the pulse after 100 m of air show a tilt, indicating a linear chirp. The spectral phase introduced by air is thus mostly quadratic. This means that such dispersion can be pre-compensated by introducing a negative chirp at the laser output with a grating compressor.

Propagation in 1 m of air of the 5 fs pulse

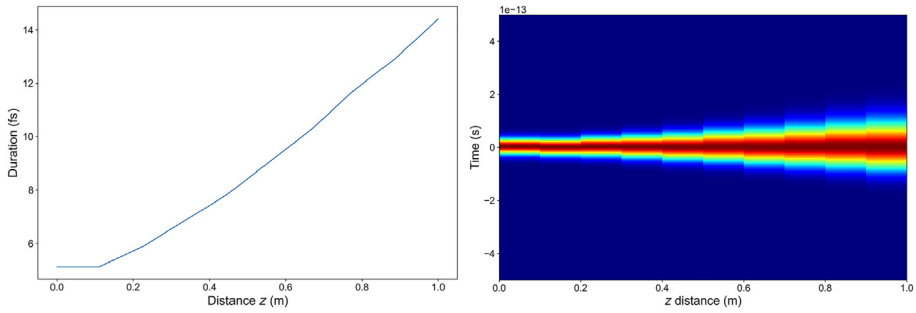

FIG. 4.19 – Left panel: Evolution of the pulse duration for an initial postcompressed pulse at 700 nm and 5 fs FWHM duration propagating through 1 m of air. Right panel: Evolution of the temporal intensity profile.

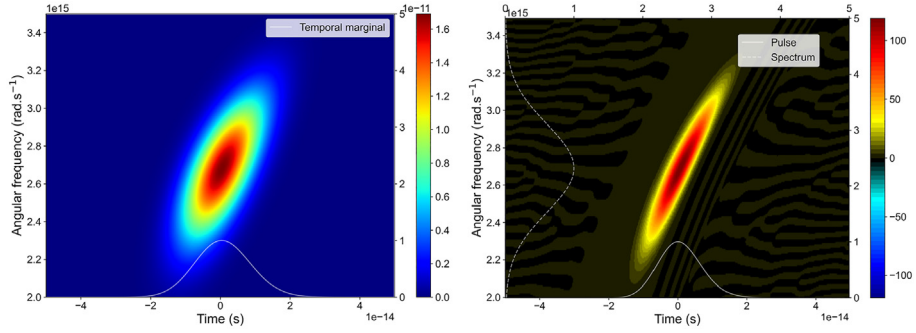

FIG. 4.20 – Left panel: Gabor transform for an initial postcompressed pulse at 700 nm and 5 fs FWHM duration after propagation through 1 m of air. Right panel: Wigner distribution.

Conclusion: The effect of air dispersion on a 5 fs pulse is critical, due to the very broad bandwidth of the pulse (see figure 4.19). The pulse duration doubles after 50 cm of propagation. The Wigner distribution obtained after 1 m of propagation shows a tilt (see right panel of figure 4.20), revealing the mostly linear chirp of the pulse, but also a curvature, indicating higher orders in the spectral phase. Gabor transform in presented in the left panel of figure 4.20.

4.3.5 Propagation in SiO_2

Let us practice !

Use the previous examples to simulate the propagation in SiO_2 of:

(1) a 300 fs pulse in 100 mm of SiO_2;
(2) a 25 fs pulse in 5 mm of SiO_2;
(3) a 5 fs postcompressed pulse in 0.5 mm of SiO_2.

4.3.6 Temporal Broadening vs. Duration of the Input Pulse

The calculations presented above show that the effect of linear dispersion on the pulse duration can be critical or insignificant, depending on the conditions. It is thus important to evaluate the potential impact of dispersion in an experiment. A common representation consists in calculating the output pulse duration as a function of the input (Fourier-limited) duration, for a given material thickness.

4.3.6.1 Propagation in 20 mm of SiO_2

```
duration=linspace(10,200,40)
medium='SiO2'
fwhm=zeros(len(duration))
L=20e-3
for i,duree in enumerate(duration):
    duree=duree*1e-15
    #duration in fs
    lambda0=800e-9 #nm
    w0=2*pi*3e8/lambda0
    I_t=calc_I_t(t,duree)
    # Field at z=0
    E_t_in=sqrt(I_t)*exp(1j*w0*t)
    E_w_in=FT(E_t_in,Nbw)
  ␣
↪FWHM,Z,E_t_z=propagation(t,w,E_w_in,L,NbPoints,tmin,tmax,
medium,
    plot1D=False,plot2D=False)
    fwhm[i]=FWHM[-1]
```

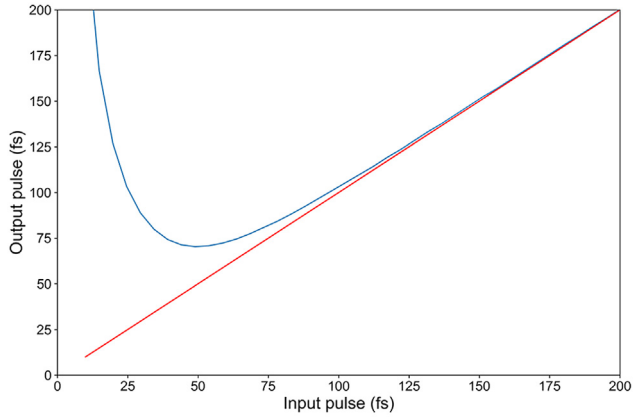

FIG. 4.21 – Temporal broadening of a 800 nm pulse after propagation in 20 mm of SiO_2 as a function of the initial pulse duration.

The red line is the zero dispersion case. It is clear from figure 4.21 that 20 mm of SiO_2 will have a significant impact on the duration of sub-100 fs pulses. The results can be compared to other materials:

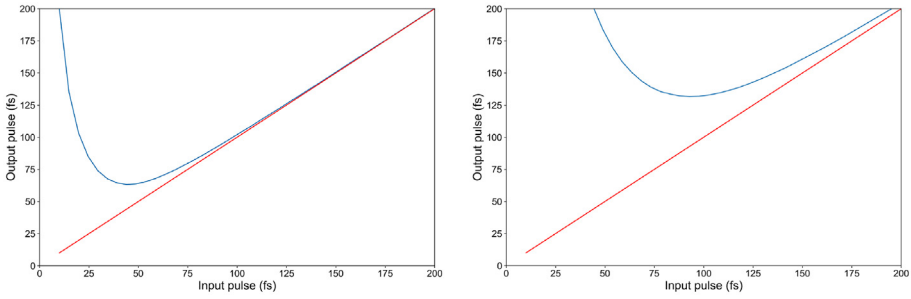

FIG. 4.22 – Left panel: Temporal broadening of a 800 nm pulse after propagation in 20 mm of BK7 as a function of the initial pulse duration. Right panel: same in SF10.

The results presented in figure 4.22 show that SF10 has a huge impact on pulse duration, which is not surprising as this material is known to be very dispersive. Dispersion in BK7 is slighltly worse than in SiO_2.

4.3.7 Compensation of Dispersion

4.3.7.1 Principle

We have seen that the main influence of linear dispersion at 800 nm and 1030 nm was to induce a linear chirp of the pulses, which appears as a tilt in the Wigner distribution. In principle, such a linear chirp can be compensated by introducing a negative linear chirp, *i.e.* a quadratic spectral phase, before propagation[5–7].

To simulate this scenario, we introduce an increasing quantity of negative quadratic phase, determined by a parameter Φ_2, and propagate the resulting pulse through a given thickness of material. We calculate the duration of the output pulse as a function of Φ_2 and plot the Wigner distributions for a few selected Φ_2.

4.3.7.2 Propagation of a Precompensated 25 fs Pulse in 10 mm of SiO_2

When no precompensation is used, the 25 fs pulse is stretched to 47 fs when propagating in 10 mm of SiO_2 (see left panel of figure 4.23). The Wigner distribution shows a positive slope, indicating a linear positive chirp (see right panel of figure 4.23). As the precompensation factor Φ_2 increases, the output pulse duration decreases. The minimum duration is reached when $\Phi_2 = -170$ fs^2. The pulse duration is slightly above 25 fs. The Wigner distribution of the optimal pulse is not perfectly symmetric and horizontal (see left panel of figure 4.24). This is due to the higher order phase distortions induced by SiO_2, which are not compensated by the quadratic dispersion we introduce. If Φ_2 is further increased, the chirp is overcompensated, such that the output pulse duration increases and the Wigner distribution shows a negative slope (see right panel of figure 4.24).

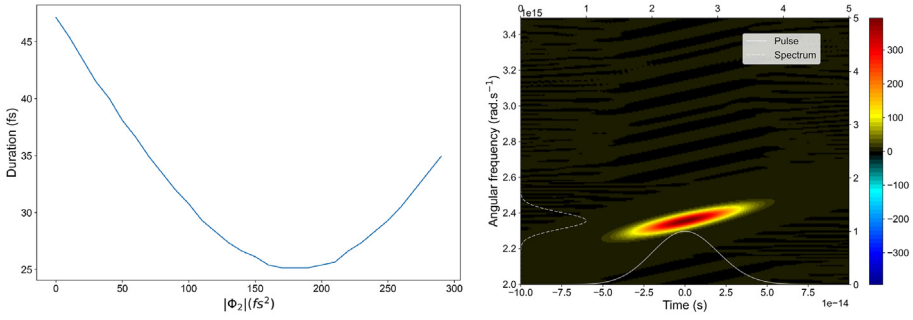

FIG. 4.23 – Left panel: Duration of a precompensated 25 fs pulse after propagation in 10 mm of SiO_2 as a function of the precompensation factor Φ_2. Right panel: Wigner distribution of a 25 fs pulse with no precompensation after propagation in 10 mm of SiO_2.

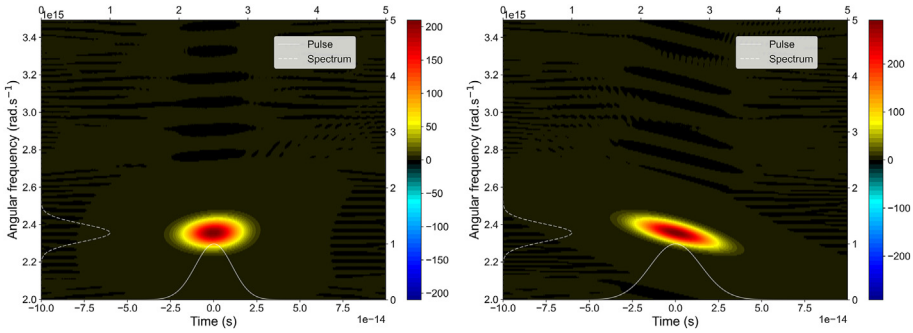

FIG. 4.24 – Left panel: Wigner distribution of a precompensated 25 fs pulse after propagation in 10 mm of SiO_2 with $\Phi_2 = -170$ fs^2. Right panel: Wigner distribution with $\Phi_2 = -290$ fs^2.

4.3.7.3 Propagation of a Precompensated 5 fs Postcompressed Pulse in 5 mm of SiO_2

The influence of dispersion on a 5 fs Fourier-limited pulse is much more drastic than on a 25 fs Fourier limited pulse, because of the broader bandwidth involved (see figure 4.25). The 5 fs pulse is stretched to 125 fs by propagation in 5 mm of SiO_2 (see left panel of figure 4.26). When a precompensation quadratic phase with $\Phi_2 = -110$ fs^2 is introduced (see right panel of figure 4.26), the output pulse duration decreases to 7.3 fs.

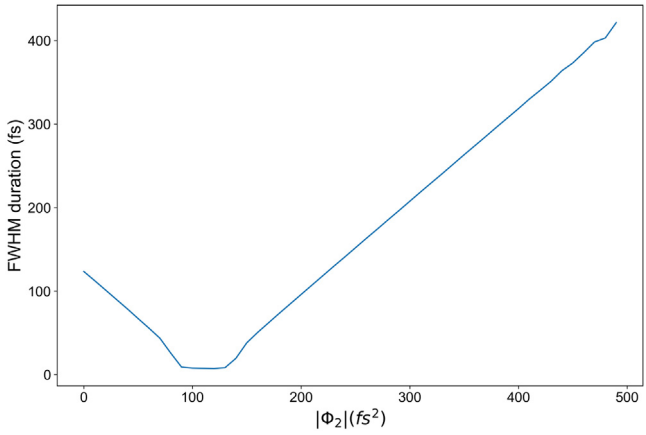

FIG. 4.25 – Duration of a precompensated 5 fs pulse after propagation in 5 mm of SiO_2 as a function of the precompensation factor Φ_2.

To visualize the effect of precompensation, we compare the Wigner distribution without or with optimal precompensation.

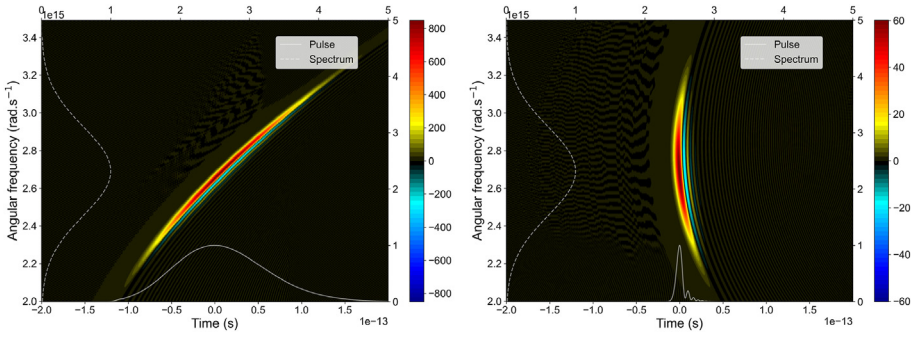

FIG. 4.26 – Left panel: Wigner distribution of a 5 fs pulse with no precompensation after propagation in 5 mm of SiO_2. Right panel: Wigner distribution with $\Phi_2 = -110$ fs^2.

Interestingly, the Wigner distribution of the optimal output pulse shows a clear bow shape, characteristic of a third-order spectral phase. The temporal profile of the pulse, obtained by projecting the Wigner distribution along the time axis (temporal marginal), consists of a main pulse followed by a series of post-pulses. This situation illustrates the importance of third-order dispersion of fused silica when broadband pulses are used. Better dispersion management can be performed using chirped mirrors specifically designed to compensate for the second- and third-order phases of SiO_2.

4.4 Self-Phase Modulation (SPM)

We have seen in the previous section that linear dispersion could significantly affect the duration of femtosecond pulses. In this section, we go one step further by investigating the effect of nonlinear dispersion. Nonlinear dispersion results from the dependence of the refractive index n on laser intensity I (Kerr effect), which can be expressed as:

$$n(I) = n_0 + n_2 \times I \tag{4.10}$$

where n_2 is the second-order refractive coefficient. The variation of n_2 with the laser wavelength over the bandwidth of the femtosecond pulses induces a dispersion of the pulse, changing its temporal profile.

The dispersion being induced by the own intensity of the pulse, the process is called **Self Phase Modulation** (SPM)[8]. SPM was already introduced and discussed in chapters 1 and 3. Since this effect depends on the intensity, the dispersion varies in space and in time. We will here focus on the effect of temporal dispersion, assuming a flat spatial profile of the beam.

4.4.1 Influence of Self-Phase Modulation on a Gaussian Pulse

To investigate the influence of self-phase modulation, we start from an initial electric field $E_{\text{in}}(t)$, and add a temporal phase proportional to its intensity:

$$E_{\text{out}}(t) = E_{\text{in}}(t) \times e^{i\sigma|E_{\text{in}}(t)|^2} \tag{4.11}$$

where σ is the magnitude of the SPM, determined by the nonlinear refractive coefficient n_2 of the medium as well as by the medium thickness L: $\sigma = \frac{2\pi}{\lambda_0} n_2 \times L$. The following function calculates the output electric field for N values of σ increasing from 0 to $(N-1)\times$ `delta_sigma`:

```
def spm(t,w,E_t_in,delta_sigma,NbSteps,tmin,tmax,plot1D=False):
    E_t_out=zeros((len(t),NbSteps),dtype=complex)
    E_w_out=zeros((len(w),NbSteps),dtype=complex)
    phi_t_out=zeros((len(t),NbSteps))
    SIGMA=zeros(NbSteps)
    Nbw=len(w)
    #Loop over increasing values of sigma
    for step in range(NbSteps):
        sigma=float(step*delta_sigma)
        SIGMA[step]=sigma
        #Calculate temporal profile and SPM
        I_t_in=abs(E_t_in)**2.0
        E_w_in=IFT(E_t_in,Nbw)
        phi_t_out[:,step]=sigma*I_t_in
        # Field after adding the phase
        E_t_out[:,step]=E_t_in*exp(1j*phi_t_out[:,step])
        E_w_out[:,step]=IFT(E_t_out[:,step],Nbw)
    return SIGMA,E_t_out
```

The SPM, defined as σI in our case, does not modify the intensity profile of the pulse: $|E_{\text{in}}(t)|^2 = |E_{\text{out}}(t)|^2$. However, because the temporal phase of the pulse is modified, its spectrum, obtained by Fourier transforming the complex electric field, is changed. As an example, we start from a 25 fs gaussian pulse at 800 nm, and increase the SPM from 0 to 9.8 rad. To monitor the influence of SPM on the pulse, we plot the Wigner distribution for three selected values of σI, where I is the peak intensity at the center of the beam.

```
#Setting the limit for plotting
tmin=-100e-15
tmax=100e-15
wmin=1.15e15
wmax=3.7e15
# Parameters for the study
delta_sigma=0.20
```

```
NbSteps=50
SIGMA_25fs,E_t_25fs_out=spm(t,w,E_t_25fs_FT,delta_sigma,NbSteps,
tmin,tmax)
W0=wigner(E_t_25fs_out[:,0],t,w)
plot_wigner(W0,t,w,tmin,tmax,wmin,wmax,'Wigner for $\\sigma I$ =␣
 ↪{:.1f}'.format(SIGMA_25fs[0]))
ind_min=int(NbSteps/2)
Wopt=wigner(E_t_25fs_out[:,ind_min],t,w)
plot_wigner(Wopt,t,w,tmin,tmax,wmin,wmax,'Wigner for $\\sigma I$␣
 ↪={:.1f}'.format(SIGMA_25fs[ind_min]))
Wfin=wigner(E_t_25fs_out[:,-1],t,w)
plot_wigner(Wfin,t,w,tmin,tmax,wmin,wmax,'Wigner for $\\sigma I$␣
 ↪={:.1f}'.format(SIGMA_25fs[-1]))
```

This provides the three following plots.

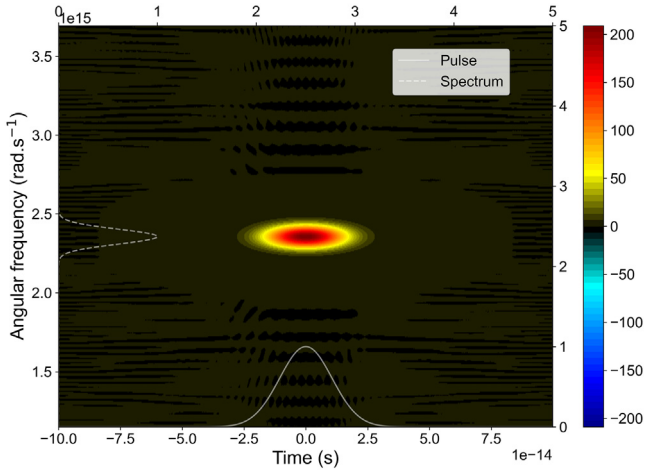

FIG. 4.27 – Wigner distribution of a 25 fs pulse at 800 nm with $\sigma I = 0$ rad.

Figure 4.27 shows the Wigner distribution of a Fourier-limited Gaussian pulse, that we have seen before. When a SPM of $\sigma I = 5$ rad is applied (see figure 4.28), the temporal profile of the output pulse remains a 25 fs Gaussian (white line at the bottom, temporal marginal of the Wigner distribution) but the spectrum broadens and shows two spectrally shifted components, with a minimum at the central frequency.

Increasing the SPM to $\sigma I = 9.8$ rad, as presented in figure 4.29 further broadens the spectrum, which extends from 1.5 to 3.7×10^{15} rad/s. The spectrum shows 3

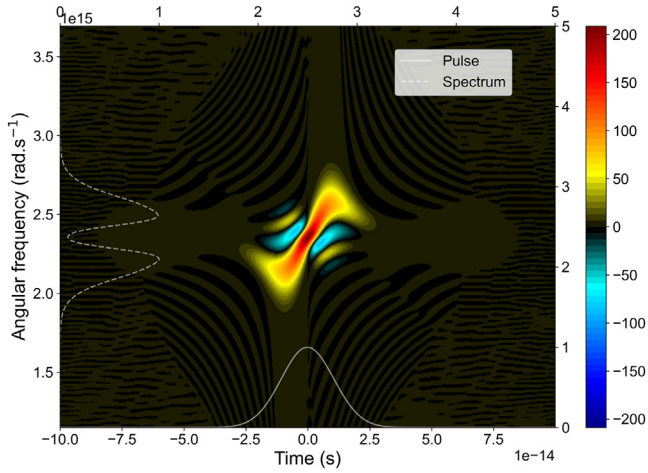

FIG. 4.28 – Wigner distribution of a 25 fs pulse at 800 nm with $\sigma I = 5.0$ rad.

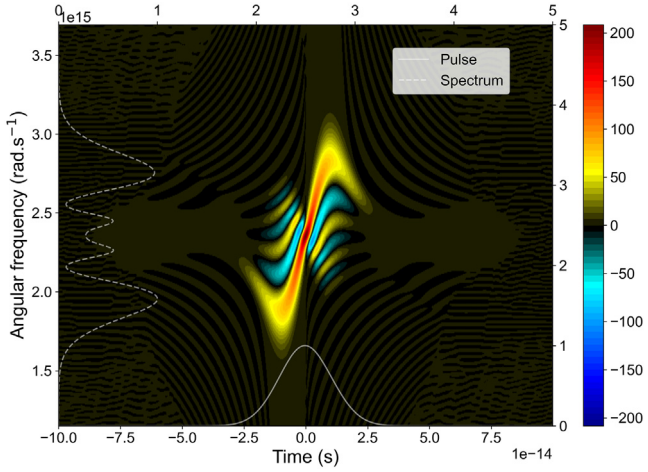

FIG. 4.29 – Wigner distribution of a 25 fs pulse at 800 nm with $\sigma I = 9.8$ rad.

dark fringes. The origin of these fringes can be understood by looking at the peak component of the Wigner distribution, which follows the instantaneous frequency of the pulse. Around the maximum of the pulse, the instantaneous frequency increases quasi-linearly with time. This reflects the fact that the Gaussian temporal phase of the pulse is quasi-quadratic in this range (quadratic phase, linear chirp, linear evolution of the instantaneous frequency). On the temporal wings of the pulse, the quadratic approximation of the Gaussian function fails. Indeed, the second

derivative of the Gaussian changes sign, causing a slope inversion of the instantaneous frequency. As a consequence, each frequency is in fact produced at two instants during the pulse. This leads to a spectral interference, and to the appearance of fringes in the spectrum. As a rule of thumb, the number of dark fringes in the spectrum can be determined by the integer part of $\sigma I/(\pi)$[9].

Let us practice !

Change the value of `delta_sigma` to study the influence of the Gaussian temporal phase on the pulse.

4.4.2 When Does Self-Phase Modulation Become a Problem?

Self-phase modulation depends on the laser intensity, and is thus a time- and spatial-varying quantity. The time-dependence of SPM induces distortions of the spectrum. Since the laser intensity varies through the beam, SPM induces spectral inhomogeneities in the beam. The linear dispersion affects differently the various parts of the beam, such that the temporal profile becomes inhomogeneous. The spatial variation of the phase can also lead to focusing of the beam ("self-focusing"). It is thus essential to determine how much SPM can be a problem in an experiment. This is usually done by evaluating the B integral, defined as:

$$B = \frac{2\pi}{\lambda_0} \int n_2 I(z)\, dz \tag{4.12}$$

where the integral is calculated along the beam propagation. In our particular case, with no absorption and where spatial distribution is not taken into account (for example for a collimated beam), B is equal to σI.

As soon as the B integral reaches a few radians, one can expect inhomogeneities to affect the beam. Let us consider a few typical cases:

(1) A 300 fs pulse from a Yb doped fiber amplifier, with a 500 μJ energy in a beam with a Gaussian spatial profile with a waist of 2 mm reaches $B = 5$ rad after propagating in 7 m of fused silica, which is a rather unlikely situation. Self-phase modulation is generally not an issue with such a beam.
(2) A Ti:Sa beam, with 10 mJ 25 fs pulses and a waist of 20 mm, reaches $B = 5$ rad in 10 mm of SiO_2. This is much more likely to happen.
(3) As a last example, let us consider 5 fs pulse carrying 3 mJ in a 10 mm waist beam. A B integral of 5 rad is reached after 1.7 mm of SiO_2.

Care must thus be taken when propagating high intensity beams, for instance by increasing the beam diameter, shortening the optical path and avoiding transmission through optics, and/or stretching the pulses to propagate them and compressing them as late as possible.

4.4.3 Compensation of Self-Phase Modulation by a Quadratic Phase

The SPM induces a spectral broadening of the pulses, but does not affect the temporal intensity. The spectrum obtained after SPM being broader, it can support shorter pulses (shorter Fourier limit). Shortening the pulses requires compensating the phase introduced by the SPM process. This phase has a strong quadratic component, inducing a linear group delay dispersion. It should thus be possible to compensate this by adding a quadratic spectral phase.

The following functions calculates the pulse obtained by adding a spectral phase $\Phi_2(\omega - \omega_0)^2$, with Φ_2 varying from 0 to $(N-1)\delta\Phi_2$ in N steps:

```
def␣
 ↪SPM_compensation(t,w,w0,E_w_spm,E_t_ft,delta_phi2,NbSteps,
 tmin,tmax,␣
 ↪plot1D=False):
```

We start from the self-phase modulated 25 fs pulse depicted in figure 4.30, using a $\sigma I = 15$ rad SPM.

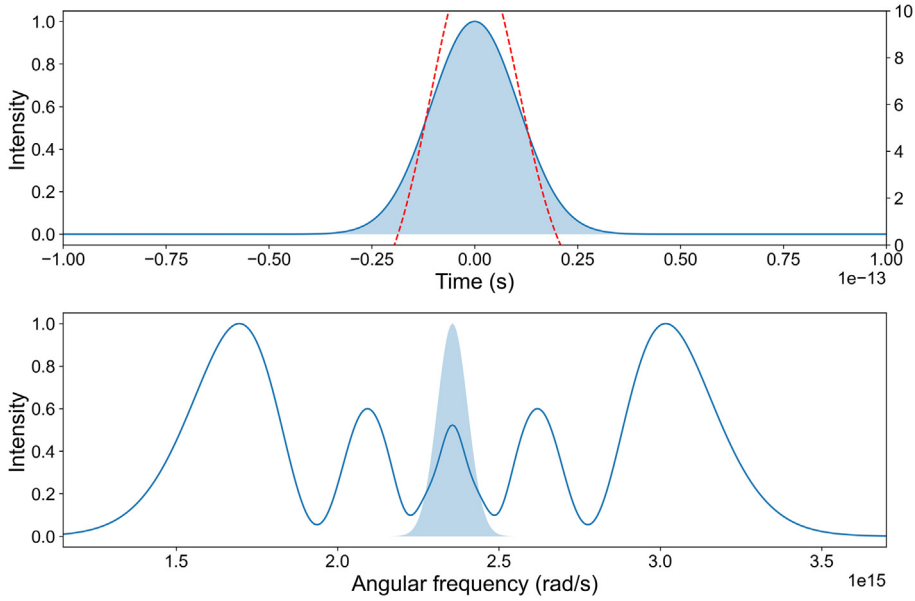

FIG. 4.30 – Upper panel: Temporal intensity profile (plain blue line) and phase (red) of the self-phase modulated 25 fs pulse with $\sigma I = 15$ rad. Lower panel: Spectrum of the self-phase modulated pulse. The light blue shaded area is the spectrum of the Fourier Transform limited pulse.

We calculate the temporal profile of the pulse as a function of the amount of additional quadratic spectral phase Φ_2 (see figure 4.31).

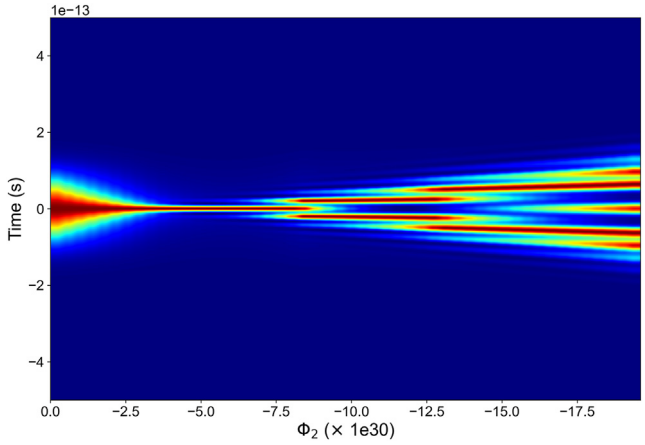

FIG. 4.31 – Temporal intensity profile of the self-phase modulated 25 fs pulse as a function of the amount of additional quadratic spectral phase Φ_2.

The pulse profile narrows down as Φ_2 varies from 0 to 5×10^{30} s^2. Further increasing the amount of quadratic phase leads to the splitting in multiple pulses. The RMS duration of the output pulse is calculated and shown in figure 4.32. Note that the sudden increase in the duration is due to the appearence of side lobes in the temporal profile of the emission.

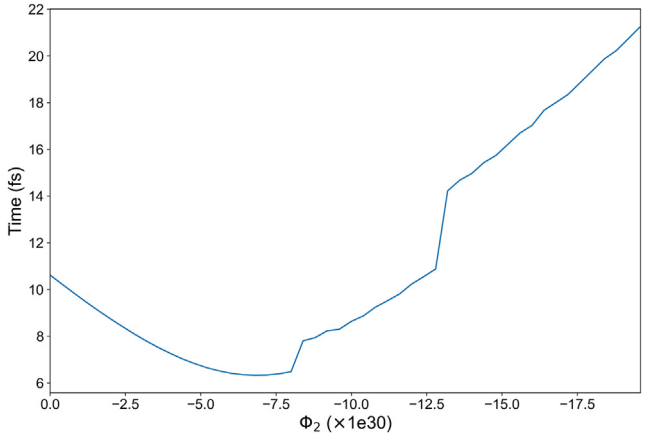

FIG. 4.32 – Duration of the self-phase modulated 25 fs pulse as a function of the amount of additional quadratic spectral phase Φ_2.

This study shows that spectral broadening by SPM followed by chirp compensation by a negative quadratic phase enables shortening the duration of a femtosecond pulse, here by a factor of 5. The effect of the quadratic phase can be further investigated by monitoring the evolution of Wigner distributions (see figures 4.33–4.35).

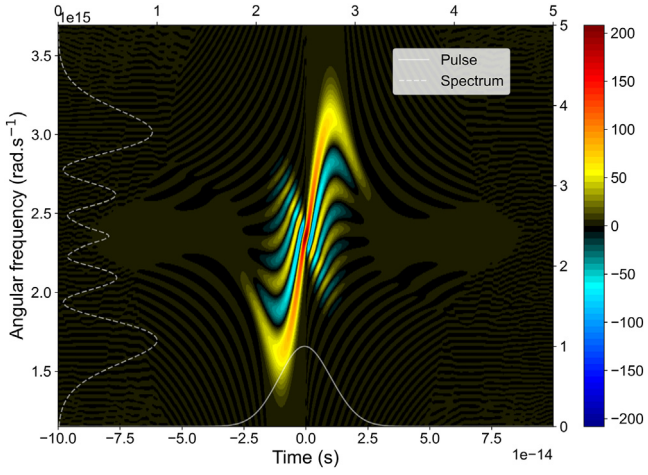

FIG. 4.33 – Wigner distribution of the self-phase modulated 25 fs pulse with no additional quadratic spectral phase Φ_2.

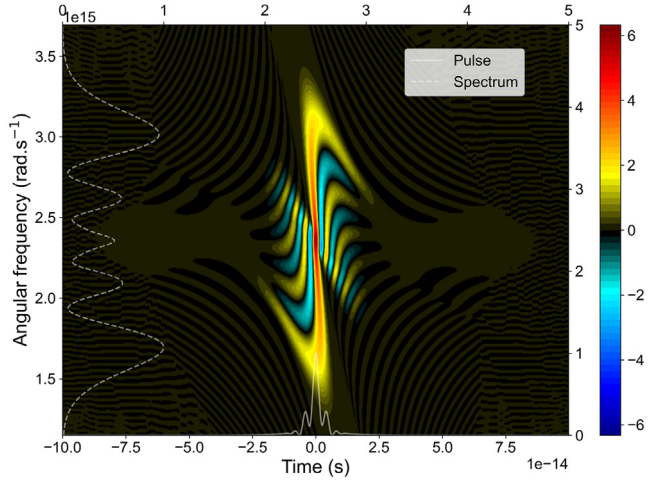

FIG. 4.34 – Wigner distribution of the self-phase modulated 25 fs pulse with an additional quadratic spectral phase $\Phi_2 = -6.8$ fs^2.

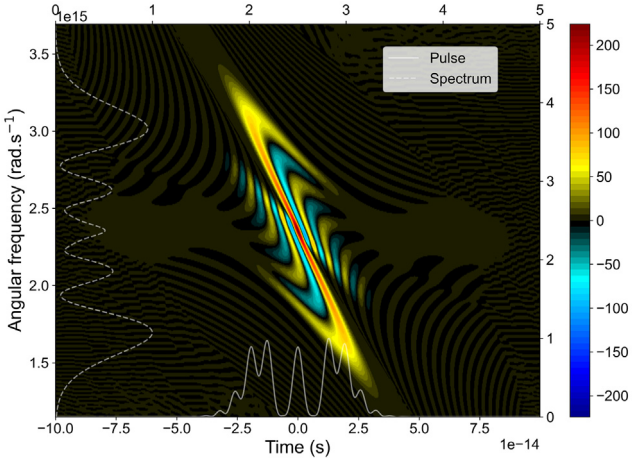

FIG. 4.35 – Wigner distribution of the self-phase modulated 25 fs pulse with an additional quadratic spectral phase $\Phi_2 = -20$ fs^2.

The quadratic dispersion acts as shear of the Wigner distribution[10]:

$$W_{\text{out}}(\omega, t) = W_{\text{in}}(\omega, t - \Phi_2\omega) \tag{4.13}$$

Increasing Φ_2 thus enables compensating for the linear chirp of the pulse, bringing the initially tilted main component of the Wigner distribution vertical. As a consequence, the pulse is temporally shorter. On the other hand, this shear causes multiple bounces to appear on the temporal profile. Indeed, the interference pattern in the Wigner distribution of the uncompensated pulse is such that positive and negative lobes cancelled out when summed over the frequency axis, leading to a clean 25 fs gaussian profile. Once the shear is applied by adding the quadratic dispersion, the positive and negative lobes of the Wigner distribution do not cancel out each other in the frequency integration, leading to multiple "fringes" in the temporal profile.

4.4.4 Post-Compression of Femtosecond Laser Pulses

4.4.4.1 Principle

The combination of self-phase modulation and negative second-order dispersion enables shortening the duration of laser pulses, in what is known as post-compression schemes. A broad range of setups has been developed in the past decades. A complete and tutorial overview can be found in[11] (see an example in chapter 1). The techniques mostly differ by the way self-phase modulation is induced.

The conceptually simplest scheme consists in propagating the beam into a thin plate of bulk material, as demonstrated more than 30 years ago[12]. The spatial variation of the laser intensity in the plate intrinsically induces an inhomogeneity of

the SPM, which can lead to self-focusing and degradation of the beam profile. To mitigate this, multiple plates with opposite group velocity dispersion can be used[13–17].

The second main family of post-compression schemes is based on propagation in a hollow core fiber[18]. In that case the nonlinear medium is a rare gas introduced into the fiber. Controlling the gas pressure enables changing the effective nonlinear optical thickness of the medium, and thus fine tuning of the SPM conditions. The propagation in the fiber ensures a homogeneous effect of the SPM across the beam profile. Some current trends in fiber post-compression research consist in increasing the average power of beams in the IR[19] or visible range[20], and reducing the pulse duration down to the few-cycle regime by cascading several post-compression modules[21,22].

The third family of post-compression schemes is based on multipass cells. The nonlinear dispersive material, gaseous or bulk, is inside a multi-pass cell in which the laser beam travels over large distances. In a typical cavity configuration with two spherical mirrors, the beam will bounce several tens of times on each mirror, accumulating several tens of meters of propagation. The propagation in a cavity enables washing out the spatial inhomogeneities introduced by the intensity-dependence of SPM. This scheme was introduced only recently[23] but is experiencing an impressive development, enabling the generation of homogeneous post-compressed pulses[24], the compression of picosecond pulses down to the few tens of femtoseconds[25], or even to the few cycle regime by cascading two cavities[26].

Note that we have only mentioned here the schemes based on simple self-phase modulation. Alternative schemes have emerged recently, offering the possibility to perform self-compression and to generate tunable pulses down to the deep ultraviolet range[27]. An extensive review is given in[11].

4.4.4.2 Simple Simulation of a Post-Compression Scheme with Chirped Mirrors

The post-compression of femtosecond pulses described here relies on two steps: spectral broadening by SPM followed by compression of the pulses by introducing a negative quadratic spectral phase.

How is the second step performed in practice? In the mid infrared range, it is possible to find transparent media with a negative group delay dispersion. For instance a bulk plate of fused silica can compress self-phase modulated pulses at 1800 nm[28]. On the other hand, in the visible-IR range the group delay dispersion of most materials is positive, as we have seen in section 4.3. In that case, chirped mirrors are used[7]. They are designed to introduce a given amount of negative quadratic phase, or group delay dispersion, per bounce. This amount is limited to a few tens to hundreds fs^2, such that multiple bounces are necessary to compress the pulses.

In the following, we propose to investigate the post-compression of a 25 fs pulse by SPM and chirped mirrors.

Let us practice !

- Define a 25 fs pulse.
- Apply a $\sigma I = 8$ rad SPM to this pulse.
- Propagate the pulse through 2 mm of SiO_2, the exit window of the post-compression cell.
- Load the GDD for a chirped mirror.
- Interpolate it over the ω grid of your pulse.
- Calculate the pulse obtained as a function of the number of bounces on the chirped mirror.
- Repeat the operation without the dispersion in the SiO_2. Conclude on the relative weight of SPM and linear dispersion in the compression requirements.

Initial 25 fs pulse with $\sigma I = 8$ rad SPM (see figure 4.36)

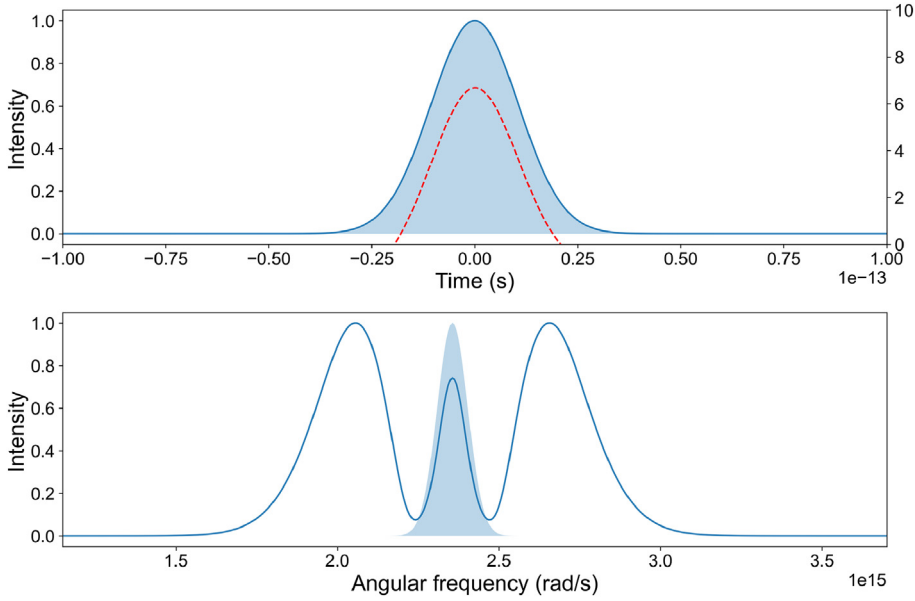

FIG. 4.36 – Temporal intensity profile (plain blue line) and phase (red) of the self-phase modulated 25 fs pulse with $\sigma I = 8$ rad. Lower panel: Spectrum of the self-phase modulated pulse. The light blue shaded area is the spectrum of the Fourier Transform limited pulse.

Propagation through 2 mm of SIO_2 (see figure 4.37)

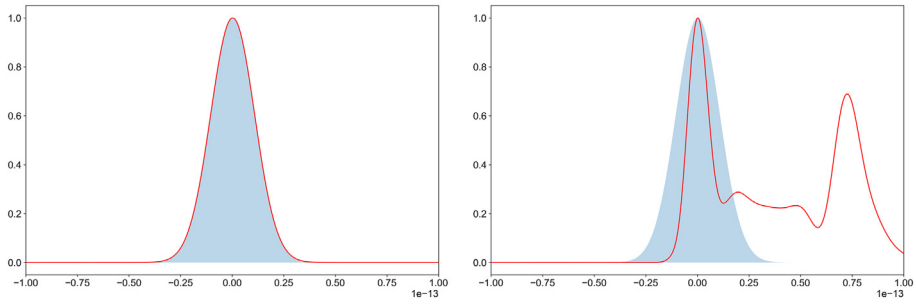

FIG. 4.37 – Left panel: Temporal intensity profile (plain red line) of the self-phase modulated 25 fs pulse with $\sigma I = 8$ rad. Right panel: Temporal intensity profile (plain red line) after propagation through 2 mm of SiO_2. Light blue shaded area corresponds to the Fourier Transform limited pulse.

Load GDD from a file (see figure 4.38)

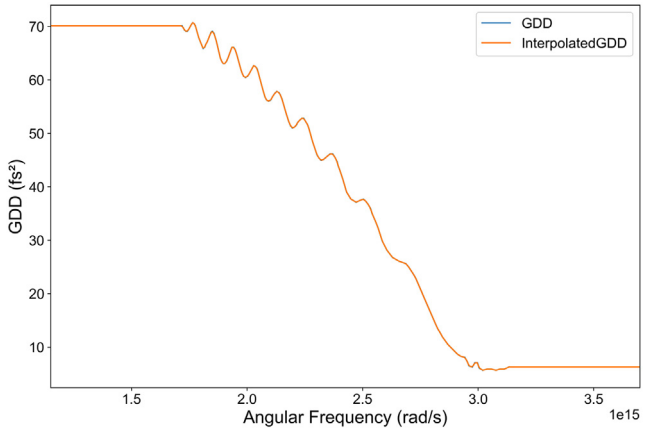

FIG. 4.38 – Interpolation of the Group Delay Dispersion (GDD) of a chirped mirror.

Pulse after N bounces on mirror ($N \in [0, 6]$), see figure 4.39

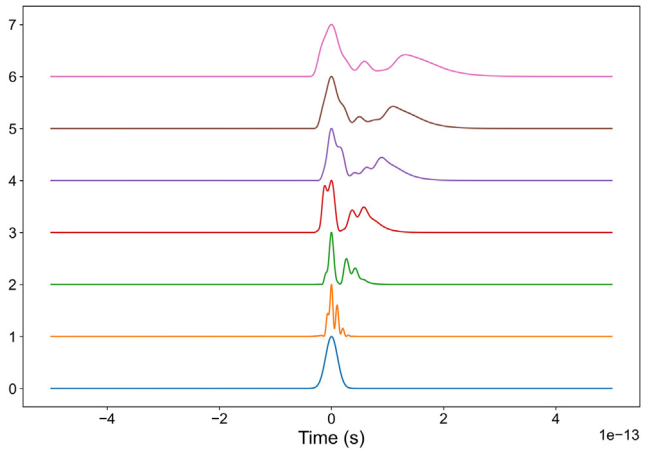

FIG. 4.39 – Temporal intensity profile of the self-phase modulated 25 fs pulse with $\sigma I = 8$ rad propagated through 2 mm of SiO_2 as a function of the number of bounces on a chirped mirror. The curves are vertically shifted to ease visualization.

4.5 Influence of Mirrors on Polarization

4.5.1 Principle

The complex refractive index of the metallic surface of the mirror gives complex reflectivity through Fresnel's equations:

$$R_S = \frac{n_1 \cos\theta_i - n_2\sqrt{1 - \left(\frac{n_1}{n_2}\sin\theta_i\right)^2}}{n_1 \cos\theta_i + n_2\sqrt{1 - \left(\frac{n_1}{n_2}\sin\theta_i\right)^2}} \tag{4.14}$$

$$R_P = -\frac{n_1\sqrt{1 - \left(\frac{n_1}{n_2}\sin\theta_i\right)^2} - n_2\cos\theta_i}{n_1\sqrt{1 - \left(\frac{n_1}{n_2}\sin\theta_i\right)^2} + n_2\cos\theta_i} \tag{4.15}$$

where S index is related to the polarization direction perpendicular to the plane of incidence and P to the parallel one. The intensity reflectivities are given by $|R_S|^2$ and $|R_P|^2$. The reflectivity curve of a mirror can often be obtained directly from the company to which you buy it. As an example, the reflectivity of an ultrafast-enhanced silver mirror from Thorlabs® website is presented in figure 4.40.

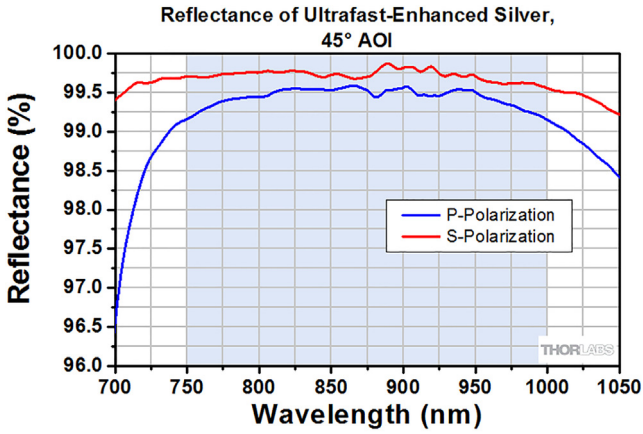

FIG. 4.40 – Reflectance of Ultrafast-Enhanced Silver. ©Thorlabs, Inc – 2021.

4.5.2 Reflectivity in Amplitude in S and P

The complex reflectivity along the S and P direction, and for a given material (aluminum in figure 4.41 or silver in figure 4.42), is given by the following function:

```
def reflectivity(w,theta_i,medium):
```

Representations of reflectivity in aluminum and silver could be obtained through:

```
# Definition of domains
Nbt=4096
Nbw=Nbt
t=linspace(-500e-15,500e-15,Nbt)
w=time2freq(t,Nbw)
#Wavelength in microns
Lambda=2*pi*c/w*1e6
#angle of incidence in degrees
theta_i=45
#Reflective material
medium='Al'
# For Aluminum
RS,RP=reflectivity(w,theta_i,medium)
figure()
subplot(1,2,1)
plot(Lambda,abs(RS)**2.0,'.',label='$R_S$')
plot(Lambda,abs(RP)**2.0,'r.',label='$R_P$')
title('Reflectivity in intensity for {} mirror at {}°'.
 ↪format(medium,theta_i))
```

```
xlabel('Wavelength in microns')
ylabel('Reflectivity')
xlim((200e-3,2))
legend()

subplot(1,2,2)
plot(Lambda,angle(RS),'b.',label='$R_S$')
plot(Lambda,angle(RP),'r.',label='$R_P$')
xlabel('Wavelength in microns')
ylabel('Phase')
xlim((200e-3,2))
legend()
```

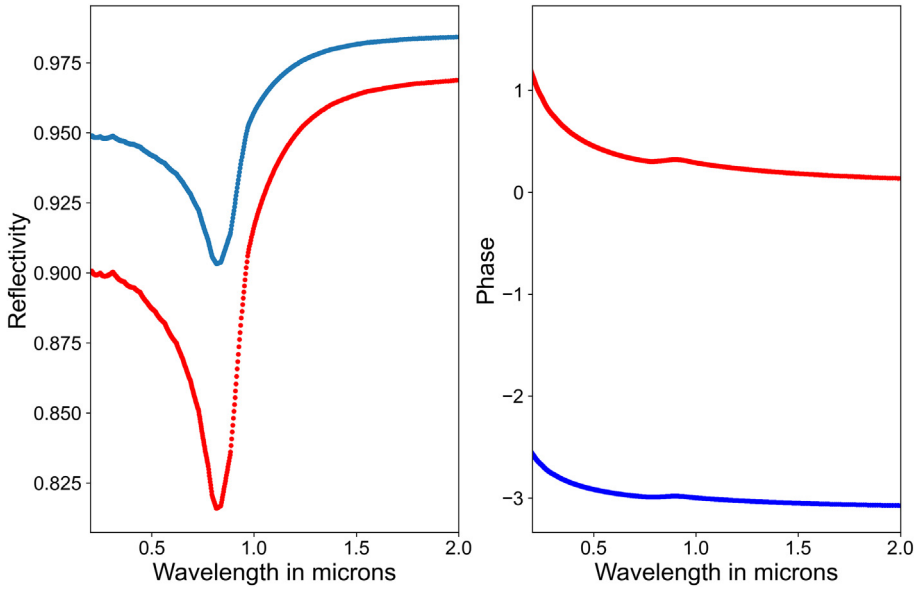

FIG. 4.41 – Complex reflectivity of an Al mirror under 45° incidence angle for S polarization (red line) and P polarization (blue line). Left panel: intensity reflectivity. Right panel: phase.

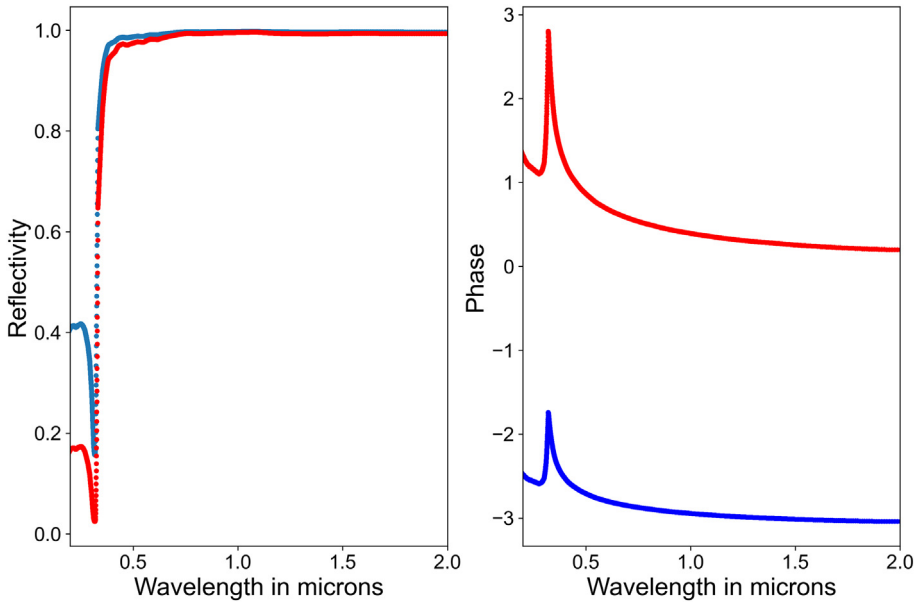

FIG. 4.42 – Complex reflectivity of an Ag mirror under 45° incidence angle for S polarization (red line) and P polarization (blue line). Left panel: intensity reflectivity. Right panel: phase.

As can be seen on the two previous figures, the reflectivity in amplitude as well as the phase acquired during the reflection is very different for the two polarization states S and P. It is important to note that these S and P states are eigenstates associated with each of the elements of the experimental setup and that they are not absolute directions in the laboratory reference frame. In these conditions, if the polarization of the incident pulse is not perfectly aligned with one of these two proper polarization states, it will be modified after reflection on the mirror. By choosing the appropriate angle of incidence, it is even possible to use a combination of metallic mirrors as a polarizer.

Let us now study the modifications of the incident polarization state after one or more reflections on a silver mirror.

4.5.2.1 Projection on S and P Polarization Direction

We suppose that the beam is polarized in the vertical plane at the exit of the laser. The mirror is placed in such a way that there is a small polarization offset angle β (called `PolarOffset` in the code). In other words, S and P polarization directions are not eigenvalues for the propagation (see figure 4.43).

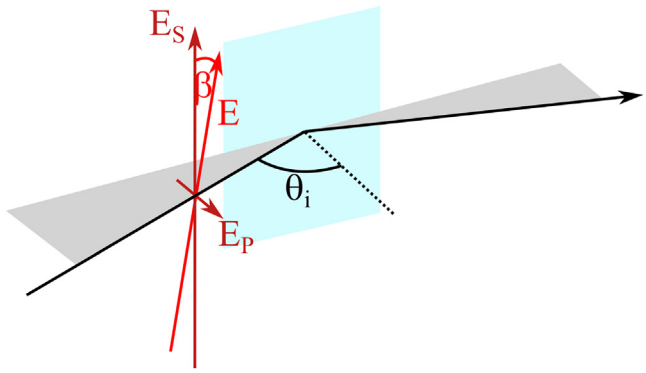

FIG. 4.43 – Schematic representation of polarization decomposition in terms of S and P components for the reflection on a mirror.

The incident polarization will be decomposed along S and P directions as:

$$E_S(\omega) = E_{\text{inc}}(\omega)\cos(\beta)$$
$$E_P(\omega) = E_{\text{inc}}(\omega)\sin(\beta)$$

```
#offset from S polarization, in degrees
PolarOffset=45
PolarOffset=PolarOffset*pi/180

#Projection on S and P direction for electric field in angular␣
↪frequency domain
E_w_S_in=E_w_0*cos(PolarOffset)
E_w_P_in=E_w_0*sin(PolarOffset)
```

4.5.2.2 Influence of the Difference in Reflectivity for a Silver Mirror

```
#Reflective material
medium='Ag'
#angle of incidence in degrees
theta_i=45
# For Aluminum
RS,RP=reflectivity(w,theta_i,medium)

NbBounces=15
for nbounce in range(NbBounces):
    E_w_S_out=E_w_S_in*RS**nbounce
    E_w_P_out=E_w_P_in*RP**nbounce

    E_t_S_out=FT(E_w_S_out,Nbt)
    E_t_P_out=FT(E_w_P_out,Nbt)
```

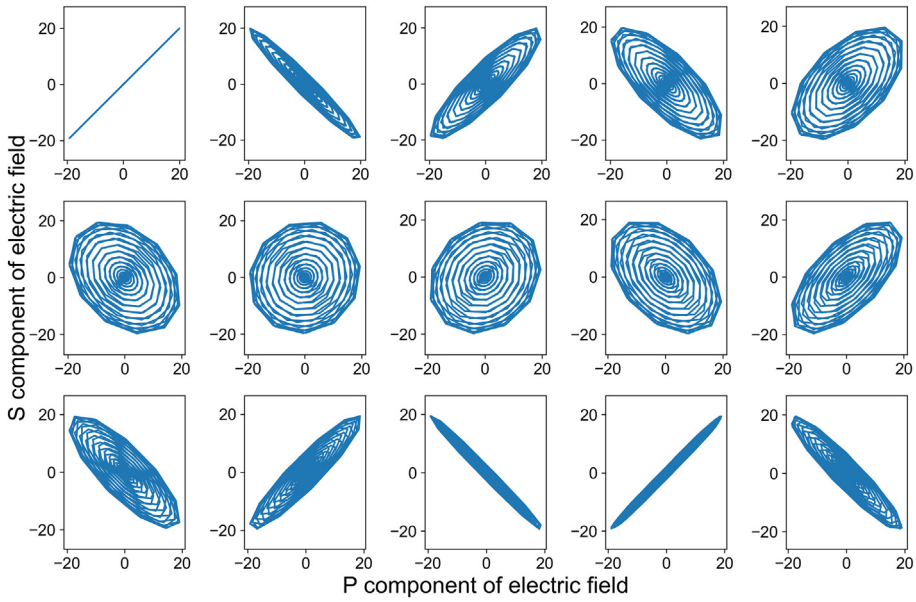

FIG. 4.44 – Evolution of the electric field shape as a function of the number of reflections on silver mirrors.

The shapes of the electric field after reflections on an increasing number of silver mirrors are presented in the successive panels of figure 4.44. We start from a linear polarization offset by 45° from the S polarization. After the first reflection, the polarization state is elliptical, and the ellipticity increases at each bounce on a mirror. The field is almost circularly polarized after 6 bounces, and the ellipticity decreases after this. This change of the polarization state is generally detrimental in experiments. On the other hand, it can be useful to manipulate the polarization of pulses without using waveplates. Indeed, for very short pulses, producing very broadband waveplates can be challenging. Superachromatic waveplates are built by stacking multiple (typically 6) plates of birefringent material, inducing significant dispersion. In the following we investigate the possibility to use a combination of mirrors to transform a linearly polarized pulse into a circularly polarized one.

4.5.2.3 Building an All-Reflective Quarter Wave-Plate

In general, the polarization state of light is manipulated using birefringent media. Half wave-plates are used to rotate the polarization direction, and quarter wave-plates enable converting linearly polarized light into elliptical or circular light. The basic principle of such wave-plates is to decompose the two polarization components of the incident radiation along two orthogonal axis with different refractive indices, and introduce a phase-shift between the two components through propagation. For a quarter wave-plate, this phase shift must be equivalent to a delay of a

quarter of an optical period, plus an arbitrary number of integers of a period. Since it is difficult to manufacture a waveplate so thin as to introduce a quarter-period delay in a single birefringent material, wave-plates are often "multi-order", *i.e.* they introduce a delay of an integer number of optical periods in addition to the wanted delay. This is not compatible with the use of ultrashort pulses. In that case, "zero-order" waveplates are used, stacking several birefringent plates with different dispersions to achieve a delay of a fraction of an optical period between the two polarization components. The second important challenge faced when manipulating the polarization state of ultrashort pulses is the bandwidth of the pulses. Again, combinations of materials with approriate dispersions can be used to ensure that the phase shift introduced at all frequencies over large bandwidths is equal. The resulting wave-plates are called "achromatic" or "super-achromatic". Such wave-plates are available from the visible to the infrared regime. However as the laser wavelength reaches the UV range, using broadband wave-plates becomes more complex, in particular due to the dispersion introduced by the stacked multiple birefringent plates. When the wavelength further decreases to the deep UV, vacuum UV and extreme UV, transmissive optics cannot be used any more. To circumvent this issue, it is possible to benefit from the phase shifts introduced by Fresnel coefficients, to design all-reflective wave-plates. In the following example, you can try to design such a quarter wave-plate, to convert a linearly polarized 5 fs pulse into circular polarization.

Let us practice !

- Define a linearly polarized 5 fs pulse at 400 nm.
- Try to convert the linear polarization into a circular one using aluminum mirrors, with the appropriate combination of offset angle, incidence angle and number of bounces.
- Does the dispersion on the Al mirror distort the temporal profile of the pulses?

In this particular example, you will see that 4 reflections on an aluminum mirror are enough to transform the incident linear polarization into a circular one. It has to be noted that the crucial parameter in this simulation, beyond the complex reflectivity of the mirror, is the polarization offset angle.

According to these simulations, a set of 4 Al mirrors is able to convert 5 fs ultraviolet pulses from linear to circular. Unfortunately things can be more complicated in practice, because the reflectivity of commercial metallic mirrors is generally not equal to that obtained from the Fresnel coefficients. Most mirrors are covered with a protective coating which affects their reflectivity. You can check this by comparing the reflectivity you calculate and the one provided by mirror companies. The difficulty is that companies do generally not provide the reflection phase, such that the only way to determine how good the polarization conversion can be achieved is to perform measurements.

Let us practice !

- Do the same using silver mirrors.
- Is the resulting polarization state constant in time?
- Is the temporal profile of the pulses modified by the reflections on the Ag mirrors?

Again, four reflections are sufficient to transform a linear polarization into a quasi-circular one. However, the polarization state does not seem constant along the pulse. The polarization state varies in time, as the result of the wavelength-dependence of the phase-shift introduced by the reflections. Examining the effect of the wavelength-dependent phase shift on the duration of the pulse reveals that the pulse is slightly stretched.

4.5.2.4 Conclusion

Through these simple simulations, we were able to highlight the influence of the complex reflectivity of metallic mirrors on the polarization state. Experimentally, it is therefore important to be aware of these effects and to design the setup accordingly. This will be even more crucial in the case of circular dichroism experiments where the polarization state must be controlled and perfectly known up to the interaction zone. In general, the final shaping of the polarization state, *e.g.* by means of waveplates, should be performed and measured just before this zone.

4.6 Conclusion

It is interesting to note that with basic tools as well as simple numerical models, we managed to account for some effects experienced by a light pulse during its propagation, from the output of the laser to the input of the experimental chamber. It is quite obvious that we do not claim to compete with more sophisticated and dedicated software designed to give accurate descriptions of the physical phenomena at play during this propagation. It is thus illusory to hope extracting from these simple models more than a simple qualitative vision. Nevertheless, they are still useful for estimating the influence of the different optical elements during propagation.

The first of these effects concerns the linear dispersion inherent to the propagation, that can affect the duration of femtosecond pulses. While the consequences are almost non-existent for long pulses or low-dispersion media, they become crucial in the case of post-compressed ultrashort pulses making the compensation of this dispersion an experimental necessity. Second-order spectral phase compensation is the easiest to implement, either through manipulation of the laser compressor or by the introduction of chirped mirrors. We have seen that even with such

compensation, higher order dispersion terms could lead to the distorsion of the femtosecond pulses. To prevent this, specially designed chirped mirrors can be purchased, which compensate for the second- and third-order phases of a given material – most of the time fused silica. More sophisticated phase manipulation devices do also exist, *e.g.* using spatial phase modulators or acousto-optic programmable filters[29].

Non-linear dispersion can be more challenging to deal with. It does not modify the pulse duration by itself but induces an intensity dependent non-linear phase, which results in the generation of new spectral components. This self-phase modulation can be beneficial and used to broaden the spectrum of a pulse, which can be further compressed by adding a quadratic spectral phase. On the other hand, its intensity dependence induces spatial distortions of the beam, for example self-focusing, and space–time couplings in the beam. The importance of these effects can be estimated with the basic numerical tools proposed in this tutorial, by increasing the dimensionality of the description to take into account these spatial aspects.

For many experiments, it is also very important to finely tune and control the polarisation state of the pulses during propagation. The differences in reflectivity for the S and P polarisation states as a function of the angle of incidence on the mirrors can substantially change the polarization of the laser beam. Beyond the importance of experimentally characterising this state, a good practice consists in placing the polarisation control elements (half and quarter waveplate for example) after a polarizer placed as close as possible to the interaction zone in order to limit unwanted modifications.

The diversity of effects which can be potentially detrimental for femtosecond pulses calls for the implementation of characterization techniques. This is discussed in chapter 5, where the main methods to characterize the temporal profile of femtosecond pulses are introduced.

References

[1] Rulliere C. (Ed.). (2005) *Femtosecond laser pulses: Principles and experiments*, 2nd edn. Advanced Texts in Physics. Springer-Verlag, New York.
[2] Trebino R. (2000) *Frequency-resolved optical gating: The measurement of ultrashort laser pulses*. Springer US.
[3] Pickering J.D. (2021) *Ultrafast lasers and optics for experimentalists*. IOP Publishing.
[4] Hirlimann C., Morhange J.-F. (1992, June) Wavelet analysis of short light pulses, *Appl. Opt.* **31**, 3263.
[5] Fork R.L., Martinez O.E., Gordon J.P. (1984, May) Negative dispersion using pairs of prisms, *Opt. Lett.* **9**, 150.
[6] Fork R.L., Brito Cruz C.H., Becker P.C., Shank C.V. (1987, July) Compression of optical pulses to six femtoseconds by using cubic phase compensation, *Opt. Lett.* **12**, 483.
[7] Szipöcs R., Ferencz K., Spielmann C., Krausz F. (1994, February) Chirped multilayer coatings for broadband dispersion control in femtosecond lasers, *Opt. Lett.* **19**, 201.
[8] Boyd R.W. (2020, January) Chapter 4 – The intensity-dependent refractive index, *Nonlinear optics*, 4th edn. (R.W. Boyd, Ed.). Academic Press, pp. 203–248.

[9] Finot C., Chaussard F., Boscolo S. (2018, December) Simple guidelines to predict self-phase modulation patterns, *J. Opt. Soc. Am. B* **35**, 3143.
[10] Walmsley I.A., Dorrer C. (2009, April) Characterization of ultrashort electromagnetic pulses, *Adv. Opt. Photon.* **1**, 308.
[11] Nagy T., Simon P., Veisz L. (2021, January) High-energy few-cycle pulses: Post-compression techniques, *Adv. Phys.: X* **6**, 1845795.
[12] Rolland C., Corkum P.B. (1988, March) Compression of high-power optical pulses, *JOSA B* **5**, 641.
[13] Lu C.-H., Tsou Y.-J., Chen H.-Y., Chen B.-H., Cheng Y.-C., Yang S.-D., Chen M.-C., Hsu C.-C., Kung A.H. (2014, December) Generation of intense supercontinuum in condensed media, *Optica* **1**, 400.
[14] Lu C.-H., Wu W.-H., Kuo S.-H., Guo J.-Y., Chen M.-C., Yang S.-D., Kung A.H. (2019, May) Greater than 50 times compression of 1030 nm Yb:KGW laser pulses to single-cycle duration, *Opt. Exp.* **27**, 15638.
[15] Tsai C.-L., Meyer F., Omar A., Wang Y., Liang A.-Y., Lu C.-H., Hoffmann M., Yang S.-D., Saraceno C.J. (2019, September) Efficient nonlinear compression of a mode-locked thin-disk oscillator to 27 fs at 98 w average power, *Opt. Lett.* **44**, 4115.
[16] Hwang S.I., Park S.B., Mun J., Cho W., Nam C.H., Kim K.T. (2019, February) Generation of a single-cycle pulse using a two-stage compressor and its temporal characterization using a tunnelling ionization method, *Sci. Rep.* **9**, 1613.
[17] Kurucz M., Flender R., Haizer L., Nagymihaly R.S., Cho W., Kim K.T., Toth S., Cormier E., Kiss B. (2020, October) 2.3-cycle mid-infrared pulses from hybrid thin-plate post-compression at 7 W average power, *Opt. Commun.* **472**, 126035.
[18] Nisoli M., De Silvestri S., Svelto O. (1996) Generation of high energy 10 fs pulses by a new pulse compression technique, *Appl. Phys. Lett.* **68**, 2793.
[19] Nagy T., Hädrich S., Hädrich S., Simon P., Simon P., Blumenstein A., Walther N., Klas R., Klas R., Buldt J., Stark H., Breitkopf S., Jójárt P., Seres I., Várallyay Z., Eidam T., Limpert J. (2019, November) Generation of three-cycle multi-millijoule laser pulses at 318 W average power, *Optica* **6**, 1423.
[20] Descamps D., Guichard F., Petit S., Beauvarlet S., Comby A., Lavenu L., Zaouter Y. (2021, April) High-power sub-15 fs nonlinear pulse compression at 515 nm of an ultrafast Yb-doped fiber amplifier, *Opt. Lett.* **46**, 1804.
[21] Rothhardt J., Hädrich S., Klenke A., Demmler S., Hoffmann A., Gotschall T., Eidam T., Krebs M., Limpert J., Tünnermann A. (2014, September) 53 W average power few-cycle fiber laser system generating soft x rays up to the water window, *Opt. Lett.* **39**, 5224.
[22] Ouillé M., Vernier A., Böhle F., Bocoum M., Jullien A., Lozano M., Rousseau J.-P., Cheng Z., Gustas D., Blumenstein A., Simon P., Haessler S., Faure J., Nagy T., Lopez-Martens R. (2020, March). Relativistic-intensity near-single-cycle light waveforms at kHz repetition rate, *Light: Sci. App.* **9**, 1.
[23] Schulte J., Sartorius T., Weitenberg J., Vernaleken A., Russbueldt P. (2016, October) Nonlinear pulse compression in a multi-pass cell, *Opt. Lett.* **41**, 4511.
[24] Lavenu L., Natile M., Guichard F., Zaouter Y., Delen X., Hanna M., Mottay E., Georges P. (2018, May) Nonlinear pulse compression based on a gas-filled multipass cell, *Opt. Lett.* **43**, 2252.
[25] Kaumanns M., Kormin D., Nubbemeyer T., Pervak V., Karsch S., Karsch S. (2021, March) Spectral broadening of 112 mJ, 1.3 ps pulses at 5 kHz in a LG10 multipass cell with compressibility to 37 fs, *Opt. Lett.* **46**, 929.
[26] Balla P., Balla P., Wahid A.B., Sytcevich I., Guo C., Viotti A.-L., Silletti L., Silletti L., Cartella A., Alisauskas S., Tavakol H., Grosse-Wortmann U., Schönberg A., Schönberg A., Seidel M., Trabattoni A., Trabattoni A., Manschwetus B., Lang T., Calegari F., Calegari F., Calegari F., Calegari F., Couairon A., L'Huillier A., Arnold C.L., Hartl I., Heyl C.M., Heyl C. M., Heyl C.M. (2020, May) Postcompression of picosecond pulses into the few-cycle regime, *Opt. Lett.* **45**, 2572.

[27] Travers J.C., Grigorova T.F., Brahms C., Belli F. (2019, April) High-energy pulse self-compression and ultraviolet generation through soliton dynamics in hollow capillary fibres, *Nat. Photon.*, 1.

[28] Schmidt B.E., Béjot P., Giguère M., Shiner A.D., Trallero-Herrero C., Bisson É., Kasparian J., Wolf J.-P., Villeneuve D.M., Kieffer J.-C., Corkum P.B., Légaré F. (2010, March) Compression of 1.8 μm laser pulses to sub two optical cycles with bulk material, *Appl. Phys. Lett.* **96**, 121109.

[29] Monmayrant A., Weber S., Chatel B. (2010, May) A newcomer's guide to ultrashort pulse shaping and characterization, *J. Phys. B: Atom. Mol. Opt. Phys.* **43**, 103001.

Chapter 5

Femtosecond Pulse Shaping and Characterization: From Simulation to Experimental Pulse Retrieval Using a Python-Based User Friendly Interface*

Sébastien J. Weber[1,**] **and Romain Géneaux**[2,***]

[1]CEMES-CNRS, Université de Toulouse, 29 rue Jeanne Marvig, 31055 Toulouse, France

[2]Université Paris-Saclay, CEA, CNRS, LIDYL, 91191 Gif-sur-Yvette, France

5.1 Introduction

Measuring short laser pulses is a mandatory and difficult task when dealing with experimental ultrashort measurements. To overcome the non-existence of fast enough measuring devices at the picosecond or femtosecond scale, many techniques have been invented. Most of them rely on a non-linear interaction to gain information on the spectro-temporal features of the laser pulse, and yield the complete phase and amplitude profile of the measured pulse. This spectro-temporal information sought is an experimental equivalent to Gabor or Wiegner functions presented in the previous chapter. So far, each invented technique has required one specific algorithm, experimental layout, and acquisition program to retrieve pulse characteristics.

The recently developed COPRA approach[1] solves the first of these issues: it provides one algorithm for all methods after noticing that most of these algorithms

*Supplementary electronic material available at: https://github.com/CEMES-CNRS/pymodaq_femto.

**sebastien.weber@cemes.fr

***romain.geneaux@cea.fr

DOI: 10.1051/978-2-7598-2719-0.c005

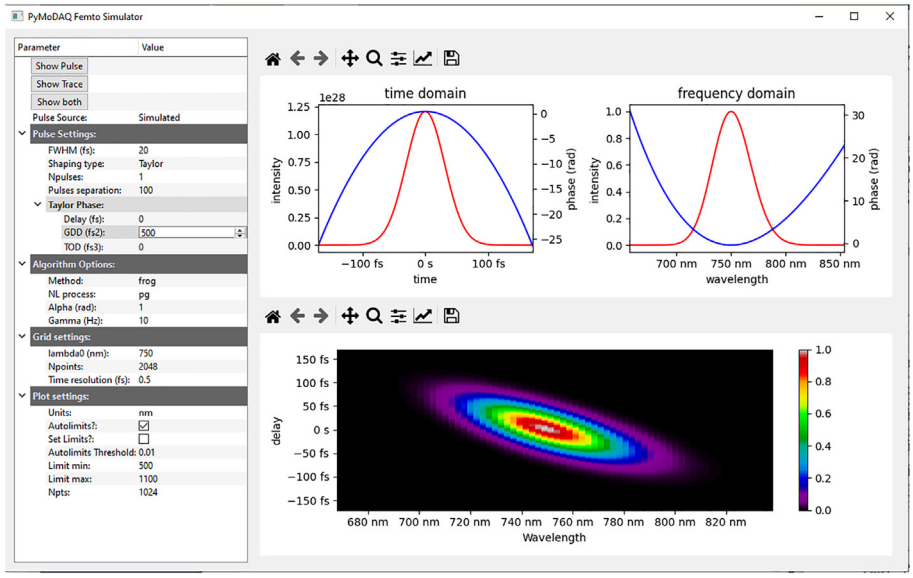

FIG. 5.1 – Simulator user interface in the case of a phase shaping using Taylor expansion with a GDD of 500 fs^2. Left panel: User settings to set the initial pulse parameters, the shaping type (here Taylor), the simulated experimental technique (here FROG with its third-order non-linearity polarisation gating variant) and some plotting options. Top right panel: temporal and spectral representation of the shaped pulse. The intensity is plotted in red (left axis), the phase in blue (right axis). Bottom right panel: time–frequency representation using the selected experimental technique (FROG) and non-linearity (PG).

share a common mathematical formulation. Indeed, all methods do measure the light spectrum after a non-linear process, as a function of a parameter (delay, dispersion…). COPRA formulates these methods together as "Parameterized Nonlinear Process Spectra" (PNPS). The COPRA article[1] gives a very detailed analysis of the reconstruction mathematical problem where both concepts and comparisons between existing algorithms are presented.

With PyMoDAQ-Femto, we take a step further and incorporate this algorithm (available in the Python for Pulse Retrieval *PyPRet*[2] package published under MIT license) within the PyMoDAQ[3] framework, in an attempt to provide an open-source and widely applicable application for pulse retrieval and simulation purposes. PyMoDAQ-Femto (available on GitHub[4]) is a PyMoDAQ extension featuring a stand-alone user interface for simulating various experimental characterization techniques and a stand-alone user interface to perform pulse retrieval using the COPRA algorithm. Because it can be integrated as a PyMoDAQ extension, all PyMoDAQ features for data acquisition can be used to produce experimental PNPS traces, which are then processed by the retrieval extension. Measurements performed by other means can also be used if converted appropriately[5].

PyMoDAQ-Femto is therefore a unified interface for acquiring and processing non-linear pulse characterisation traces. The following sections focus on how to use both the simulator and the retriever on specific examples. More specific details can be found on the documentation websites[6,7].

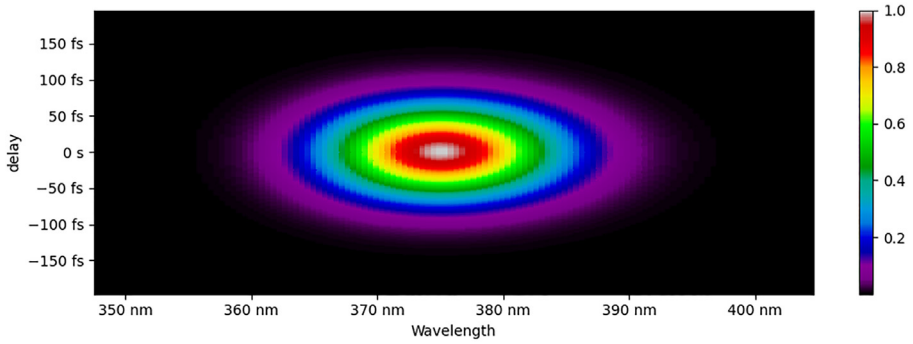

FIG. 5.2 – SHG-FROG trace for a 20 fs FWHM pulse duration having a GDD of 500 fs^2.

5.2 Simulation and Retrieval of Synthetic Laser Pulses

PyMoDAQ-Femto has two main python modules: the *Simulator* and the *Retriever*. Both will be illustrated here using two typical shaped femtosecond pulses. The first one has second-order and third-order spectral phase due, for instance, to dispersion during propagation in air and materials. The second one presents a Gaussian temporal phase due to self-phase modulation typically used for production of ultrashort pulses ($<$10 fs).

5.2.1 Pulse Shaping and Field Representation

As stated in chapter 4, the temporal profile of a light pulse is obtained by Fourier transforming its complex spectrum. The spectral intensity $I(\omega)$ is a relevant quantity but it does not contain all the information about the pulse. For example, let us take two pulses sharing the same spectral intensity, one with a constant spectral phase and the other with a quadratic one. This leads to different temporal lengths: Fourier limited for the former and broadened for the latter.

A Fourier-limited Gaussian narrow-band pulse and a chirped broadband Gaussian pulse can have the same spectral intensity. However, these two pulses have a different spectral phase, constant for the former, quadratic for the latter. To aid with visualizing the interplay between time and spectral features, time–frequency representation has been introduced, such as the Gabor analysis or the Wigner distribution. Time–frequency distributions show the temporal evolution of the instantaneous frequency of a pulse, exactly like a music score where different notes (*i.e.* frequency components) are depicted as a function of time.

The goal of experimental characterisation techniques is therefore to obtain as much information as possible in the form of a time–frequency representation in order to extract valuable information from the pulse. Among the zoology of experimental time–frequency techniques, FROG[8] and d-scans[9] are widely used ones. This section will focus on simulation of FROG traces while the section on experimental data will focus on the d-scan technique. In the FROG technique, the pulse to characterize is split into two delayed replicas recombined into a non-linear process (second harmonic generation for its most widespread variant) where the non-linear signal outcome is spectrally resolved. By varying the delay, one obtains a FROG time–frequency trace.

5.2.2 Simulation Module

The main purpose of this module is to become familiar with pulse shaping and associated time–frequency non-linear traces one can obtain using various techniques. It is also used to test the efficiency of the *Retriever* module.

The initial pulse used in this paragraph has a Gaussian shape. In the *Simulator* module, the initial conditions can be set in the *Settings* panel (see figure 5.1 left), in the *Pulse Settings* section comprising Fourier limited pulse duration and the possibility to define a sequence of pulses. Two types of shaping are available at the moment, Taylor spectral phase expansion or Gaussian temporal phase.

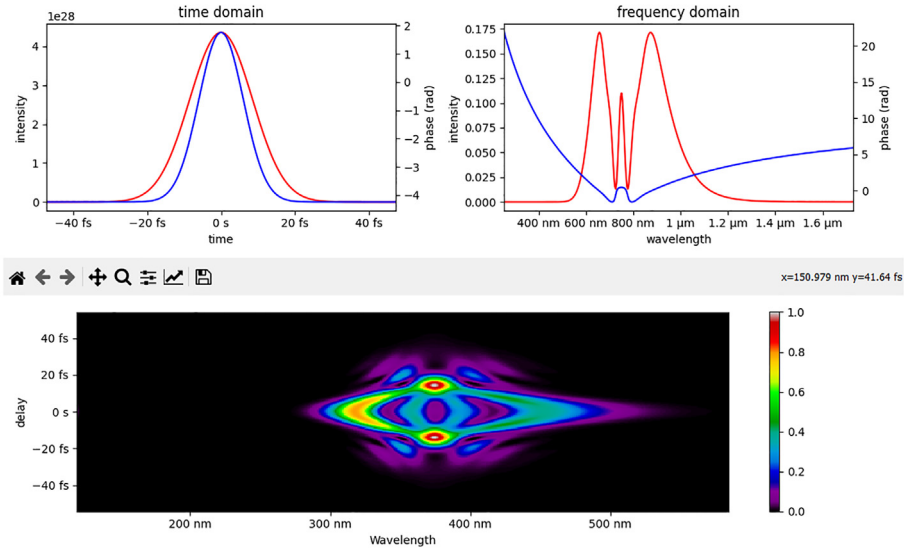

FIG. 5.3 – Time–frequency representation of a pulse which experienced self-phase modulation using SHG-FROG. On the top row, intensity and phase are shown in red and blue, respectively.

5.2.2.1 Taylor Phase

Let us first consider a 20 fs FWHM long pulse undergoing dispersion in air or a transparent material leading to a Group Delay Dispersion (GDD) of 500 fs^2. The GDD will lead to a longer pulse duration with a linear arrival time delay of the frequency components within the pulse envelope, hence a well known chirped pulse. The *Simulator* module represents both the temporal and spectral intensities (see figure 5.1 upper panels). One clearly see a longer duration of the Gaussian shape up

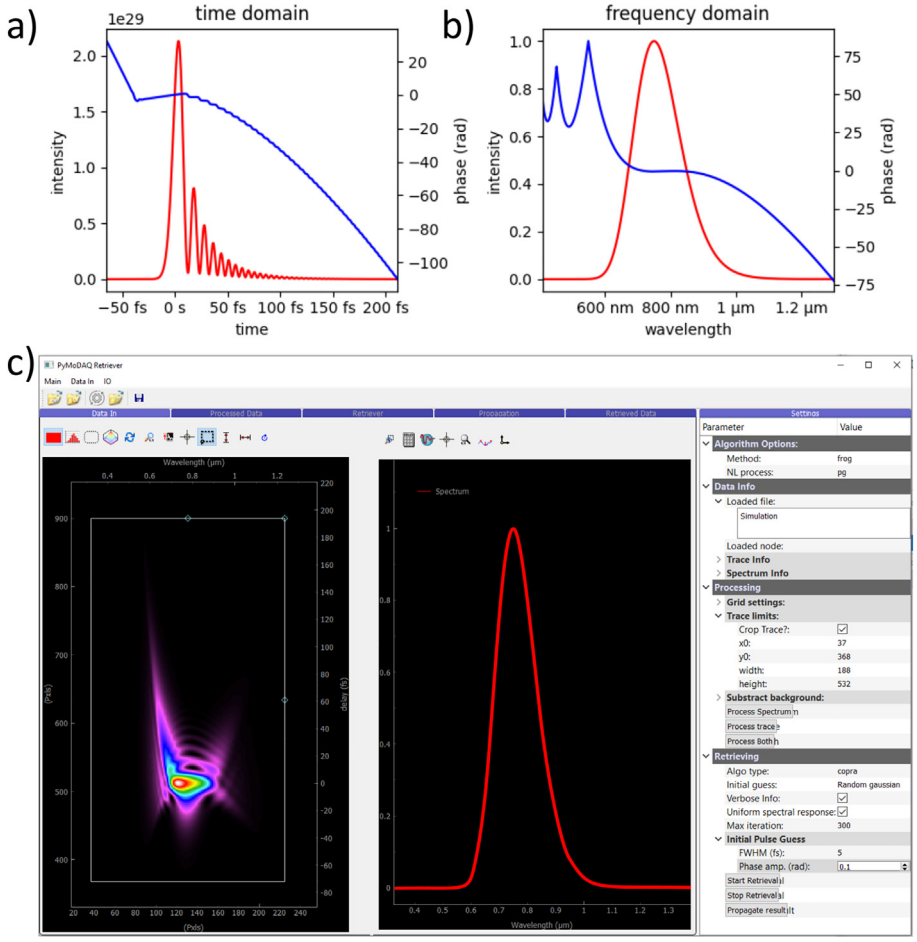

FIG. 5.4 – Ultrashort pulse (5 fs FWHM) shaped with 50 fs^2 GDD and 500 fs^3 TOD plotted in (a) the time domain, (b) the spectral domain. (c) Screenshot of the retriever module where the time–frequency representation of the above pulse using PG-FROG has been loaded. The loaded fundamental spectrum is displayed in the middle. The *Retriever*'s settings are visible on the right.

to about 80 fs. The choice of the characterization technique and its non-linearity can be made in the *Settings* panel, *Algorithm Options* section. Here, we choose the polarisation gating FROG (pg-frog) representation (bottom panel), which uses a third-order non-linear process. It clearly displays the linear arrival time delay of the spectral components. Depending on the technique, some other parameters have to be set (for instance with the d-scan, a dispersive material has to be chosen and its minimum and maximum insertion set to create the dispersion scan). The chosen non-linearity can have a great impact on the readability of the time–frequency trace and its interpretation. For instance, if using second harmonic generation FROG (shg-frog), as shown in figure 5.2, the temporal axis is symmetric and no clear information can be directly interpreted without running a retrieval algorithm[10]. It also means that the direction of time obtained from the algorithm is random in that case. However, for other details about the pulse shape, SHG-FROG is a good choice as it is easier to implement in the laboratory.

5.2.2.2 Self Phase Modulation

Let us now consider self-phase modulation (SPM), which is an often encountered pulse shaping effect due to a third-order non-linear process, and induces the creation of new spectral components. It is mathematically formulated by adding a temporal Gaussian phase to the pulse:

$$E^{\mathrm{SPM}}(t) = E(t)e^{-\alpha\frac{t^2}{\delta t^2}} \tag{5.1}$$

The outcome of the shaping is represented in figure 5.3. The Gaussian phase is clearly visible in blue and the pulse duration is not modified. Compared to the pulse in figure 5.1, the spectral intensity is here broader and highly modulated. The consequence is that a shorter Fourier-limited pulse is produced. The real pulse duration can therefore be decreased if the remaining spectral phase is properly compensated for. Physically, SPM can be produced by the interaction of the pulse with a rare gas leading to chirp on top of the SPM effect. To get close to the Fourier-limited duration, only the GDD should be compensated for, for instance, using reflections on chirped mirrors[11].

5.2.2.3 Other Shaping

At the moment, only Taylor spectral phase and Gaussian temporal phase can be simulated. Sequence of pulses with identical shape can also be produced. If the need arises, please contact the authors to add some other shaping types or dive into python and propose some modification of the source code on GitHub[12]!

Using the *Simulator* module it is therefore easy to explore various pulse shaping and experimentally achievable[13] time–frequency representations in order to be familiar with what to expect in an experiment. The chosen non-linearity has an impact on the clarity of the raw trace, but has no real impact on the retrieval details of the tested pulse (except the direction of time if using SHG-FROG, which can be of importance in some circumstances).

5.2.3 Retrieving Traces

Once the time–frequency trace has been obtained (either using the *Simulator* or an experimental one), pulse characterization can be performed using the *Retriever* module. It allows some pre-processing of the trace (cropping, re-sampling, background substraction) and after the correct settings (mostly the experimental technique used to produce the trace, for instance PG-FROG in the top right of figure 5.4c) have been entered, the reconstruction algorithm can be chosen and run for a given amount of iteration. Figure 5.4c displays the data loaded into the module. Both a PG-FROG trace and the fundamental spectrum have been loaded corresponding to 5 fs FWHM shaped with 50 fs^2 GDD and 500 fs^3 TOD (Third-order dispersion term of the Taylor expansion). Section 5.3.3 fully explains how to use pre-processing on real experimental data where it becomes mandatory for the cleanest possible algorithm outcome.

While it is recommended to use the COPRA algorithm (as it has been fully tested), implementation of other algorithms has been done. The user can therefore compare various outcomes of the reconstruction mostly for education purposes.

Figure 5.5 shows the ongoing reconstruction at the 4th iteration of the COPRA algorithm. The left part displays the current retrieved temporal intensity while the right part displays information on the chosen algorithm and the current error value. The temporal shape is, at that iteration, still far from the expected one from figure 5.4a. However, after a few tens of iterations, both the temporal and spectral shapes (intensity and phase) are very close to the original one.

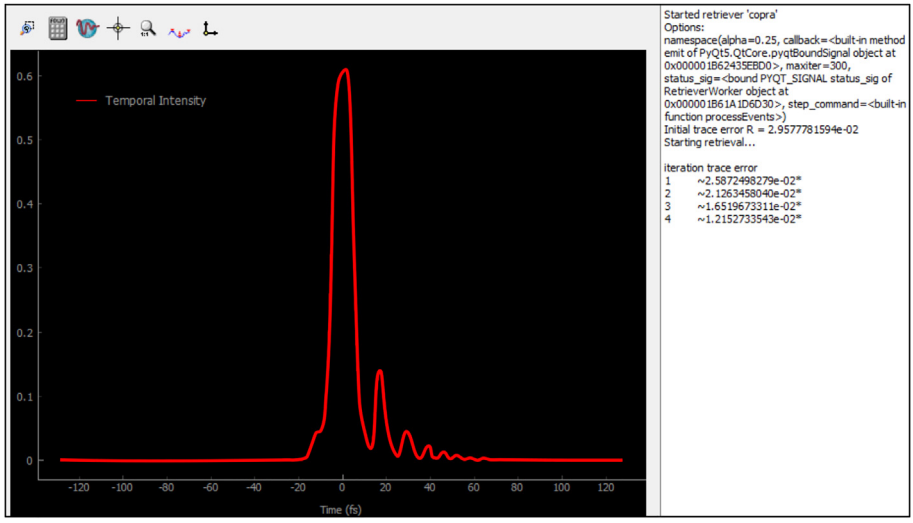

FIG. 5.5 – Live temporal intensity retrieved at the 4th iteration of the COPRA algorithm.

Figure 5.6 displays the final result from the algorithm as directly saved from the *Retriever* module. From there, the pulse is entirely characterized and numerical values can be saved from the module for further processing. Considerations on the initial phase/amplitude guess and the convergence criteria are discussed in the following section.

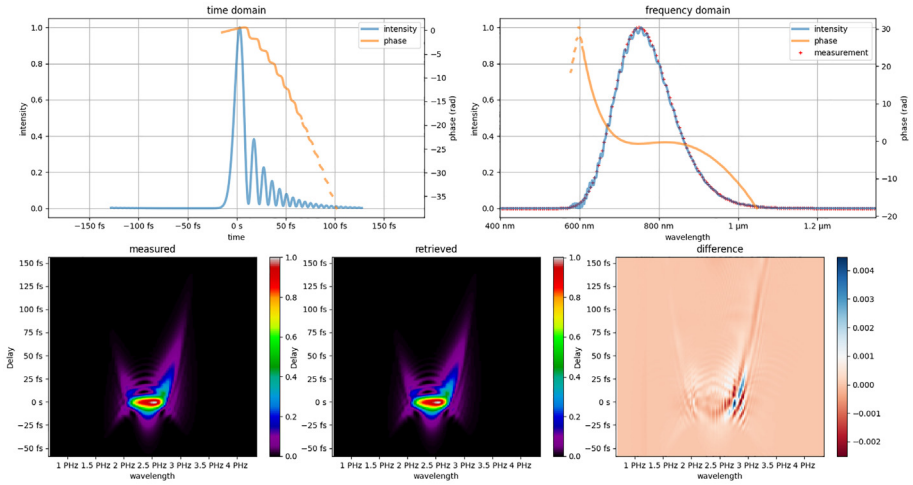

FIG. 5.6 – Retrieved pulse after the retrieval has been stopped at the 30th iteration, using the input trace and pulse shown in figure 5.4a. From top left to bottom right are, respectively, displayed (*i*) the temporal intensity and phase, (*ii*) the spectral intensity, phase and measured intensity, (*iii*) the normalized measured time–frequency trace, (*iv*) the normalized retrieved trace and (*v*) the difference between these normalized measured and retrieved traces.

5.3 Implementation in the Laboratory and Retrieval of Experimental Data

5.3.1 Experimental Pulse Retrieval: The Example of Post-Compression in a Hollow-Core Fiber

We now present the use of PyMoDAQ-Femto to characterize real pulses in a real experiment. As an illustration, we consider the problem of post-compressing femtosecond laser pulses to the few-cycle regime using a hollow-core fiber.[14] As explained above, this technique combines self-phase modulation in a waveguide and subsequent negative second-order dispersion to shorten a femtosecond pulse. A significant difficulty in optimizing such a setup lies in obtaining the maximal spectral

broadening while avoiding high-order spectral phase components, which are very challenging to compensate. Therefore, a fast and robust pulse characterization interface is essential when setting up the device.

Several resources can be found on the physics and implementation of hollow-core fiber compressor; for instance, the review by T. Nagy *et al.*[15] or the thesis of F. Böhle.[16] Here, we briefly describe the components of such a setup. We used a 25 fs (close to its Fourier limited duration), 2 W, 1 kHz laser system, which we aimed to post-compress down to less than 5 fs. In the setup, sketched in figure 5.7, the beam is focused into a 1.5 m long stretched hollow cylindrical fiber (few-cycle Inc.) with 400 μm diameter and filled with neon. A telescope allows fine tuning of the beam size to obtain optimal incoupling with the fiber eigenmodes. The beam angle and position are actively stabilized using the leak of the last mirror, and we use circularly polarized light to reduce self-focusing and ionization.[17] The output beam is then converted back to linear polarization, collimated, and the pulse is compressed using double angle chirped mirrors (PC1332, Ultrafast Innovations) which compensate the group delay dispersion.

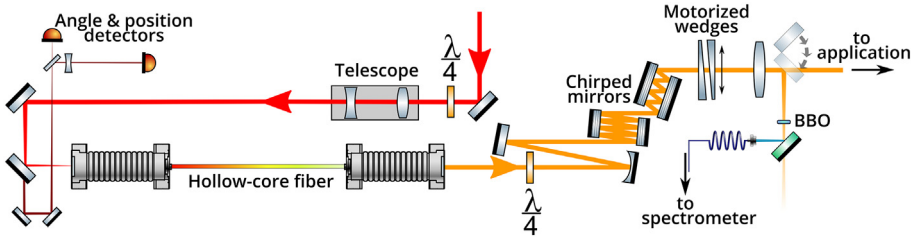

FIG. 5.7 – A typical post-compression setup using a hollow-core fiber, a chirped mirror compressor, and a simple dispersion scan setup.

Here, we choose to implement a dispersion-scan (d-scan) characterization,[9] which consists in measuring the second harmonic spectrum as a function of dispersion added to the pulse. This is typically done by translating a wedge of a known material. The method is particularly simple to formulate as a Parameterized Nonlinear Process Spectrum (PNPS), and thus readily compatible with the COPRA algorithm.[1] It also has the advantage of only necessitating a motorized set of wedges. The same wedges can be used to finely optimize the pulse compression in the experiment. As shown in figure 5.7, a fraction of the short pulses is focused into a 5 μm-thick BBO crystal (which is thin enough to phase-match the entire bandwidth of a short pulse[18]), and the second harmonic generation (SHG) is separated from the fundamental using a dichroic mirror.

5.3.2 Interfacing a Dispersion Scan Measurement in PyMoDAQ

The d-scan module must work with two hardware elements: a motorized translation for the moving glass wedge (in our case from Smaract), and a spectrometer covering the spectrum of interest (StellarNet Inc). The interfacing and data acquisition are performed with PyMoDAQ, as shown in figure 5.8: we use one adequate PyMoDAQ plugin to communicate with each instrument. In our case, both plugins had already been written[19] and were freely available in the PyMoDAQ plugin database[20]. The plugins are wrappers of manufacturer functions, which are typically given as dll/py/pyd/… files upon purchase. The plugin translates all hardware functionalities onto a set of mandatory functions common to all PyMoDAQ instruments, so that their operation is transparent regardless of the actual hardware. Here, the wedge linear translation is cast as a DAQ_Move object, and the spectrometer as a DAQ_Viewer generating 1D data.

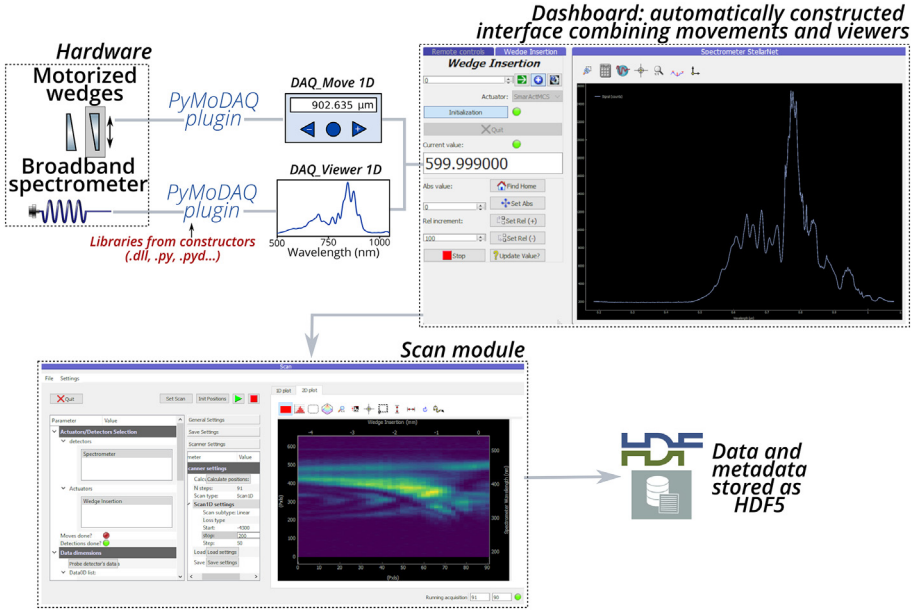

FIG. 5.8 – PyMoDAQ Workflow to construct an interface and perform a dispersion scan. The hardware is connected using PyMoDAQ plugins and combined in a dashboard. Then, the scan module performs the measurement and stores the results and metadata as a HDF5 file. For a demonstration of PyMoDAQ features, see the videos at https://youtu.be/ZdYpQIZHMCY or https://youtu.be/PWuZggs_HwM.

Once the plugins are installed, all PyMoDAQ functionalities can be used directly. When the plugins already exist (which is increasingly the case as more users do contribute to PyMoDAQ), the scanning program is thus constructed in a few

minutes and later loaded in less than a minute. As illustrated in figure 5.8, the DAQ_Move and 1D DAQ_Viewer are combined into a dashboard, providing an interface to optimize the acquisition settings. Then, the scan module is used to scan the wedge insertion while measuring the SHG spectrum. Figure 5.8 shows a screenshot of the live display of a d-scan measurement; this particular trace is not exceptionally nice (it is tilted and a lot of rebounds are present), directly indicating poor post-compression conditions. At the end, all data and metadata are stored into an HDF5 file, which is an open source, portable and self-describing file format well suited to storing heterogeneous and potentially large datasets.

5.3.3 Retrieving the Temporal Profile of Few-Cycle Pulses Using PyMoDAQ-Femto

From this point, the PyMoDAQ-Femto retriever module can be directly loaded from the scan program, and will automatically load the last measured trace. Otherwise, it can also be launched separately and load any previously measured experimental file, in a manner similar to that of synthetic traces (see section 5.2.3). The module requires two inputs: a measured PNPS trace, and the measurement of the fundamental spectrum of the characterized pulses. This spectrum can serve as a starting point for the algorithm, as a comparison to gauge the quality of the retrieval, or even be used to constrain the solution to have the same spectrum. In practice, its measurement can be done sequentially (by moving the spectrometer or by switching the beam path arrangement), or in parallel using two spectrometers.

5.3.3.1 Pre-Processing

Upon loading the trace and fundamental spectrum, much information is extracted from the data: the central wavelengths, the spectral widths, as well as the size of each axis. An option allows to rescale either axis to standard units in case the instruments used different ones.

The next important step is the pre-processing of the PNPS trace. Because of the variety of measurement types that can be retrieved in PyMoDAQ-Femto, as well as the various kinds of hardwares that can be used, it seemed unwise to try to automatize this process in a way that would work for all users. Instead, our philosophy has been to provide as much freedom to the users as possible for all parameters. This is perhaps off-putting at first, especially compared to more specialized and integrated commercial softwares, but the interface could easily be simplified by each user to fit their specific needs, after finding the optimal parameters. The first parameter to set is the type of measurement that was performed. All measurements supported by COPRA are available and summarized in table 5.1.

Three aspects must be then considered:

(1) Any non-zero background in the measured trace or the fundamental spectrum must be carefully subtracted. Otherwise, a static error between retrieved and measured data will persist and prevent convergence. As shown in figure 5.10a, the user can graphically select a spectral region corresponding to the background level, which will be subtracted to the trace or spectrum.

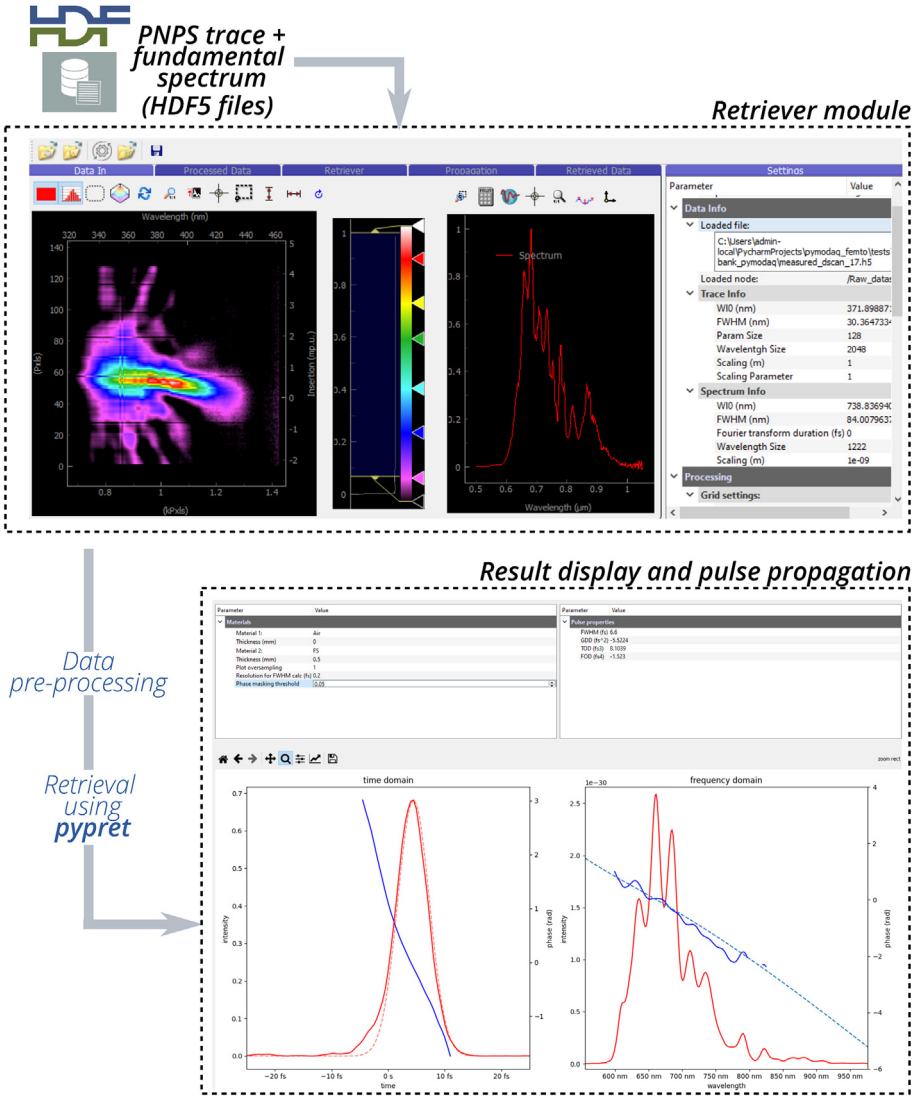

FIG. 5.9 – Structure and workflow of pulse analysis using PyMoDAQ-Femto.

(2) The input trace must be cropped over a well-chosen region, both as a function of wavelength and measurement parameter (insertion for d-scan). This is particularly important here, as hollow-core fiber compressors can yield octave-spanning spectra; for instance, at a fundamental wavelength of 780 nm, it is possible to obtain spectra covering 400 nm to 1050 nm. This will cause

TAB. 5.1 – Available measurement types, with their full names, and supported non-linear processes: shg (Second Harmonic Generation), thg (Third Harmonic Generation), sd (Self Diffraction), pg (Polarization Gating), tg (Transient Grating).

Method	Full name	Supported non-linear processes
frog	Frequency-resolved optical gating	shg, pg, tg
d-scan	Dispersion scan	shg, thg, sd
ifrog	Interferometric frequency-resolved optical gating	shg, thg, sd
miips	Multiphoton intrapulse interference phase scan	shg, thg, sd
tdp	Time-domain ptychography	shg, thg, sd

some parts of the fundamental to spectrally overlap with the second harmonic radiation, perturbing the retrieval. Thus the retrieval must be restricted to regions without the fundamental. This only marginally affects the retrieval, as the robustness of d-scan allows the retrieval of the pulse over a wider spectral range[21] than the chosen one. An option allows the user to graphically select the retrieval region.

(3) Finally, a proper grid in the spectral dimension must be chosen. We follow the convention of *pypret* (which is used for the retrieval) and use a centered frequency axis. It is defined by the user with the most physically meaningful quantities: a center wavelength, a number of points for the grid (in the time and energy domain), and the spacing between two grid points in the time domain (in fs) (default settings are calculated from the loaded traces). The spacing corresponds to the time resolution of the retrieval. After setting these options, the trace and fundamental spectrum are pre-processed and interpolated on the new grid, and displayed in the "Processed Data" panel. The Fourier transform limited duration corresponding to the measured spectrum is also calculated. The user must ensure from these plots that the options are adequate (that is enough points to properly sample the trace features, but not too many to not lengthen the retrieval time); for instance, figure 5.10b and c shows two poor grid choices which are under-sampled in time and frequency domains, respectively. These options, in particular the points in each axis, have an impact on the calculation time needed for convergence – from seconds to a few minutes in some cases.

5.3.3.2 Retrieval

The pre-processing step converts the measured data onto instances of *pypret* classes: a MeshData object (the trace), a Pulse object (the fundamental spectrum), and a PNPS object. Again, we purposely chose to give the user as many options for the retrieval as possible:

Algorithm type: The *pypret* module implements several reconstruction algorithms (COPRA, PCGPA...), which allows to compare their efficiency in various situations.

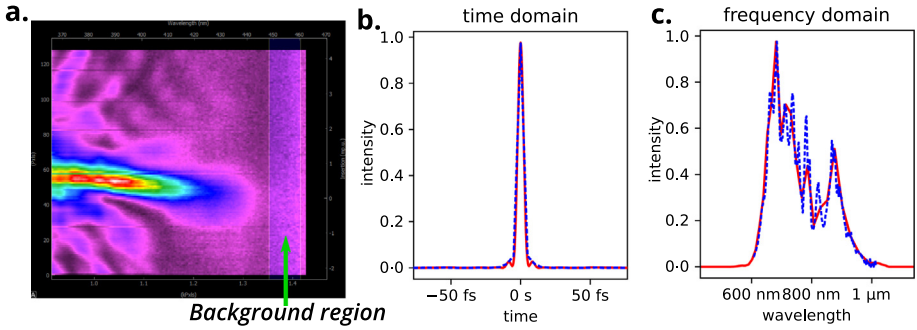

FIG. 5.10 – Pre-processing of data prior to retrieving. (a) Graphical tools allow the user to select several regions: here, the background region, whose average signal will be subtracted to the trace. (b) The time profile of the Fourier transform limited pulse after interpolation on a chosen grid; (c) the spectral intensity interpolated on the grid. The two curves show two poor choices of an interpolation grid: the full-red interpolation is good in time but poor in frequency while the dashed blue one is under-sampled in time but good in frequency.

However, we have only used and tested the COPRA algorithm, which readily works on all PNPS methods. In the future, other algorithms could be tested and debugged, and the interface could be modified to display only algorithms compatible with the chosen PNPS.

Verbose information: Displays the error between retrieved and measured traces at each iteration, together with the spectral and temporal intensity of the current solution.

Maximum iteration: In our implementation, we simply let the algorithm run for a given number of iterations. Other approaches, such as specifying a convergence criterion in terms of trace error, could also be implemented in the future.

Uniform spectral response: This parameter determines whether we assume the entire apparatus to have a flat spectral response, or an energy-dependent one. In a real experiment, the measured SHG spectrum will be convoluted by several factors which in our case are: the reflectivity of the dichroic mirror, the coupling and the propagation into the fiber, the spectral response of the spectrometer, and the phase matching curve of the BBO. If we assume a flat spectral response, the algorithm, which computes the ideal SHG from a given pulse, will converge towards a flawed solution. Instead of trying to calibrate the absolute response of the entire apparatus, the overall spectral response can be factored into an energy-dependent weighting function in the algorithm.[9]

Initial guess: We experimented with two approaches for the starting point of the algorithm. The initial guess can either be taken as the transform limited pulse obtained from the fundamental spectrum, which can favor convergence towards a

similar spectrum. This can however be seen as a bias to gauge the algorithm performances. Alternately, the algorithm can use a gaussian pulse with a random phase as a starting point, with user-defined duration and phase noise amplitude. In some cases, this choice actually gave faster convergence and lower residual error.

Fixed spectral intensity: Finally, this last option depends entirely on the user's strategy. When retrieving a pulse, it can be difficult to gauge the validity of the retrieval. It is customary to compare the retrieved spectral intensity with the measured one – this way, one can assess if the solution is realistic. Another approach is to constrain the algorithm to match the measured spectral intensity.[22] If this option is ticked, the intensity of the guessed pulse at each iteration is replaced by the measured one. In other words, only the spectral phase is allowed to evolve during the retrieval. Since less variables are let free to evolve, this will typically result in a slower convergence and larger residual error, but with the benefit of a possibly more realistic solution. Below we show the retrieval of the same trace, with and without this option.

5.3.4 Examples of Retrieved Pulses

Figure 5.11 displays the retrieved trace obtained with relatively little gas in the hollow-core fiber. The solution is obtained after 200 iterations using a 4096 points spectral grid, a random gaussian pulse as a starting point and a non-uniform spectral response. In figure 5.11b, both the spectral amplitude and phase are let free to evolve. The retrieval error, defined as the normalized root mean square error between the measured and retrieved trace, is 1.45%. Note that the final error cannot be lower than the Gaussian noise present in the experiment (stemming from intensity fluctuations and measurement noise).[1] In addition, the retrieved spectrum matches fairly well with the measured one (figure 5.11d), suggesting a satisfactory pulse measurement retrieval. In figure 5.11c we also show the retrieved trace obtained while constraining the fundamental spectral intensity to the measured one. The retrieval quality is slightly worse (1.78% error), which is expected as explained before.

Finally, in the last step of the retriever module, we allow the user to propagate the retrieved pulse through a chosen amount of common optical materials (air, fused silica, KDP…) and to observe the resulting temporal shape. This allows a quick (but manual) feedback with the experiment: exactly how much material should be added to obtain the shortest pulse on-target? How can the measured spectral phase best be compensated? In figure 5.11e, inserting 0.50 mm of glass gives the optimal pulse duration (5.88 fs FWHM). The retrieval with free or fixed fundamental spectra gives very similar pulse profiles for this dataset. In this particular case, the pulses were sent into a vacuum chamber to produce high harmonic generation, and the entrance window was 0.5 mm thick – the pulses were therefore optimal for the application.

In figure 5.12 we display a measured and retrieved trace for even shorter pulses (obtained with higher pressure in the hollow core fiber). The trace is visibly thinner

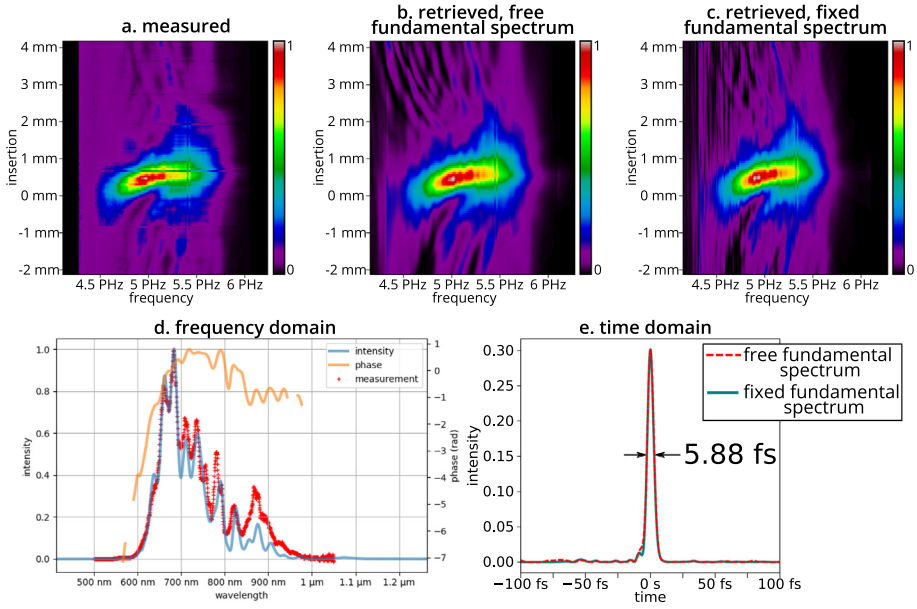

FIG. 5.11 – Retrieval of a dispersion scan trace. (a) Measured trace. Retrieved traces using either an unconstrained fundamental spectrum (b) or a spectrum fixed to the experimentally measured one (c). (d) Retrieved spectral intensity and phase, together with the measured fundamental spectrum (red crosses); (e) Propagated pulse after 0.5 mm of fused silica, obtained using free (dashed red) or fixed (filled blue) fundamental spectra.

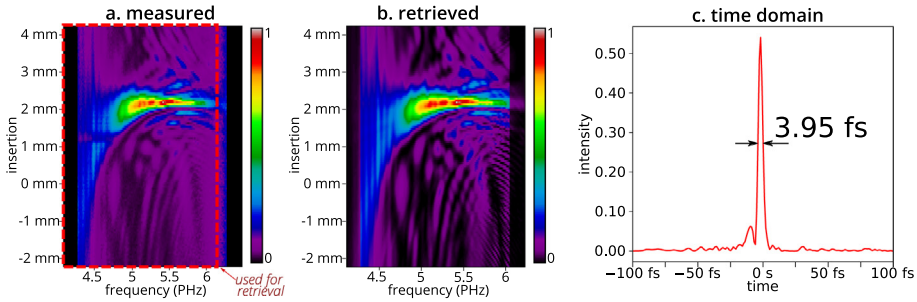

FIG. 5.12 – Retrieval of a dispersion scan trace with a sub-4 fs pulse. (a) Measured and (b) Retrieved traces; (c) Propagated pulse after 2.23 mm of fused silica.

in the insertion dimension, and shows more complex structures, which do arise due to higher order phase terms. Yet, the COPRA retriever manages to reconstruct the trace with a 1.59% error. Propagating the pulse through 2.23 mm of fused silica yields a 3.95 fs-long pulse. Note that less glass was present in the beam path compared to the previous measurement, explaining the large difference in optimal insertion.

5.4 Conclusion

We have presented the capabilities of the PyMoDAQ-Femto module, which allows to simulate and retrieve PNPS traces. The possibility of quickly visualizing the shape of various traces is particularly helpful to understand measurement techniques for short femtosecond pulses. Besides its educational value, this open-source software can also be used in real conditions with experimental data, as we demonstrate in a hollow-core fiber post-compression experiment. When set up in combination with PyMoDAQ, it allows to measure femtosecond pulse reliably and transparently to the user, regardless of the used hardware. We hope that the large flexibility in pre-processing and retrieving options encourages its use in diverse situations, and stimulates collaborative contributions to the software. Code modification or issues can be made using the public PyMoDAQ-Femto GitHub repository.

References

[1] Geib N.C., Zilk M., Pertsch T., Eilenberger F. (2019) Common pulse retrieval algorithm: A fast and universal method to retrieve ultrashort pulses, *Optica* **6**, 495.
[2] Geib N. Pypret GitHub repository. https://github.com/ncgeib/pypret.
[3] Weber S.J. (2021) PyMoDAQ: An open-source Python-based software for modular data acquisition, *Rev. Sci. Instrum.* **92**, 045104.
[4] https://github.com/CEMES-CNRS/pymodaq_femto.
[5] PyMoDAQ-Femto contains a utility python script to convert your data (in *numpy* format) to a valid *hdf5* PyMoDAQ file.
[6] https://pymodaq.cnrs.fr.
[7] https://pymodaq-femto.readthedocs.io.
[8] Trebino R., Kane D.J. (1993) Using phase retrieval to measure the intensity and phase of ultrashort pulses: Frequency-resolved optical gating, *J. Opt. Soc. Am. A* **10**, 1101.
[9] Miranda M., Fordell T., Arnold C., L'Huillier A., Crespo H. (2012) Simultaneous compression and characterization of ultrashort laser pulses using chirped mirrors and glass wedges, *Opt. Exp.* **20**, 688.
[10] The clearest non-linear trace would be one mimicking the Gabor transform, but for this, one must shear the tested pulse by a real function. This is why some third order non-linearities give clearer shape. In PG-FROG the pulse field is first mixed with its conjugate, giving a real quantity that will shear the third field of this third order non-linearity.
[11] A chirped mirror is a multi-layer dielectric mirror reflecting spectral components at different depth within the mirror effectively inducing GDD. It is tailored to produce negative GDD therefore compensating for the natural positive dispersion in gas or materials (See chapter 2, figure 9).

[12] https://github.com/CEMES-CNRS/pymodaq_femto.
[13] The Simulation module excludes more theoretical time-frequency representations such as Gabor or Wiegner functions. Their peculiarities are however discussed in the previous chapter.
[14] Nisoli M., De Silvestri S., Svelto O. (1996) Generation of high energy 10 fs pulses by a new pulse compression technique, *Appl. Phys. Lett.* **68**, 2793.
[15] Nagy T., Simon P., Veisz L. (2021) High-energy few-cycle pulses: Post-compression techniques, *Adv. Phys.: X* **6**, 1845795.
[16] Böhle F. (2017) *Near-single-cycle laser for driving relativistic plasma mirrors at kHz repetition rate - Development and application.* Ph.D. thesis, Université Paris Saclay (COmUE). https://pastel.archives-ouvertes.fr/tel-01806334.
[17] Chen X. *et al.* (2009) Generation of 4.3 fs, 1 mJ laser pulses via compression of circularly polarized pulses in a gas-filled hollow-core fiber, *Opt. Lett.* **34**, 1588.
[18] Baltuska A., Pshenichnikov M., Wiersma D. (1999) Second-harmonic generation frequency-resolved optical gating in the single-cycle regime, *IEEE J. Quantum Electron.* **35**, 459.
[19] If your instrument is not available yet, please watch https://youtu.be/9O6pqz89UT8 for an introduction on how to write your own plugin.
[20] For the list of actually available plugins, see: https://github.com/CEMES-CNRS/pymodaq_plugin_manager.
[21] Silva F. *et al.* (2014) Simultaneous compression, characterization and phase stabilization of GW-level 14 cycle VIS-NIR femtosecond pulses using a single dispersion-scan setup, *Opt. Exp.*
[22] Miranda M. *et al.* (2017) Fast iterative retrieval algorithm for ultrashort pulse characterization using dispersion scans, *J. Opt. Soc. Am. B* **34**, 190.

Chapter 6

High-Order Harmonic Generation (HHG): From Concept to Applications

Sophie Kazamias*

University Paris-Saclay, IJC lab, bat 200, Campus d'Orsay,
91405 Orsay Cedex

High-order harmonic generation is a highly non-linear phenomenon occurring when an intense laser field is irradiating a gas (or solid) target. It can produce an exceptional source of light in the extreme ultra-violet spectral range with extremely short duration and high properties of coherence. The present chapter details the characteristics of the source, the history of its discovery, the basic physical explanation of the phenomenon and gives a brief state of the art of HHG sources in the 2020s.

The basic characteristics of high-order harmonic generation (HHG) in terms of spectral, spatial, and temporal aspects are detailed. This explains why this phenomenon can be used to produce a unique source of light.

The theory of atomic high harmonic generation in a semi-classical framework is presented and explains how an atom behaves in the presence of a strong laser field. First by intuitive physicist approaches and then in the frame of the strong field approximation that allows the calculation of the nonlinear harmonic dipole amplitude and phase.

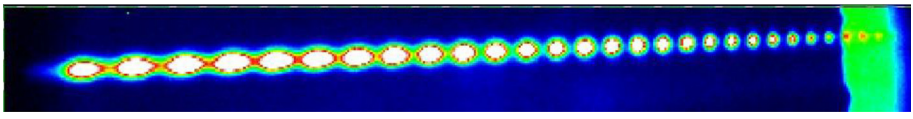

FIG. 6.1 – Typical HHG spectrum obtained in Neon: each spot is the source image corresponding to a given harmonic order. The harmonic order is increasing from left to right; the rightmost spot corresponds to H99.

*sophie.kazamias@universite-paris-saclay.fr

DOI: 10.1051/978-2-7598-2719-0.c006

The macroscopic approach is necessary to understand the link between the single-atom response and the harmonic source efficiency in terms of photon yield: this is the problem of phase-matching in HHG.

HHG can be used to produce attosecond sources: the reason for that is connected to the high coherence of the process as regards the infrared driving field. The first experimental proof of that was done using the RABBITT technique. This was also the beginning of attophysics.

To conclude, recent modern instrumental developments of the HHG source show that it is still a very active field of research more than 30 years after its discovery.

6.1 Basic Characteristics of a HHG Source and Historical Context

The HHG is a physical effect that belongs to nonlinear optics at high orders. The word harmonic generation indicates that some radiation can be produced by the interaction of a pump laser and a nonlinear medium. This radiation is composed of photons with energies corresponding to an integer number (called q in the following) multiplied by the energy of the initial pump beam photons: $E_q = q\hbar\omega$.

Historically, the experimental demonstration of second harmonic generation ($q = 2$)[1] was obtained in a nonlinear crystal very soon after the first LASER demonstration by Maiman in 1960[2]. By high order, we generally consider q of the order of a few tens. Such orders were obtained for the first time after the technological breakthrough of the chirp pulse amplification (CPA) technique at the end of the 1980s[3]. At that time, the high intensities required of the order of 10^{14} W/cm^2 to obtain a significant nonlinear response by the medium were available at a repetition rate larger than 10 Hz, and for short pulse durations (few tens of femtoseconds). The golden age of harmonic generation in rare gases spanned typically from 1993 to 2003. During this decade, there was continuous and parallel progress in the theoretical formulation as well as in the experimental results to establish the fundamental understanding of the source and its properties including its attosecond pulse duration.

Since then, it was the age of pure attophysics and the race to high repetition rate and compact sources with more specific characteristics in terms of polarization, pulse duration, tunability, etc. High harmonic generation from molecules, solid targets, and surfaces has also been successfully demonstrated in recent years.

In the following, we will concentrate on basic HHG, *i.e.*, HHG from rare gases using femtosecond lasers. A typical spectrum, as shown in figure 6.1, is composed of a range of odd harmonic orders of almost constant efficiency: this is called the plateau region. The maximum order that can be reached depends on the gas used and the **laser-focused** intensity: it is called the cutoff order. Rare gases are used as the target because of their higher ionization potential: the lighter the gas, the higher the accessible photon energies. Efficient harmonic generation exists at the limit of ionization: the nonlinear behavior comes from the excursion of an electron being almost ionized, but which returns to the nucleus and recombines to emit radiation. The art of HHG consists in playing with this limit, dictated by the electron dynamics

in the laser field. The cutoff law demonstrated both experimentally[4] and theoretically[5], is the following: $q_{\max}\hbar\omega = I_p + 3.17\,U_p$ where I_p is the ionization potential of the gas, U_p is the ponderomotive potential of the laser defined as $U_P = \frac{e^2}{8m\varepsilon_0 c^3\pi^2}\lambda^2 I$. The maximum intensity that can be used to generate high harmonics from neutral atoms is determined by the saturation intensity at which the whole medium is ionized. This can be estimated by calculating the Barrier Suppression Intensity, which leads to the following cutoff laws: $q_{\max}\hbar\omega(\text{Argon}) = 62\,\text{eV}$, $q_{\max}\hbar\omega(\text{Neon}) = 185\,\text{eV}$, $q_{\max}\hbar\omega(\text{Xenon}) = 28\,\text{eV}$. These values are calculated for a pump having a wavelength of 800 nm for which the photon energy is 1.5 eV. Generally, the maximum harmonic energy scales almost quadratically with the pump wavelength. This explains why HHG from mid-IR lasers has been widely studied in the past years[6].

– Quite low conversion efficiency from the infrared pump laser to the HHG: typically, 10^{-4} at maximum for heavy atoms and down to 10^{-7} for light ones, high harmonic orders.

Experimental aspect and some experimental orders of magnitude:

Important characteristics of the radiation produced by HHG are:

– linear polarization when the pump laser is linearly polarized;
– relatively large spectral width for one harmonic order alone: $\frac{\delta\lambda}{\lambda} = 10^{-2}$;
– short pulse duration for one harmonic order alone: typically, twice shorter than the pump laser duration;
– the attosecond temporal structure comes from the coherent superposition of a large set of phase locked harmonics;
– low divergence of the beam: typically, below 1 mrad and at least lower than the pump laser itself;
– very good optical quality and spatial coherence of the beam: at least better than the pump laser itself.

From an experimental point of view, HHG is a straightforward technique provided one has the proper pump laser with a sufficient level of energy to reach a high enough intensity at focus to obtain a significant harmonic response: the target harmonic order must be in the plateau region. The laser must be focused in the vacuum on a gas target: it can be either a cell, a jet, or a pulsed valve. The gas can flow continuously or be pulsed to reduce the load on the vacuum pumps installed in the experimental chamber. Let us recall that extreme ultraviolet wavelengths are strongly absorbed by air or generating gas. Typically, if the pressure in the chamber is higher than a few 10^{-3} mbar, reabsorption by the residual gas is too strong for a 1 m propagation of the harmonics. The focusing system is generally a lens or a spherical mirror (to avoid chromatic aberrations when very short pulses are used) whose focal length is chosen following the available pump energy and pulse duration: it must be the longest one that enables efficient dipole response at the focus. An iris is placed before the lens to finely adjust the laser intensity and focusing geometry. Long focusing has the advantage to increase both longitudinally and radially the volume over which HHG can be generated. On the other hand, this leads to a reduction in the focused intensity. The gas medium size has to be close to the

Rayleigh range of the laser: it can be several cm for relatively loose focusing ($f = 1$ to 10 m for pump lasers above 5 mJ per pulse) and the ideal medium is a gas cell filled with few tens of mbar depending on the gas species, or as short as 1 mm for short focusing (few tens of cm) when the pump laser is working at high repetition rates (>MHz) with less than 1 mJ per pulse. The gas target is a high-pressure gas jet (up to several bars) in these conditions.

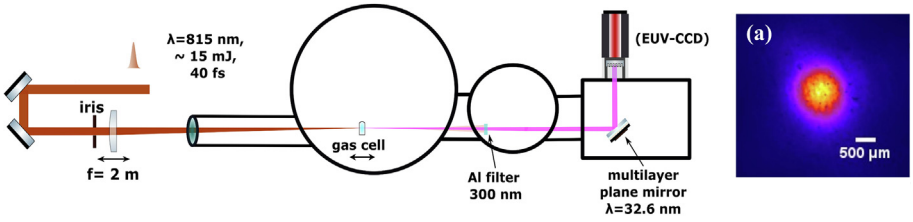

FIG. 6.2 – Schematic of a HHG experimental setup: the laser is propagating from the left to the right.

After being generated close to the pump laser focus, all harmonic orders do propagate collinearly with the pump laser that has been only very weakly absorbed by the generating gas. This is a real experimental challenge to remove the pump laser energy that is typically 6 orders of magnitude more intense than the harmonic beam and hence represents a real danger for all XUV diagnostics downstream the beam. One generally uses metallic filters that are opaque to the infrared radiation but let the harmonic beam go through with absorption of the order of 50%. This can be obtained for example with aluminum filters having a thickness of a few hundred nanometers.

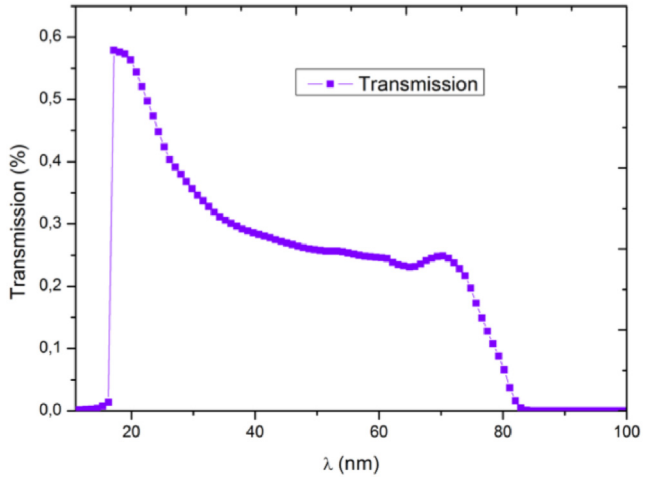

FIG. 6.3 – Transmission of an aluminum filter with 200 nm thickness having an oxidized layer of 10 nm on both sides.

As an example, the transmission as a function of wavelength is shown in figure 6.3 where we see the aluminum cutoff at 17.5 nm. To be able to work with higher harmonic orders, other materials such as Indium, Zirconium, Beryllium (more expensive and fragile) have to be used. There is an issue about where to put these filters in the experimental set-up: they have to be far enough from the focus not to be damaged by the laser. Note that this becomes more and more challenging as the laser average power increases, in particular with Yb-based high repetition rate sources. Such metallic filters can eventually be avoided if the diagnostics on the HHG line are insensitive to infrared or if an optical device such as a grating spatially separates XUV and IR. After this filtering, HHG can be used for applications or characterization, individually or the full spectrum together. It is important to note that extreme UV optics required to manipulate the beam are still not obvious: for high efficiency, near-normal incidence multilayer optics have to be used but work only for a reduced spectral range and may induce temporal widening of the beam. High efficiency for a wide spectrum is obtained at grazing incidence for pure silica optics for example.

6.2 Semi-Classical Model for HHG: From Three-Step Model to SFA by Lewenstein

(a) The so-called three-step model was proposed by Kulander and Corkum in 1993[5] and is very efficient to explain physically the origin of HHG.

(1) *First step from the fundamental state (initial step in figure 6.4):*
The initial state is an electron in a bound state of a rare gas atom, its energy is thus $-I_p$ where I_p is the ionization potential of the atom. The shape of the potential well is given by the Coulomb potential of the core: $-\frac{Ze^2}{4\pi\varepsilon_0 r}$, where Ze is the charge of the nucleus, $-e$ the charge of the electron, and r the distance between electron and nucleus. In the presence of a strong monochromatic laser field, the atomic potential is periodically modified by the potential energy of the laser: $V(r) = -E.r.\cos\omega t$, r being the algebraic distance to the nucleus along with the linear polarization of the pump laser, E is the amplitude of the laser electric field. We immediately see that every half cycle the sign changes. When the field is at its maximum (second picture in figure 6.4), the barrier that the electron has to overcome to reach the continuum *i.e.* the region in which it is free from the nucleus is minimum or even suppressed given the laser amplitude is high enough. In the case when there is still a small barrier, tunnel ionization can occur with a rate that scales very rapidly with time as $\exp\left(-\frac{\sqrt{I_p}}{E}\right)$. This is the first step of the model: the electron is then ionized with zero initial kinetic energy and enters the continuum.

(2) *Second step, acceleration in the continuum (third image in figure 6.4).* An important parameter for the rest of the story is the time of electron

ionization (t') as compared to the maximum of the laser field ($t = 0$). The electron is then accelerated by the laser field in the direction of polarization following the classical Newton's equation of motion:

$$a(t) = \frac{-eE\cos\omega t}{m},$$

$$v(t) = \frac{-eE}{m\omega}(\sin\omega t - \sin\omega t'),$$

$$x(t) = \frac{eE}{m\omega^2}(\cos\omega t - \cos\omega t') + \frac{eE}{m\omega}(t - t')\sin\omega t'$$

(3) *Third step, recombination (fourth image in figure 6.4):* If the polarization is strictly linear, for a given set of ionization times t', the equation $x(t'') = 0$ can have a numerical (not analytical) solution, which means the electron can recombine with its parent ion since the laser field direction has changed to opposite. What is important with HHG is that the time t'' of recombination only depends on t' but not on the amplitude of the field E. It is then possible to calculate the kinetic energy gain $\Delta E_c = \frac{1}{2}mv^2(t'')$ that depends on t' and scales linearly with the laser intensity.

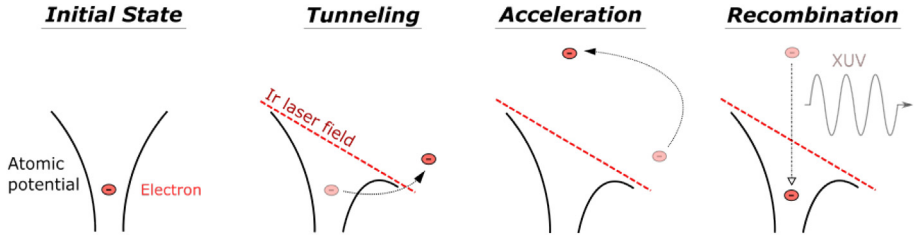

FIG. 6.4 – Schematic picture of the three-step model.

One can also show that for a given kinetic energy gain, there are mainly 2 possible values of (t', t''): one corresponds to an early emission in the continuum and quite a late recombination, and the second one to a later emission but with closer recombination. This is what we will call later the long and short quantum paths, respectively (see also figure 6.15). When it radiatively recombines, the electron produces a photon with an energy equal to the ionization potential of the gas plus the kinetic energy gain in the continuum due to the laser acceleration. It is to note that the maximum kinetic energy gain corresponds to a set of (t', t'') that provides $\Delta E_c = 3,17\,U_p$. This is the origin of the cutoff law. In this simple calculation, the gain in kinetic energy is continuous and not discrete as it is in harmonic spectra.

The origin of the harmonic structure comes from the fact that the phenomenon is periodic and occurs twice per optical cycle (T is the period), this indicates that the difference in energy between two consecutive orders will be $2\hbar\omega$. But there is a sign change every half-cycle since the polarization sign, thus the algebraic value of the dipole changes. Moreover, for two half-cycle emissions to add constructively in time, the term $-\exp\left(i\omega_q T/2\right)$ which is the phase difference between two consecutive bursts must be equal to 1. The conclusion is that $\exp(iq\pi) = -1$ and thus q must be an integer odd number.

(b) This three-step model played an important role in the explanation of the HHG since it presents an intuitive picture without complex mathematical formulations. It succeeded in explaining not only the cutoff law and the origin of the harmonic structure but also the existence of two quantum paths for the same harmonic order, each one corresponding to different times spent in the continuum thus different atomic phases as compared to the reference pump field. One year later in 1994, M. Lewenstein[7] proposed a more refined model based on quantum mechanics for the electron: he did set the basis of the strong-field approximation (SFA) for which the photon energy of the pump pulse must be small as compared to the ionization potential of the gas so that ionization cannot occur by single or few photon absorptions. The pulse duration of the pump laser must be large enough to consider harmonic generation from many cycles and finally, the atomic potential is considered sufficiently low to be negligible when the electron moves in the continuum. Lewenstein proposed an almost analytic and extremely physical way to calculate the nonlinear harmonic dipole using the Schrödinger equation. The details of the equations are given in annex at the end of the document: $i\hbar\partial\left|\Psi\right\rangle/\partial t = (-1/2m\nabla^2 + V(x) - eE\cos(t)x(t))|\Psi\rangle$ that controls electron wavepacket evolution in the laser field, the first term is the kinetic energy, the second one the nuclear potential, the third one the laser potential. The harmonic dipole is then given by $-\mathrm{ex}(t) = \langle\psi(t)| - \mathrm{ex}(t)|\psi(t)\rangle$. After some calculations, Lewenstein showed that:

$$x(t) = i\int_0^t dt' \int d^3p E\cos t' \, d(p - A(t')) \, d*(p - A(t))\exp(-iS(p, t, t'))$$

$$\text{With } S(p, t, t') = \int_{t'}^{t} dt'' \left(I_p + (p - A(t''))^2\right)/2$$

A is the laser potential vector, p the electron momentum, t' the time of ionization, t the time of recombination, d, and d^* are the amplitudes of ionization and recombination, respectively. This equation shows that the harmonic dipole is the result of the interference of all possible trajectories. The ones that will play a major role are those for which the phase S is stationary as regards p, t,

and t'. It can be shown that the stationary phase conditions lead to physical conditions such as $x(t) = x(t')$ or $v(t) = 0$ already considered in the three-step model. The atomic phase value can also be calculated with the stationary phase method and Lewenstein obtained the two quantum path phase values showing that the atomic phase corresponds to $\varphi = -\alpha I$; α is equal to $3.10^{-14}\,\mathrm{cm}^2/\mathrm{W}$ for the first path whereas it reaches $26.10^{-14}\,\mathrm{cm}^2/\mathrm{W}$ for the second one. This phase difference between the trajectories leads to different behaviors in terms of phase matching, spatial and spectral beam profiles. The absolute value of $x(t)$ can then be calculated numerically and the amplitude of the atomic dipole for a given harmonic frequency $d(\omega_q)$ is obtained by Fourier transform of $x(t)$. Figure 6.5 shows the dipole amplitude and phase for the 45th harmonic generated in Neon as a function of laser intensity. The cutoff intensity *i.e.*, the intensity above which the harmonic response is becoming significant is clearly visible, close to $2.10^{14}\,\mathrm{W/cm}^2$. An abrupt change of phase slope is observed together with a considerable increase of dipole intensity which is characteristic of the plateau region. We also note that the atomic dipole response follows a power law of intensity within the plateau (typically, $d(q\omega) \approx I^5$). This law is of course characteristic of nonlinear physics, but the dipole behavior is far from more usual nonlinear optics in the perturbative regime where the medium response scales as I^n, where n is the order of nonlinearity. What is typical of HHG is the existence of an almost equivalent response from the medium for a large set of orders independently of n in the plateau. This is what is called the nonperturbative regime.

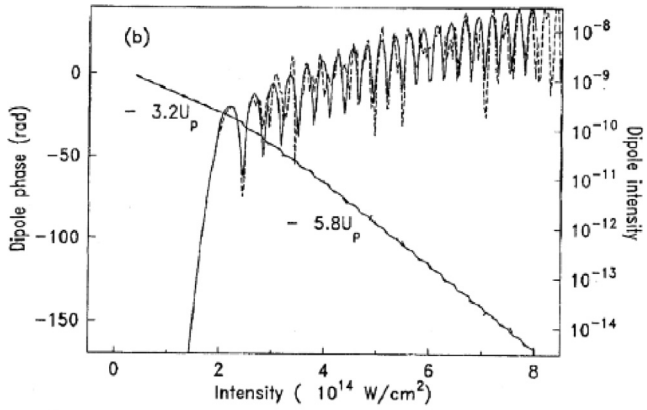

FIG. 6.5 – Harmonic dipole phase (the decreasing curve) and amplitude (the increasing modulated curve) as a function of laser intensity for H45 in neon, this figure is taken from Lewenstein *et al.* (1995) *Phys. Rev. A* **52**, 4747, Copyright 2021 by the American Physical Society[8].

The value of α for the different quantum paths can be obtained from the results in figure 6.5 by a sort of Fourier transform of the dipole as a function of intensity[9].

$$d_{q,I_0}(\alpha) = \int_0^{I_{\max}} d_q(I)\, e^{-i\alpha I}\, G(I, I_0)\, dI$$

where G is an apodization function to ensure the convergence of the integral. A typical plot of d as a function of α is presented in figure 6.6, where we observe not only the first and second quantum paths but also much higher order paths corresponding to even longer excursion of the electron in the continuum.

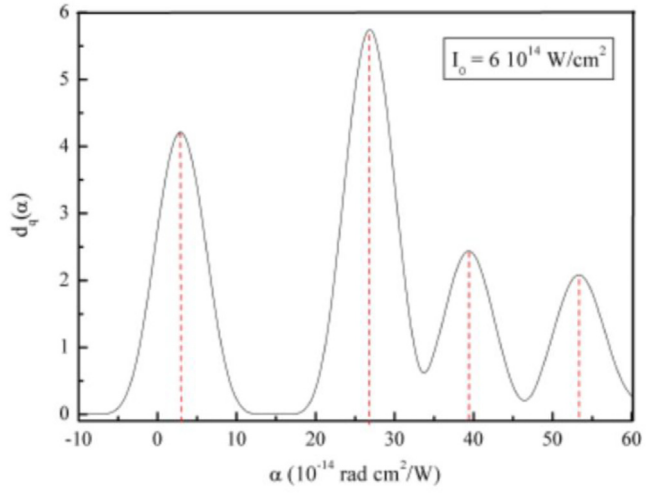

FIG. 6.6 – Amplitude of the dipole for harmonic 45 generated in Neon for the intensity of 6.10^{14} W/cm^2 as a function of the reciprocal parameter α.

Since then, with the strong increase of computing performances, and the development of HHG generated by few cycles, time-demanding ab initio calculations are performed using TDSE methods with a realistic description of both the atomic potential and time dependence of the laser field. The harmonic dipole phase and amplitude and also simply the ionization rates are calculated from the electron wavepacket evolution as a function of time when the SFA is no more valid.

6.3 Macroscopic Study of HHG: The Problem of Phase-Matching and Re-Absorption Limit

(a) **General frame:** We saw that the interaction between an intense laser pulse and an atom can generate a nonlinear dipole that becomes the source of harmonic radiation. The resolution of Maxwell equations in the presence of a nonlinear polarization source will be explained theoretically but the most important thing is to realize that each atom subjected to the laser field is a sort of harmonic radiation emitter. The total harmonic field at the exit of the generating medium is the sum of all contributions with their amplitude and phase. The phase is due to the intrinsic phase of the emission plus the propagation phase which corresponds to the time needed for the radiation to propagate from the emitter location until the exit of the medium. These phases will be evaluated with respect to the pump laser phase and of course, if all the emitters are in phase, their radiation adds constructively and the total harmonic intensity at the exit will scale quadratically with the number of atoms. On the contrary, for certain conditions, we can imagine at least theoretically that pure destructive interference could lead to no harmonic signal at exit even if the single-atom response is high.

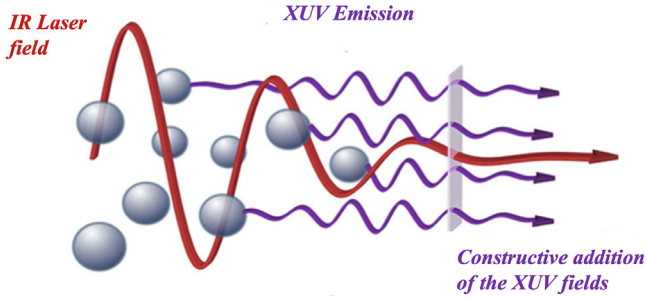

FIG. 6.7 – Artist's view of the phenomenon of phase matching.

According to Maxwell's equations, the general expression for an electromagnetic field E of frequency ω propagating in a medium with polarization $P^{\mathrm{NL}}(\omega)$ and index $n(\omega)$ can be written as:

$$\nabla^2 E(\omega) + n^2(\omega)\frac{\omega^2}{c^2}E(\omega) = \frac{-\omega^2}{\varepsilon c^2}P^{\mathrm{NL}}(\omega)$$

We obtain in the paraxial approximation with $E(\omega) = E_0 e^{-ikz}$, and $k = n\omega/c$, the wave vector:

$$2ik(\omega)\frac{\partial E_0}{\partial z} = \frac{\omega^2}{\varepsilon_0 c^2} P(\omega) e^{ik(\omega)z}$$

Integrating this equation gives the expression of the electric field for the harmonic q:

$$\varepsilon_q = \frac{q\omega}{2i\varepsilon_0 c n_q} \int P_q e^{ik_q z} dz$$

The polarization P_q corresponds to the product of the medium density ρ (number of atoms/cm^3) and d_q, the dipole presented in the previous section. As already mentioned, the total phase of the harmonic field is the sum of the intrinsic atomic phase and the phase due to propagation. The phase shift between the harmonic and the fundamental beam is written at any point z of the propagation axis as:

$$\phi(z) = (k_q - qk_{IR})z - \phi_{\text{at},k}$$

This makes it possible to write the expression of the harmonic field emitted by a medium of length l_{med}:

$$E_q \propto \int_0^{l_{\text{med}}} \rho \left| d_q(z) \right| e^{i\phi(z)} dz$$

The above expression indicates that the harmonic field at each position z is the result of interference between the fields emitted at all positions of the upstream generation medium.

If the phenomenon of reabsorption of XUV photons by the generating medium is not taken into account, the number of harmonic photons along the z-axis per unit of time is given by:

$$N_{\text{photons}} = \frac{q\omega}{4c\varepsilon_0\hbar} \left| \int_0^{l_{\text{med}}} \rho \left| d_q(z) \right| e^{i\phi(z)} dz \right|^2$$

Assuming that the medium is homogeneous, so that ρ does not depend on z and that the amplitude of the dipole is the same for all z positions. The phase can be linearized ($\varphi(z) = z\delta k$) and the expression becomes:

$$N_{\text{photons}} = \frac{q\omega\rho^2 \left| d_q(z) \right|^2}{4c\varepsilon_0\hbar} \left| \int_0^{l_{\text{med}}} e^{i\delta k z} dz \right|^2$$

$$N_{\text{photons}} \propto \left| d_q \right|^2 l_{\text{med}}^2 \frac{1}{\delta k^2} \left(4\sin^2\left(\frac{\delta k l_{\text{med}}}{2} \right) \right)$$

This expression consists of two independent parts: (1) a propagation part and (2) a purely atomic part expressed by the square modulus of the harmonic dipole. In the case of perfect phase matching ($\delta k = 0$), the total photon number generated

varies quadratically with the length of the medium. For a given number of emitters, even if the phase-matching condition is not completely satisfied, the harmonic signal is evaluated using the concept of coherence length in a one-dimensional (1D) study[10].

$$\delta k = k_q - qk_{\text{laser}} - K$$

The optimum phase-matching conditions are obtained when $\delta k \to 0$. If this condition is fulfilled, the longer the generation medium, the stronger the harmonic signal. The coherence length l_{coh} is defined as the length between two source points of the medium, emitting harmonic waves with a phase difference of π. The interference between their respective harmonic emission will be destructive.

$$l_{\text{coh}} = \left|\frac{\pi}{\delta k}\right|$$

If l_{med} is less than l_{coh}, the harmonic field is built gradually with the medium length, but if l_{med} exceeds this value, each pair of points separated by l_{coh} is canceled by interference and at the end of $2l_{\text{coh}}$ the harmonic signal is theoretically zero.

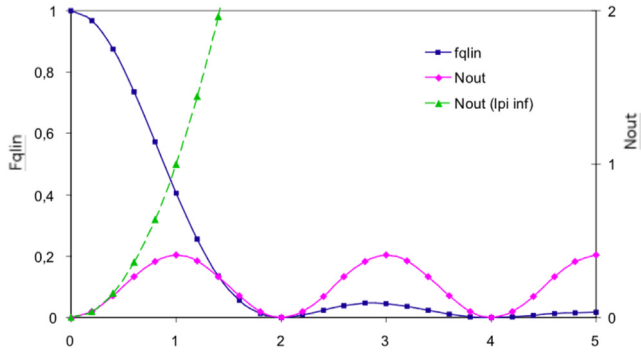

FIG. 6.8 – In pink harmonic signal as a function of medium length in units of coherence length, in green the same for perfect phase-matching conditions, in blue the phase-matching factor.

(b) **The role of absorption:** In a dense generation medium, the XUV absorption by the gas must also be taken into consideration[11]. If it is important, the radiation emitted at the beginning of the medium will be progressively absorbed by the gas after a certain length called the absorption length. It is defined as the length for which the signal is attenuated by a factor $1/e$ (S_{out} and S_{in} are, respectively, the harmonic signal at the exit and entrance of the medium):

$$T = \frac{S_{\text{out}}}{S_{\text{in}}} = e^{-\frac{l_{\text{med}}}{l_{\text{abs}}}}$$

with T the transmission of the generating medium can be found on the CXRO website (http://www-cxro.lbl.gov). It is to note that

$$l_{\text{abs}} = \frac{1}{\sigma\rho}$$

where σ is the photoabsorption cross-section of the gas and ρ the atomic density.

The absorption length logically decreases with the gas pressure. To give an order of magnitude, figure 6.9 presents the evolution of the absorption length as a function of wavelength for the three most used gases for HHG. The calculation was performed for a pressure equal to 15 mbar for argon, neon, and xenon.

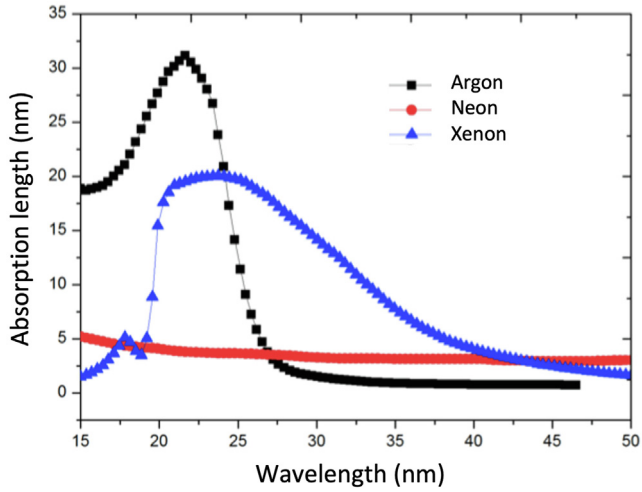

FIG. 6.9 – Absorption lengths for argon, neon, and xenon as a function of harmonic wavelength in nm for a reference gas pressure of 15 mbar.

By making the same approximations as before, *i.e.*, a linear phase φ in z and a harmonic dipole independent of z, we can write:

$$N_{\text{out}} = \frac{\rho^2 q\omega}{4c\epsilon_0 h}\left|\int_0^{l_{\text{med}}} |d_q| \exp\left(\frac{z - l_{\text{med}}}{2l_{\text{abs}}}\right) \exp(i\delta k.z)\, dz\right|^2$$

$$N_{\text{out}} = \frac{\rho^2 q\omega}{4c\epsilon_0 h}|d_q|^2 \left|\exp\left(\frac{-l_{\text{med}}}{2l_{\text{abs}}}\right) \frac{\exp\left(\frac{l_{\text{med}}}{2l_{\text{abs}}} + i\delta k l_{\text{med}}\right) - 1}{\frac{1}{2l_{\text{abs}}} + i\delta k}\right|^2$$

$$N_{\text{out}} = \frac{\rho^2 q\omega}{4c\epsilon_0 h}\left|d_q\right|^2 \frac{4l_{\text{abs}}^2}{1+4\delta k^2 l_{\text{abs}}^2}\left(1+\exp\left(-\frac{l_{\text{med}}}{l_{\text{abs}}}\right)-2\cos(\delta k.l_{\text{med}})\exp\left(-\frac{l_{\text{med}}}{2l_{\text{abs}}}\right)\right)$$

A compromise must be found on the density of the generating medium so that the number of emitters is sufficient to obtain a strong emission but not too high so that absorption is not a limiting factor. E. Constant *et al.* in PRL 82[11] have shown that the optimum emission is obtained when the absorption length, the length of the medium, and the coherence length satisfy the following conditions:

$$l_{\text{med}} > 3l_{\text{abs}}$$

$$l_{\text{coh}} > 5l_{\text{abs}}$$

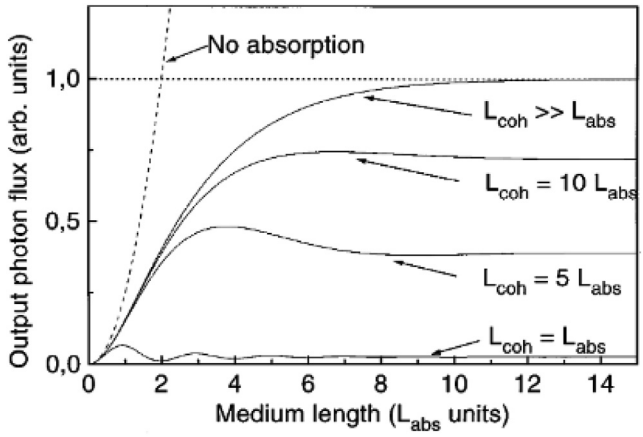

FIG. 6.10 – Number of harmonic emitted photons as a function of medium length for different coherence lengths (this graph is taken from[11] Copyright 2021 by the American Physical Society).

(c) **The different physical origins of phase mismatch[12]:** In this part, we will detail the origin of phase mismatch in HHG in a simplified 1D model along the propagation direction. We will propose some ways to avoid this phenomenon that strongly reduces the HHG conversion efficiency. The phase mismatch is given by:

$$\boldsymbol{\delta k} = \boldsymbol{k_q} - \boldsymbol{q k_1} - \boldsymbol{\nabla \phi_{\text{at}}}$$

In this work, we will consider that $k_q = 1$ since for the EUV wavelengths the dispersion terms are negligible. The laser wave vector amplitude k_1 is the most sensitive term of the equation. On the one hand, the focusing of the beam

induces a phase shift known as the Gouy phase, on the other hand, the atomic and electronic dispersion also play a significant role.

Gouy phase: The generation of high-order harmonics requires high laser intensities, which is why the gaseous medium is placed near the focal zone. However, when passing the focus, a Gaussian beam increases its propagation phase in addition to its natural propagation phase ($\varphi(z) = -k^* z + \psi(z)$). The sign convention is the one used by Siegman in his reference book on lasers. For a Gaussian beam, this Gouy phase $\psi(z) = \arctan(z/z_0)$ is mostly acquired by the beam over a length characteristic of the focal zone: the Rayleigh length (z_0), its derivative provides:

$$\delta k_{\text{Gouy}} = \frac{d}{dz}\left(-\arctan\left(\frac{z}{z_0}\right)\right) = \frac{-1/z_0}{1+\left(\frac{z}{z_0}\right)^2}$$

δk_{gouy} is therefore negative regardless of the sign of z and will be maximum at focus ($z = 0$). It can be considerably reduced if z_0 is increased, which means soft focussing.
The relationship between the index of a medium and the modulus of the wave vector is given by the dispersion equation $k = n\omega/c$. In the generation of harmonics, the dispersion terms induce a temporal modification of the index of the medium: there are both atomic and electronic dispersions.

The atomic dispersion:

The index of refraction of rare gases is slightly higher than 1 but this is sufficient to induce significant effects on phase matching. The atomic dispersion is positive and is more important for heavy gases: it is 10 times more important for xenon than for neon. For a reference pressure of 1 bar at room temperature, the index for neon is $1 + 6.70.10^{-5}$, for Argon $1 + 2.51.10^{-4}$, and $1 + 6.21.10^{-4}$ for Xenon. The contribution of the atomic dispersion to the index is proportional to the pressure and the quantitative value is given below per 1 mbar:

$$\delta k_{\text{at}}(\text{Ne}) = \frac{\omega}{c} 6.7.10^{-8}$$

$$\delta k_{\text{at}}(\text{Ar}) = \frac{\omega}{c} 2.51.10^{-7}$$

$$\delta k_{\text{at}}(\text{Xe}) = \frac{\omega}{c} 6.21.10^{-7}$$

This positive contribution to the refractive index is only valid as long as the atom is not ionized because the ions produced have much lower polarizability than the atom.

The electronic dispersion:

The wave vector amplitude k_1 of the infrared laser is dependent on the ionization of the medium *via* the plasma dispersion law:

$$n(\omega) = \sqrt{1 - \frac{n_e}{n_c(\omega)}}$$

with n_e the electronic density and the critical density n_c:

$$n_c = \frac{\omega^2 m_e}{\mu_0 c^2 e^2}$$

In the case when $n_e << n_c$, we have:

$$\delta k_1 = \delta n \frac{\omega}{c} = -\frac{n_e}{2n_c}\frac{\omega}{c}$$

In total for all dispersion terms, we have:

$$k_1 = n\frac{\omega}{c} - \frac{d}{dz}\arctan\left(\frac{z}{z_0}\right) = \frac{\omega}{c}\left(1 - \frac{n_e}{2n_c} + \delta n_{\text{at}}\right) - \frac{d}{dz}\arctan\left(\frac{z}{z_0}\right)$$

One can notice that the atomic and electronic dispersion terms depend on time if the ionization in the medium is significant. They have opposite signs, with an atomic dispersion likely to compensate for the Gouy phase gradient. There will be sufficient compensation if the sign of the total wave vector amplitude detuning is negative before ionization occurs in the medium. Ionization induces an increase of the wave vector amplitude detuning through the increase of n_e and the decrease of n_{at}. The Gouy phase gradient term does not depend on the pressure nor time, whereas the atomic dispersion increases linearly with the density of the medium. *Therefore, for HHG conditions with low ionization in the medium, phase matching can be reached by tuning the pressure: the stronger the focusing, the higher the balance pressure, the higher the signal*[14]. This is generally the case for HHG from high repetition rate pump lasers with reduced pump energy per pulse.

The exponential increase in the harmonic signal as a function of pressure for a laser intensity of 2.10^{14} W/cm^2 ($z_0 = 5$ mm, cell length 2 mm) presented in figure 6.2c from Seres *et al.*[30] can be explained by an increase in phase matching with the pressure and not only by an increase in the number of phase-matched emitters which would "only" lead to a quadratic law. *On the contrary, if the laser intensity is high enough, HHG occurs on the rising front of the laser pulse in a progressively ionizing medium.* Figure 6.11 shows the temporal variation of the coherence length for different values of argon pressure. The maximum laser intensity is 3.10^{14} W/cm^2, it occurs at $t = 50$ fs for a pulse duration of 30 fs FWHM. Under the experimental conditions presented here, for pressures below 40 torr, the coherence length never becomes infinite, whereas this phenomenon can occur for higher pressures with a few percents of ionization. We also note that higher pressures make it possible to delay the time of infinite coherence length closer to the maximum of the laser pulse, which favors a greater atomic response of the medium (higher intensity).

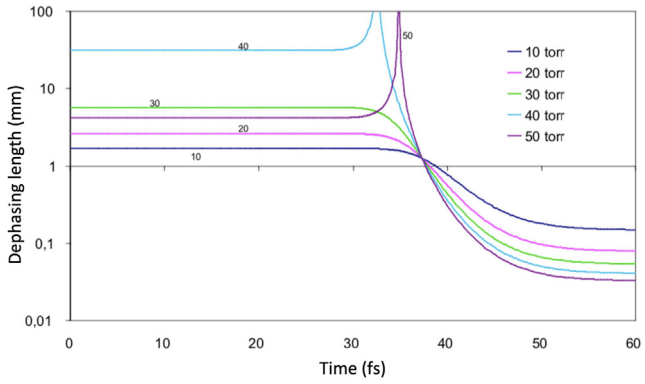

FIG. 6.11 – Evolution of the coherence length for H25 and a set of argon pressures. The laser peak intensity 3.10^{14} W/cm^2 is at 50 fs and the pulse duration is 30 fs FWHM.

More generally, we can analytically calculate the ionization rate P_{ionis} which allows the coherence length to take an infinite value by balancing the two dispersion terms and the Gouy phase (N_0 is the atomic density):

$$P_{\text{ionis}} = \frac{\delta n_{\text{at}} - \frac{c}{\omega}\left(\frac{1/z_0}{1+(z/z_0)^2}\right)}{\frac{N_0}{2n_c} + \delta n_{\text{at}}}$$

To get the maximum single-atom response at the time of phase matching, it is interesting to have the largest P_{ionis} by increasing the pressure of the medium or the Rayleigh length of the laser. The only term for phase mismatch induced by the harmonic waves themselves comes from the atomic phase of the dipoles. It varies proportionally to the spatial derivative of the pump laser intensity and the contribution to wave vector amplitude detuning is, for a Gaussian beam of maximum intensity I_0 and Rayleigh length z_0:

$$K = -\alpha\frac{\partial I}{\partial z} = \frac{2\alpha I_0 z/z_0^2}{\left(1+\left(\frac{z}{z_0}\right)^2\right)^2}$$

This term is the only one to introduce asymmetry on either side of the focus because it changes sign with z. The phase-agreement will be better on the axis for positive z because K is then positive and can compensate for the negative electronic dispersion term for example. The opposite effect will occur for negative z, *i.e.*, when the cell is placed before the laser focus. The atomic phase effect on phase matching is much stronger for the second quantum path and is increased for short focusing but as it scales with laser intensity, the temporal window of phase matching is quite short. As an illustration of the phase-matching study, I show why it is interesting to slightly close the iris before the lens while generating HHG with sufficient energy in the pump laser[14]. A typical optimization curve is shown in figure 6.12.

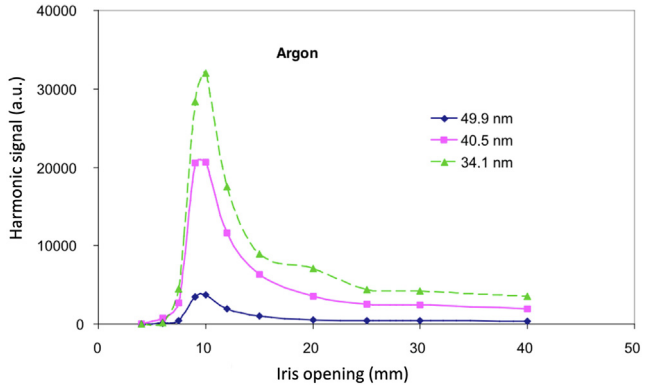

FIG. 6.12 – Variation with the iris diameter of the harmonic signal generated in 10 torr of argon for 3 different harmonics, an incident pump laser energy of 6 mJ, 2 mm cell.

This could be counterintuitive as a first approach since when closing the iris, the laser intensity at focus strongly decreases so that the single-atom response should be reduced. First, because the iris transmission in energy is reduced, but also because the focusing geometry is changed following the laws of diffraction for Gaussian beams. The smaller the aperture, the larger the Rayleigh range and beam waist at focus: this effect increases both transversally and longitudinally the volume over which HHG can occur. A time-dependent study of phase matching clearly shows the behavior for three important cases.

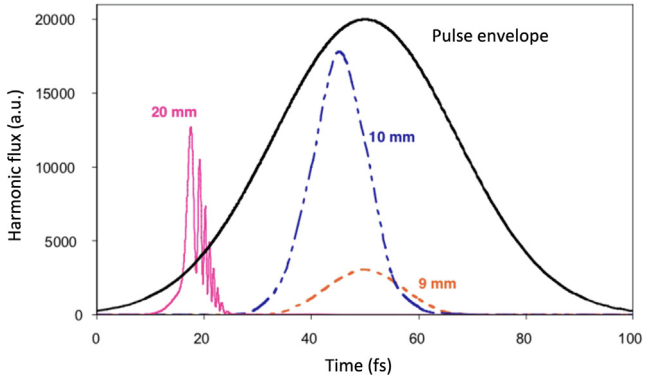

FIG. 6.13 – Time-dependent HHG signal produced by a 6 mJ, 40 fs, laser pulse centered at 50 fs for 3 different iris apertures.

For the 9 mm aperture, the phase-matching conditions are quite good because the Rayleigh length is longer and there is no ionization, but the laser intensity is too low to produce a significant single-atom response. Under these conditions, the time

for maximum harmonic emission is the same as the one of the pump laser. If the iris is opened to 10 mm, the laser intensity increases sufficiently to produce a large atomic response, at a time close to the maximum of the pulse when there is still little ionization. For a 20 mm iris, the intensity is really high, phase matching is poor since z_0 is much smaller, and strong ionization occurs very early in the rising edge of the laser pulse. Ionization-induced phase-mismatch completely deteriorates the signal level when the laser intensity is at its maximum.

(d) **Conclusion:** In conclusion, efficient HHG is obtained when two conditions are fulfilled: (1) a strong atomic response and (2) efficient phase matching. It is challenging to attain them at the same time since high intensity means ionization and ionization induces phase mismatch. The difficulty is increasing with the harmonic order through the factor qk_1 in the dephasing wavevector amplitude. In addition to this, higher harmonic order means higher laser intensity thus higher ionization level.

HHG is a phenomenon that requires playing with the limits to find the compromise between antagonistic effects such as ionization, absorption, single-atom response, etc. The best experimental configuration has to be designed following the pump laser properties: energy in the beam, pulse duration, and beam size. This will control the appropriate focusing system needed to reach sufficient intensity for a given harmonic to be in the plateau. The medium-length shall then be chosen following the Rayleigh range, and the pressure optimization will depend on phase matching and absorption.

After almost three decades of experimental optimization, the maximum conversion efficiency that could be reached with HHG generated in Argon (typically around H25) with Ti:Sa pump lasers is close to 10^{-4} and it seems difficult to further increase it without changing the pump wavelength (the smaller the wavelength, the higher the efficiency[15]). This value is even smaller for much higher harmonic orders generated in Neon or Helium.

6.4 The Attosecond Structure of HHG

Here we will discuss one of the most impressive features of HHG that explains why the research activity on this source has been so intense for the past decades. HHG is a coherent phenomenon driven by an ultra-short laser pulse that allows for the production of attosecond pulses with almost no effort. This property had been predicted theoretically in the mid-'90s and since the first experimental demonstration in 2001 by Paul *et al.*[16], HHG has become the shortest source of radiation: world record is now below 100 as. The beginning of the 21st century was the beginning of "attoscience": how to measure, characterize and use these ultra-short pulses for applications. The only candidate to reach even shorter pulses is XFEL (X Ray Free Electron Laser) but the size and cost of the installation needed are orders of magnitude larger.

First of all, to reach such ultra-short pulses, one needs a coherent source of radiation in a wavelength range corresponding to high energy photons in the extreme UV and X-ray domain. As a comparison, the ultimate pulse duration limit for the near-infrared is a few femtoseconds since it has to be larger than the optical cycle (2.6 fs for 800 nm and 1.5 eV photons). Second, a broad spectrum is required since the temporal envelope width is given by the Fourier transform of the spectrum if there is a coherent phase relation between all the spectral components: the broader the spectrum the narrower the pulse. For a given spectral width, the minimum duration is obtained when all the spectral components are in phase. On the contrary, if they are chirped, we will observe a temporal widening[17].

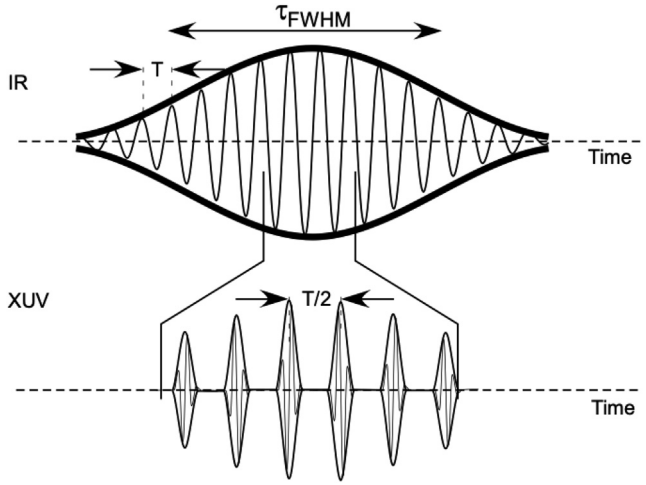

FIG. 6.14 – Temporal structure of harmonic emission as compared to the pump laser pulse (review document by Thierry Ruchon[18]).

If we come back to the process of HHG in the three-step model, we see from figure 6.14 that as compared to the pump laser, the harmonic emission occurs at precise times in the optical cycle, depending on the quantum path. Ionization occurs when the electric field of the laser is high enough to produce tunnel ionization. Then, for a given ionization time, the recombination time is fully determined, together with the kinetic energy gain. The time precision of harmonic emission is thus impressively high (in the 10 as range): this will be the origin of the harmonic spectral phase. If we consider the whole spectrum, harmonics are emitted as bursts whose duration is given by the temporal envelop of the spectrum: this occurs twice per optical cycle.

Sources of single attosecond pulses: We saw that HHG sources generally emit a train of attosecond bursts but for some specific applications it is desirable to have only one single attosecond pulse. Note that if this condition is fulfilled, the harmonic spectrum is no more harmonic since the harmonic structure comes from the periodicity of the phenomenon: in that case, the spectrum is a large continuum in the EUV. The

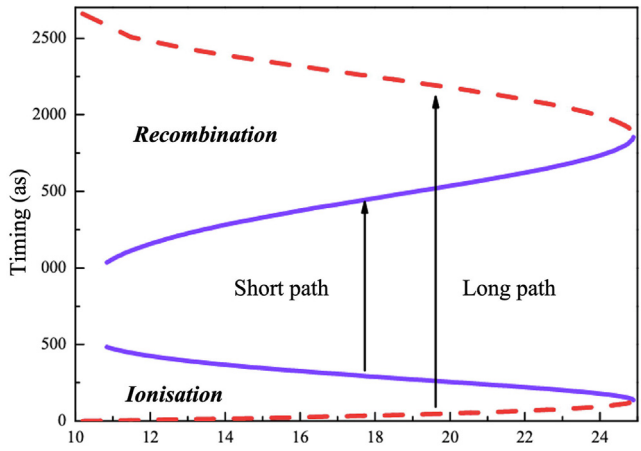

FIG. 6.15 – Ionization and recombination times as a function of the harmonic order for a generation in argon at 1.2 10^{14} W/cm^2, in blue the first quantum path, in red the second one, the cutoff is clearly visible (Ph.D. thesis of Yann Mairesse[17]).

general idea to generate a *single* attosecond pulse (SAP) is to make the 3-step generation process possible only once during the laser pulse. Two approaches have been explored: one either reduces sufficiently the duration of the laser pulse so that the first step (ionization) occurs only once or one tailors the laser pulse so that the electron is driven back only once to the core (step 2: excursion in the continuum). Both techniques do require ultra-short driving pulses (less than 10 fs, FWHM), and consequently, as shown in figure 6.16, the carrier-envelope phase (CEP) of the lasers should be controlled.

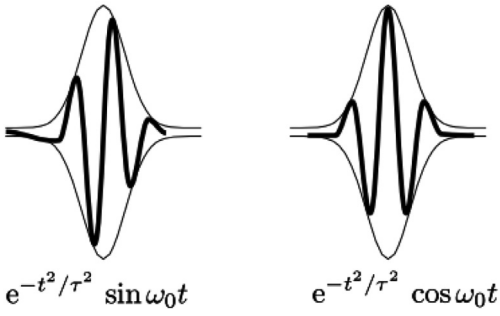

FIG. 6.16 – Two different pulses with the same pulse duration (FWHM) but different CEP.

The first demonstration of SAP was achieved using the first technique in Vienna in 2004 by Kienberger *et al.* They used 5 fs laser pulses with a 750 nm central wavelength, CEP stabilized, achieving 250 as SAP with 90 eV central energy.

Recently, the same group has improved their laser source making it as short as 3.3 fs. Using it, they could generate 80 as long pulses in Neon[20].

A slightly less demanding technique as for lasers, which still allows achieving single attosecond pulses, is to tailor the IR electric field so that electrons come back to the vicinity of the core only once during the IR pulse. Back in the early '90s, it was shown that HHG is more efficient using linearly compared to elliptically polarized lasers[19]. The idea proposed is thus to synthesize an IR field that would be circular at all times but with a short "temporal gate" during which it would be linearly polarized. An electron in the continuum driven by such a laser field, flies away from the core, except during the "polarization gate" *i.e.* when the field is linearly polarized. It was shown later that using a combination of quarter waveplates, one can synthesize such an electric field[22].

Using such a technique on a CEP stabilized 7 fs laser pulse in Milano, Sola *et al.*[23] obtained a continuous spectrum generating harmonics in argon. Moreover, varying the CEP, they could switch from a continuous spectrum to a modulated spectrum, as shown in figure 6.17, indicating that either one isolated or a double attosecond pulse could be achieved on demand. This radiation was further temporally characterized[24]. They obtained 130 as long pulses centered around 45 eV.

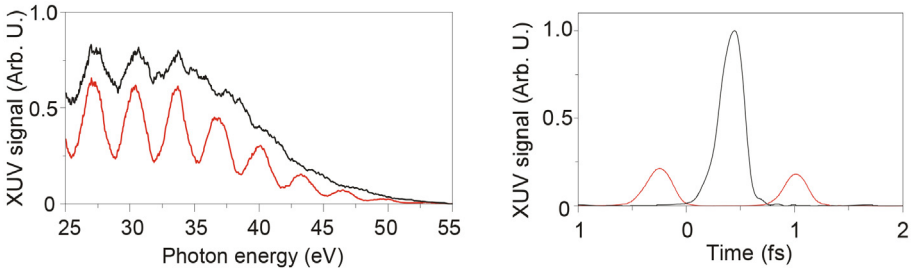

FIG. 6.17 – Effect of a change of the CEP on the spectrum (left panel) and corresponding temporal profile (right panel) for an attosecond source driven by a polarization gate field (from[23]).

The temporal characterization of short light pulses is usually carried out in the spectral domain, measuring, on the one hand, their spectral intensity and on the other hand, their spectral phase. As for the spectral intensity, well-known techniques are available in the XUV domain: one may either use a photon spectrometer (XUV grating in combination with a microchannel plate or XUV CCD camera) or an electron spectrometer (Time of Flight spectrometer, Magnetic bottle electron spectrometer, Velocity Map Imaging Spectrometer…) using a target gas having a well-known response. Measuring the spectral phase requires more advanced techniques. Indeed, the IR-visible range techniques (FROG, SPIDER, Autocorrelation…) are not directly transferable to the XUV domain for: (1) no beam splitter is available in this spectral range, (2) fluxes are too low to get two-photon transitions

over a broad spectrum and (3) nonlinear crystals are not available. It has been proposed to resort to photoionization in a two-color field, namely a XUV+IR cross-correlation, to implement an optical gating scheme. Several variants have been proposed. The most general one is called the FROG-CRAB technique[25]. It fully characterizes an arbitrary XUV temporal profile. In the case of a train of attosecond pulses, it simplifies into the RABBITT technique[16], which measures an average pulse in the train. In the following, we present the principle of this latter technique.

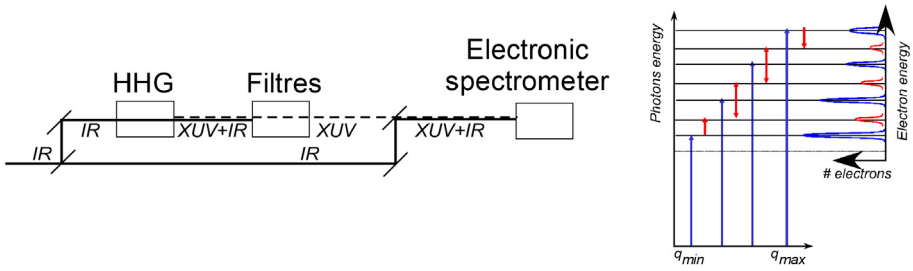

FIG. 6.18 – Principle of the RABBITT technique. (left) The laser IR beam is split into two parts: one used for HHG, the other for dressing. Filters are used to remove the remaining IR after HHG. (Right) Cartoon of the spectra obtained. Sidebands show up right in between odd harmonics electrons coming from XUV photoionization by the attosecond pulse (taken from a review paper by Thierry Ruchon[18]).

We consider an XUV attosecond pulse train spatially and temporally overlapping with an IR beam. They both enter an electron spectrometer filled with a gas whose transition matrix elements for XUV photoionization are well known. The gas can be ionized by single XUV photon absorption and the corresponding photoelectrons are recorded on the spectrometer: their energies correspond to harmonic photon energies minus atomic ionization potential (blue peaks in figure 6.18 also called odd peaks). In the presence of an IR dressing beam, for some adjustable delays, additional red peaks (called even peaks or sidebands) appear in between the others: they correspond to photoelectrons produced by the "simultaneous" absorption of a harmonic photon plus an infrared one (see figure 6.18). The same energy for the photoelectron can be obtained *via* the absorption of the consecutive harmonic order followed by the emission of an infrared photon.

It can be shown that the total yield of even harmonic electrons is then modulated with the IR/XUV delay τ, the phase of the oscillations being given by the phase difference between two consecutive harmonics:

$$2\omega\tau + \Psi_{q'+1} - \Psi_{q'-1}$$

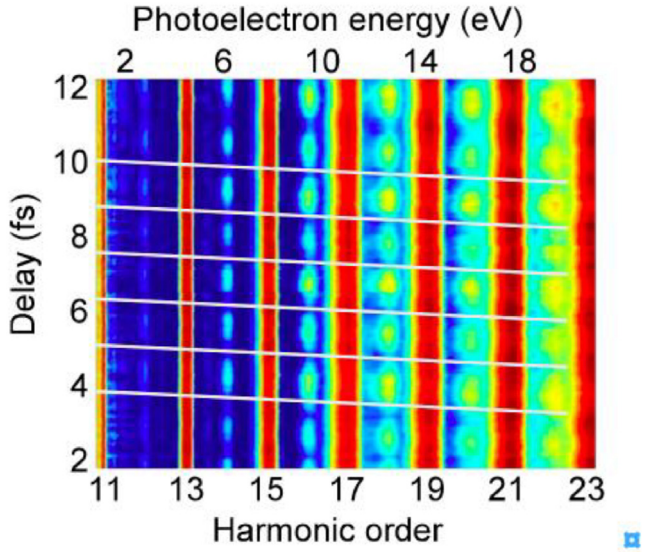

FIG. 6.19 – Example of a RABBITT trace taken in Ar for both the generating and detecting gas. The minima in the sidebands vs the delay drift from one sideband to the next signaling a lack of synchronization of the harmonics (superimposed white lines). This figure is taken from a review paper by Thierry Ruchon[18].

Figure 6.19 shows such a spectrum recorded for variable XUV-IR delays. The $2\omega\tau$ oscillation of the sidebands is clearly visible. Pointing to the phase of these oscillations, one gets the harmonic chirp of the attosecond pulses, also known as atto-chirp, which appears almost constant on this example (superimposed white lines).

This technique was (and is still) widely used by attophysics groups in the world for the measurement of the relative phase between consecutive harmonics, which enables the reconstruction of the temporal profile of the attosecond pulses in a train. This method assumes that all attosecond pulses in the train are identical, *i.e.* it provides a characterization of the average pulse profile. Measuring the full profile of the attosecond pulse train requires more advanced analysis, *e.g.* FROG-CRAB[25]. Note also that the measurement is averaged over multiple laser shots, and also over the spatial profile of the XUV beam, which can be problematic when aberrations do exist in the XUV beamline[26]. More recently, this kind of a method was used to measure how much time is needed for the single photoionization of an atom, whereas the photoelectric effect was considered instantaneous until the beginning of the century[27]. This is an example of how experimental progress in science changes the way we consider the world.

6.5 New Trends in HHG

In conclusion, this chapter gives a general view of the basic and general physics of HHG in gases as it was progressively elaborated in the '90s and beginning of 2000. Since then, intensive work was done to not only develop applications, especially in attophysics, but also to be able to generate HHG with more compact, higher repetition rate sources. In recent years, the fiber lasers based on Ytterbium amplifiers have made such progress with post compression devices that they can quite efficiently generate HHG at MHz repetition rate[28]. New promising developments are done with HHG from solid targets or HHG with doubled or tripled photon sources (see for example figure 6.20 taken from ref.[29] where the authors show the state of the art of HHG sources as a function of the repetition rate).

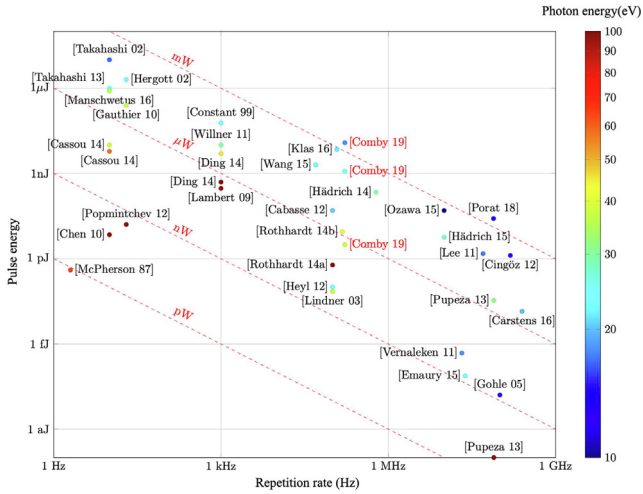

FIG. 6.20 – State of the art of high-order harmonic sources. The fundamental lasers used from 10 Hz to 1 kHz are Ti:Sa, from 100 kHz to 1 MHz are TDFA, and above 1 MHz are enhancement cavities. This figure is taken from Antoine Comby's thesis, 2019[29].

Some commercial companies in Europe and the US even propose such devices and researchers from other scientific communities can use HHG sources as turnkey black boxes for their experiments without knowing really how it works as I hope you do know now after this lecture. This is amazing to me if I remember the beginning of my thesis and this is a real achievement due to the active work of a whole community of researchers and engineers for thirty years.

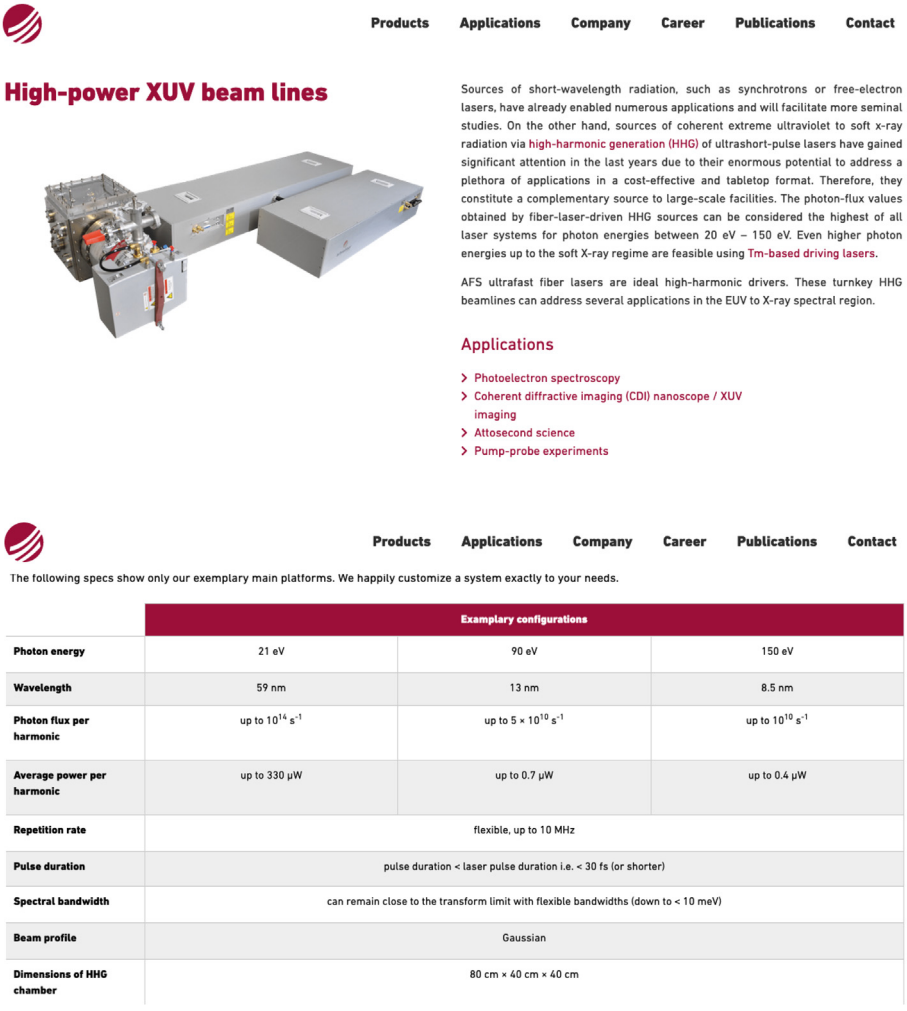

Products Applications Company Career Publications Contact

High-power XUV beam lines

Sources of short-wavelength radiation, such as synchrotrons or free-electron lasers, have already enabled numerous applications and will facilitate more seminal studies. On the other hand, sources of coherent extreme ultraviolet to soft x-ray radiation via high-harmonic generation (HHG) of ultrashort-pulse lasers have gained significant attention in the last years due to their enormous potential to address a plethora of applications in a cost-effective and tabletop format. Therefore, they constitute a complementary source to large-scale facilities. The photon-flux values obtained by fiber-laser-driven HHG sources can be considered the highest of all laser systems for photon energies between 20 eV – 150 eV. Even higher photon energies up to the soft X-ray regime are feasible using Tm-based driving lasers.

AFS ultrafast fiber lasers are ideal high-harmonic drivers. These turnkey HHG beamlines can address several applications in the EUV to X-ray spectral region.

Applications

- Photoelectron spectroscopy
- Coherent diffractive imaging (CDI) nanoscope / XUV imaging
- Attosecond science
- Pump-probe experiments

Products Applications Company Career Publications Contact

The following specs show only our exemplary main platforms. We happily customize a system exactly to your needs.

	Examplary configurations		
Photon energy	21 eV	90 eV	150 eV
Wavelength	59 nm	13 nm	8.5 nm
Photon flux per harmonic	up to 10^{14} s^{-1}	up to 5×10^{10} s^{-1}	up to 10^{10} s^{-1}
Average power per harmonic	up to 330 µW	up to 0.7 µW	up to 0.4 µW
Repetition rate	flexible, up to 10 MHz		
Pulse duration	pulse duration < laser pulse duration i.e. < 30 fs (or shorter)		
Spectral bandwidth	can remain close to the transform limit with flexible bandwidths (down to < 10 meV)		
Beam profile	Gaussian		
Dimensions of HHG chamber	80 cm × 40 cm × 40 cm		

FIG. 6.21 – A commercial HHG-beamline; adapted from the brochure of Active Fibers system, Jena, Germany.

References

[1] Franken P.A., Hill A.E., Peters C.W., Weinreich G. (1961) Generation of optical harmonics, *Phys. Rev. Lett.* **7**(4), 118.

[2] Maiman T.H. (1960) Optical and microwave-optical experiments in ruby, *Phys. Rev. Lett.* **4** (11), 564.

[3] Strickland D., Mourou G. (1985) Compression of amplified chirped optical pulses, *Opt. Commun.* **55**(6), 447.

[4] Wahlström C.G. *et al.* (1993) *Phys. Rev. A* **48**, 4709.
[5] Corkum P.B. *et al.* (1993) *Phys. Rev. Lett.* **71**, 1994.
[6] Popmintchev T. *et al.* (2012) *Science* **336**(6086), 1287.
[7] Lewenstein M. *et al.* (1994) *Phys. Rev. A* **49**, 2117.
[8] Lewenstein M. *et al.* (1995) *Phys. Rev. A* **52**, 4747.
[9] Balcou P. *et al.* (1999) *J. Phys. B* **32**, 2973.
[10] Balcou P. *et al.* (1997) *Phys. Rev. A* **55**, 3204.
[11] Constant E. *et al.* (1999) *Phys. Rev. Lett.* **82**, 1668.
[12] Kazamias S. *et al.* (2003) *Phys. Rev. Lett.* **90**(19), 193901.
[13] Kazamias S. *et al.* (2011) *Phys. Rev. A* **83**, 063405.
[14] Kazamias S. *et al.* (2002) *EPJD* **21**, 353.
[15] Comby A. *et al.* (2019) *Opt. Exp.* **27**(15), 20383.
[16] Paul P.M. (2001) *Science* **292**(5522), 1689.
[17] Mairesse Y. (2005) Génération et caractérisation d'impulsions attosecondes, PhD. https://tel.archives-ouvertes.fr/tel-00011620/document.
[18] Ruchon Th., Lecture in Optique de l'extrême, Institut d'Optique Graduate School.
[19] Muller H.G. (2002) Reconstruction of attosecond harmonic beating by interference of two-photon transitions, *Appl. Phys. B* **74**, 17.
[20] Goulielmakis E. (2008) *Science* **320**(5883), 1614.
[21] Budil K.S. (1993) *Phys. Rev. A* **48**, R3437.
[22] Tcherbakoff O. (2003) *Phys. Rev. A* **68**, 0438040.
[23] Sola I.J. *et al.* (2006) *Nat. Phys.* **2**, 319.
[24] Sansone G. (2006) *Science* **314**, 443.
[25] Quéré F. (2005) *J. Mod. Opt.* **52**, 339.
[26] Bourrassin Bouchet Ch. (2013) *Opt. Exp.* **21**, 2506.
[27] Dahlström J.M., L'Huillier A., Maquet A., https://arxiv.org/abs/1205.6624.
[28] Cabasse A. *et al.* (2012) *Opt. Lett.* **37**, 4618.
[29] Comby A. (2019) *Dynamiques ultrarapides de molécules chirales en phase gazeuse. Physique [physics].* Université de Bordeaux.
[30] Seres J. *et al.* (2010) *Nat. Phys.* **6**, 455.

Acknowledgements

It was an honor for me to prepare this lecture, thank you to the organizers. Part of this document was "directly inspired" by the PhD works of Sophie Kazamias, Sameh Daboussi, Fabrice Sanson, Yann Mairesse, Antoine Comby, and a review by Thierry Ruchon on attosecond science. I want to thank all the French community of HHG. I am proud to be one of them. I hope this work will help young researchers take an active part in the progress of this field of science. I want to warmly thank Kristal Bontemps and Alok Pandey for their help in editing equations and figures and correcting my English. Thank you also to the reviewers who helped increasing the quality of the document.

Bonus: The Lewenstein Model for Dummies

I wrote this document during my PhD preparation with the help of a manuscript notebook from Philippe Balcou, co-author of the famous paper. This is a detailed explanation of the calculus in the article by Lewenstein et al. (1994) Theory of high harmonic generation by low-frequency laser fields, Phys. Rev. A ***49****(3), 2117. I am convinced that this is important to make things as clear and simple as possible, I hope you will enjoy it.*

This article proposes an almost analytical way to calculate the harmonic single-atom dipole as the solution of the Schrödinger equation in the presence of a strong laser field.

(1) **Dipole formula:**
We consider a unique electron in a bound state of an atom in the presence of electric field $E\cos(t)$ of an intense laser. The polarization is linear along the x-axis. The Schrödinger equation for the electron wavefunction is (*):

$$i\hbar\frac{\partial|\Psi(t,x)\rangle}{\partial t}=\left(-\frac{1}{2}\nabla^2+V(x)-E\cos(t).x(t)\right)|\Psi(t,x)\rangle$$

The first term in the right-hand side of the above equation is the kinetic energy, the second one is the Coulomb potential of the nucleus, and the third one the laser potential through the dipolar electric term.
In the following, physical constants such as the laser pulsation, the electron mass, and charge, the Planck constant are set to one. The equations are no more homogeneous.

(a) **Approximation of validity domain**
The initial state of the atom is written $|0\rangle$, this is the one for which the electron is linked to the nucleus with bound energy equal to $-I_p$. We are in the conditions for which $I_p >> \hbar\omega$ which means that the number of infrared photons needed to be absorbed by the electron to reach ionization is very high (typically 10 for argon).
In the following $I_p << U_p$, where U_p is the ponderomotive energy:

$$U_p=\frac{e^2E^2}{4m\omega_{\text{laser}}^2}.$$

This allows us to neglect I_p, $V(x)$, $\nabla V(x)$. The formula for U_p can be found using the fact that it is the average kinetic energy acquired by an electron oscillating in the laser electric field over one laser cycle.

$$ma=qE\cos(\omega t)\rightarrow v=\frac{qE}{m\omega}\sin(\omega t)\rightarrow U_p=\frac{1}{T}\int\frac{1}{2}mv^2=\frac{e^2E^2}{4m\omega_{\text{laser}}^2}$$

Note that the above conditions correspond to a Keldysh parameter $\gamma<<1$ for which the Ammosov–Delone–Krainov (ADK) rates equations for

tunnel ionization are valid. We introduce U_{sat}, the so-called saturation intensity, for which the laser intensity is so high that the electron is surely ionized. For efficient HHG, the typical range for intensities is several 10^{13} W/cm^2 to 10^{15} W/cm^2.

(b) **Atomic dipole**

To solve the Schrödinger equation, we suppose the solution to be of the following form (**):

$$|\Psi(t,x)\rangle = e^{\frac{I_p t}{i\hbar}}\left(a(t)|0\rangle + \int d^3v\, b(v,t)|v\rangle\right)$$

This is a decomposition of the electronic wavefunction over the continuous base of the velocities. The initial state is:

$$a(t)\,|0\rangle$$

and

$$U_p \ll U_{\text{sat}} \Rightarrow a(t) \approx 1$$

This means that the second term is only a small perturbation to the initial state. The $b(v,\, t)$ terms are the decomposition of the electronic wavefunction as a function of velocity and time; $e^{\frac{iI_p t}{\hbar}}$ is the natural oscillation of a stationary state with energy $-I_p$.

After time derivation of equation (**), we substitute in (*) to obtain an equation for b by projection on a v state (***):

$$\frac{\partial b}{\partial t} = -i\left(\frac{v^2}{2} + I_p\right) b(v,t) - E\cos t \frac{\partial b}{\partial v_x} + iEa(t)\cos t d_x(v)$$

If we project on the $\langle 0|$ state, we obtain ($\omega = 1$)):

$$\dot{a} = iE\cos t \int d^3v d_x(v) b(v,t)$$

$$d_x(v) = \langle\, v|\, x\,|0\,\rangle$$

It is the dipolar matrix element for the bound->free transition.

$$\frac{\partial b}{\partial v_x} = -ixb$$

$$b(\vec{v},t) = \left(\frac{1}{2\pi}\right)^{\frac{3}{2}} \int e^{-i\vec{x}.\vec{v}} b(\vec{x},t)\, d^3\vec{x}$$

$$\left(-\frac{1}{2}\nabla^2 + V(x)\right)|0\rangle = -I_p|0\rangle$$

is the Schrödinger equation of the electron without the laser field. Integration of (***) explained in annex yields:

$$b(\vec{v},t) = i\int_0^t dt' E\cos t' d_x(\vec{v}+\vec{A}(t)-\vec{A}(t')) \cdot \exp\left(-i\int_{t'}^t dt''\left[I_p + \frac{\left(\vec{v}+\vec{A}(t)-\vec{A}(t'')\right)^2}{2}\right]\right)$$

The dipole is then given by:

$$x(t) = \langle \Psi(t)|x|\Psi(t)\rangle$$

Here it yields:

$$\left(a^*(t)\langle 0| + \int d^3v b^*(v,t)\langle v|\right)x\left(a(t)|0\rangle + \int d^3v b(v,t)|v\rangle\right)$$

In the development, we keep only the terms that do correspond to a dipolar transition between the bound state and the continuum:

$$x(t) = \int d^3v d_x^*(v) b(v,t) + c.c.$$

with $p = v + A$, and by introducing b into x, we obtain (****):

$$x(t) = i\int_0^t dt' \int d^3p E\cos t' d_x(p - A(t')) d_x^*(p - A(t)) \exp(-iS(p,t,t'))$$

$$S(p,t,t') = \int_{t'}^t dt''\left(I_p + \frac{(P - A(t''))^2}{2}\right)$$

(c) **The physical interpretation of the above formulas**
$x(t)$ is thus the integral of all probability amplitudes that do correspond to the several steps of HHG, and

$$E\cos t' d_x(p - A(t'))$$

is the probability amplitude of ionization by dipolar transition with a momentum p at a time t'. Then, the electron propagates in the continuum until the time t when recombination occurs. The integral is done over all the p and t' values.
There are thus 3 different times in the formulas:

(I) t' is the time of ionization.
(II) t is the time of recombination.
(III) $\tau = t - t'$ is the time spent in the continuum.

(2) **The saddle point method:**

(a) **Technical point:** Let us consider

$$I = \int_{-\infty}^{+\infty} f(x) e^{i\Phi(x)} dx$$

If x_0 is the x value for which the phase is stationary:

$$\left(\frac{\partial \Phi}{\partial x}\right) x_0 = 0.$$

The Taylor expansion around x_0 is:

$$\Phi(x) = \Phi(x_0) + \frac{1}{2}\left(\frac{\partial^2 \Phi}{\partial x^2}\right) x_0 (x - x_0)^2$$

In that case,

$$I = e^{i\Phi(x_0)} \int_{-\infty}^{+\infty} f(x) e^{\frac{i}{2}\left(\frac{\partial^2 \Phi}{\partial x^2}\right) x_0 (x - x_0)^2} dx$$

Then $f(x)$ is replaced by $f(x_0)$ since we consider that far from x_0, the $\cos^2$ function oscillates so fast that the contribution to the integral is zero. To put it differently, only the physical phenomena corresponding to

$$\frac{\partial \Phi}{\partial x} = 0$$

are relevant to I. Finally, we obtain:

$$I = e^{i\Phi(x_0)} f(x_0) \int_{-\infty}^{+\infty} e^{\frac{i}{2}\left(\frac{\partial^2 \Phi}{\partial x^2}\right)_{x_0} (x - x_0)^2} dx$$

$$I = e^{i\Phi(x_0)} f(x_0) \sqrt{\frac{\pi}{\frac{i}{2}\left(\frac{\partial^2 \Phi}{\partial x^2}\right)_{x_0}}}$$

(b) **Stationary phase condition for the dipole:**
We now concentrate on $x(t)$ as defined by (****) and we try to integrate on d^3p. The stationary phase condition is written as:

$$\vec{\nabla}_p S(\vec{p}, t, t') = 0 = x(t) - x(t')$$

This relation comes from the Lagrangian equation:

$$S(\vec{p}, t, t') = \int_{t'}^{t} L(t'')dt''$$

and

$$\frac{\partial L}{\partial p} = \dot{x}$$

Physically, this means that the predominant trajectory is the one that recombines at the same place where it enters the continuum and it must be close to the nucleus since it is related to the initial bound state.
Considering

$$\left(\frac{\partial^2 S(p, t, t')}{\partial p^2}\right)_{\text{st}} = \frac{\partial}{\partial p}(x(t) - x(t')) = t - t' = \tau$$

we obtain:

$$x(t) = i\int_0^\infty d\tau \left(\frac{\pi}{\epsilon + i\frac{\tau}{2}}\right)^{\frac{3}{2}} d_x^*(p_{\text{st}}(t,\tau) - A(t))d_x(p_{\text{st}}(t,\tau) - A(t-\tau))E\cos(t-\tau)\exp(-iS_{\text{st}}(t,\tau)) + c.c.$$

- The 3/2 coefficient comes from the fact that the trajectory is in 3D.
- The variable change $\tau = t - t'$ was done.
- The ε term has no physical meaning; it is introduced mathematically to ensure the convergence of the integral.

The condition $x(t) = x(t-\tau) = 0$ allows to calculate p_{st} using classical mechanics with $E\cos t$ as the laser electric field:

$$p_{\text{st}}(t,\tau) = \frac{E}{\tau}[\cos(t) - \cos(t-\tau)]$$

Then S_{st} can be calculated using $A(t) = -E\sin(t)$:

$$S_{\mathrm{st}}(t,\tau) = \int_{t-\tau}^{t} dt'' \frac{(p_{\mathrm{st}} - A(t''))^2}{2} + I_p$$

With the following trigonometric identities,

$$\cos p - \cos q = -2\sin\frac{p+q}{2}\sin\frac{p-q}{2},$$

$$\sin(a-b) = \sin a\cos b - \sin b\cos a$$

$$et\ \sin^2\ a = \frac{1-\cos 2a}{2}$$

and by clearly separating the dependence with t from the rest of the equation, we obtain:

$$S_{\mathrm{st}}(t,\tau) = \big(I_p + U_p\big)\tau - \frac{2U_p}{\tau}(1-\cos\tau) - U_p C(\tau)\cos(2t-\tau)$$

$$C(\tau) = \sin(\tau) - 4\frac{\sin^2\left(\frac{\tau}{2}\right)}{\tau}$$

(c) **The physical interpretation of some relevant terms:**

The term $\frac{\pi}{\varepsilon + i\frac{\gamma}{2}}$ indicates that $x(t)$ decreases with the time spent in the continuum. The origin of this is due to the wavefunction spreading when the electron spends time far from the nucleus; this scales linearly with time. At the time of recombination, if the spatial size of the electron wavefunction is too large, the scalar product with the initial state will be geometrically lower. This explains also why electron trajectories longer than one optical cycle are not favorable for HHG.
If we neglect I_p as regards to U_p, the stationary phase technique can be applied to the integration over τ and $\frac{\partial S}{\partial \tau} = 0$ is equivalent to:

$$\frac{\partial}{\partial\tau}\int_{t-\tau}^{t} dt''(p_{\mathrm{st}}(t,\tau) - A(t''))^2 = 0$$

$$\int_{t-\tau}^{t} dt'' \frac{\partial}{\partial\tau}(p_{\mathrm{st}}(t,\tau) - A(t''))^2 + (p_{\mathrm{st}}(t,\tau) - A(t-\tau))^2 = 0$$

When integrating, the first term is equal to zero and the second term leads to the condition:

$$v(t-\tau) = p_{\mathrm{st}}(t,\tau) - A(t-\tau) = 0$$

This shows that the dominant trajectories are those for which the initial kinetic energy when the electron is ionized in the continuum is zero. This corresponds to the hypothesis of the three-step model and the properties of tunnel ionization.
Note that if I_p is not neglected, the condition becomes:

$$\frac{\partial S}{\partial \tau} = \frac{[p - A(t-\tau)]^2}{2} + I_p = 0$$

Considering that I_p is positive implies negative kinetic energy at the time of ionization: this is a characteristic of the tunnel effect.

(3) **Spectral analysis:**

(a) The harmonic spectrum will be given by the Fourier transform of $x(t)$. If we only concentrate on the odd harmonics with photon energies equal to $E = (2M+1)\hbar\omega$, the dipole amplitude in the frequency domain for this harmonic is: $x^*_{2M+1} = \int_0^{2\pi} x(t)\, e^{i(2M+1)t} dt$.
With the stationary phase approach, the most important term in this equation is the one for which the phase derivative is zero. This means

$$\frac{\left(p_{\mathrm{st}}(t-\tau) - A(t)\right)^2}{2} + I_p = 2M+1$$

which is simply the energy conservation for the harmonic photon: ionization potential plus kinetic energy gain in the continuum. We see that the intuition of the three-step model is confirmed.

(b) The cutoff law which is the maximum harmonic order reachable for a given gas target and given laser intensity can be obtained in this frame by calculating τ for which $\frac{\partial S}{\partial \tau} = 0$. The solution is 4.18 and corresponds to the cutoff law in the three-step model: the maximum kinetic energy gain is 3.17 U_p whatever the gas.

(4) **Influence of some physical parameters:**

(a) Atomic potential: In the SFA model, the exact shape (especially spatially speaking) of the atomic potential is not taken into account since the bound state is only described by I_p. Resonance effects with higher level bound states can be described using TDSE approaches and explain for example the existence of Cooper minimum and the generation of circularly polarized harmonic radiation. The Lewenstein model is too simple to describe them.

(b) Electron rescattering: This effect of electron rescattering on the nucleus is not taken into account in the model since the term $v'|x|v$ is neglected very early in the calculation. This assumption is relevant since there is almost no difference in the calculation when comparing the integration of S from $\tau = 0 \text{ to } 2\pi$ to $\tau = 0 \text{ to } \infty$. The electron wave-packet spreading is at the origin of this phenomenon.

(c) Pump laser wavelength: In the race towards short harmonic wavelengths, the fact that U_p is scaling with λ^2 together with the cutoff law shows that long wavelengths for the pump laser are appropriate to generate short harmonic wavelengths, *i.e.* to allow a given harmonic to be in the plateau region.

Besides, if a given harmonic photon energy is in the plateau for two different kinds of pump wavelengths, the shorter the pump wavelength, the higher the harmonic dipole energy. This effect was predicted by Lewenstein in 1994–95: he predicted theoretically that doubling the pump laser frequency could increase the single-atom response for a given harmonic by a factor of 10–100. The explanation for this comes first from the efficiency of the ionization step, and then the fact that for shorter pump wavelength, the electron wave-packet spreading in the continuum is reduced. We can also add that phase matching issues not taken into account in the atomic model are also favorable to short pump wavelengths since the electronic dispersion term is reduced (a factor four for doubling the pump laser in frequency). Many experimental investigations did confirm it afterward (for example Comby *et al.* recently).

(d) Depletion of the fundamental bound state: In the previous calculations we considered that $a(t) = 1$ all over the pump laser pulse duration. This means that the "amount of electron being in the continuum" is considered always negligible as compared to the part of the wavefunction that corresponds to the atomic fundamental bound state. In reality, if the laser intensity is high enough, we know that the ionization rate becomes important and even surely close to unity if the intensity reaches the barrier suppression value. To take this effect into account, we should consider the time variation of $a(t)$ as a function of the number of optical cycles in the laser pulse. On the contrary, the Lewenstein model does not take into account the laser pulse duration, nor the shape of the temporal envelope: E is considered constant all over the pulse.

It is of course better to take this effect into account with TDSE calculations, but an improvement in the analytical formulas can be proposed using:

$$\dot{b} = -i\left(\frac{v^2}{2} + I_p\right) b(v,t) - E\cos t \frac{\partial b}{\partial v_x} + iEa(t)\cos t d_x(v)$$

$$\dot{a} = iE\cos t \int d^3v d_x(v) b(v,t)$$

$$\dot{a}(t) = -\gamma(t)a(t)$$

$$\gamma(t) = \int d^3p \int_0^{\text{infty}} d\tau E\cos t d_x(p - A(t))E\cos(t-\tau)d_x(p - A(t-\tau))e^{iS(p,t,\tau)}$$

$\gamma(t)$ can be a complex number: its real part is a kind of depletion rate for the fundamental, similar to the ADK rates, whereas its imaginary part corresponds to an energy shift of the fundamental.
Implementing this in the calculation of the harmonic spectrum leads to the same cutoff law, but a gradual decrease in the global efficiency for the plateau region. To avoid this effect, for the same maximum intensity, if the pulse duration is shorter, the ionization of the atom will be smaller, and its instantaneous harmonic response will be larger.

Chapter 7

Ultra-Intense Laser Pulses and the High Power Laser System at Extreme Light Infrastructure – Nuclear Physics

Daniel Ursescu*

National Institute for Physics and Nuclear Engineering, Extreme Light Infrastructure – Nuclear Physics Reactorului 30, 077125, Magurele, Ilfov, Romania

Physics Department Doctoral School, Bucharest University, Bucharest, Romania

Lasers make possible the production and ultimate control of electromagnetic fields in terms of spectral purity, spatial confinement down to the micrometer scale, pulse duration down to a single cycle in the femtosecond domain or shorter and electromagnetic field strengths, corresponding to the highest intensities achieved by mankind in the laboratory. Ultra-intense laser facilities are pushing the limits of the achievable pulse intensity, hence the coined term of "extreme light". They make possible fundamental and applied investigations in physics and material science with emergent societal impact. Extreme Light Infrastructure is the most advanced project dedicated to the production and use of such extreme fields.

The Extreme Light Infrastructure project will be outlined, with emphasis on the extreme light capabilities of its three facilities in Czech Republic, Hungary and Romania. The architecture of the first finalized 10 PW high power laser system (HPLS) will be highlighted. This dual arm, 10 PW each, laser system, at Extreme Light Infrastructure Nuclear Physics (ELI-NP), in Romania, delivers beams to five experimental areas that address research centered on nuclear physics, materials in extreme environments and exotic physics.

*daniel.ursescu@eli-np.ro

DOI: 10.1051/978-2-7598-2719-0.c007

7.1 Introduction

These lecture notes were written for the FEMTO UP School 2020, which took place in 2021 in an on-line form instead of at Strasbourg, France, due to the COVID19 pandemic.

The present manuscript aimed to introduce the reader to the field of ultra-intense laser pulses and to the machines and technologies used to produce them. To begin, it is essential to place the laser beam in the broader context of fundamental forces in physics and to provide a quick introduction to the concept of laser beam and laser pulse, without going in depth. The specification of the geometry and time distribution in highly intense laser beams is essential for the description of the laser-driven experiments, for the simulations of the laser-matter interaction processes and for the metrology of the laser pulses. The Gaussian laser pulses described here are a simplified model of the reality. However, they are widely used as reference in ultra-intense laser pulses research field because the scientists in the field need to share a unique definition of the object under study to be able to compare results from one team to another. The spatial and temporal extensions of ultrashort pulses vary orders of magnitude. As an example, the 10 PW pulses from ELI-NP have an aperture of approximately 50 cm after compression and should reach 4 μm in the focal spot, while the initial pulse duration from the laser oscillator is 6 fs and reaches 1 ns after the temporal stretching of the pulse, in the final laser amplifier, before compression. Also, the real-life pulses often present deviations from the ideal Gaussian pulses taken as a model reference. The unwanted temporal and spatial distortions might generate deleterious hot spots that affect the experimental conditions and harm the laser components, so they are carefully measured and suppressed. However, such deviations are sometimes introduced with the purpose of enhancing the experiment results.

The second part of the presentation will concentrate on the description of the most powerful laser system that operates to date, namely the High Power Laser System (HPLS) at Extreme Light Infrastructure – Nuclear Physics.

The third part will present the international context and technological developments related to the high power laser systems, highlighting concerted efforts of developments worldwide and in particular the Extreme Light Infrastructure pan-European project.

7.2 From Fundamental Forces to the Technology for Producing the Highest Intensities

7.2.1 Laser Beam and Laser Pulse

Out of the four fundamental interaction types, the electromagnetic type is the easiest one to control. This is reflected not only in the myriad of devices and the ubiquitous power plug but also through the applications based on mastering light,

from spectroscopic investigations of chemicals to laser eye surgery. The detailed behavior in space and time of the electromagnetic field is described through the microscopic Maxwell equations which connect the electric ($\boldsymbol{E}(\boldsymbol{r}, t)$) and magnetic ($\boldsymbol{B}(\boldsymbol{r}, t)$) fields to the electrical current density ($\boldsymbol{J}(\boldsymbol{r}, t)$) and charge density ($\rho(\boldsymbol{r}, t)$):

$$\nabla \cdot \boldsymbol{E}(\boldsymbol{r}, t) = \frac{\rho(\boldsymbol{r}, t)}{\epsilon_0} \tag{7.1}$$

$$\nabla \cdot \boldsymbol{B}(\boldsymbol{r}, t) = 0 \tag{7.2}$$

$$\nabla \times \boldsymbol{E}(\boldsymbol{r}, t) = -\frac{\partial \boldsymbol{B}(\boldsymbol{r}, t)}{\partial t} \tag{7.3}$$

$$\nabla \times \boldsymbol{B}(\boldsymbol{r}, t) = \mu_0 \boldsymbol{J}(\boldsymbol{r}, t) + \mu_0 \epsilon_0 \frac{\partial \boldsymbol{E}(\boldsymbol{r}, t)}{\partial t} \tag{7.4}$$

where ϵ_0 and μ_0 are the electric and magnetic constants of the vacuum, also known as electrical permittivity and magnetic permeability of free space.

In the absence of the electric charges and currents, one can deduce the electromagnetic wave equations starting from Maxwell's equations. They read:

$$\frac{\partial^2 \boldsymbol{E}(\boldsymbol{r}, t)}{\partial t^2} - c_0^2 \nabla^2 \cdot \boldsymbol{E}(\boldsymbol{r}, t) = 0 \tag{7.5}$$

$$\frac{\partial^2 \boldsymbol{B}(\boldsymbol{r}, t)}{\partial t^2} - c_0^2 \nabla^2 \cdot \boldsymbol{B}(\boldsymbol{r}, t) = 0 \tag{7.6}$$

where c_0 is the speed of light and the relation $c_0^2 = \epsilon_0 \mu_0$ holds. These equations describe the behavior of arbitrary electromagnetic fields across the entire spectra of frequencies. The equations accept as a solution the harmonic function, expressing a plane wave (pw):

$$\boldsymbol{E}_{\mathrm{pw}}(\boldsymbol{r}, t, \hat{k}, v) = \boldsymbol{E}_{\mathrm{pw0}} \cos(2\pi v t - 2\pi \frac{v}{c} \hat{k} \cdot \boldsymbol{r}) \tag{7.7}$$

with v the frequency of the field and $\hat{k}$ a unit vector. For $\boldsymbol{B}_{\mathrm{pw}}$ the form is similar, as equations (7.5) and (7.6) have the same form. It can be shown that the sum of two particular fields that are solutions for the wave equation is also a solution for the wave equation. As a consequence, the plane wave is widely used in the description of electromagnetic phenomena and there is a widely used mathematical approach to handle it, namely the Fourier transform, which can be understood as a summation of plane waves over the entire range of frequencies and directions:

$$\boldsymbol{E}(\boldsymbol{r}, t) = \int \boldsymbol{E}_{\mathrm{pw}} dv d\hat{k} \tag{7.8}$$

One peculiarity of these wave fields is that they correspond to orthogonal $\boldsymbol{E}$ and $\boldsymbol{B}$ vector fields that oscillate in phase. The propagation direction of the wave is defined through the vector, which is locally orthogonal to both electric and magnetic fields. It can be shown from Maxwell's equations that this direction corresponds to the $\hat{k}$ and the following relation holds:

$$\boldsymbol{B} = \frac{\boldsymbol{k}}{\omega} \times \boldsymbol{E} \tag{7.9}$$

Before proceeding, it is important to note that one can replace the sine function that we get in the plane wave through a combination of complex exponential functions, thanks to the mathematical identities:

$$\cos x = \frac{e^{ix} + e^{-ix}}{2} = \frac{1}{2}(e^{ix} + \overline{e^{ix}}) \tag{7.10}$$

where $\overline{e^{ix}}$ represents the complex conjugate term of e^{ix}. Often, this complex conjugate terms are not explicitly included in calculations, as the math is similar for the complex conjugate part. Then the field of equations (7.7) and (7.8) are written in the form:

$$\boldsymbol{E}_{\mathrm{pw}}(\boldsymbol{r}, t) = \boldsymbol{E}_{\mathrm{pw0}}\, e^{i(\boldsymbol{k}\cdot\boldsymbol{r} - \omega t)} \tag{7.11}$$

and

$$\boldsymbol{E}(\boldsymbol{r}, t) = \int \boldsymbol{E}_{\mathrm{pw0}}\, e^{i(\boldsymbol{k}\cdot\boldsymbol{r} - \omega t)}\, d\boldsymbol{k} \tag{7.12}$$

The plane wave description of the electromagnetic fields has the drawback that it uses functions that are oscillating at infinity with finite amplitudes. Such a single pure plane wave cannot be achieved in practice. Hence, in order to describe electromagnetic fields produced in the laboratory, *i.e.* that are localized in space, one has to sum up an infinite number of plane waves so as to suppress the resulting field beyond a finite distance in order to obtain a localized wave packet.

An alternative to the plane wave solution of equation (7.11) is to use the Gaussian beam approximate solution (see for example chapters 16–19 of reference[1] detailed description of the derivation and mathematical properties). The starting point is the separation of the spatial and temporal parts in the wave equation, assuming a well defined frequency of the light oscillations and a linear polarization for the electric field in order to reduce the equation to a scalar equation for one component:

$$E(\boldsymbol{r}, t) = u(\boldsymbol{r})\, T(t) \tag{7.13}$$

Replacing the result in the wave equation for the electric field 7.5, one can separate the equation into two parts, one depending only on the space coordinate $\boldsymbol{r}$ and the other involving only the temporal coordinate. In this way, one can extract the differential equation for the spatial part of the electric field as:

$$\nabla^2 u(\boldsymbol{r}) + k^2 u(\boldsymbol{r}) = 0, \tag{7.14}$$

while the temporal part is described by:

$$\frac{d^2T(t)}{dt^2} + c^2k^2T(t) = 0. \tag{7.15}$$

In addition, one is interested in a solution associated with the propagation direction through the $\hat{k}$ unit vector, which is chosen to be along the z axis of the orthogonal reference system without losing the generality of the result. An approximate solution of this spatial part of the electric field $u(\boldsymbol{r})$ in cylindrical coordinates is then given by the following formula:

$$u(\boldsymbol{r}) = u(r,z) = u_0 \quad \frac{w_0}{w(z)} \exp\left(\frac{-r^2}{w(z)^2}\right) \exp\left[-i\left(kz + k\frac{r^2}{2R(z)} - \psi(z)\right)\right], \tag{7.16}$$

where

$$w(z) = w_0\sqrt{1+\left(\frac{z}{z_R}\right)^2}, \tag{7.17}$$

$$R(z) = z\left[1+\left(\frac{z}{z_R}\right)^2\right], \tag{7.18}$$

$$\psi(z) = \arctan\left(\frac{z}{z_R}\right), \tag{7.19}$$

with

$$z_R = \frac{\pi w_0^2 v}{c} \tag{7.20}$$

This solution has the advantage of being localized in space on two directions (x and y axes, by convention) and to form a Gaussian beam when the temporal part is included using the result of equation (7.15). It is important to note that this is an approximate solution for Maxwell's equations, as an approximation to equation (7.14) was used. Exact analytical solution close to the Gaussian beam form exists[2–4] in the form of an infinite Taylor series, whose lowest order corresponds to the Gaussian beam.

For Gaussian laser beams, there are some basic rules concerning the relation between their divergence and their waist of the beam, w_0,

$$w_0 = \frac{c}{\pi\theta v} \tag{7.21}$$

where θ is the beam's half divergence in the far field.

The *f*-number is introduced through the relation $f\# = F/D$ where D corresponds to collimated Gaussian beam diameter measured at an amplitude equal to $1/e$ from the maximum amplitude, and F represents the focal distance of the focusing

element. Then one can connect the f-number of a focusing component to the achievable waist w_0, using the known approximation for small angle θ expressed in radian:

$$\theta \approx \tan(\theta) = \frac{D}{2F} = \frac{1}{2f\#} \tag{7.22}$$

In practice, there is no infinite laser beam available and, moreover, we are interested in short laser pulses, in the range from a few to a few hundreds of cycles. The description of such a pulse can be achieved by summing up Gaussian beams with different frequencies. When the beams are in phase at a well defined point in space and time, the superposition of the beams with various wavelengths will lead to constructive addition of the electric field in a limited region in space and also in time. The result can come close to a Gaussian beam modulated in time with a Gaussian envelope when the amplitudes and phases of the beams are carefully chosen:

$$E(\boldsymbol{r}, t) = u(\boldsymbol{r}) \exp\left[-\left(\frac{z - ct}{c\tau}\right)^2\right] \cdot \exp(i\omega t) \tag{7.23}$$

The real part of the temporal terms in the electric field description from equation (7.23) is depicted in figure 7.1. The phase information is included in the oscillations of the field amplitude while the Gaussian envelope shows the overall pulse shape.

Most of the articles describe the output of the ultrafast laser emission in terms of Gaussian pulses. Some of the properties are defined through comparison with an ideal pulse, often considered to be Gaussian in shape, for simplicity.

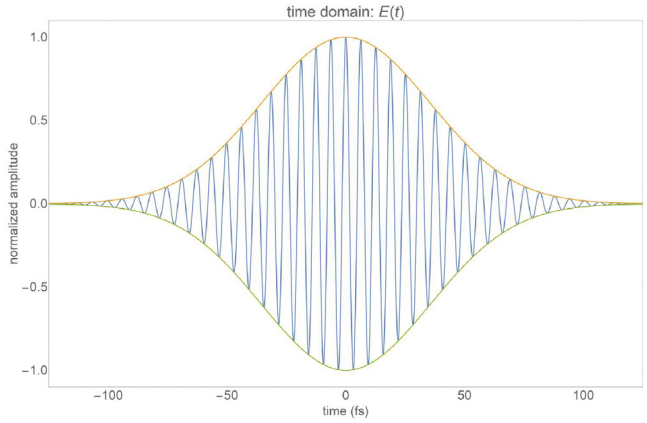

FIG. 7.1 – Illustration of a temporal evolution of the field in a Gaussian pulse, corresponding to the temporal part of equation (7.23).

7.2.2 Why Does Intensity Matter?

The optical intensity of the electromagnetic field, in vacuum, is then defined by the cycle-averaged modulus of the Poynting vector $\boldsymbol{S}$:

$$I = |\boldsymbol{S}| = c^2 \epsilon_0 |\boldsymbol{E} \times \boldsymbol{B}| = \frac{1}{2} c \epsilon_0 |\boldsymbol{E}|^2 \tag{7.24}$$

where equation (7.9) was used. The intensity has units of Watt/meter^2. It corresponds to the electric field energy density multiplied with the speed of light, and corresponds to the transmitted optical power per unit area through an imaginary surface placed perpendicular to the propagation direction $\boldsymbol{k}$ of the electromagnetic field. Optical intensity has the advantage that it can be determined experimentally through measurements of the pulse energy, duration and diameter.

For a Gaussian beam having the optical power P and beam waist w, one can compute the peak intensity using the relation:

$$I = \frac{2P}{\pi w^2} \tag{7.25}$$

The peak power of a rectangular pulse in time can then be computed as the ratio between the measured energy of the pulse and its duration (considered to be the full width at half maximum (FWHM) of the energy envelope). To obtain the peak intensity for a Gaussian temporal pulse, one may then multiply by a correction factor of 0.939:

$$I_G = 0.939 I \tag{7.26}$$

To visualize the need of this correction factor, the energy envelope for a rectangular pulse of width t_0 and a Gaussian pulse of duration t_0 FWHM, having the same integrated energy in time, is represented in figure 7.2. The peak amplitude of the Gaussian envelope reaches only 0.939 from the maximum amplitude of the rectangular pulse.

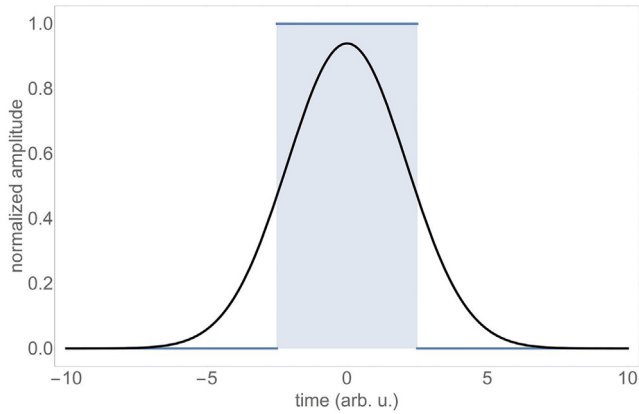

FIG. 7.2 – Comparison of a Gaussian pulse against a rectangular pulse with the same full width at half maximum and with the same area under the curve, corresponding to the same total enclosed energy.

To illustrate the achievable peak intensities, figure 7.3 depicts the iso-contours for peak powers of 100 TW, 1 PW and 10 PW in a plot displaying the peak intensity on the vertical axis. The stars indicate the previously demonstrated highest intensities[5,6], reaching $5.5 \cdot 10^{22} \frac{\mathrm{W}}{\mathrm{cm}^2}$. Please note that optical components with *f#* of the order of unity are extremely costly and difficult to produce for large aperture beams.

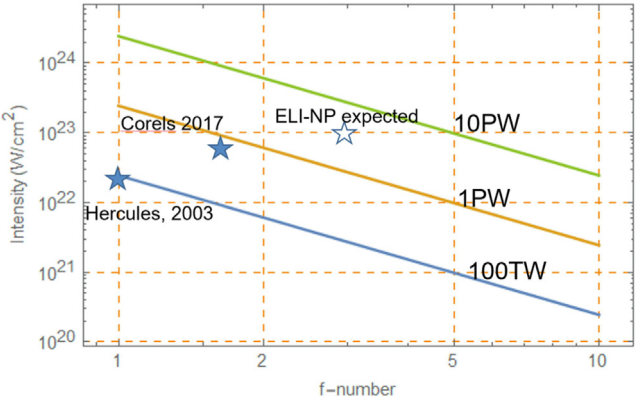

FIG. 7.3 – The achievable intensity in reach with 100 TW, 1 PW and 10 PW ideal Gaussian pulses. The stars correspond to measurements at Hercules laser reported in 2008 and at CoReLS laser reported in 2019.

With these details and with equations (7.9) and (7.24) in mind, several practical evaluations of the electric and magnetic fields can be made[7,8]. The electric field associated with the intensity of the pulse is given by the formula:

$$E[\mathrm{V/cm}] = 27.5 \times \sqrt{I[\mathrm{W/cm}^2]} \tag{7.27}$$

while the magnetic field can be described with a similar relation, depending only on intensity:

$$B[\mathrm{Gauss}] = 9.2 \times 10^{-2} \sqrt{I[\mathrm{W/cm}^2]} \tag{7.28}$$

The magnetic field produced with intensities of the order $10^{22} \frac{\mathrm{W}}{\mathrm{cm}^2}$[5,6] are the largest ever produced in controlled manner. The associated magnetic field of such laser pulses reaches 9.2 GGauss or 920 kT. In comparison, the magnetic field generated in a laboratory was 1.2 kT[9] while that produced in plasma with the help of a laser of almost $10^{20} \frac{\mathrm{W}}{\mathrm{cm}^2}$ intensity was 34 kT[10].

One can also compute the associated light pressure[7] for a given laser pulse intensity as:

$$p[\mathrm{bar}] = 3.3 \times 10^{-2} I[\mathrm{W/cm}^2](1 + R) \tag{7.29}$$

where R is the surface reflectivity. A pressure similar to the one in diamond anvil cells can be achieved with intensities of the order of $10^{16}\,\frac{\mathrm{W}}{\mathrm{cm}^2}$, an intensity several orders of magnitude below the achievable intensities in modern ultra-intense lasers. Notice that, unlike electric or magnetic fields in laser pulses, the light pressure scales linearly with the intensity.

From the above comparisons, it is obvious that such magnetic fields and pressures are above what is currently achievable in other controlled experimental conditions. When comparing electrical fields with the ones that can be observed in the laboratory, this is no longer the case. The electric fields that can be obtained with ultra-intense laser pulses are smaller than electric fields that are associated with the electrostatic (Coulomb) forces in the inner shells of the atoms. This is due to the fact that the Coulomb force has a proportionality with $1/r^2$ hence it is singular (infinite) in the origin. Regions with much higher fields do exist close to the nucleus of the atoms. For example, the expression of the Bohr radius associated with H-like atoms is given by:

$$r_{Bn} = 0.529\text{Å} \cdot \frac{n^2}{Z} \tag{7.30}$$

where Z is the number of protons in nucleus and n the principal quantum number. Hence the electric field at that orbiting distance reaches

$$E_{rBn} = \frac{1}{4\pi\epsilon_0}\frac{Ze^2}{r_{Bn}^2} \sim Z^3 \tag{7.31}$$

However, the electric field associated with ultra-intense laser pulses is strong enough to suppress the Coulomb forces for the outer bound electrons in atoms, for up to 10 electrons, inducing multiple direct field ionization. This process can take place in the volume of the focal spot region, which is huge when compared with the volume of an atom. The volume of the focal region where the intensity is significant to induce multiple direct ionization, exceeding several cubic micrometers, can contain more than 10^9 atoms.

Another practical assessment of the electric field strength is to compare the energy gained by an electron in the electric field with the rest mass energy of the electron $m_e c^2$. This defines the so-called normalized vector potential $\boldsymbol{a}$. This dimensionless parameter equals one when the energy gained by the electron placed in the laser field is equal to the rest mass hence a relativistic treatment of the electron dynamics is mandatory. The a parameter depends not only on the intensity of the pulse, but also on the wavelength of the field, according to the formula:

$$a = 0.86 \cdot 10^{-9}\lambda[\mu\mathrm{m}] \times \sqrt{I[\mathrm{W/cm}^2]} \tag{7.32}$$

For intensities larger than $10^{18}\,\frac{\mathrm{W}}{\mathrm{cm}^2}$ and wavelengths of 1 μm, we find that $a \approx 1$.

Of course, these evaluations correspond to transient electromagnetic fields and pressures over extremely short time scales, of the order of the laser pulse duration, typically in the femtosecond range.

7.2.3 Temporal Contrast

The real shape of the laser pulses is not perfectly Gaussian in time. Often, the pulse is accompanied by pre-pulses, post-pulses or a pedestal of light (background light) at an intensity level several orders of magnitude lower than the peak intensity. Even in such cases, the background light can produce significant damage to the target, often transforming it to a plasma before the main pulse arrives.

The three typical sources of background light are the longitudinal amplified spontaneous emission in the amplifiers, multiple reflections on the surfaces of optical components that operate in reflection and also the light scattering from the diffraction gratings used in optical stretchers or compressors[11].

The methods that are implemented to enhance the temporal contrast of the pulses include the use of the polarization rotation in a nonlinear crystal with third order non-linearity[12,13]. The crystal is placed between two crossed polarizers, hence the name of cross polarized wave (XPW) generation. Only the light field generated through the non-linear process with the appropriate polarization is further amplified. The XPW is the temporal domain analogue of the optical spatial filter.

A complementary method for temporal contrast enhancement is related to the use in the laser amplifiers of optical parametric amplification process instead of using laser active media with population inversion and storage of the energy[14]. The seed pulse is amplified through energy transfer from a laser pump pulse, mediated by a non-linear crystal. The specific advantage in this case is given by the fact that there is no amplified spontaneous emission outside the time interval defined by the pump pulse duration.

A third approach to enhance the temporal contrast of the pulse a few picoseconds before the arrival of a main laser pulse is with the help of plasma mirror[15,16]. This can be understood as an ultrafast reflectvity switch. The intense laser pulses reaching the optical surface of the transparent material can generate, when high intensities (typically above 10^{14} W/cm^2) are used, a plasma that behaves as a mirror. All the prepulses at lower intensities pass through the transparent material while the high intensity part of the pulse is reflected to be used for experiments. The temporal contrast of the laser pulse can be enhanced by about two orders of magnitude in this way.

The most common method to measure the temporal contrast is based on non-collinear third-order autocorrelation of the pulse in a non-linear crystal[17,18]. The pulse is split into two pulses and one of the two replica is frequency doubled. Then a non-collinear autocorrelation curve is measured between the second harmonic replica and the other pulse, through delay scanning. The signal is detected usually using a photo-multiplier. Several companies are selling devices that can cover more than 11 orders of magnitude in dynamic range to qualify the picosecond temporal contrast of ultrashort pulses. Also, new methods to measure the temporal contrast in single shot manner are being actively investigated[19–21].

7.2.4 Chirped Pulse Amplification (CPA) Architecture

One specific aspect in most high power laser systems is the need of significant energy in the laser pulse. Handling the amplification of pulse energy in laser systems involves the use of optical components that will not be affected by the laser pulse. Common issues to be considered are surface damage of optical components and non-linear effects such as self-phase modulation. Laser induced damages take place for fluences in the range from tens of mJ/cm^2 to a few J/cm^2, depending on parameters such as pulse duration, pulse repetition rate, and on the optical component preparation. For laser pulses below 100 fs pulse duration, such components are able to handle typically between 100 mJ/cm^2 and 300 mJ/cm^2, corresponding to tens of square centimeters for optical components to be used with pulse energies of the order of 10 J. The self-phase modulation is a process associated with the non-linear behavior of the refractive index of a material, also known as optical Kerr effect. For high intensity laser, the refractive index of most materials can be described with the formula:

$$n = n_0 + n_2 I \tag{7.33}$$

where n_0 is the linear part of the refractive index of the material and n_2 is the coefficient of the non-linear part of the refractive index. Typical values for the refractive index[22] correspond to $1-16 \cdot 10^{-20}$m/W. When the pulse propagates through a material, the associated optical path for a ray can be written as:

$$OP = n\delta = n_0\delta + n_2 I\delta = OP_l + OP_{nl}, \tag{7.34}$$

where the first term corresponds to the usual, linear part of the refractive index while the second part can be associated with the non-linear part of the refractive index. For the spatial regions of the laser pulse with high intensity, the non-linear part of the optical path can become significant, but it remains negligible at the periphery of the beam, where the intensity is low. As a consequence, the material starts to behave as a gradient refractive index lens that focuses the pulse. Through the focusing of the laser pulse, the intensity further increases and the non-linear part of the optical path is further increasing locally, inducing spectral modulation and filamentation of the beam or even damage to the material. This is a good example of a positive feedback loop which is extremely difficult to control. To avoid the self-phase modulation effect, the accumulated break-up integral (B-integral), defined as the phase associated with the non-linear part of the optical path:

$$B = 2\pi \frac{OP_{nl}}{\lambda} = \frac{2\pi}{\lambda} \int n_2 I dz \tag{7.35}$$

has to give values lower than 1 rad, corresponding to wavefront distortions of $\lambda/6$.

Trying to directly amplify ultrashort pulses, with durations below 100 fs, to energies of the order of 1 J, in solid or liquid active media with reasonable sizes, quickly increases the B-integral above this value. As a consequence, direct amplification of ultrashort pulses to high energies would be extremely difficult. To overcome this problem, Donna Strickland and Gerard Mourou[23] used a method to

reduce the intensity (hence *B*-integral) through stretching in time the pulses to be amplified. After amplification, the pulses can be compressed back to short duration using a so called optical compressor. This approach, known as Chirped Pulse Amplification (CPA), allows now to extend the pulse duration by up to 100 000 times, to amplify and to re-compress them close to the Fourier limit pulse duration. The technique was rewarded with the Nobel prize for Physics in 2018 for making possible intensities in excess of $10^{22}\frac{W}{cm^2}$ when pulses from CPA laser systems are focused and also for their use in applications, including eye surgery. In the following section, the most powerful (10 PW) functional laser system reported in a scientific journal[24], the High Power Laser System (HPLS) at the ELI-NP facility, will be presented, followed in section 7.4 by the review of the implementation status of the CPA laser systems at the Extreme Light Infrastructure.

7.3 The ELI-NP HPLS Laser System

This section intends to present a way to read the description of ultra-intense laser systems, such as HPLS, keeping intensity and temporal contrast in mind. It uses the images from the reference[24] which presents a more detailed technical description of the HPLS system and its performance. The HPLS laser system is representative of the state of the art in the high power laser systems in 2020, as pointed out in section 7.4. It was built to specifications by Thales company and installed at the National Institute for Physics and Nuclear Engineering, placed at the outskirts of Bucharest, Romania.

The laser is hosted in a clean room with an area of 2800 m^2, as shown in the central image of figure 7.4. The building that hosts the laser, the control room, the experimental area that host the beam transport and the inside of the 1 PW experimental chamber in preparation for ion acceleration experiments are also presented in figure 7.4.

7.3.1 The HPLS Architecture

The ultra-intense laser system can be split into three main parts, front-end, amplifiers and compression. The front-end includes a laser oscillator, optical stretcher and initial amplification to an energy level that can be achieved at high repetition rate, in this case at 10 Hz, with reasonable cost. The front end also includes most of the non-linear shaping and control applied to the laser pulses.

The HPLS front-end is depicted in figure 7.5. Here, the front-end starts with a Ti:Sa oscillator that delivers 6 fs pulses at 800 nm central wavelength with a bandwidth that is extended to 1064 nm. The oscillator pulse is optically stretched, amplified in a cavity-based amplifier that runs at 1 kHz repetition rate thanks to the diode pumped Jade laser, and subsequently compressed close to the Fourier limit. The high repetition rate front-ends allow to close fast feedback loops such as the ones that stabilize beam pointing or carrier-envelope phase drift. Once a reasonable level of energy is achieved in this way, the next critical aspect, the temporal contrast,

FIG. 7.4 – Upper row, left: ELI-NP special building, that hosts the laser system and the experimental areas. Upper row, right: E1 experimental chamber for 2 × 10 PW pulses and the beam transport for the long focal distance mirror for 10 PW pulses at E6 experimental area. Middle row: laser room, hosting the two laser amplification arms; Lower row, left: inside the 1 PW experimental chamber in E5 experimental area; lower row, right: the large screen in laser control room showing synthetic information on the HPLS status.

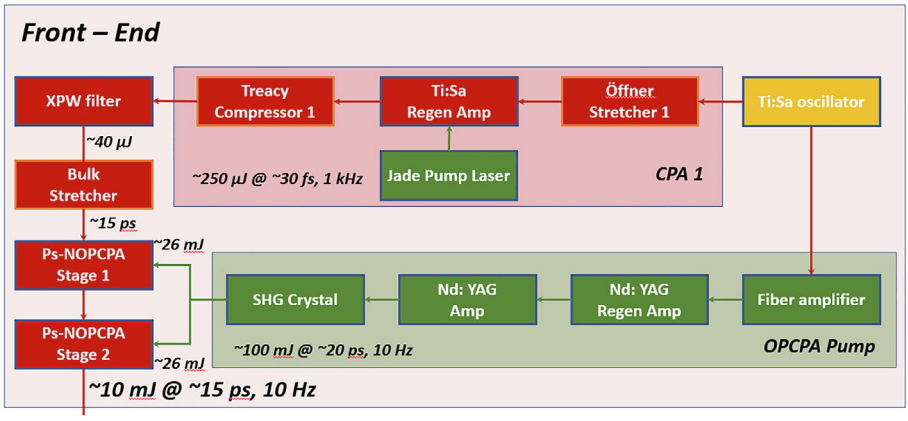

FIG. 7.5 – Front-end of HPLS. Copyright CC BY[24].

has to be tackled. This is made using the cross polarized wave filter (XPW) principle, as described in section 7.2.3. This non-linear filter of the pulse not only enhances the temporal contrast, broadens and smooths the spectrum but also significantly reduces the useful energy of the pulse. The seed for the XPW filter has to be at best compression, this is why the Treacy compressor is present after the regenerative amplifier (see figure 7.5).

In order to recover the pulse's energy without affecting the temporal contrast, two non-colinear optical parametric chirped pulse amplifiers (OPCPA) need to be implemented. The energy increases three orders of magnitude, from 10 μJ to 10 mJ. The temporal window of the amplification is defined by the 20 ps pulse duration of the OPCPA pump pulses. These are produced starting from the same oscillator, with the major benefit of optical synchronization with intrinsic low temporal jitter, in the femtosecond domain, in contrast to the electronic synchronized systems where the jitter easily stretches into the picosecond domain. A narrow spectral part of the oscillator pulses around the 1064 nm wavelength is selected using a fiber Bragg grating and then amplified using established technologies including fiber and Nd: YAG crystals as active media. The amplified pulses at 1064 nm wavelength are frequency doubled and then used for pumping the OPCPA amplifiers. The low jitter optical synchronization of the seed and the pump provides the temporal contrast enhancement, up to three orders of magnitude, outside the temporal amplification window defined by the pump pulse duration of 20 ps.

At this stage, the 10 mJ output of the front-end is divided into two equal energy pulses and sent into two similar, parallel amplification chains, as depicted in figure 7.6. As discussed in 7.2.4, the pulse has to be stretched significantly in order to avoid self phase modulation and damage to the optical components in the amplification chain. An optical stretcher that brings the pulse to 1 ns duration is appropriate for the amplification of up to 350 J, but it is not necessary for lower amplification levels. For going up to 40 J pulses, 600 ps would be enough and the major advantage would be to keep the corresponding 100 TW and 1 PW compressors more compact. This is why there is a partial compressor implemented after the 1 ns stretcher, that reduces the pulse duration to 600 ps when the specific 1 PW or 100 TW compressors are used.

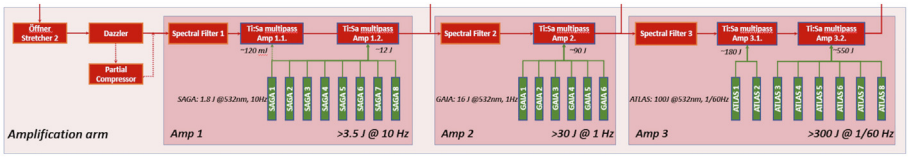

FIG. 7.6 – Amplifiers Amp1, Amp2 and Amp3 of HPLS. Copyright CC BY[24].

After the partial compressor, an acusto-optic programmable dispersion filter is implemented, as the beam size is still small. It has the role of controlling the spectral phase, hence it helps to fine tune the pulses in order to achieve best compression at the output of the HPLS, corresponding to the highest intensity of the pulse.

Amplification is realized in Ti:Sapphire crystals using pump lasers that operate at 10 Hz repetition rate with a moderate energy of 1.8 J at 532 nm wavelength (Amp1 in figure 7.6). Once the pulse reaches 4 J, much more energy is needed for pumping the crystal and this presents the challenge of producing it at 1 Hz repetition rate. Here, the six pump lasers are delivering up to 96 J total energy in the crystal of the second amplifier (Amp2 in figure 7.6).

The last stage of amplification is based on two more large Ti:sapphire crystals, pumped with a total of eight laser systems delivering each up to 100 J per pulse at 1 shot per minute repetition rate. Note that all pump lasers for the last amplifiers are using Nd:glass and are flash-lamp pumped. Their thermal management is the limiting factor that determines the repetition rate for the operation of the amplifiers. Solutions similar to those investigated at L2 line in ELI-Beamlines, at HF-2PW in ELI-ALPS or at the PW-class laser system from the group of Jorge Rocca[25] would make it possible to significantly increase the repetition rate of the amplifiers.

One important aspect in the amplification section of the CPA laser systems is related to the preservation of the bandwidth for the pulse after amplification. This in a non-trivial task, as the gain shape and limited bandwidth tends to amplify a narrower portion of the input pulse spectrum and might also shift the central wavelength. To mitigate this gain-narrowing process, spectral filtering in front of the amplifiers is helpful. These filters are flat mirrors with tailored spectral reflectivity curves, reduced to 60% at around 825 nm wavelength, as proposed in[26].

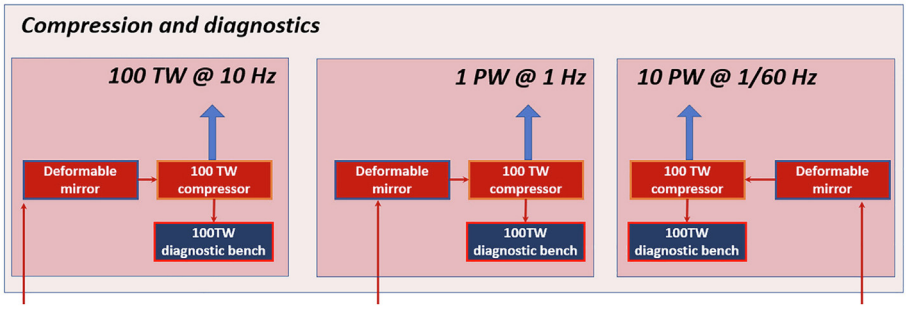

FIG. 7.7 – The deformable mirrors, the compressors and the diagnostic benches associated with each of the three main amplifier systems of HPLS. Copyright CC BY[24].

The energy from each amplifier stage is then directed to a dedicated combination of adaptive mirror, optical compressor and diagnostic bench, as depicted in figure 7.7. The adaptive mirror is the spatial equivalent of the acousto-optic programmable dispersion filter, namely it adjusts the wavefront of the laser pulse in order to obtain the smallest focal spot from the laser pulse, hence the highest intensity.

The compressors are using reflective diffraction gratings, in order to avoid the self-phase modulation of the pulses in bulk optical materials for the compressed pulses. They are also placed in vacuum, in order to avoid the self-phase modulation of the pulses in air (one meter of propagation in air is similar to 1 mm propagation in

glass, from the non-linear refractive index perspective). The 2.4 J energy from the Amp1 in conjunction with the pulse duration of about 24 fs corresponds to a peak power of 100 TW at 10 Hz repetition rate for each arm. For the Amp2, the achieved peak power exceeds 1 PW at 1 Hz repetition rate while the 230 J and 23 fs pulses of Amp3 correspond to 10 PW peak power at one shot per minute repetition rate. The damage threshold of the gratings is typically around 100 mJ/cm^2. This value, in combination with the intended output energy determines the beam size in and after the compressor. In the HPLS case, the 100 TW output has 55 mm, the one from 1 PW has 200 mm and the one from the 10 PW pulses is about 550 mm full aperture beam diameter.

The diagnostic benches implemented after the compressors contain the essential tools for measuring the pulses. They include spatial characterization devices in the form of video cameras to record the collimated beam profile, the shape of the focused beam and also the wavefront of the pulse. For the temporal aspect, there is a self-referenced spectral interferometry device for the spectral phase determination of the pulse, a spectrometer, a single shot second-order autocorrelator for the pulse duration evaluation and also a spectrometer. The energy is also monitored with a calibrated photodiode. All these three sets of devices, for spatial, temporal and energy characterization provide the information about the achievable intensity at the specific output of the laser. In addition to these devices, a third-order non-collinear autocorrelator with more than 11 orders of magnitude in dynamic range is used to appraise the temporal contrast of the pulses.

7.3.2 HPLS Compliance with Specifications

The pulses after compression are sampled at full aperture through a leaky mirror and then they are extracted from vacuum back to air through a window. Then they are de-magnified using a set of telescopes to reach few mm in beam diameter, to suit the diagnostic devices used. The laser pulse sampling method for metrology

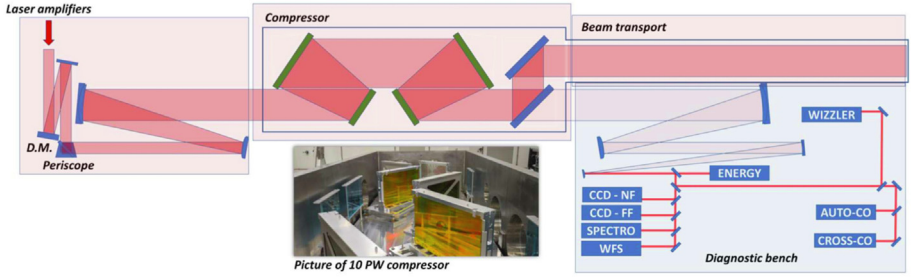

FIG. 7.8 – Set-up for HPLS output characterization at 10 PW. The HPLS 10 PW compressor and diagnostics' diagram; the inset is a picture of one of the two ELI-NP 10 PW compressors using the meter size gratings. D.M., deformable mirror; WFS, wavefront sensor; CCD-NF, near-field CCD; CCD-FF, far-field CCD; AUTO-CO, single-shot autocorrelator; CROSS-CO, third-order cross-correlator. Copyright CC BY[24].

purposes might introduce noise and distortions into the measurements. It is a subject of careful calibration and distortion compensation for all specific parameters that are relevant for the determination of the focused pulses' intensity.

The measurement of the beam profile and of the wavefront of the pulses is camera-based in all high power laser system characterization benches. The size of the beam is exceeding the size of the largest chip-sets for such video cameras. This is why the de-magnification of the beam is mandatory. In this respect, the telescopes used for reducing the beam diameter on the sensor are part of the beam profile and wavefront measurement system. The distortions are coming from the alignment precision, from the surface and spectral flatness quality of the optical components used. The most challenging part is the wavefront distortions introduced by the sampling system. In the HPLS case, these distortions were separately measured using an auxiliary laser in a double pass configuration, which was sent through a high quality, small aperture beam splitter placed in front of the wavefront sensor through the telescopes and back reflected with a high flatness mirror back on the same optical path to the wavefront sensor. The recorded distortions were below a tenth of a wavelength in our case and they are now subtracted from the raw wavefront data in order to provide accurate information on the pulse wavefront after compressor.

On the temporal and spectral characterization side, a similar situation appears. The pulses at the exit of the compressors pass through a specially designed flat spectral transmission leaky mirror and through the compressor window. The total thickness of the traversed glass is determined by the size of the beam: it has to be at least a tenth of the beam size, in order to reach the specified flatness during the polishing, coating and installation of the mirror. The window must not collapse under the 1 bar pressure difference exerted on it by the ambient air, when the compressor is under high vacuum. At the beam diameters mentioned above, the dispersion introduced by the glass is significant: for the 55 mm at 100 TW output it corresponds to more than 35 mm of glass and fourier limited pulses temporally stretch in excess of 160 fs, while for 1 PW and 10 PW pulses the dispersion contribution corresponds to temporal stretched pulses longer than 500 fs. However, through careful design of the system, the acousto-optic parametric dispersive filter implemented in the amplification chain at the entrance in Amp1 (see figure 7.6) can compensate for the mentioned spectral phase distortions corresponding to the dispersion of the glass.

Finally, the energy measurements provide two further challenges. First of all, the aperture of the beam reaches dimensions for which energy measurement devices operating in the femtosecond domain in the tens to hundreds of Joule range are prohibitively expensive. Here, it is customary to characterize the attenuated beam using a reduced beam diameter before sending the pulses in the optical compressor in vacuum, using available energy meters on the market. Further, the transmission of the compressor is measured or compared with the diffraction efficiencies of the grating compressors used. The typical values for the diffraction efficiency for one grating range from 90% to 94% for a high quality grating. As the optical compressors use four diffraction gratings, their overall transmission lies in the 65%–78% range and degrades easily over time if the gratings are contaminated with thin layers

of residuals in vacuum. Second challenge is related to the suppression of the full energy, ultrashort pulses that are measured. A suitable beam-dump has to be built in order to absorb the energy of the pulse after successfully passing through the compressor. Hence, it has to be placed in vacuum and it must have large aperture, good absorption and good thermal management in the case of high repetition rate lasers. It must also be positioned in such a way that no back reflection from the beam-dump finds its way back into the amplification chain. Such an unwanted event might generate a focused pulse that destroys optical components in the amplification chain up to the front-end.

The attainable peak power of HPLS at full amplification was determined[24] using the set-up depicted in figure 7.8. The spatial properties of the laser pulses, the collimated beam profile, the focal spot and the wavefront were measured after the demagnification with the telescopes. The wavefront was corrected with the help of the deformable mirror DM placed before the periscope and beam expander in front of the optical compressor. The wavefront calibration was performed as detailed above. Temporally, the pulse was measured using self-referenced spectral interferometry[27]. The spectral phase can be controlled with the acousto-optic programmable dispersion filter to achieve the best compression of 22.7 fs at the diagnostic bench. The energy measurement was calibrated. The estimated energy after compression, of 242.6 J, is obtained after subtracting the 25.8% losses of the compressor, calculated using the factory measured diffraction efficiencies of the gratings. When taking into account the temporal shape of the pulse as measured on the diagnostic bench, the pulse is not Gauss-shaped, the correction factor in formula 7.26 is numerically computed to take the value of 0.87. Hence the achievable power demonstrated at that moment was 9.34PW.

7.3.3 Beam Transport to the Experimental Areas

Laser pulse control at the output of the laser system is essential for the performance of the experiments, but it is not sufficient. The beam has to be transported to the experimental area in vacuum, avoiding self-phase modulations. There, the pulse is focused often using off-axis parabolic mirrors to achieve the highest intensity for experiments.

The transportation of such large aperture beams, involving meter-sized mirrors in vacuum is challenging. Several aspects have to be properly taken into account, as detailed in[28]. The challenges are related to the pointing stability, temporal contrast, polarization control, wavefront control, spectral phase control for the pulses and also back reflection isolation.

The laser beam transport system (LBTS) implemented at ELI-NP was built with simplicity in mind. After exiting the laser room, the LBTS uses only one or two flat mirrors in order to deliver the pulses to the focusing mirror.

The strategy for alignment of the laser pulses to be focussed with micrometer accuracy on the target in focus includes using auxiliary guiding laser beams, monitoring the position and direction of the pulses at each mirror, automation and remote control of the mirrors using high precision, high load, vacuum actuators.

The vacuum system is modular, allowing the independent access and maintenance for the two 10 PW pulses. The final vacuum sections of the LBTS are interfaced with full aperture gate valves with the vacuum interaction chambers in the E1, E6 and E7 experimental areas. The vacuum chambers for E1 and E6, simillar in dimensions (3 m length, 4 m width and 2 m in height) are already installed and connected to the LBTS, with vacuum levels below 10^{-6} mbar.

7.4 Extreme Light Infrastructure

Ultra-intense pulsed laser facilities have blossomed on the contemporary scientific and technological scene. They represent state-of-the-art scientific tools with outstanding properties that allow to investigate matter and applications at time scales not accessible otherwise until now. As presented in the previous sections, the magnetic and pressure fields produced in the form of laser pulses correspond to the largest ones created in controlled manner by humankind. Towards the end of the second decade of the 21st century, more than 130 operational laser systems emitting peak power above 10 TW or intensities exceeding 10^{19} W/cm^2 were identified by the ICUIL (https://www.easymapmaker.com/map/ICUIL_World_Map_v3). An extended review of the on-going developments towards ExaWatt laser facilities can be found in:[29]. In Europe, a strong network of advanced laser laboratories known as LASERLAB Europe has been funded for over two decades, with outstanding results. Currently, the LASERLAB network of laboratories includes 24 laser facilities that provide transnational access for experiments based on the scientific merit of the proposal.

With the strong support of LASERLAB, the European Union included in the European Strategy Forum on Research Infrastructures (ESFRI) Roadmap an ambitious project of a pan-European distributed research facility dedicated to the most innovative light sources and their applications, known as Extreme Light Infrastructure (ELI). The facility is advancing complementary laser technologies at three locations in three countries, namely the Czech Republic, Hungary and Romania. The three sites that are part of the ELI are designated with the "pillar" term. A fourth pillar shall host a laser system capable of exceeding the 10 PW actual technology barrier and to access in the 100 PW region and beyond.

The proposal was backed by an extended study on the relevance of extreme light for the future of the knowledge-based European society and for mankind in the form of a White Book[30]. We refer the reader to the available public text for an overall picture of the fundamental and applied research to be addressed, ranging from studies of the quantum vacuum structure and particle accelerators to life sciences and the management of nuclear waste.

In the following, a short description of the most advanced laser sources at each ELI pillar is provided, while secondary sources from the THz region to the extreme ultraviolet attosecond pulses and gamma rays are beyond the scope of this lecture.

7.4.1 ELI-Beamlines

The pillar in the Czech Republic, known as ELI-Beamlines hosts four major laser systems L1–L4. The L1 ALLEGRA laser system[31–33] is a Ti:Sa oscillator seeded OPCPA system pumped at 515 nm. It is operated at 1 kHz and delivers pulses of about 15 fs after optical compression 3 ps, using more than 30 reflections on chirped mirrors. It already reaches 30 mJ, one third of the design value for the pulse energy to be achieved after amplification in the sixth and seventh amplifiers (100 mJ), corresponding to the average power of 30 W. The temporal contrast of 10^{-9}:1 at 2 ps from the main peak is another unique feature of the laser system. It already produced UV light at 20 nm wavelength for the first experiments.

The L2 Amos laser system is a 100TW laser system designed to operate at more than 20 Hz, delivering 2 J pulses in 20 fs. It uses a 10 J pump laser head developed by Rutherford Appleton Lab, U.K. When it will be ready in 2021 or 2022, it will serve as the driver for generating the needed electron bunches for a free electron laser[34].

The L3 HAPLS laser system is planned to be used for laser-plasma diagnosis[35], for proton acceleration[36] and for electron acceleration[37]. The system is using amplification in Ti:Sa crystals at 800 nm wavelength, coupled with diode pumping technology. It already demonstrated a repetition rate of 3.3 Hz with an energy of 13.3 J and a pulse duration of 27.3 fs, corresponding to 0.49PW peak power and an average power of about 44 W. The nominal design parameters are a pulse energy of 30 J at a repetition rate of 10 Hz with a pulse duration of less than 30 fs.

The L4 ATON laser system is a kJ-class laser system with two planned outputs, one for long pulses, in nanosecond domain (L4n)[38], and one intended to deliver pulses of 150 fs after compression in vacuum (L4f)[39]. Unlike the other systems at ELI-Beamlines, L4 operates using amplification in Nd-doped glass at a central wavelength of 1053 nm, at a targeted repetition rate of 1 shot per minute. The beam shape is a 20th order super-Gaussian square with a diagonal of 45 cm. The energy for the long pulses reaches 1.9 J and the temporal shape of the pulse can be adjusted in the range from 100 ps to 10 ns with a precision of 150 ps.

The amplifiers for L4f output have already demonstrated energies of up to 1.5 kJ, and enough bandwidth to support 150 fs Fourier limited pulses at a repetition rate of one shot every 7 min. The compression of such pulses remains challenging and its targeted transmission efficiency is estimated to be in the 60% range, corresponding to 6 PW output peak power, when the gratings-based optical compressor will be built.

7.4.2 ELI-ALPS

In ELI-ALPS, the core developments are addressing technologies for accessing time scales below 1 fs, namely the attosecond regime, at high repetiton rates[40,41]. The sources developed here shall provide electromagnetic pulses in the spectral domain from THz to x-rays.

The 100 kHz laser systems developed here, HR1 and HR2[42,43] share the same approach for the amplification, namely the use of the coherent combination from 8

diode-pumped amplifiers, delivering 300 fs pulses and subsequent spectral broadening and re-compressing of the pulse using a hollow-core fiber and chirped mirrors. HR1 is available for user access, providing at this time 1.5 mJ in 30 fs pulses at a central wavelength of 1030 nm. HR2 was operated to deliver 10 fs pulses with an average power of 318 W corresponding to a pulse energy of 3.18 mJ.

A second 100 kHz laser technology is employed in the mid-infrared (MIR) source, operated at a central wavelength of 3100 nm[44], more suitable for a variety of applications including high-order harmonics generation and attosecond pulse generation. The pulse energy is 70 μJ and the 20 fs pulse duration corresponds to only two oscillation cycles of the electromagnetic field.

Single Cycle Laser group from ELI-ALPS worked on the development of few cycle laser pulses at a central wavelength of 900 nm at a repetition rate of 1 kHz[45,46]. SYLOS2 laser delivers 4.8 TW pulses of more than 30 mJ at a duration of 6.6 fs, corresponding to 2.3 optical cycles. The SYLOS3 upgrade which, is now under implementation in collaboration with Light Conversion company until end of 2022, will push the energy of the pulses to 120 mJ coresponding to a peak power of 15 TW. An additional alignment laser for SYLOS, SEA, can deliver similar pulses at a repetition rate of 10 Hz. The SEA laser produces 42.5 mJ, 12 fs pulses.

HF-2PW is a 2 PW laser system planned to run at 10 Hz. The key technology there is a pump laser able to deliver significant energy at 10 Hz repetiton rate; in this case, a 50 J at 10 Hz is under development for ELI-ALPS[47]. To date, 10 J at 10 Hz repetition rate for 17 fs pulses were declared operational, corresponding to an average power of 100 W and to more than 0.5 PW of peak power. Complementarily, a 100 Hz laser system is planned to operate at up to 0.5 J while the operational front-end delivers 8 mJ in 25 fs[48].

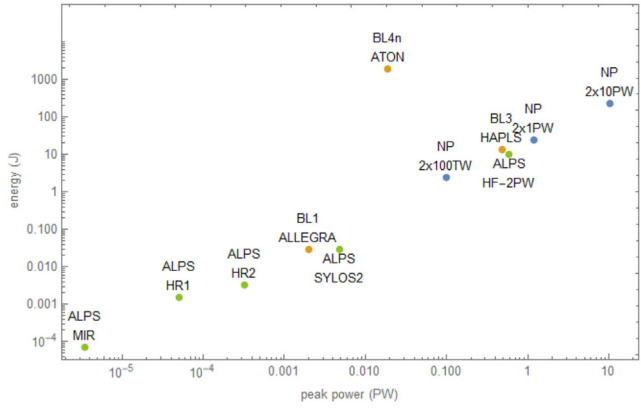

FIG. 7.9 – The reported tested peak power and energy parameters of the ELI main laser systems.

7.4.3 ELI-NP

At ELI-NP, the High Power Laser System (HPLS) described in section 7.3 and produced by a consortium within the THALES company, is based on Ti:Sa oscillator amplified up to 10 mJ at the repetition rate of 10 Hz. Then the pulse is split into two and distributed for amplification in two arms, each arm containing Ti:sa crystals and pump lasers. Each arm has three outputs with dedicated optical compressor and diagnostic bench: at 100 TW with 10 Hz repetition rate, at 1 PW with 1 Hz repetition rate and one at 10 PW having one shot per minute repetition rate. The pulse duration at each output is about 23 fs. The laser was commissioned in 2019[24], experiments at the 100 TW output with the nominal peak power were performed in the dedicated experimental area (E4) and in addition, demonstration of 10 PW pulse generation has been publicly performed twice to demonstrate the capability of 10 PW pulses transport to the experimental areas E7 and E1–E6, in vacuum, at nominal parameters. In addition to the HPLS, ELI-NP contracted a gamma source (VEGA) based on inverse Compton scattering of laser light with ultra-relativistic electrons obtained in a conventional accelerator to produce photons with energies per quanta of up to 19 meV, which is under construction and shall operate in 2023.

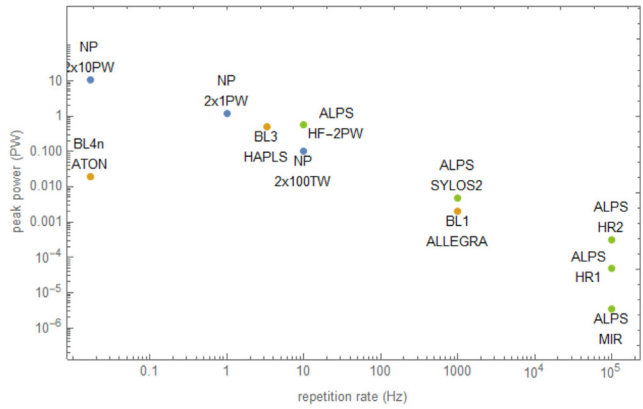

FIG. 7.10 – The achieved peak power as a function of the repetition rate for the ELI main laser systems.

7.4.4 ELI Status

To summarize this section, figure 7.9 illustrates the reported peak power and peak energy parameters of each major laser system in ELI facility, as reported in the literature up to now.

Figure 7.9 shows the high degree of complementarity of the ELI laser systems. The figure indicates that the HPLS of ELI-NP reached the highest peak power not only at ELI, but also worldwide, meeting specifications. The other laser systems

belong also to best-in-class category, although they often did not reach the nominal design parameters, to date. Figure 7.10 presents the peak power as a function of the repetition rate of the laser system.

It is important to note that figures 7.9 and 7.10 have logarithmic scales on both axes. A simplified interpretation of the two figures would be that the increase in the repetition rate of the laser systems favors industrial applications. For example, secondary sources of radiation can be produced with significant flux of particles. On the other hand, achieving higher peak power makes possible investigations of phenomena in new regimes, hence pushing the boundaries of our knowledge. Together, the industrial developments and the scientific research drive the progress of the human society.

7.5 Summary

The basic concept of peak intensity of ultrashort laser pulses was introduced. Its relation to the electric field, magnetic field and pressure was discussed, pointing out that the achievable values for these fields correspond to the largest ones ever produced by humankind in a controlled manner. Then, the most powerful laser worldwide, HPLS from ELI-NP, was briefly described in order to familiarize the reader with specific CPA subsystems which are often used to reach extreme intensities. Finally, one of the most advanced research facilities worldwide, the Extreme Light Infrastructure was presented in order to give an overview at the state-of-the-artlaser technology.

Acknowledgements

Extreme Light Infrastructure Nuclear Physics (ELI-NP) Phase II, is a project co-financed by the Romanian Government and the European Union through the European Regional Development Fund and the Competitiveness Operational Programme (1/07.07.2016, COP, ID 1334). The contributions of the entire Thales and ELI-NP teams and collaborators are gratefully acknowledged.

References

[1] Siegman A. (1986) *Lasers*. University Science Books, Mill Valley.
[2] Barton J.P., Alexander D.R. (1989) Fifth-order corrected electromagnetic field components for a fundamental gaussian beam, *J. Appl. Phy.* **66**, 2800, https://doi.org/10.1063/1.344207.
[3] Salamin Y.I., Hu S.X., Hatsagortsyan K.Z., Keitel C.H. (2006) Relativistic high-power laser–matter interactions, *Phys. Rep.* **427**, 41.
[4] Salamin Y.I., Keitel C.H. (2002) Electron acceleration by a tightly focused laser beam, *Phys. Rev. Lett.* **88**, 095005.
[5] Yanovsky V., Chvykov V., Kalinchenko G., Rousseau P., Planchon T., Matsuoka T., Maksimchuk A., Nees J., Cheriaux G., Mourou G., Krushelnick K. (2008) Ultra-high intensity-300 TW laser at 0.1 Hz repetition rate, *Opt. Express* **16**, 2109.

[6] Yoon J.W., Jeon C., Shin J., Ku Lee S., Lee H.W., Choi I.W., Kim H.T., Sung J.H., Nam C.H. (2019) Achieving the laser intensity of $5.5 \cdot 10^{22}\mathrm{W/cm}^2$ with a wavefront-corrected multi-PW laser, *Opt. Express* **27**, 412.
[7] Eliezer S. (2002) *The Interaction of high-power lasers with plasmas.* Institute of Physics.
[8] Mulser P., Bauer D. (2010) *High power laser-matter interaction.* Springer Tracts in Modern Physics, Springer-Verlag, Berlin Heidelberg.
[9] Nakamura D., Ikeda A., Sawabe H., Matsuda Y.H., Takeyama S. (2018) Record indoor magnetic field of 1200 t generated by electromagnetic flux-compression, *Rev. Sci. Instrum.* **89**, 095106, https://doi.org/10.1063/E5044557.
[10] Tatarakis M., Watts I., Beg F.N., Clark E.L., Dangor A.E., Gopal A., Haines M.G., Norreys P. A., Wagner U., Wei M.-S., Zepf M., Krushelnick K. (2002) Measuring huge magnetic fields, *Nature* **415**, 280.
[11] Hooker C., Tang Y., Chekhlov O., Collier J., Divall E., Ertel K., Hawkes S., Parry B., Rajeev P.P. (2011) Improving coherent contrast of petawatt laser pulses, *Opt. Express* **19**, 2193.
[12] Jullien A., Albert O., Chériaux G., Etchepare J., Kourtev S., Minkovski N., Saltiel S.M. (2006) Two crystal arrangement to fight efficiency saturation in cross-polarized wave generation, *Opt. Express* **14**, 2760.
[13] Jullien A., Albert O., Burgy F., Hamoniaux G., Rousseau J.-P., Chambaret J.-P., Augé-Rochereau F., Chériaux G., Etchepare J., Minkovski N., Saltiel S.M. (2005) 10^{-10} temporal contrast for femtosecond ultraintense lasers by cross-polarized wave generation, *Opt. Lett.* **30**, 920.
[14] Dubietis A., Butkus R., Piskarskas A.P. (2006) Trends in chirped pulse optical parametric amplification, *IEEE J. Sel. Top. Quantum Electron.* **12**, 163.
[15] Dromey B., Kar S., Zepf M., Foster P. (2004) The plasma mirror—a subpicosecond optical switch for ultrahigh power lasers, *Rev. Sci. Instrum.* **75**, 645, https://doi.org/10.1063/E1646737.
[16] Thaury C., Quéré F., Geindre J.-P., Levy A., Ceccotti T., Monot P., Bougeard M., Réau F., d'Oliveira P., Audebert P., Marjoribanks R., Martin Ph. (2007) Plasma mirrors for ultrahigh-intensity optics, *Nat. Phys.* **3**, 424.
[17] Luan S., Hutchinson M.H.R., Smith R.A., Zhou F. (1993) High dynamic range third-order correlation measurement of picosecond laser pulse shapes, *Meas. Sci. Technol.* **4**, 1426.
[18] Stuart N., Robinson T., Hillier D., Hopps N., Parry B., Musgrave I., Nersisyan G., Sharba A., Zepf M., Smith R.A. (2016) Comparative study on the temporal contrast of femtosecond mode-locked laser oscillators, *Opt. Lett.* **41**, 3221.
[19] Oksenhendler T., Bizouard P., Albert O., Bock S., Schramm U. (2017) High dynamic, high resolution and wide range single shot temporal pulse contrast measurement, *Opt. Express* **25**, 12588.
[20] Wang P., Shen X., Liu J., Li R. (2019) Generation of high-energy clean multicolored ultrashort pulses and their application in single-shot temporal contrast measurement, *Opt. Express* **27**, 6536.
[21] Wang Y., Ma J., Wang J., Yuan P., Xie G., Ge X., Liu F., Yuan X., Zhu H., Qian L. (2014) Single-shot measurement of $>10^{10}$ pulse contrast for ultra-high peak-power lasers, *Sci. Rep.* **4**, 3818.
[22] Kabacinski P., Kardas T.M., Stepanenko Y., Radzewicz C. (2019) Nonlinear refractive index measurement by SPM-induced phase regression, *Opt. Express* **27**, 11018.
[23] Strickland D., Mourou G. (1985) Compression of amplified chirped optical pulses, Opt. Commun. **55**, 447.
[24] Lureau F., Matras G., Chalus O., Derycke C., Morbieu T., Radier C., Casagrande O., Laux S., Ricaud S., Rey G., Pellegrina A., Richard C., Boudjemaa L., Simon-Boisson C., Baleanu A., Banici R., Gradinariu A., Caldararu C., De Boisdeffre B., Ghenuche P., Naziru A., Kolliopoulos G., Neagu L., Dabu R., Dancus L., Ursescu D. (2020) High-energy hybrid femtosecond laser system demonstrating 2×10 PW capability, *High Power Laser Sci. Eng.* **8**, https://doi.org/10.1017/hpl.2020.41.

[25] Wang Y., Wang S., Rockwood A., Luther B.M., Hollinger R., Curtis A., Calvi C., Menoni C.S., Rocca J.J. (2017) 0.85 PW laser operation at 3.3 Hz and high-contrast ultrahigh-intensity $\lambda =$ 400 nm second-harmonic beamline, *Opt. Lett.* **42**, 3828.

[26] Giambruno F., Radier C., Rey G., Chériaux G. (2011) Design of a 10 PW (150 J/15 fs) peak power laser system with Ti:Sapphire medium through spectral control, *Appl. Opt.* **50**, 2617.

[27] Oksenhendler T., Coudreau S., Forget N., Crozatier V., Grabielle S., Herzog R., Gobert O., Kaplan D. (2010) Self-referenced spectral interferometry, *Appl. Phys. B* **99**, 7.

[28] Ursescu D., Cheriaux G., Audebert P., Kalashnikov M., Toncian T., Cerchez M., Kaluza M., Paulus G., Priebe G., Dabu R., Cernaianu M.O., Dinescu M., Asavei T., Dancus I., Neagu L., Boianu A., Hooker C., Barty C., Haefner C. (2016) Laser beam delivery at ELI-NP, *Romanian Rep. Phys.* **68**, S11.

[29] Danson C.N., Haefner C., Bromage J., Butcher T., Chanteloup J.-C.F., Chowdhury E.A., Galvanauskas A., Gizzi L.A., Hein J., Hillier D.I., Hopps N.W., Kato Y., Khazanov E.A., Kodama R., Korn G., Li R., Li Y., Limpert J., Ma J., Nam C.H., Neely D., Papadopoulos D., Penman R.R., Qian L., Rocca J.J., Shaykin A.A., Siders C.W., Spindloe C., Szatmári S., Trines R.M.G.M., Zhu J., Zhu P., Zuegel J.D. (2019) Petawatt and exawatt class lasers worldwide, *High Power Laser Sci. Eng.* **7**, https://doi.org/10.1017/hpl.2019.36.

[30] Mourou G.A., Korn G., Sandner W., Collier J.L. Eds. (2010), *ELI - Extreme Light Infrastructure Whitebook*. THOSS Media GmbH.

[31] Bakule P., Antipenkov R., Novák J., Batysta F., Boge R., Green J.T., Hubka Z., Greco M., Indra L., Špacek A., Naylon J.A., Majer K., Mazurek P., Erdman E., Šobr V., Tykalewicz B., Mazanec T., Strkula P., Rus B. (2020) Readiness of L1 ALLEGRA Laser System for User Operation at ELI Beamlines," in *OSA High-brightness Sources and Light-driven Interactions Congress 2020 (EUVXRAY, HILAS, MICS) (2020), paper HF1B.7* (Optical Society of America) p. HF1B.7.

[32] Batysta F., Antipenkov R., Green J.T., Naylon J.A., Novák J., Mazanec T., Hríbek P., Zervos C., Bakule P., Rus B. (2014) Pulse synchronization system for picosecond pulse-pumped OPCPA with femtosecond-level relative timing jitter, *Opt. Express* **22**, 30281.

[33] Batysta F., Antipenkov R., Novák J., Green J.T., Naylon J.A., Horácek J., Horácek M., Hubka Z., Boge R., Mazanec T., Himmel B., Bakule P., Rus B. (2016) Broadband OPCPA system with 11 mJ output at 1 kHz, compressible to 12 fs, *Opt. Express* **24**, 17843.

[34] Wills S. (2020) ELI: open for business, *Opt. Photonics News* **31**, 33.

[35] Tryus M., Grepl F., Chagovets T., Velyhan A., Giuffrida L., Stancek S., Kantarelou V., Istokskaia V., Schillaci F., Zakova M., Psikal J., Nevrkla M., Lazzarini C.M., Grittani G.M., Goncalves L., Nawaz M.F., Cupal J., Koubíkova L., Buck S., Weiss J., Peceli D., Szotkowski P., Majer K., Alexander Naylon J., Green J.T., Kramer D., Rus B., Korn G., Levato T., Margarone D. (2020) TERESA target area at ELI beamlines, *Quantum Beam Sci.* **4**, 37.

[36] Margarone D., Pablo Cirrone G.A., Cuttone G., Amico A., Andò L., Borghesi M., Bulanov S. S., Bulanov S.V., Chatain D., Fajstavr A., Giuffrida L., Grepl F., Kar S., Krasa J., Kramer D., Larosa G., Leanza R., Levato T., Maggiore M., Manti L., Milluzzo G., Odlozilik B., Olsovcova V., Perin J.-P., Pipek J., Psikal J., Petringa G., Ridky J., Romano F., Rus B., Russo A., Schillaci F., Scuderi V., Velyhan A., Versaci R., Wiste T., Zakova M., Korn G. (2018) ELIMAIA: a laser-driven ion accelerator for multidisciplinary applications, *Quantum Beam Science* **2**, 8.

[37] Levato T., Bonora S., Grittani G.M., Lazzarini C.M., Nawaz M.F., Nevrkla M., Villanova L., Ziano R., Bassanese S., Bobrova N., Casarin K., Chacon-Golcher E., Gu Y., Khikhlukha D., Kramer D., Lonza M., Margarone D., Olšovcová V., Rosinski M., Rus B., Sasorov P., Versaci R., Zaras-Szydlowska A., Bulanov S.V., Korn G. (2018) HELL: high-energy electrons by laser light, a user-oriented experimental platform at eli beamlines, *Appl. Sci.* **8**, 1565.

[38] Jourdain N., Chaulagain U., Havlík M., Kramer D., Kumar D., Majerová I., Tikhonchuk V. T., Korn G., Weber S. (2020) The L4n laser beamline of the P3-installation: towards high-repetition rate high-energy density physics at ELI-Beamlines, *Matter Radiat. Extremes* **6**, 015401.

[39] Chériaux G., Gaul E., Antipenkov R., Borger T., Green J.T., Batysta F., Friedman G., Jochmann A., Kramer D., Rus B., Trojek P., Vyhlídka Š., Ditmire T. (2019) kJ-10 PW class laser system at 1 shot a minute (Conference Presentation), in *High Power Lasers for Fusion Research V*, Vol. 10898 (International Society for Optics and Photonics) p. 1089806.

[40] Ciappina M.F., Pérez-Hernández J.A., Landsman A.S., Okell W.A., Zherebtsov S., Förg B., Schötz J., Seiffert L., Fennel T., Shaaran T., Zimmermann T., Chacón A., Guichard R., Zaïr A., Tisch J.W.G., Marangos J.P., Witting T., Braun A., Maier S.A., Roso L., Krüger M., Hommelhoff P., Kling M.F., Krausz F., Lewenstein M. (2017) Attosecond physics at the nanoscale, *Rep. Prog. Phys.* **80**, 054401.

[41] Krausz F., Ivanov M. (2009) Attosecond physics, *Rev. Mod. Phys.* **81**, 163.

[42] Hädrich S., Kienel M., Müller M., Klenke A., Rothhardt J., Klas R., Gottschall T., Eidam T., Drozdy A., Jójárt P., Várallyay Z., Cormier E., Osvay K., Tünnermann A., Limpert J. (2016) Energetic sub-2-cycle laser with 216 W average power, *Opt. Lett.* **41**, 4332.

[43] Nagy T., Hädrich S., Simon P., Blumenstein A., Walther N., Klas R., Buldt J., Stark H., Breitkopf S., Jójárt P., Seres I., Várallyay Z., Eidam T., Limpert J. (2019) Generation of three-cycle multi-millijoule laser pulses at 318 W average power, *Optica* **6**, 1423.

[44] Thiré N., Maksimenka R., Kiss B., Ferchaud C., Gitzinger G., Pinoteau T., Jousselin H., Jarosch S., Bizouard P., Di Pietro V., Cormier E., Osvay K., Forget N. (2018) Highly stable, 15 W, few-cycle, 65 mrad CEP-noise mid-IR OPCPA for statistical physics, *Opt. Express* **26**, 26907.

[45] Budriunas R., Stanislauskas T., Adamonis J., Aleknavicius A., Veitas G., Gadonas D., Balickas S., Michailovas A., Varanavicius A. (2017) 53 W average power CEP-stabilized OPCPA system delivering 5.5 TW few cycle pulses at 1 kHz repetition rate, *Opt. Express* **25**, 5797.

[46] Toth S., Stanislauskas T., Balciunas I., Budriunas R., Adamonis J., Danilevicius R., Viskontas K., Lengvinas D., Veitas G., Gadonas D., Varanavicius A., Csontos J., Somoskoi T., Toth L., Borzsonyi A., Osvay K. (2020) SYLOS lasers – the frontier of few-cycle, multi-TW, kHz lasers for ultrafast applications at extreme light infrastructure attosecond light pulse source, *J. Phys.: Photonics* **2**, 045003.

[47] Falcoz F., Gontier E., Courjaud A., Branly S., Paul P.-M., Vigroux L., Riboulet G. (2019) Latest developments at amplitude in the frame of the eli-hu projects. pw laser at high repetition rate, in *Conference on Lasers and Electro-Optics,* Optical Society of America. p. STu4E.1.

[48] Cao H., Nagymihaly R.S., Khodakovskiy N., Pajer V., Bohus J., Lopez-Martens R., Borzsonyi A., Kalashnikov M. (2021) Sub-7 fs radially-polarized pulses by post-compression in thin fused silica plates, *Opt. Express* **29**, 5915.

Chapter 8

Coherent Multidimensional Spectroscopies: Advanced Spectroscopic Techniques to Unveil Complex Dynamics

Elisabetta Collini*

Department of Chemical Sciences, University of Padova, via Marzolo 1-35131 Padova, Italy

Abstract. Femtosecond coherence spectroscopy is a family of ultrafast techniques that utilize ultrafast laser pulses to prepare and monitor coherent states in resonant or non-resonant samples. Among coherence spectroscopies, 2D electronic spectroscopy (2DES) techniques have recently gained particular interest given their capability of following ultrafast processes in real-time. Indeed, 2DES is widely exploited to unveil subtle details of ultrafast relaxation dynamics, including energy and charge transport, in complex media such as biological and artificial light-harvesting complexes and solid-state materials. Particularly meaningful is the possibility of assessing coherent mechanisms active in the transport of excitation energy in these materials. In this chapter, the main technical aspects of 2DES will be reviewed by illustrating specific relevant applications to different systems. Current challenges and still debated perspectives will be presented.

8.1 Introduction

The ability to spectroscopically probe ultrafast events in the femtoseconds (fs) time regime has been crucial for understanding fundamental scientific questions in biology, chemistry, and physics.[1–4] Examples of such investigations include

*elisabetta.collini@unipd.it

DOI: 10.1051/978-2-7598-2719-0.c008

transition-state dynamics of chemical reactions,[5] solute–solvent interactions,[6,7] energy and charge transfer,[8–10] excitonic interactions,[11–13] and quantum coherence,[14–19] just to cite a few.

Several ultrafast spectroscopy techniques have been developed to address these issues, including pump-probe (probably the most famous and widespread among the fs techniques), various types of photon echo, transient grating, resonant coherent Raman, hole-burning spectroscopies, and optical Kerr spectroscopy.[20,21] All these techniques can be broadly classified as four-wave mixing (FWM) techniques.[21,22] Four-wave mixing is a well-known nonlinear optical effect. It describes a mixing process in which three propagating light waves interact non-linearly in a medium and generate a fourth wave (the 'signal'). Different techniques can then be defined within this broad family, depending on the excitation geometry, the time and frequency properties of the exciting waves, the detection scheme, etc. In a perturbative approach, the process is governed by the third-order nonlinear response function, which naturally exhibits resonances that are characteristic of the medium and can be probed through the resonant enhancement of the FWM output.[21,23–25]

Coherent multidimensional spectroscopy (CMDS) is an extension of the FWM techniques, and several analogies may be drawn with conventional 'monodimensional' (1D) spectroscopies like photon echo and pump-probe; it is not by chance that, within the CMDS family, we may enumerate bidimensional (2D) photon echo (2DPE) and 2D pump-probe (2DPP), as indeed representing the 2D analogous of the corresponding 1D techniques. What distinguishes a 2D from a 1D technique is that in 2D techniques, each of three light-matter interactions is carefully controlled in time. In this way, the medium's response can be cast into 2D spectra, which provide more straightforward and direct access to signal contributions hidden within the broad line-shapes of 1D spectra. This allows revealing with improved reliability details on molecular structure, vibrational and electronic motions, interactions, couplings and relaxation processes.

This is particularly advantageous in the investigation of condensed phases, in which complex inter- or intramolecular interactions and environmental heterogeneity may be blended within the broad spectral features of 1D measurements. 2D techniques instead permit the spreading of congested spectra along multiple time or frequency coordinates.

This approach was first proposed, starting from the 60s, in nuclear magnetic resonance (NMR) spectroscopy, where many different schemes, with varying sequences of pulses, have been established to access specific information and enable quantitative determination of couplings, anharmonicities, relative dipole orientations, structural properties, and dynamical processes.[26] The development of the analogous 2D techniques in the optical frequencies' range came at least two decades later because of various experimental challenges. The critical ingredient in the first implementations of 2D spectroscopy[27] is that the nonlinear signal is detected interferometrically, and this implies measuring the signal phase and maintaining phase stability between all pulses. This is the so-called 'phase stability' of the setup, which must be held for a time on the order of a fraction of the wavelength of the interacting pulses.[28] This is relatively straightforward for radiofrequencies (used in NMR spectroscopy) and becomes increasingly more challenging as the frequency of the exciting

pulses increases. Indeed, for wavelengths in the IR, robust mechanical components within a sealed box are enough to minimize phase variations among the multiple beams.[29] 2D techniques in the IR range (2D vibrational spectroscopy) started to be developed from the 80s,[30] whereas it took another two decades to arrive at the first realization of 2D spectroscopies in the Vis range (2D electronic spectroscopy, 2DES). The first theoretical proposal of a 2DES dates back to 1998,[27] but it was only a few years later, thanks to the development of diffractive optics-based heterodyne detection[31] that it was practically possible to build the first setups for 2DES. For similar reasons, the extension to the UV frequency range is even more recent.[32–34]

At the dawn of 2DES in the early 2000s, the technique was mainly applied to biological light-harvesting antenna complexes.[14,17,18,35,36] Indeed, it appeared as the ideal technique to investigate the possible presence and the relevance of coherent quantum mechanisms active during the biological light-harvesting processes. In fact, the development of 2DES, now recognized as the primary tool to obtain clear and definitive experimental proof of such effects, has been central in the advent of quantum biology.[37–39] Although the effective role of quantum phenomena on the biological light-harvesting process is still a matter of intense debate,[40–42] trying to imitate nature,[43] spectroscopists started to move their attention on bio-mimetic artificial systems, from organic multi-chromophore systems[11,19,44–47] to fully inorganic,[48–50] hybrid materials,[51,52] and to functioning solid-state devices[15,53]. Based on this wealth of evidence, the enormous potential of 2DES techniques to impact the field of nanosystems, semiconductors, quantum technologies, and quantum devices must now be recognized.

With this in mind, this chapter, rather than trying to provide an exhaustive overview of technical details (many excellent books and reviews are already available[54–60]), has the ambition of helping the reader in forming a discerning view about the limits of this technique by exploring its strengths and weaknesses and describing a few examples of successful applications on different materials.

Let us right away look at the two main assets of 2DES:

(1) First, in 2D spectra, the couplings between different states or transitions are mapped as cross-peaks, far from the diagonal region where the remaining relaxation dynamics occur. Cross-peaks are achievable only in multidimensional techniques. They are the 'smoking gun' witnessing the presence of interactions and couplings between states. It is also possible to follow their time behavior, assessing the strength of couplings and the associated dynamics. (see section 8.2.3)
(2) Second, the technique is sensitive to coherent dynamics and quantum evolution manifested as oscillations of the signal amplitude at specific coordinates of the 2D maps. The study of frequency, amplitude distribution, and dephasing time of such oscillations allows a full characterization of any coherent dynamics (electronic, vibrational, vibronic, etc.) taking place during the system relaxation. (see section 8.2.4)

To give a physical insight into what is determining these capabilities, the main technical aspects of 2DES and the physical origin of the signal outputted by a 2DES experiment will be quickly outlined in section 8.2. In section 8.3, different

experimental schemes and layouts currently available will be described, with the purpose of evaluating for which uses each configuration is best suited. Finally, section 8.4 summarizes a few examples of relevant applications on innovative materials.

8.2 Electronic Transitions in 2DES Spectra

8.2.1 How a 2DES Map is Built

2DES is a FWM experiment in which a sequence of three fs pulses interacts with the sample and causes the stimulation of a third-order coherent response.

To understand how the technique works, a comparison to the more familiar pump-probe technique will be useful. In a typical pump-probe experiment, a short pump pulse from a femtosecond laser impulsively excites the sample to an electronic excited state. Using the perturbative approach, this first event implies two simultaneous interactions with the exciting field. After a time delay T, a weak probe pulse (representing the third interaction between the system and the field) records the changes in the absorption due to the action of the pump (figure 8.1a,c). The transmittance of the probe can be increased ('bleaching' or 'stimulated emission') or decreased ('excited state absorption') in different spectral regions. A typical pump-probe spectrum plots differential transmission as a function of probe frequency ω_{probe} (figure 8.1e). A convenient way to get acquainted with 2DES spectroscopy is to think about how a pump-probe spectrum could be expanded into a 2D spectrum.[17,55,61] In a 2D spectrum the third-order signal is plotted along two frequency axes: the axis ω_3, typically denoted 'emission' frequency, is analogous to the ω_{probe} axis in the pump-probe response. The new frequency axis ω_1 ('excitation' frequency) can be thought of as the distribution of frequencies excited by the pump pulse. One can imagine resolving the excitation axis by repeating a pump-probe experiment scanning a single narrowband pump pulse in frequency. The use of a narrow spectrum implies a reduction of the time resolution of the experiment because, according to the time-bandwidth product relation, a pulse with a narrow spectrum is characterized by a long time duration. This will induce a trade-off between the excitation axis resolution and the time resolution necessary to study ultrafast relaxation dynamics. The problem is bypassed by acquiring the excitation axis in the time domain while scanning the delay t_1 between the first two interactions (figure 8.1b,d). The generated signal oscillates as a function of the delay time t_1 allowing the excitation frequency axis to be recovered by Fourier transform (FT), as in conventional Fourier-Transformed spectroscopy[62]. In this situation, the broader the pulse spectrum the larger the excitation frequency window explored in the experiment. The resulting representation has both high temporal and spectral resolution.

Overall, a 2D map can be interpreted as a frequency-frequency correlation spectrum at a fixed value of the delay time t_2 (analogous of T in the pump-probe

experiment): $\boldsymbol{S}^{(3)}(\omega_1, t_2, \omega_3)$, (figure 8.1f). This signal is plotted as a function of the frequency ω_1 (= FT (t_1)), representing the initial excitation, and the frequency ω_3 (= FT (t_3)), which can be interpreted as the ensuing emission:

$$\boldsymbol{S}^{(3)}(\omega_1, t_2, \omega_3) = \int_{-\infty}^{\infty} dt_1 \int_{-\infty}^{\infty} dt_3 \boldsymbol{S}^{(3)}(t_1, t_2, t_3) e^{-i\omega_1 t_1} e^{-i\omega_3 t_3} \tag{8.1}$$

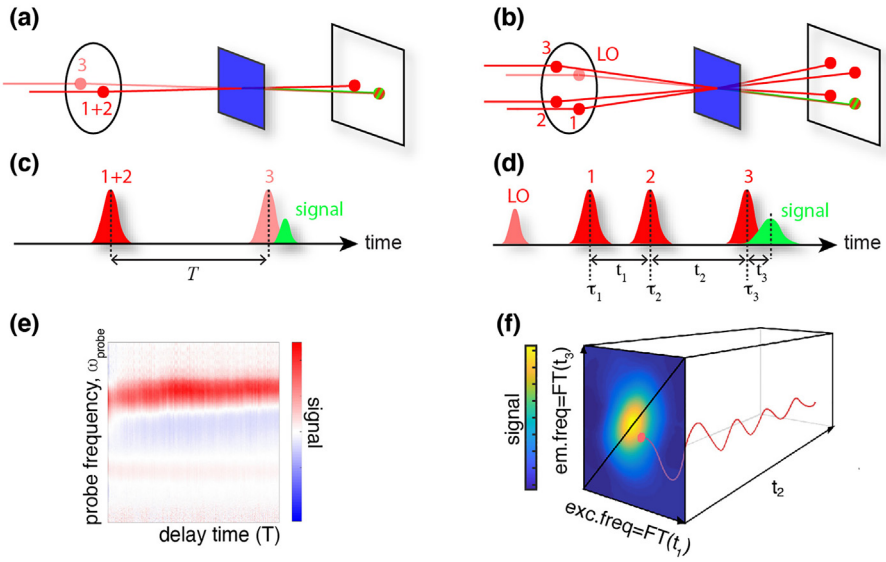

FIG. 8.1 – Excitation geometry for (a) pump-probe and (b) 2DES experiments. The associated pulse sequence and time delay definition is reported in (c) and (d), respectively. In the pump-probe experiment (c), the first two interactions (collectively indicated as 'pump') are simultaneous, and the two exciting beams (E_1 and E_2) propagate along the same direction. The third interaction is with the 'probe' beam (E_3), characterized by lower intensity. The signal (green) is emitted in the same direction as the one of the probe, it is self-heterodyned by it, and it is measured as a function of the delay time T between the pump and probe beams. In 2DES experiments (d), the three fields interacting with the sample (E_1, E_2 and E_3) and a fourth beam used only for detection purposes (LO = local oscillator) are arranged at the vertices of a square (BOXCARS geometry). The LO is aligned in the same direction as the emitted signal (defined by phase-matching conditions) so that the measured quantity indeed results from the interference between the signal and the LO (heterodyne detection). (e) Example of a typical plot ω_{probe} *vs.* T obtained as a result of a pump-probe experiment. (f) Pictorial representation of the matrix dataset obtained with a 2DES experiment; the two frequency axes ω_1 and ω_3 are obtained by Fourier transforming the delay times t_1 and t_3. The evolution of the 2D (ω_1, ω_3) maps is followed along t_2.

8.2.2 Third-Order Signal in a 2DES Map

The signal plotted in a 2DES map can be formalized in the perturbative approach framework, which allows expressing the total polarization $\boldsymbol{P}$ as a perturbative expansion in powers of the incoming fields. The critical quantity to determine any FWM nonlinear signal (including the 2DES signal) is the third-order polarization $\boldsymbol{P}^{(3)}$, to which the signal is proportional. $\boldsymbol{P}^{(3)}$ can be expressed as the convolution of the nonlinear response function $R^{(3)}(t_1, t_2, t_3)$ with the fields $E_j(\boldsymbol{k}_j, t_j)$:[17,21,55,56]

$$\boldsymbol{E}_j(t) = A_j(t-\tau_j)\, e^{-i\omega(t-\tau_j)+i\boldsymbol{k}_j\cdot\boldsymbol{r}+i\phi_j} + \text{ complex conjugate} \tag{8.2}$$

$$\begin{aligned}\boldsymbol{P}^{(3)}(t_1,t_2,t_3) \propto \int_0^\infty dt_3 \int_0^\infty dt_2 \int_0^\infty dt_1\, \boldsymbol{R}^{(3)}(t_1,t_2,t_3)\, \boldsymbol{E}(t-t_3) \\ \boldsymbol{E}(t-t_3-t_2)\, \boldsymbol{E}(t-t_3-t_2-t_1)\end{aligned} \tag{8.3}$$

where the jth laser pulse is centered at τ_j and $\boldsymbol{k}_j$, ω, $A_j(t)$ and ϕ_i are the wavevector, carrier frequency, temporal envelope and phase of the field. t_1, t_2, and t_3 are the time intervals between interactions, as illustrated in figure 8.1d.

The third-order polarization can be described as the sum of many contributions, each of which corresponding to a specific time evolution of the system – described by a density operator – and resulting from a specific sequence of three successive interactions with the total electric field.

Each of these terms can be associated with a specific time evolution of the density matrix, known as Liouville pathways. The density matrix is the representation of the density operator. It describes the quantum state of a physical system in a more generalized way than the more usual state vectors or wavefunctions.[63] Diagonal terms in the density matrix are called 'populations' while off-diagonal terms are named 'coherences' and are characterized by an oscillating time behavior.[63]

In spectroscopy, the pathways describing the evolution of the density matrix under the action of electric fields are usually graphically visualized by means of diagrams capable of highlighting the temporal sequence of the field interactions and the transitions promoted in the systems by these interactions. The most famous ones are the double-sided Feynman diagrams. Figure 8.2 reports an example of a pathway contributing to the time evolution of the density matrix in terms of a Feynman diagram (figure 8.2a) and the coordinates in the 2D map at which the corresponding signal is expected to appear (figure 8.2b).

In figure 8.3 the Feynman diagrams most relevant for the interpretation of 2DES responses are shown.

Each pathway corresponds to different pulse sequences and phase matching conditions, so that $\boldsymbol{k}_{\text{sig}} = \pm\boldsymbol{k}_1 \pm \boldsymbol{k}_2 \pm \boldsymbol{k}_3$ and $\phi_{\text{sig}} = \pm\phi_1 \pm \phi_2 \pm \phi_3$. In general, only a few pathways give a non-negligible contribution to the final signal and, based on these, rephasing ($\boldsymbol{k}_R = -\boldsymbol{k}_1 + \boldsymbol{k}_2 + \boldsymbol{k}_3$), non-rephasing ($\boldsymbol{k}_{NR} = +\boldsymbol{k}_1 - \boldsymbol{k}_2 + \boldsymbol{k}_3$), and double-quantum ($\boldsymbol{k}_{2Q} = -\boldsymbol{k}_1 - \boldsymbol{k}_2 + \boldsymbol{k}_3$) signals are typically defined. Rephasing and non-rephasing signals are named accordingly with the convention used for the

classical photon echo spectroscopy[21] and provide complementary information on ground and excited states dynamics. When summed, they result in the so-called 'purely absorptive' or 'total' signal, particularly relevant if one is interested in the analysis of the shape and broadening of the peaks as a consequence of the system-environment interaction.[56] The double quantum signal is instead useful to explore doubly-excited states.[11,64]

A full treatment of third-order responses goes beyond the scope of this chapter and we refer the interested reader to refs.[21,22,55] for an in-depth analysis. In practice, once relevant pathways/diagrams contributing to the response function are identified for the particular third-order experiment of interest, the total signal can be constructed by adding together the contributions from each individual diagram. Each of these contributions contains different factors: (i) a sign representing its contribution to the radiated signal (absorption/emission factor); (ii) an amplitude depending on the transition dipole moments excited by the fields, and (iii) an oscillatory term from the free evolution in between two interactions. These factors can be derived directly from the diagrams using the optical transition frequencies and the transition dipoles between each pair of levels.

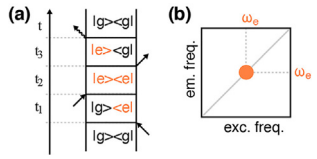

FIG. 8.2 – (a) Example of pathway contributing to the time evolution of the density matrix under the interaction with three laser pulses in terms of a Feynman diagram. The black straight arrows represent the exciting fields while the wavy arrow the emitted signal. A two-level system (ground state g and excited state e) is considered. (b) The signal corresponding to this diagram is expected to appear in the 2D map as a diagonal peak at coordinates (ω_e, ω_e), with ω_e the frequency of the transition $g \rightarrow e$.

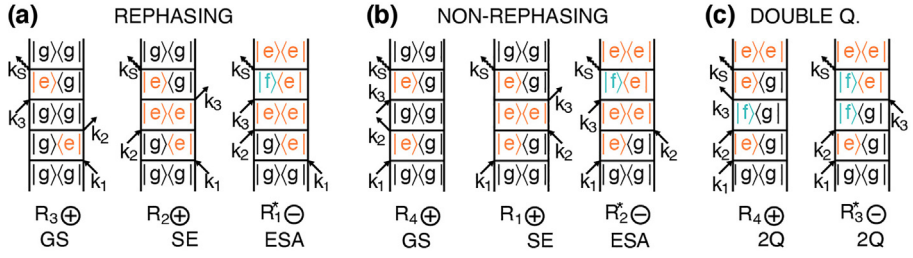

FIG. 8.3 – Feynman diagrams contributing to (a) rephasing, (b) non-rephasing and (c) double-quantum signals. Orange is used to label singly excited states and green is used to label doubly excited states. GSB = ground state bleaching; SE = stimulated emission; ESA = excited state absorption. The diagrams are conventionally numbered R_i, with $i = 1{-}4$.[21] The asterisk indicates the complex conjugate of a contributing term.

8.2.3 Diagonal and Off-Diagonal Signals

As exemplified in figure 8.2, each diagram contributing to the total $R^{(3)}$ gives rise to a signal at a specific (ω_1, ω_3) coordinate in the 2D map. However, typically, more than one diagram will contribute to any relevant position, making the final interpretation of the peaks appearing in the 2D maps often tricky. Nonetheless, a few simplified guidelines can be drawn. The axis ω_1 reflects information about the first coherence excited just after the first interaction. It can be considered as a label of the initial excitation frequency. In contrast, the axis ω_3 reveals the frequency of the optical coherence that produces the detected polarization after the third interaction.

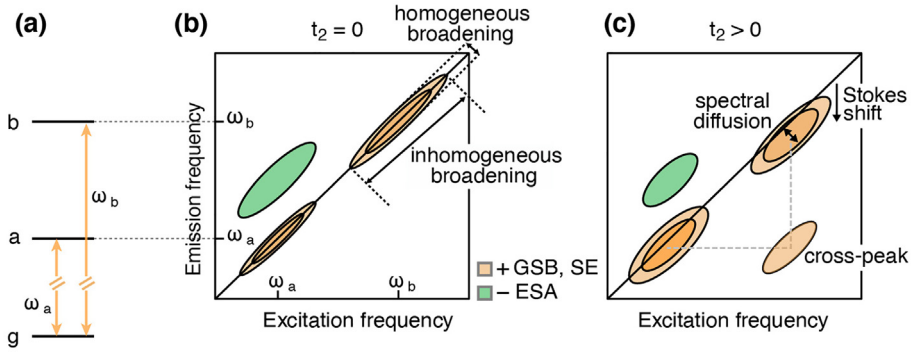

FIG. 8.4 – Schematic representation of a 2D spectrum for a multilevel system. (a) Energy levels and transition frequencies. (b) At early population times, the GSB and SE features of two levels with frequency ω_a and ω_b appear as (yellow, positive) signals elongated on the diagonal. (c) As the population time evolves, the spectral diffusion produces a broadening of the features, the Stokes shift produces a redshift of the signals along the emission axis and a cross-peak may appear in the lower part of the map as a consequence of the relaxation from the high energy level to the low energy one. Negative ESA signals (green, negative) can also appear.

Inspecting the corresponding Feynman diagrams, it is easy to demonstrate that signals appearing on the diagonal ($\omega_1 = \omega_3$) provide information on the electronic structure of the system under investigation, *i.e.*, on the frequencies of the transitions falling in the experimental window. For example, in the rephasing map schematized in figure 8.4, two transitions with frequencies ω_a and ω_b, are found, suggesting the presence of two excited states, a and b.[29,55,56]

The intensity and the shape of these bands change as the populations of the two states decay to the ground electronic state. The shape of the peaks (particularly their diagonal and anti-diagonal width) depends on the interactions with the environment and broadening mechanisms. Typically, as t_2 increases, a broadening and

rounding of the peaks is observed due to the loss of correlation (figure 8.4c); this phenomenon is known as spectral diffusion and the study of its time evolution is particularly relevant in the study of the configurational changes of the local environment and the time scales for the evolution of the bath.[65]

Relaxation within the same energy band during t_2 may also manifest itself as a shift of the signals at lower emission frequencies. Ultrafast Stokes shifts due to the reorganization of the electronic clouds of the system and the solvent appear as drifts of the features below the diagonal.[7]

Relaxation between different energy levels, or also energy transfer between different molecules, produces rising cross-peaks ($\omega_1 \neq \omega_3$) below the diagonal with simultaneous decay of the diagonal signals associated with the initial states (figure 8.5). Excitation and emission coordinates of the cross-peaks directly provide the energy of the states involved. For example, excitation energy transfer or internal relaxation from one absorption band at energy ω_a to another at lower energy ω_b produces a cross-peak at ($\omega_1 = \omega_a$; $\omega_3 = \omega_b$), revealing the kinetics by which the ω_a state relaxes to the ω_b state. If the energy transfer proceeds downhill in energy, then the cross-peak appears in the lower diagonal part of the 2D spectrum. Note that ω_a and ω_b can just as well be two vibronic states lying on the same electronic state. In this case, the cross-peak between ω_a and ω_b captures the vibrational relaxation process.

Cross-peaks can also arise in the presence of resonance interaction between two states, for example in a molecular dimer. In this case, the molecular states are no longer the eigenstates of the dimer, which are the delocalized excitations, termed excitonic states or excitons.[13,66] The 2D spectrum of such a system (figure 8.5c) contains cross-peaks, arising from the coupling between the monomers, already at $t_2 = 0$. Since they would not be present if the interaction between the molecular states was negligible, the presence of cross-peaks at very early times in 2D spectra implies coupling between the constituents of the observed system.

More generally, cross-peaks will appear every time two levels are coupled and share a common ground state. The cross-peaks' position can be used to identify which states are interacting, and the presence (or absence) of cross-peaks in a 2D map can provide insights into the nature of the electronic system (figure 8.5).

This capability also extends to dynamic processes involving dark states, which can be identified through the appearance of ESA cross-peaks. Indeed, dark states can be populated through relaxation from higher energy bright states and once populated, an absorption from here to a higher excited state can be activated (figure 8.5d). Conventional 1D femtosecond pump-probe experiments typically struggle to elucidate questions concerning the nature and significance of dark electronic states because their signals are overwhelmed by contributions from other strongly allowed transitions. As their name suggests, dark states cannot be caught through direct excitation because they lack a transition dipole moment with the ground state. Nevertheless, the relaxation dynamics are strongly affected by the presence of such states, often involved in transfer, quenching, or photoprotection processes. Examples are the leading role of the dark S_1 state of carotenoids in light-harvesting complexes[67,68] and of the dark type-II excitons having the long lifetime required for their Bose–Einstein condensation in GaAs based quantum wells.[69]

In summary, one can say that, by taking advantage of the sensitive detection of coupling among states via cross-peaks attainable in 2DES, it is possible to detect not only the spectral signatures and kinetics of various (bright and dark) electronic states but also their interaction pathways.[68]

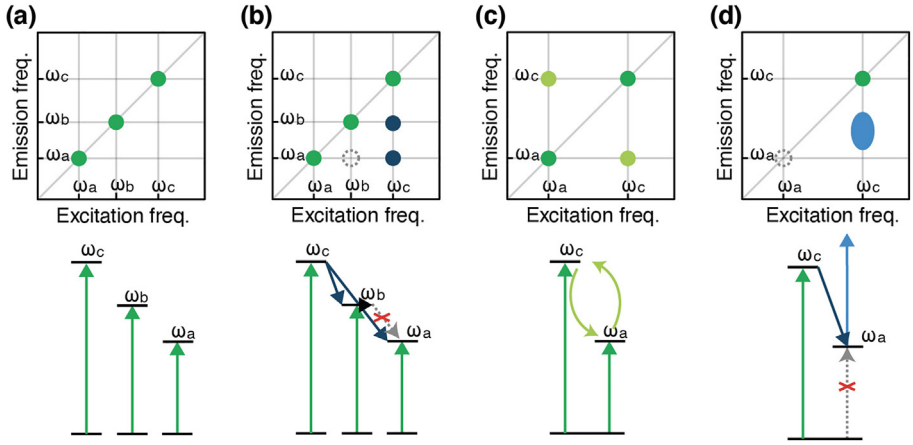

FIG. 8.5 – The position of the cross-peaks can be used to identify which states are interacting. (a) A system that produces multiple diagonal peaks but no cross-peaks can be modeled as a set of isolated non-interacting two-level systems. (b) The cross-peaks at coordinates (ω_c, ω_b) and (ω_c, ω_a) appearing at $t_2 > 0$ indicate that state c is coupled *via* energy transfer with states a and b. No coupling exists between states a and b because no cross peak appears at (ω_b, ω_a). (c) In the presence of resonance interactions between two states, cross-peaks appear already at $t_2 = 0$: the system can be modeled as a molecular (excitonic) dimer. (d) A dark state (ω_a) can be characterized by the coupling with a bright state (ω_c) in ESA processes.

8.2.4 *Signal as a Function of t_2: Population and Coherence Decay*

We already discussed that in the response function formalism, the third-order signal could be expressed as a sum of contributions represented graphically by double-sided Feynman diagrams. These contributions can be classified into two groups depending on the signal's evolution during t_2, as shown in figure 8.6. The first group includes non-oscillating pathways, represented by Feynman diagrams where the system reaches a population (diagonal element of the density matrix) after the first two interactions. The second group consists of oscillating contributions described by Feynman diagrams where, after the first two interactions, the system is in a coherent superposition of states.[70]

In the first case, the signal evolves in t_2 following the relaxation dynamics of the excited states that can be quantified through the solutions of suitable kinetic differential equations ('populations' dynamics). For example, in the simplest case of parallel relaxation processes, the solutions of the rate equations are real exponential functions.[71,72] In the second case, the signal oscillates during t_2 with a frequency proportional to the energy gap of the states that generate the coherence. These oscillations dampen over time according to their dephasing rates, depending on the nature of states themselves, on the temperature, on the environment, etc., and are well described by complex exponential functions.

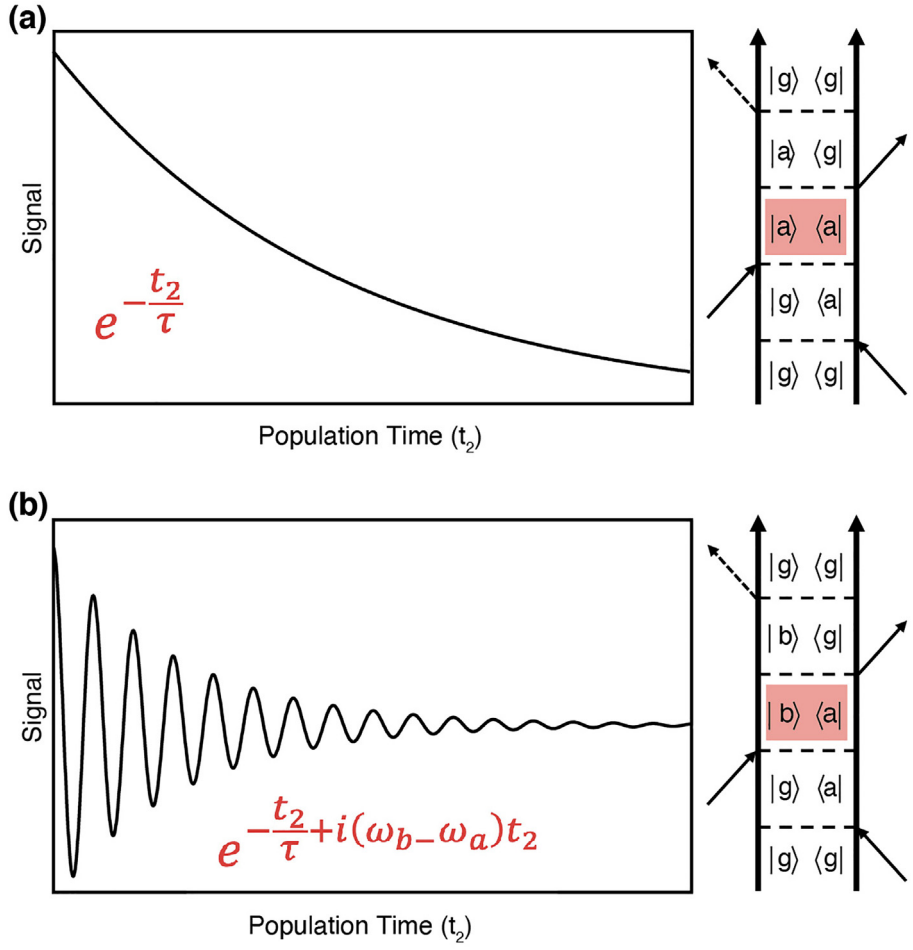

FIG. 8.6 – (right) Examples of Feynman diagrams representing (a) non-oscillating and (b) oscillating contributions to the signal. The oscillation frequency corresponds to the difference between the frequencies of the states involved in the coherent superposition evolving during t_2 (highlighted in red). Left panels sketch the dynamics of the corresponding signals as a function of t_2.

The presence of these oscillations in the amplitude of the signal at specific coordinates is direct evidence for coherent dynamics, *i.e.*, the time evolution of a coherent superposition of states. In other words, the capability of the technique to exploit the phase and coherence information in the time evolution of the optical polarization makes it sensitive to the presence of coherent mechanisms during the time evolution.

Depending on the character of the states involved, vibrational or electronic coherences can be distinguished. The amplitude patterns of the oscillations on the 2D spectra are different in the two cases and they can be used to identify the nature of the observed coherence.[73–76]

Despite the significant differences between electronic and vibrational coherence signatures, because of the broadening of the observed features and laser spectrum distortions, it is not always easy to make a specific assignment.[77] Furthermore, when the electronic coupling between chromophores in the system generates mixed vibro-electronic states ('vibronic' states) the distinction becomes less rigorous and a range of intermediate cases is possible.[78–81]

The identification of coherent beatings in the evolution of 2D maps, the analysis of their frequency and time behavior and the ensuing interpretation of their possible electronic, vibronic or vibrational nature is typically one of the essential steps in the analysis of the results of a 2DES experiment. Actually, it is precisely the sensitivity of 2DES to these beatings and the possibility of spreading their content information along three dimensions (ω_1, ω_3, t_2) that makes this technique so powerful to detect signatures of coherent dynamics, especially in connection with energy, charge or information transport.[17]

8.3 Experimental Considerations and Implementations

One of the key requirements for coherent nonlinear spectroscopy is phase matching, which is achieved by properly adjusting the wavevectors $\boldsymbol{k_i}$ of the incident beams. Depending on the experimental geometry of the incident pulses, the phase-matching condition determines the direction of the signal emission. A range of geometries has been employed for 2DES measurements, including (i) fully non-collinear geometry in which every pulse has a different wavevector (2D photon echo, BOXCARS geometry, figure 8.1b), (ii) partially non-collinear pump-probe geometry in which the first two pulses are collinear and are followed by a probe pulse at a small angle (2D pump-probe) and (iii) fully collinear geometry in which every pulse has the same direction. All implementations have their advantages and disadvantages.[82,83]

The fully non-collinear BOXCARS setup is probably the most frequently employed. In this implementation the signal is generated in a background-free direction, and thus a pivotal advantage is a high signal-to-noise ratio. A fourth pulse called local oscillator (LO) is mixed with the signal in order to recover the phase information from the interference pattern of the two pulses.[84,85]

The main disadvantages of this implementation are the complexity of the setup, whose design must include a passive phase stabilizer, and the fact that the final pulse comes with an arbitrary constant phase that must be determined. The pump-probe projection theorem is usually invoked for the phasing of the signal.[29]

Collinear setups are intrinsically phase-stable because all the interacting pulses travel the same optical path.[86] In these schemes, a pulse shaper is usually used to generate collinear pump pulses, with a known and adjustable relative phase. In the partially non-collinear pump-probe geometry, the probe beam can be either an attenuated replica of the pump or a spectrally broader white light continuum.[87] The advantage of this scheme is that the signal is generated collinearly with the probe beam so that it is heterodyned with the probe itself and, therefore, automatically phased. The most relevant drawbacks are the strong background contribution, which lowers the sensitivity, and the difficulty of accessing the rephasing and non-rephasing portions of the signal separately in a straightforward manner. Indeed, the approaches so far successfully used to isolate the desired signal in a collinear geometry all rely on phase cycling[88,89] or phase modulation[90,91] and some form of lock-in detection. Both approaches are based on the principle that the signal phase depends on the phase of the excitation pulses. In phase cycling schemes, the phases of the excitation pulses are independently rotated by controlled amounts. Different spectra are recorded for any phase combination and then combined to remove any signals that do not depend on the phase of all three excitation pulses as predicted by the response function theory. In a similar way, in phase modulation techniques, a continuous phase oscillation is applied to each of the beams. Therefore, the signal phase will be modulated at different frequencies corresponding to specific linear combinations of the three frequencies used to modulate the phase of the input beams. Signals corresponding to different pathways (for example the rephasing and non-rephasing signals) will be modulated at different frequencies. The rotation or modulation of the phases of the exciting pulses is typically performed by exploiting the same pulse shaper apparatus used to generate the pulse sequence. Thus, additional equipment is not required.

While in its first applications the BOXCARS noncollinear geometry was preferred, lately, collinear setups are quickly gaining ground because of the possibility to switch to the so-called 'action detected' techniques.[92–95] In these configurations, a fourth pulse is added to the pulse sequence to drive the system into an excited or ground state population. In phase modulation or phase cycling schemes, the excited state population is also modulated, and then it can be read out by some other means, for example, photocurrent or photoluminescence. These techniques are interesting in view of characterizing operating devices (see section 8.4).

8.4 Application to Complex Dynamics

Since its first realizations, at the beginning of the 2000s, 2DES has been applied to a wealth of different systems, ranging from biological protein complexes to organic multi-chromophore systems to hybrid and inorganic nano-systems, also in solid-state and in operating devices. In all these applications, 2DES revealed its enormous potential to untangle complex ultrafast dynamics, including coherent and transport dynamics. In the following sections, a few examples of these applications are summarized.

8.4.1 Biological Light Harvesting and Photosynthesis

2DES, especially in the first decade after its practical development, has been often associated with the investigation of energy and charge transfer dynamics in biological photosynthetic processes. Since the first examples of investigations on the excitonic structure and dynamics in the Fenna–Mathew–Olson (FMO) complex,[14,96] 2DES has been applied to many systems and problems in photosynthesis research. For instance, it was used to uncover the mechanisms of charge separation in Photosystem II,[78,97–99] Photosystem I[100,101] and the bacterial reaction centers,[102] untangle the intricate pathways in the light-harvesting antennas of green photosynthetic bacteria,[96,103,104] purple bacteria,[35,68,105] cryptophyte algae,[18,106,107] brown algae,[67,108,109] and green plants.[110–112] Variants of the technique have also been developed to follow the excitation energy flow in intact living cells of photosynthetic organisms.[113,114]

A lot of attention was also paid to studying the dynamics of isolated biologically relevant chromophores in vitro. For example, the ultrafast relaxation dynamics in the sub 100 fs time regime of chlorophyll *a*,[115–118] chlorophyll *b*,[119] bacteriochlorophyll *a*[120] and carotenes[121,122] have been elucidated through 2DES. A thorough characterization of these dynamics is crucial for a complete understanding of the mechanisms regulating the ultrafast dynamics of the relaxation processes in the more complex multi-chromophore light-harvesting systems in which these molecules are embedded.

Several of these studies have been devoted to analyzing the role of quantum coherences in the photosynthetic processes. Despite two decades of investigations, this remains a highly engaging albeit controversial issue. For example, it is not fully clear to what extent it is possible to reliably distinguish contributions from electronic and vibrational coherences, nor if these coherences are fully relevant to the biological functions.[40,42] Nonetheless, apart from this specific aspect, 2DES allowed (and still allows) resolving the dynamics and pathways of energy and electron transport in various light-harvesting antenna systems and reaction centers with an unsurpassed level of detail.

8.4.2 Artificial Molecular Nano-Systems

The investigation on the role of quantum effects in the dynamics of photosynthetic complexes, regardless of whether or not these effects are relevant in nature, had the merit to trigger important new lines of research. Indeed, it is questionable whether quantum effects, even if nature does not exploit them, can be engineered into artificial systems, designed *ad hoc* to control quantum coherent energy or charge transfer.[42,43]

In this sense, 2DES played a crucial role in inspiring new technologies and materials where quantum coherence is used as a new foundational principle to realize devices with improved performances.[123] The challenge is now moving from fundamental studies to real technology, and this requires the development of suitable materials where quantum phenomena are sufficiently controllable to be exploitable. The main complication is that quantum coherence is fragile: the coupling to external

degrees of freedom spoils the unitary quantum evolution very quickly, causing decoherence and loss of information.[124] Indeed, energy and charge transfer dynamics are inevitably affected by the thermal fluctuations of nuclear motions. This is because the magnitude of the fluctuations in site energy and electronic coupling can be comparable with the magnitude of the electronic coupling that causes excitation energy and charge transfer.[125] Therefore, microscopic understanding of the coupling between the electronic system and the environmental bath has been a focus of many studies on exciton and charge transport dynamics. The presence of thermal noise surely indicates the deterioration of system coherence. However, experimental and theoretical works seem to indicate that a fine-tuning of the environmental parameters can lead to a noise-assisted transport.[126–128]

The system-environment coupling is now emerging as one of the key factors to be controlled (and engineered) to be able to fully exploit the quantum nature of the transport processes. Photosynthetic protein complexes represent one of the best examples of how nature can tune the electronic properties of chromophores, their interactions and relaxation and transport dynamics by embedding such chromophores in a suitably 'engineered' environment, *i.e.*, the protein scaffold.[129–134] Inspired by this, several artificial bio-mimetic multi-chromophore systems have been proposed, where the photoactive chromophores were embedded into 'structured environments' by covalent linking or by supramolecular self-assembly techniques. Examples of this approach are: dimers of interacting chromophores mounted on DNA strands,[135–137] chromophores covalently attached to polymeric chains,[138] self-assembled aggregates of dye-functionalized short amino acid sequences[47], porphyrin nanorings,[139] J-aggregates[11], and H-bonded dimers.[140]

This growing amount of evidence is now permitting to extract important structure-to-property relationships for the design of new materials where the control of at least a few relevant aspects of the system-environment coupling leads to the control of coherent dynamics. For example, refs.[129,140] suggest that the establishment of specific and directional interactions like H-bonds, can have very strong consequences for the electronic coupling and thus for the ultrafast dynamics of coupled chromophores. In particular, new intra- and inter-molecular ultrafast relaxation channels can be activated, mediated by the vibrational motions of the hydrogen donor and acceptor groups, even when the coupled chromophores are at significant distances. These findings suggest that the design of H-bonded structures is a particularly powerful tool to drive the ultrafast dynamics in complex materials.

Another significant emerging aspect deals with the flexibility of the scaffold and the different degree of conformational disorder.[16,135,138] It has been verified that conformational disorder affects especially low-frequency vibrational modes, delocalized on the chromophores and the scaffold. The role of low-frequency vibrational modes in the coherent dynamics of complex systems represents a nodal issue in the identification of mechanisms capable of preserving electronic coherence in biological, organic, and inorganic assemblies.[141–143] The decoherence dynamics promoted by conformational disorder is thus emerging as an essential ingredient to describe dynamics and properties of multi-chromophore compounds.

8.4.3 Colloidal Semiconductor Nanocrystals (Quantum Dots)

Semiconductor nanocrystals (quantum dots, QDs) have attracted vast interest given their peculiar size-dependent optical and electronic properties. Since the early 1990s, colloidal synthesis has opened extraordinary possibilities for tuning their optical and electronic properties by controlling size, shape and crystallographic structure. Numerous hetero and hybrid nanostructures have also been proposed.[144–147] The applications of these colloidal nanostructures range from optoelectronic, including photovoltaics, diodes, and photodetectors, to bioimaging and photocatalysis.[148–150] Although the technological exploitation of QDs is an already mature field, several even more promising additional applications can be envisioned, mainly connected with the possibility of exploiting their ultrafast photo-physics, a still under-explored domain. 2DES spectroscopy appears ideally suited for this purpose, but it is only recently that it has been effectively applied to QDs.[151]

For example, ref.[48] represents an excellent example of how it is possible to benefit from the combined use of different 2DES experimental schemes to achieve a comprehensive understanding of the ultrafast relaxation phenomena in QDs samples. As shown in figure 8.7, a fully noncollinear BOXCARS setup has been selected for its better time resolution to access the sub-picosecond dynamics of hot excitons cooling, whereas a partially collinear 2D pump-probe setup granted access to multi-exciton relaxations, whose characterization requires higher fluence and longer time windows. These measurements provided a unique global visualization of the sample dynamics, in view of application to novel and innovative nanomaterials.

A particularly debated topic is the possibility of recording coherent beating in the 2D signal amplitude of QDs samples. The capability to exploit coherent quantum phenomena in nanometer scale materials is at the forefront of the most recent quantum technological applications. However, the development of this technology is strongly dependent on a deep understanding of how to generate, manipulate, and characterize a coherent superposition of quantum states in the nanosystems.[152]

In view of using QDs as candidates for quantum technological devices, the time evolution of coherent superpositions of electronic levels is of fundamental interest not only to understand the mechanisms of dephasing but also to harness the quantum nature of the coherent phenomena in devices.

Although the first investigations on the ultrafast coherent dynamics in semiconductors date back to the 1980s,[153,154] 2DES could really provide remarkable new insights into this topic. Despite the noteworthy recent advancements in data acquisition and analysis techniques, the experimental reports about coherent superpositions of different excitonic bands in QD samples remain limited,[155–159] and the debate about their effective experimental detection is still open.[151]

The main reasons that complicate the detection of coherent dynamics in QDs samples are (i) the inhomogeneous broadening, intrinsically affecting QDs samples and resulting in a quick ensemble dephasing ("fake decoherence")[160] and (ii) the contribution of the non-resonant response of the solvent affecting the dynamics at short time delays (coherent artifact) and also contributing at longer times through impulsive Raman modes.[156,159,161–163] Nonetheless, it was recently found that these

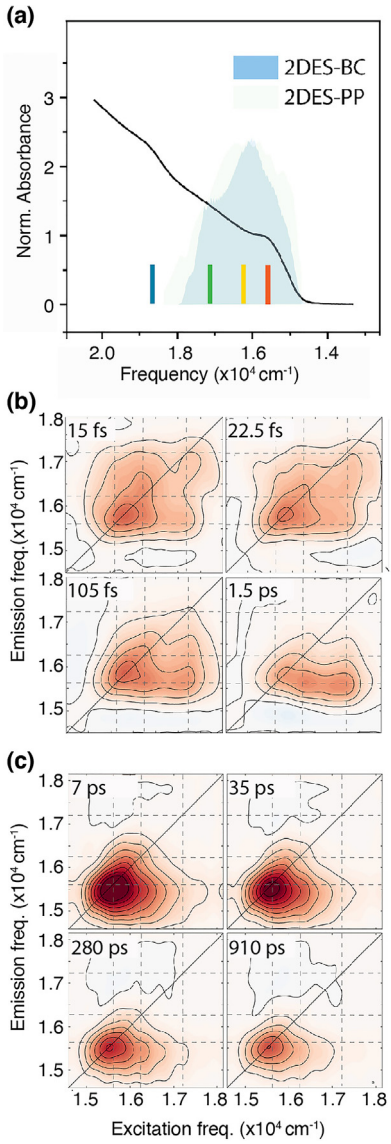

FIG. 8.7 – (a) Absorption spectrum of CdSe/ZnS QDs in chloroform (black solid line). Colored thick lines indicate the peaks of exciton transitions as estimated through a multi-gaussian deconvolution. Green shadowed areas represent the laser bandwidths employed for the 2D experiments. (b) Purely absorptive 2DES maps recorded in the BOXCARS (BC) configuration at selected values of t_2. Dashed lines indicate the energy position of exciton transitions, as assigned in panel (a). (c) Purely absorptive 2D maps recorded in the pump-probe (PP) configuration at selected values of t_2. (Adapted from ref.[48]).

two hindering effects can be overcome through a suitable choice of size dimensions, ligands, and solvent.[15,49] The demonstration that coherent dynamics can emerge even from a sizeable inhomogeneous ensemble is a particularly relevant issue in view of quantum technology applications and coherent control.

8.4.4 Solid-State Materials Based on Semiconductor Nanocrystals

The up-to-date proposals for the realization of QD-based quantum devices are mainly using very low temperatures or room temperature isolated units, where a single excitation per dot is considered, to minimize decoherence effects.[124] However, the possibility of assembling networks of coherently interacting dots at ambient conditions, especially in the solid-state, is particularly interesting for the possibility of large-scale integration and the development of complex connectivity. Indeed, in the context of optical information processing in solids, establishing controlled channels of coupling within an ensemble of isolated units represents a truly challenging but highly rewarding goal.[164,165]

To this aim, solid-state assemblies of colloidally grown QDs[166] appear highly promising. In solid-state assemblies of colloidal QDs, depending on size dimensions and interdot distances, the coupling between different QD units (*inter*-dot coupling) ranges from weak dipole–dipole interactions to a strong exchange interaction, the last involving delocalization of wavefunctions over two or more dots. The collective nature of excitations in these strongly interacting samples can be ascertained by the presence of red-shifted bands in the absorption and photoluminescence spectra[167,168] and improved charge transport[166], as a result of coherent delocalization. However, the effective exploitation of strongly interacting QDs networks envisioned as fundamental units of quantum circuits also requires the dynamical characterization of these collective quantum mechanically coupled states in the ultrafast timescale, although the challenging nature of these measurements hindered for long time a thorough investigation of these dynamics.[160]

In refs.[15,169], 2DES has been applied to disordered solid-state materials of strongly interacting QDs. The results captured the dynamic evolution of a coherent superposition of states delocalized over more than one QD. These data provided important evidence of inter-dot coherences in such solid-state materials, opening new avenues for the effective exploitation of these materials for quantum technologies purposes.

8.4.5 Operating Devices and Chemical Reactions

One of the latest and most promising developments of 2DES is the possibility to replace the coherent optical detection of a third-order signal with the detection of a signal directly generated by an excited state population stimulated by a four pulses sequence. As described in section 8.3, these new action-detected configurations are based on fully collinear geometries.[170]

The first advantage of the collinear alternative is that it allows reducing the interaction volume, for instance using high NA objectives, leading to a better spatial resolution. This points towards the extremely interesting possibility of performing coherent multidimensional spectroscopy at the level of the single molecule. In this context, local microscopic 2DES using fluorescence detection has already been demonstrated by Brixner and Ogilvie groups.[90,171]

Moreover, this configuration intrinsically calls for the combination of 2DES with other spectroscopic techniques. Indeed, the detection is not limited to the nonlinear polarization but potentially extends to any kind of observable proportional to population conditions after the fourth pulse interaction, like fluorescence or photocurrent. In 2014 Karki *et al.* applied photocurrent-detected 2DES to a PbS quantum dot photocell. Sub-picosecond evolution consistent with multiple exciton generation has been found. Since the measurement is based on detecting the photocell current *in situ*, the method is particularly suited to study the fundamental ultrafast processes that affect the function of the device. This opens new avenues to investigate and implement coherent optimization strategies directly within working devices. Ref.[172] discusses all the aspects that make photocurrent-detected 2DES a technique of choice when device photo-physics is concerned.

The correlation with additional observables holds excellent promises to expand the range of physical problems tackled by 2DES. The Brixner group proposed the study of isolated photophysical and photochemical systems by introducing mass spectrometry detection in 2DES.[89] They implemented molecular-beam coherent 2D electronic mass spectrometry, combining 2D spectroscopy in effusive molecular beams with cation detection for probing the final-state population. By investigating the ionization pathways in nitrogen dioxide, they proved that coherent 2D spectroscopy on molecular beams could serve as a complementary tool to condensed-phase techniques resolving otherwise congested 2D spectra of transitions in complex systems due to the narrow linewidths of a gas-phase sample, enabling the 2D spectroscopic study on isolated systems of photophysical and photochemical reactions.

8.5 Concluding Remarks

We hope that at this point, the reader will have been able to recognize the enormous potential and versatility of the 2DES techniques in the investigation of nano-systems, semiconductors, quantum technologies and quantum devices. Several variants of the technique have been developed during these two decades to try to answer specific questions and to adapt them to the characterization of particular systems. It can be predicted that in the coming years even more developments will be proposed. Moreover, while so far 2DES has been mainly performed in advanced spectroscopy labs, the recognized capacity of the techniques in solving complex dynamics calls for technical solutions leading to a more widespread and popular use.

References

[1] Beck A.R., Neumark D.M., Leone S.R. (2015) Probing ultrafast dynamics with attosecond transient absorption, *Chem. Phys. Lett.* **624**, 119. https://doi.org/10.1016/j.cplett.2014.12.048.

[2] Dantus M. (2001) Coherent nonlinear spectroscopy: from femtosecond dynamics to control, *Annu. Rev. Phys. Chem.* **52**, 639. https://doi.org/10.1146/annurev.physchem.52.1.639.

[3] Sundström V. (2008) Femtobiology, *Annu. Rev. Phys. Chem.* **59**, 53. https://doi.org/10.1146/annurev.physchem.59.032607.093615.

[4] Berera R., van Grondelle R., Kennis J.T.M. (2009) Ultrafast transient absorption spectroscopy: principles and application to photosynthetic systems, *Photosynth. Res.* **101**, 105. https://doi.org/10.1007/s11120-009-9454-y.

[5] Motzkus M., Pedersen S., Zewail A.H. (1996) Femtosecond real-time probing of reactions. 19. Nonlinear (DFWM) techniques for probing transition states of uni- and bimolecular reactions, *J. Phys. Chem.* **100**, 5620. https://doi.org/10.1021/jp960265t.

[6] Jimenez R., Fleming G.R., Kumar P.V., Maroncelli M. (1994) Femtosecond solvation dynamics of water, *Nature* **369**, 471. https://doi.org/10.1038/369471a0.

[7] Bolzonello L., Polo A., Volpato A., Meneghin E., Cordaro M., Trapani M., Fortino M., Pedone A., Castriciano M.A., Collini E. (2018) Two-dimensional electronic spectroscopy reveals dynamics and mechanisms of solvent-driven inertial relaxation in polar BODIPY dyes, *J. Phys. Chem. Lett.* **9**, 1079. https://doi.org/10.1021/acs.jpclett.7b03393.

[8] Zewail A.H. (2000) Femtochemistry: atomic-scale dynamics of the chemical bond, *J. Phys. Chem. A.* **104**, 5660. https://doi.org/10.1021/jp001460h.

[9] Li C., Wang A., Deng X., Wang S., Yuan Y., Ding L., Hao F. (2020) Insights into ultrafast carrier dynamics in perovskite thin films and solar cells, *ACS Photonics* **7**, 1893. https://doi.org/10.1021/acsphotonics.0c00677.

[10] Wasielewski M.R. (2006) Energy, charge, and spin transport in molecules and self-assembled nanostructures inspired by photosynthesis, *J. Org. Chem.* **71**, 5051. https://doi.org/10.1021/jo060225d.

[11] Bolzonello L., Fassioli F., Collini E. (2016) Correlated fluctuations and intraband dynamics of J-aggregates revealed by combination of 2DES schemes. *J. Phys. Chem. Lett.* **7**, 4996. https://doi.org/10.1021/acs.jpclett.6b02433.

[12] Collini E., Ferrante C., Bozio R., Lodi A., Ponterini G. (2006) Large third-order nonlinear optical response of porphyrin J-aggregates oriented in self-assembled thin films, *J. Mater. Chem.* **16**, 1573. https://doi.org/10.1039/B517591G.

[13] Scholes G.D., Rumbles G. (2006) Excitons in nanoscale systems, *Nat. Mater.* **5**, 683.

[14] Engel G.S., Calhoun T.R., Read E.L., Ahn T.-K., Mančal T., Cheng Y.-C., Blankenship R. E., Fleming G.R. (2007) Evidence for wavelike energy transfer through quantum coherence in photosynthetic systems, *Nature* **446**, 782. https://doi.org/10.1038/nature05678.

[15] Collini E., Gattuso H., Kolodny Y., Bolzonello L., Volpato A., Fridman H.T., Yochelis S., Mor M., Dehnel J., Lifshitz E., *et al.* (2020) Room-temperature inter-dot coherent dynamics in multilayer quantum dot materials, *J. Phys. Chem. C* **124**, 16222. https://doi.org/10.1021/acs.jpcc.0c05572.

[16] Collini E., Scholes G.D. (2009) Electronic and vibrational coherences in resonance energy transfer along MEH-PPV chains at room temperature', *J. Phys. Chem. A* **113**, 4223. https://doi.org/10.1021/jp810757x.

[17] Collini E. (2013) Spectroscopic signatures of quantum-coherent energy transfer, *Chem. Soc. Rev.* **42**, 4932. https://doi.org/10.1039/c3cs35444j.

[18] Collini E., Wong C.Y., Wilk K.E., Curmi P.M.G., Brumer P., Scholes G.D. (2010) Coherently wired light-harvesting in photosynthetic marine algae at ambient temperature, *Nature* **463**, 644. https://doi.org/10.1038/nature08811.

[19] Lim J., Paleček D., Caycedo-Soler F., Lincoln C.N., Prior J., Von Berlepsch H., Huelga S.F., Plenio M.B., Zigmantas D., Hauer J. (2015) Vibronic origin of long-lived coherence in an artificial molecular light harvester, *Nat. Commun.* **6**, 1. https://doi.org/10.1038/ncomms8755.
[20] Hannaford P. (2005) *Femtosecond laser spectroscopy*. P. Hannaford (ed.) Springer, Boston, MA. https://doi.org/10.1007/b101192.
[21] Mukamel S. (1995) *Principles of nonlinear optical spectroscopy*. Oxford University, Oxford.
[22] Sung J., Silbey R.J. (2001) Four wave mixing spectroscopy for a multilevel system, *J. Chem. Phys.* **115**, 9266. https://doi.org/10.1063/1.1413979.
[23] Mukamel S. (1991) Transient gratings, 4-wave-mixing and polariton effects in nonlinear optics, *Phys. Reports.* **205**, 1. https://doi.org/10.1016/0370-1573(91)90051-M.
[24] Yan Y.J., Fried L.E., Mukamel S. (1989) Ultrafast pump-probe spectroscopy: femtosecond dynamics in liouville space, *J. Phys. Chem.* **93**, 8149. https://doi.org/10.1021/j100362a006.
[25] Carlson R.J., Hurst G.B., Steehler J.K., Riebe M.T. (1991) Molecular, multiresonant coherent 4-wave-mixing spectroscopy, *Int. Rev. Phys. Chem.* **10**, 349. https://doi.org/10.1080/01442359109353262.
[26] Ernst R.R. (1987) *Principles of nuclear magnetic resonance in one and two dimensions*. Clarendon press, Oxford.
[27] Hybl J.D., Albrecht A.W., Gallagher Faeder S.M., Jonas D.M. (1998) Two-dimensional electronic spectroscopy, *Chem. Phys. Lett.* **297**, 307. https://doi.org/10.1016/S0009-2614(98)01140-3.
[28] Prokhorenko V.I., Halpin A., Miller R.J.D. (2009) Coherently-controlled two-dimensional photon echo electronic spectroscopy, *Opt. Express* **17**, 9764. https://doi.org/10.1364/OE.17.009764.
[29] Hybl J.D., Ferro A.A., Jonas D.M. (2001) Two-dimensional fourier transform electronic spectroscopy, *J. Chem. Phys.* **115**, 6606. https://doi.org/10.1063/1.1398579.
[30] Hamm P., Zanni M. (2011) *Concepts and methods of 2D infrared spectroscopy*. Cambridge University Press. https://doi.org/10.1017/CBO9780511675935.
[31] Ogilvie J.P., Armstrong M., Nagy A., Miller R.J.D. (2002) Diffractive optics-based heterodyne detected three-pulse photon echo. In: The Thirteenth International Conference on Ultrafast Phenomena, 2002 OSA Technical Digest Series; Optical Society of America, Vancouver, p. WD20. https://doi.org/10.1364/UP.2002.WD20.
[32] Borrego-Varillas R., Nenov A., Ganzer L., Oriana A., Manzoni C., Tolomelli A., Rivalta I., Mukamel S., Garavelli M., Cerullo G. (2019) Two-dimensional UV spectroscopy: a new insight into the structure and dynamics of biomolecules, *Chem. Sci.* **10**, 9907. https://doi.org/10.1039/C9SC03871J.
[33] Maiuri M., Garavelli M., Cerullo G. (2020) Ultrafast spectroscopy: state of the art and open challenges, *J. Am. Chem. Soc.* **142**, 3. https://doi.org/10.1021/jacs.9b10533.
[34] Mukamel S., Abramavicius, D., Yang L., Zhuang W., Schweigert I.V, Voronine D.V. (2009) Coherent multidimensional optical probes for electron correlations and exciton dynamics: from NMR to X-rays, *Acc. Chem. Res.* **42**, 553. https://doi.org/10.1021/ar800258z.
[35] Zigmantas D., Read E.L., Mancal T., Brixner T., Gardiner A.T., Cogdell R.J., Fleming G.R. (2006) Two-dimensional electronic spectroscopy of the B800–B820 light-harvesting complex, *Proc. Natl. Acad. Sci. U.S.A.* **103**, 12672. https://doi.org/10.1073/pnas.0602961103.
[36] Ishizaki A., Fleming G.R. (2012) Quantum coherence in photosynthetic light harvesting, *Annu. Rev. Condens. Matter Phys.* **3**, 333. https://doi.org/10.1146/annurev-conmatphys-020911-125126.
[37] Huelga S.F., Plenio M.B. (2013) Vibrations, quanta and biology, *Contemp. Phys.* **54**, 181. https://doi.org/10.1080/00405000.2013.829687.
[38] Ball P. (2018) Is photosynthesis quantum-ish? *Physics World*.
[39] Ball P. (2011) Physics of life: the dawn of quantum biology, *Nature* **474**, 272. https://doi.org/10.1038/474272a.

[40] Duan H.-G., Prokhorenko V.I., Cogdell R.J., Ashraf K., Stevens A.L., Thorwart M., Miller R. J.D. (2017) Nature does not rely on long-lived electronic quantum coherence for photosynthetic energy transfer, *Proc. Natl. Acad. Sci.* **114**, 8493. https://doi.org/10.1073/pnas.1702261114.

[41] Cao J., Cogdell R.J., Coker D.F., Duan H.-G., Hauer J., Kleinekathöfer U., Jansen T.L.C., Mančal T., Miller R.J.D., Ogilvie J.P., *et al.* (2020) Quantum biology revisited, *Sci. Adv.* **6**, eaaz4888. https://doi.org/10.1126/sciadv.aaz4888.

[42] Scholes G.D., Fleming G.R., Chen L.X., Aspuru-Guzik A., Buchleitner A. Coker D.F., Engel G.S., Van Grondelle R., Ishizaki A., Jonas D.M., *et al.* (2017) Using coherence to enhance function in chemical and biophysical systems, *Nature* **543**, 647. https://doi.org/10.1038/nature21425.

[43] Scholes G.D., Fleming G.R., Olaya-Castro A., van Grondelle R. (2011) Lessons from nature about solar light harvesting, *Nat. Chem.* **3**, 763.

[44] Kriete B., Lüttig J., Kunsel T., Malý P., Jansen T.L.C., Knoester J., Brixner T., Pshenichnikov M.S. (2019) Interplay between structural hierarchy and exciton diffusion in artificial light harvesting, *Nat. Commun.* **10**, 4615. https://doi.org/10.1038/s41467-019-12345-9.

[45] Brixner T., Hildner R., Koehler J., Lambert C., Wuerthner F. (2017) Exciton transport in molecular aggregates - from natural antennas to synthetic chromophore systems, *Adv. Energy Mater.* **7**. https://doi.org/10.1002/aenm.201700236.

[46] Butkus V., Alster J., Bašinskaitė E., Augulis R., Neuhaus P., Valkunas L., Anderson H.L., Abramavicius D., Zigmantas D. (2017) Discrimination of diverse coherences allows identification of electronic transitions of a molecular nanoring, *J. Phys. Chem. Lett.* **8**, 2344. https://doi.org/10.1021/acs.jpclett.7b00612.

[47] Collini E., Meneghin E., Biscaglia F., Volpato A., Bolzonello L., Pedron D., Frezza E., Ferrarini A., Gobbo M. (2020) Biomimetic nanoarchitectures for light harvesting: self-assembly of pyropheophorbide-peptide conjugates, *J. Phys. Chem. Lett.* **11**, 7972. https://doi.org/10.1021/acs.jpclett.0c02138.

[48] Righetto M., Bolzonello L., Volpato A., Amoruso G., Panniello A., Fanizza E. Striccoli M., Collini E. (2018) Deciphering hot- and multi-exciton dynamics in core–shell QDs by 2D electronic spectroscopies, *Phys. Chem. Chem. Phys.* **20**, 18176. https://doi.org/10.1039/C8CP02574F.

[49] Collini E., Gattuso H., Bolzonello L., Casotto A., Volpato A., Dibenedetto C.N., Fanizza E., Striccoli M., Remacle F. (2019) Quantum phenomena in nanomaterials: coherent superpositions of fine structure states in CdSe nanocrystals at room temperature, *J. Phys. Chem. C* **123**, 31286. https://doi.org/10.1021/acs.jpcc.9b11153.

[50] Guo L., Wu M., Cao T., Monahan D.M., Lee Y.-H., Louie S.G., Fleming G.R. (2019) Exchange-driven intravalley mixing of excitons in monolayer transition metal dichalcogenides, *Nat. Phys.* **15**, 228. https://doi.org/10.1038/s41567-018-0362-y.

[51] Takemura N., Trebaol S., Anderson M.D., Kohnle V., Léger Y., Oberli D.Y., Portella-Oberli M.T., Deveaud B. (2015) Two-dimensional fourier transform spectroscopy of exciton-polaritons and their interactions, *Phys. Rev. B - Condens. Matter Mater. Phys.* **92**, 125415. https://doi.org/10.1103/PhysRevB.92.125415.

[52] Takahashi S., Watanabe K. (2020) Decoupling from a thermal bath *via* molecular polariton formation, *J. Phys. Chem. Lett.* **11**, 1349. https://doi.org/10.1021/acs.jpclett.9b03789.

[53] Karki K.J., Widom J.R., Seibt J., Moody I., Lonergan M.C., Pullerits T., Marcus A.H. (2014) Coherent two-dimensional photocurrent spectroscopy in a PbS quantum dot photocell, *Nat. Commun.* **5**, 1–7. https://doi.org/10.1038/ncomms6869.

[54] Tollerud J.O., Davis J.A. (2017) Coherent multi-dimensional spectroscopy: experimental considerations, direct comparisons and new capabilities, *Prog. Quantum Electron.* **55**, 1–34. https://doi.org/10.1016/j.pquantelec.2017.07.001.

[55] Gelzinis A., Augulis R., Butkus V., Robert, B., Valkunas L. (2019) Two-dimensional spectroscopy for non-specialists, *Biochim. Biophys. Acta - Bioenerg.* **1860**, 271. https://doi.org/10.1016/j.bbabio.2018.12.006.

[56] Brańczyk A.M., Turner D.B., Scholes G.D., Brańczyk A.M., Turner D.B., Scholes G.D. (2014) Crossing disciplines - a view on two-dimensional optical spectroscopy, *Ann. Phys.* **526**, 31–49. https://doi.org/10.1002/andp.201300153.
[57] Cho M. (2008) Coherent two-dimensional optical spectroscopy, *Chem. Rev.* **108**, 1331. https://doi.org/10.1021/cr078377b.
[58] (2019) *Coherent multidimensional spectroscopy*, M. Cho (Ed.) Springer.
[59] Lambrev P.H., Akhtar P., Tan H.S. (2020) Insights into the mechanisms and dynamics of energy transfer in plant light-harvesting complexes from two-dimensional electronic spectroscopy, *Biochim. Biophys. Acta - Bioenerg.* **1861**, 148050. https://doi.org/10.1016/j.bbabio.2019.07.005.
[60] Oliver T.A. (2021) Recent advances in multidimensional ultrafast spectroscopy, *R. Soc. Open Sci.* **5**, 171425. https://doi.org/10.1098/rsos.171425.
[61] Shim S.-H., Zanni M.T. (2009) How to turn your pump-probe instrument into a multidimensional spectrometer: 2D IR and Vis spectroscopies *via* pulse shaping, *Phys. Chem. Chem. Phys.* **11**, 748. https://doi.org/10.1039/b813817f.
[62] Bell R.J. (1972) *Introductory fourier transform spectroscopy*. Academic Press, New York.
[63] Blum K. (2012) *Density matrix theory and applications*. Springer, Berlin Heidelberg, 2012.
[64] Nemeth A., Milota F., Mančal T., Pullerits T., Sperling J., Hauer J., Kauffmann H.F., Christensson N. (2010) Double-quantum two-dimensional electronic spectroscopy of a three-level system: experiments and simulations, *J. Chem. Phys.* **133**, 94505. https://doi.org/10.1063/1.3474995.
[65] Roberts S.T., Loparo J.J., Tokmakoff A. (2006) Characterization of spectral diffusion from two-dimensional line shapes, *J. Chem. Phys.* **125**, 84502. https://doi.org/10.1063/1.2232271.
[66] van Amerongen H., van Grondelle R., Valkunas L. (2000) *Photosynthetic excitons*. World Scientific, Singapore, https://doi.org/doi:10.1142/3609.
[67] Meneghin E., Volpato A., Cupellini L., Bolzonello L., Jurinovich S., Mascoli V., Carbonera D., Mennucci B., Collini E. (2018) Coherence in carotenoid-to-chlorophyll energy transfer, *Nat. Commun.* **9**, 3160. https://doi.org/10.1038/s41467-018-05596-5.
[68] Ostroumov E.E., Mulvaney R.M., Cogdell R.J., Scholes G.D. (2013) Broadband 2D electronic spectroscopy reveals a carotenoid dark state in purple bacteria, *Science* **340**, 52. https://doi.org/10.1126/science.1230106.
[69] Kavoulakis G.M. (2003) Bose–Einstein condensation of indirect excitons in coupled quantum wells, *J. Low Temp. Phys.* **132**, 297. https://doi.org/10.1023/A:1024848516551.
[70] Valkunas L., Abramavicius D., Mančal T. (2013) *Molecular excitation dynamics and relaxation. Quantum theory and spectroscopy*. Wiley-VCH, Weinheim.
[71] van Stokkum I.H.M., Larsen D.S., van Grondelle R. (2004) Global and target analysis of time-resolved spectra, *Biochim. Biophys. Acta - Bioenerg.* **1657**, 82. https://doi.org/10.1016/j.bbabio.2004.04.011.
[72] Volpato A., Bolzonello L., Meneghin E., Collini E. (2016) Global analysis of coherence and population dynamics in 2D electronic spectroscopy, *Opt. Express* **24**, 24773. https://doi.org/10.1364/oe.24.024773.
[73] Butkus V., Zigmantas D., Valkunas L., Abramavicius D. (2012) Vibrational *vs.* electronic coherences in 2D spectrum of molecular systems, *Chem. Phys. Lett.* **545**, 40. https://doi.org/10.1016/j.cplett.2012.07.014.
[74] Butkus V., Zigmantas D., Abramavicius D., Valkunas L. (2013) Distinctive character of electronic and vibrational coherences in disordered molecular aggregates, *Chem. Phys. Lett.* **587**, 93. https://doi.org/10.1016/j.cplett.2013.09.043.
[75] Turner D.B., Wilk K.E., Curmi P.M.G., Scholes G.D. (2011) Comparison of electronic and vibrational coherence measured by two-dimensional electronic spectroscopy, *J. Phys. Chem. Lett.* **2**, 1904. https://doi.org/10.1021/jz200811p.
[76] Perlík V., Lincoln C., Šanda F., Hauer J. (2014) Distinguishing electronic and vibronic coherence in 2D spectra by their temperature dependence, *J. Phys. Chem. Lett.* **5**, 404. https://doi.org/10.1021/jz402468c.

[77] Camargo F.V.D.A., Grimmelsmann L., Anderson L., Meech S.R., Heisler I.A. (2017) Resolving vibrational from electronic coherences in two-dimensional electronic spectroscopy: the role of the laser spectrum, *Phys. Rev. Lett.* **118**, 033001. https://doi.org/10.1103/PhysRevLett.118.033001.

[78] Fuller F.D., Pan J., Gelzinis A., Butkus V., Senlik S.S., Wilcox D.E., Yocum C.F., Valkunas L., Abramavicius D., Ogilvie J. P. (2014) Vibronic coherence in oxygenic photosynthesis, *Nat. Chem.* **6**, 706. https://doi.org/10.1038/nchem.2005.

[79] Milota F., Prokhorenko V.I., Mancal T., von Berlepsch H., Bixner O., Kauffmann H.F., Hauer J. (2013) Vibronic and vibrational coherences in two-dimensional electronic spectra of supramolecular J-Aggregates, *J. Phys. Chem. A* **117**, 6007. https://doi.org/10.1021/jp3119605.

[80] Butkus V., Valkunas L., Abramavicius D. (2014) Vibronic phenomena and exciton–vibrational interference in two-dimensional spectra of molecular aggregates, *J. Chem. Phys.* **140**, 34306. https://doi.org/10.1063/1.4861466.

[81] Bašinskaitė E., Butkus V., Abramavicius D., Valkunas L. (2014) Vibronic models for nonlinear spectroscopy simulations, *Photosynth. Res.* **121**, 95. https://doi.org/10.1007/s11120-014-0002-z.

[82] Heisler I.A., Moca R., Camargo F.V.A., Meech S.R. (2014) Two-dimensional electronic spectroscopy based on conventional optics and fast dual chopper data acquisition, *Rev. Sci. Instrum.* **85**, 63103. https://doi.org/10.1063/1.4879822.

[83] Fuller F.D., Ogilvie J.P. (2015) Experimental implementations of two-dimensional fourier transform electronic spectroscopy, *Annu. Rev. Phys. Chem.* **66**, 667. https://doi.org/10.1146/annurev-physchem-040513-103623.

[84] Levenson M.D., Eesley G.L. (1979) Polarization selective optical heterodyne detection for dramatically improved sensitivity in laser spectroscopy, *Appl. Phys.* **19**, 1. https://doi.org/10.1007/BF00900531.

[85] Lepetit L., Chériaux G., Joffre M. (1995) Linear techniques of phase measurement by femtosecond spectral interferometry for applications in spectroscopy, *J. Opt. Soc. Am. B* **12**, 2467. https://doi.org/10.1364/JOSAB.12.002467.

[86] Tian P.F., Keusters D., Suzaki Y., Warren W.S. (2003) Femtosecond phase-coherent two-dimensional spectroscopy, *Science* **300**, 15553.

[87] Tekavec P.F., Myers J.A., Lewis K.L.M., Ogilvie J.P. (2009) Two-dimensional electronic spectroscopy with a continuum probe, *Opt. Lett.* **34**, 1390. https://doi.org/10.1364/OL.34.001390.

[88] Zhang Z., Wells L., Hyland E., Tan H.-S. (2012) Phase-cycling schemes for pump–probe beam geometry two-dimensional electronic spectroscopy, *Chem. Phys. Lett.* **550**, 156. https://doi.org/10.1016/j.cplett.2012.08.037.

[89] Roeding S., Brixner T. (2018) Coherent two-dimensional electronic mass spectrometry, *Nat. Commun.* **9**, 2519. https://doi.org/10.1038/s41467-018-04927-w.

[90] Tiwari V., Matutes Y.A., Gardiner A.T., Jansen T.L.C., Cogdell R.J., Ogilvie J.P. (2018) Spatially-resolved fluorescence-detected two-dimensional electronic spectroscopy probes varying excitonic structure in photosynthetic bacteria, *Nat. Commun.* **9**, 4219. https://doi.org/10.1038/s41467-018-06619-x.

[91] Tiwari V., Matutes Y.A., Konar A., Yu Z., Ptaszek M., Bocian D.F., Holten D., Kirmaier C., Ogilvie J.P. (2018) Strongly coupled bacteriochlorin dyad studied using phase-modulated fluorescence-detected two-dimensional electronic spectroscopy, *Opt. Express* **26**, 22327. https://doi.org/10.1364/OE.26.022327.

[92] Damtie F.A., Wacker A., Pullerits T., Karki K.J. (2017) Two-dimensional action spectroscopy of excitonic systems: explicit simulation using a phase-modulation technique, *Phys. Rev. A* **96**, 53830. https://doi.org/10.1103/PhysRevA.96.053830.

[93] Nardin G., Autry T.M., Silverman K.L., Cundiff S.T. (2013) Multidimensional coherent photocurrent spectroscopy of a semiconductor nanostructure, *Opt. Express* **21**, 28617. https://doi.org/10.1364/OE.21.028617.

[94] Osipov V.A., Shang X., Hansen T., Pullerits T., Karki K.J. (2016) Nature of relaxation processes revealed by the action signals of intensity-modulated light fields, *Phys. Rev. A* **94**, 53845. https://doi.org/10.1103/PhysRevA.94.053845.

[95] Vella E., Li H., Grégoire P., Tuladhar S.M., Vezie M.S., Few S., Bazán C.M., Nelson J., Silva-Acuña C., Bittner E.R. (2016) Ultrafast decoherence dynamics govern photocarrier generation efficiencies in polymer solar cells, *Sci. Rep.* **6**, 29437. https://doi.org/10.1038/srep29437.

[96] Brixner T., Stenger J., Vaswani H.M., Cho M., Blankenship R.E., Fleming G.R. (2005) Two-dimensional spectroscopy of electronic couplings in photosynthesis, *Nature* **434**, 625. https://doi.org/10.1038/nature03429.

[97] Romero E., Augulis R., Novoderezhkin V.I., Ferretti M., Thieme J., Zigmantas D., van Grondelle R. (2014) Quantum coherence in photosynthesis for efficient solar-energy conversion, *Nat. Phys.* **10**, 676. https://doi.org/10.1038/nphys3017.

[98] Duan H.-G., Prokhorenko V.I., Wientjes E., Croce R., Thorwart M., Miller R.J.D. (2017) Primary charge separation in the photosystem II reaction center revealed by a global analysis of the two-dimensional electronic spectra, *Sci. Rep.* **7**, 12347. https://doi.org/10.1038/s41598-017-12564-4.

[99] Pan J., Gelzinis A., Chorošajev V., Vengris M., Senlik S.S., Shen J.-R., Valkunas L., Abramavicius D., Ogilvie J.P. (2017) Ultrafast energy transfer within the photosystem II core complex, *Phys. Chem. Chem. Phys.* **19**, 15356. https://doi.org/10.1039/C7CP01673E.

[100] Akhtar P., Zhang C., Liu Z., Tan H.-S., Lambrev P.H. (2018) Excitation transfer and trapping kinetics in plant photosystem I probed by two-dimensional electronic spectroscopy, *Photosynth. Res.* **135**, 239. https://doi.org/10.1007/s11120-017-0427-2.

[101] Lee Y., Gorka M., Golbeck J.H., Anna J.M. (2013) Ultrafast energy transfer involving the red chlorophylls of cyanobacterial photosystem I probed through two-dimensional electronic spectroscopy, *J. Am. Chem. Soc.* **140**, 11631. https://doi.org/10.1021/jacs.8b04593.

[102] Ma F., Romero E., Jones M.R., Novoderezhkin V.I., van Grondelle R. (2019) Both electronic and vibrational coherences are involved in primary electron transfer in bacterial reaction center, *Nat. Commun.* **10**, 933. https://doi.org/10.1038/s41467-019-08751-8.

[103] Dostál J., Mančal T., Augulis R., Vácha F., Pšenčík J., Zigmantas D. (2012) Two-dimensional electronic spectroscopy reveals ultrafast energy diffusion in chlorosomes, *J. Am. Chem. Soc.* **134**, 11611. https://doi.org/10.1021/ja3025627.

[104] Thyrhaug E., Žídek K., Dostál J., Bína D., Zigmantas D. (2016) Exciton structure and energy transfer in the Fenna–Matthews–Olson complex, *J. Phys. Chem. Lett.* **7**, 1653. https://doi.org/10.1021/acs.jpclett.6b00534.

[105] Ferretti M., Hendrikx R., Romero E., Southall J., Cogdell R.J., Novoderezhkin V.I., Scholes G.D., van Grondelle R. (2016) Dark states in the light-harvesting complex 2 revealed by two-dimensional electronic spectroscopy, *Sci. Rep.* **6**, 20834.

[106] Richards G.H., Wilk K.E., Curmi P.M.G., Quiney H.M., Davis J.A. (2012) Excited state coherent dynamics in light-harvesting complexes from photosynthetic marine algae, *J. Phys. B At. Mol. Opt. Phys.* **45**, 154015. https://doi.org/10.1088/0953-4075/45/15/154015.

[107] Harrop S.J., Wilk K.E., Dinshaw R., Collini E., Mirkovic T., Teng C.Y., Oblinsky D.G., Green B.R., Hoef-Emden K., Hiller R.G., *et al.* (2014) Single-residue insertion switches the quaternary structure and exciton states of cryptophyte light-harvesting proteins, *Proc. Natl. Acad. Sci. U.S.A.* **111**. https://doi.org/10.1073/pnas.1402538111.

[108] Butkus V., Gelzinis A., Augulis R., Gall A., Büchel C., Robert B., Zigmantas D., Valkunas L., Abramavicius D. (2015) Coherence and population dynamics of chlorophyll excitations in FCP complex: two-dimensional spectroscopy study, *J. Chem. Phys.* **142**, 212414. https://doi.org/10.1063/1.4914098.

[109] Gelzinis A., Butkus V., Songaila E., Augulis R., Gall A., Büchel C., Robert B., Abramavicius D., Zigmantas D., Valkunas L. (2015) Mapping energy transfer channels in fucoxanthin–chlorophyll protein complex, *Biochim. Biophys. Acta - Bioenerg.* **1847**, 241. https://doi.org/10.1016/j.bbabio.2014.11.004.

[110] Son M., Pinnola A., Bassi R., Schlau-Cohen G.S. (2019) The electronic structure of lutein 2 is optimized for light harvesting in plants, *Chem.* **5**, 575. https://doi.org/10.1016/j.chempr.2018.12.016.
[111] Schlau-Cohen G.S., Calhoun T.R., Ginsberg N.S., Read E.L., Ballottari M., Bassi R., van Grondelle R., Fleming G.R. (2009) Pathways of energy flow in LHCII from two-dimensional electronic spectroscopy, *J. Phys. Chem. B.* **113**, 15352. https://doi.org/10.1021/jp9066586.
[112] Duan H.-G., Stevens A.L., Nalbach P., Thorwart M., Prokhorenko V.I., Miller R.J.D. (2015) Two-dimensional electronic spectroscopy of light-harvesting complex II at ambient temperature: a joint experimental and theoretical study, *J. Phys. Chem. B.* **119**, 12017. https://doi.org/10.1021/acs.jpcb.5b05592.
[113] Dahlberg P.D., Fidler A.F., Caram J.R., Long P.D., Engel G.S. (2013) Energy transfer observed in live cells using two-dimensional electronic spectroscopy, *J. Phys. Chem. Lett.* **4**, 3636. https://doi.org/10.1021/jz401944q.
[114] Dostál J., Pšenčík J., Zigmantas D. (2016) *In situ* mapping of the energy flow through the entire photosynthetic apparatus, *Nat. Chem.* **8**, 705. https://doi.org/10.1038/nchem.2525.
[115] Meneghin E., Pedron D., Collini E. (2018) Raman and 2D electronic spectroscopies: a fruitful alliance for the investigation of ground and excited state vibrations in chlorophyll *a*, *Chem. Phys.* **514**, 132. https://doi.org/10.1016/j.chemphys.2018.03.003.
[116] Moca R., Meech S.R., Heisler I.A. (2015) Two-dimensional electronic spectroscopy of chlorophyll *a*: solvent dependent spectral evolution, *J. Phys. Chem. B* 119, 8623. https://doi.org/10.1021/acs.jpcb.5b04339.
[117] Meneghin E., Leonardo C., Volpato A., Bolzonello L., Collini E. (2017) Mechanistic insight into internal conversion process within Q-bands of chlorophyll *a*, *Sci. Rep.* **7**, 11389. https://doi.org/10.1038/s41598-017-11621-2.
[118] Senlik S.S., Policht V.R., Ogilvie J.P. (2015) Two-color nonlinear spectroscopy for the rapid acquisition of coherent dynamics, *J. Phys. Chem. Lett.* **6**, 2413. https://doi.org/10.1021/acs.jpclett.5b00861.
[119] Fresch E., Collini E. (2020) Relaxation dynamics of chlorophyll *b* in the sub-ps ultrafast timescale measured by 2D electronic spectroscopy, *Int. J. Mol. Sci.* **21**, 2836. https://doi.org/10.3390/ijms21082836.
[120] Meneghin E., Pedron D., Collini E. (2019) Characterization of the coherent dynamics of bacteriochlorophyll *a* in solution, *Chem. Phys.* **519**, 85. https://doi.org/10.1016/j.chemphys.2018.12.008.
[121] Calhoun T.R., Davis J.A., Graham M.W., Fleming G.R. (2012) The separation of overlapping transitions in beta-carotene with broadband 2D electronic spectroscopy, *Chem. Phys. Lett.* **523**, 1. https://doi.org/10.1016/j.cplett.2011.10.051.
[122] Christensson N., Milota F., Nemeth A., Sperling J., Kauffmann H.F., Pullerits T., Hauer J. (2009) Two-dimensional electronic spectroscopy of beta-carotene, *J. Phys. Chem. B* **113**, 16409. https://doi.org/10.1021/jp906604j.
[123] Schleich W.P., Ranade K.S., Anton C., Arndt M., Aspelmeyer M., Bayer M., Berg G., Calarco T., Fuchs H., Giacobino E., *et al.* (2016) Quantum technology: from research to application, *Appl. Phys. B* **122**, 130. https://doi.org/10.1007/s00340-016-6353-8.
[124] Schlosshauer M.A. (2007) *Decoherence and the quantum-to-classical transition.* Springer-Verlag Berlin Heidelberg, Berlin.
[125] May V., Kühn O. (2011) *Charge and energy transfer dynamics in molecular systems*, 3rd edn. Wiley Online Books, Wiley-VCH Verlag GmbH, Weinheim. https://doi.org/10.1002/9783527633791.fmatter.
[126] Maier C., Brydges T., Jurcevic P., Trautmann N., Hempel C., Lanyon B.P., Hauke P., Blatt R., Roos C.F. (2019) Environment-assisted quantum transport in a 10-qubit network, *Phys. Rev. Lett.* **122**, 50501. https://doi.org/10.1103/PhysRevLett.122.050501.
[127] Plenio M.B., Huelga S.F. (2008) Dephasing-assisted transport: quantum networks and biomolecules, *New J. Phys.* **10**, 113019. https://doi.org/10.1088/1367-2630/10/11/113019.
[128] Rebentrost P., Mohseni M., Kassal I., Lloyd S., Aspuru-Guzik A. (2009) Environment-assisted quantum transport, *New J. Phys.* **11**, 33003. https://doi.org/10.1088/1367-2630/11/3/033003.

[129] Fresch E., Meneghin E., Agostini A., Paulsen H., Carbonera D., Collini E. (2020) How the protein environment can tune the energy, the coupling, and the ultrafast dynamics of interacting chlorophylls: the example of the water-soluble chlorophyll protein. *J. Phys. Chem. Lett.* **11**, 1059. https://doi.org/10.1021/acs.jpclett.9b03628.

[130] Dean J.C., Scholes G.D. (2017) Coherence spectroscopy in the condensed phase: insights into molecular structure, environment, and interactions. *Acc. Chem. Res.* **50**, 2746. https://doi.org/10.1021/acs.accounts.7b00369.

[131] Cui X., Yan Y., Wei J. (2020) Theoretical study on the effect of environment on excitation energy transfer in photosynthetic light-harvesting systems, *J. Phys. Chem. B* **124**, 2354. https://doi.org/10.1021/acs.jpcb.0c00266.

[132] Yeh S.-H., Hoehn R.D., Allodi M.A., Engel G.S., Kais S. (2019) Elucidation of near-resonance vibronic coherence lifetimes by nonadiabatic electronic-vibrational state character mixing, *Proc. Natl. Acad. Sci.* **116**, 18263. https://doi.org/10.1073/pnas.1701390115.

[133] Oh S.A., Coker D.F., Hutchinson D.A.W. (2019) Optimization of energy transport in the fenna-matthews-olson complex via site-varying pigment-protein interactions, *J. Chem. Phys.* **150**, 85102. https://doi.org/10.1063/1.5048058.

[134] Son M., Pinnola A., Gordon S.C., Bassi R., Schlau-Cohen G.S. (2020) Observation of dissipative chlorophyll-to-carotenoid energy transfer in light-harvesting complex II in membrane nanodiscs, *Nat. Commun.* **11**, 1295. https://doi.org/10.1038/s41467-020-15074-6.

[135] Cipolloni M., Fresch B., Occhiuto I., Rukin P., Komarova K.G., Cecconello A., Willner I., Levine R.D., Remacle F., Collini E. (2017) Coherent electronic and nuclear dynamics in a rhodamine heterodimer-DNA supramolecular complex, *Phys. Chem. Chem. Phys.* **19**, 23043. https://doi.org/10.1039/c7cp01334e.

[136] Fresch B., Cipolloni M., Yan T.-M., Collini E., Levine R.D.D., Remacle F. (2015) Parallel and multivalued logic by the two-dimensional photon-echo response of a rhodamine-DNA complex, *J. Phys. Chem. Lett.* **6**, 1714. https://doi.org/10.1021/acs.jpclett.5b00514.

[137] Sohail S.H., Otto J.P., Cunningham P.D., Kim Y.C., Wood R.E., Allodi M.A., Higgins J.S., Melinger J.S., Engel G.S. (2020) DNA scaffold supports long-lived vibronic coherence in an indodicarbocyanine (Cy5) dimer, *Chem. Sci.* **11**, 8546. https://doi.org/10.1039/D0SC01127D.

[138] Volpato A., Zerbetto M., Bolzonello L., Meneghin E., Fresch B., Benelli T., Giorgini L., Collini E. (2019) Effect of different conformational distributions on the ultrafast coherence dynamics in porphyrin-based polymers, *J. Phys. Chem. C* **123**, 10212.

[139] Butkus V., Alster J., Bašinskaite E., Augulis R.R.R., Neuhaus P., Valkunas L., Anderson H. L., Abramavicius D., Zigmantas D., Bašinskaitė E., *et al.* (2017) Discrimination of diverse coherences allows identification of electronic transitions of a molecular nanoring, *J. Phys. Chem. Lett.* **8**, 2344. https://doi.org/10.1021/acs.jpclett.7b00612.

[140] Fresch E., Peruffo N., Trapani M., Cordaro M., Bella G., Castriciano M.A., Collini E. (2021) The effect of hydrogen bonds on the ultrafast relaxation dynamics of a BODIPY dimer, *J. Chem. Phys.* **154**, 084201.

[141] Rolczynski B.S., Zheng H., Singh V.P., Navotnaya P., Ginzburg A.R., Caram J.R., Ashraf K., Gardiner A.T., Yeh S.H., Kais S., *et al.* (2018) Correlated protein environments drive quantum coherence lifetimes in photosynthetic pigment-protein complexes, *Chem* **4**, 138. https://doi.org/10.1016/j.chempr.2017.12.009.

[142] Pal S., Nijjar P., Frauenheim T., Prezhdo O.V. (2017) Atomistic analysis of room temperature quantum coherence in two-dimensional CdSe nanostructures, *Nano Lett.* **17**, 2389. https://doi.org/10.1021/acs.nanolett.6b05368.

[143] Brédas J.-L., Silbey R. (2009) Excitons surf along conjugated polymer chains, *Science* **323**, 348. https://doi.org/10.1126/science.1168821.

[144] Panniello A., Trapani M., Cordaro M., Dibenedetto C.N., Tommasi R., Ingrosso C., Fanizza E., Grisorio R., Collini E., Agostiano A., *et al.* (2021) High-efficiency FRET processes in BODIPY-functionalized quantum dot architectures, *Chem. - A Eur. J.* **27**, 2371. https://doi.org/10.1002/chem.202003574.

[145] Cui J., Panfil Y.E., Koley S., Shamalia D., Waiskopf N., Remennik S., Popov I., Oded M., Banin U. (2019) Colloidal quantum dot molecules manifesting quantum coupling at room temperature, *Nat. Commun.* **10**, 5401. https://doi.org/10.1038/s41467-019-13349-1.
[146] Wu J., Wang Z.M. (2014) *Quantum dot molecules*. J. Wu, Z.M. Wang, Eds., Lecture Notes in Nanoscale Science and Technology, Springer.
[147] Cohen E., Komm P., Rosenthal-Strauss N., Dehnel J., Lifshitz E., Yochelis S., Levine R.D., Remacle F., Fresch B., Marcus G., *et al.* (2018) Fast energy transfer in CdSe quantum dot layered structures: controlling coupling with covalent-bond organic linkers, *J. Phys. Chem. C* **122**, 5753. https://doi.org/10.1021/acs.jpcc.7b11799.
[148] Woggon U. (2014) *Optical properties of semiconductor quantum dots*. Springer Tracts in Modern Physics, Springer-Verlag, Berlin-Heidelberg.
[149] (2013) *Colloidal quantum dot optoelectronics and photovoltaics*. G. Konstantatos, E.H. Sargent, Eds., Cambridge University Press, Cambridge.
[150] Klimov V.I. (2010) *Nanocrystal quantum dots,* 2nd edn. CRC Press, Boca Raton, FL.
[151] Cassette E., Dean J.C., Scholes G.D. (2016) Two-dimensional visible spectroscopy for studying colloidal semiconductor nanocrystals, *Small* **12**, 2234. https://doi.org/10.1002/smll.201502733.
[152] MacFarlane A.G.J., Dowling J.P., Milburn G.J. (2003) Quantum technology: the second quantum revolution, *Philos. Trans. R. Soc. London. Ser. A Math. Phys. Eng. Sci.* **361**, 1655. https://doi.org/10.1098/rsta.2003.1227.
[153] Langer V., Stolz H., von der Osten W. (1990) Observation of quantum beats in the resonance fluorescence of free excitons, *Phys. Rev. Lett.* **64**, 854. https://doi.org/10.1103/PhysRevLett.64.854.
[154] Masumoto Y., Shionoya S., Takagahara T. (1983) Optical dephasing of excitonic polaritons in CuCl studied by time-resolved, nondegenerate four-wave mixing, *Phys. Rev. Lett.* **51**, 923. https://doi.org/10.1103/PhysRevLett.51.923.
[155] Kohler D.D., Block S.B., Kain S., Pakoulev A.V., Wright J.C. (2014) Ultrafast dynamics within the 1S exciton band of colloidal PbSe Quantum dots using multiresonant coherent multidimensional spectroscopy, *J. Phys. Chem. C* **118**, 5020. https://doi.org/10.1021/jp412058u.
[156] Caram J.R., Zheng H., Dahlberg P.D., Rolczynski B.S., Griffin G.B., Fidler A.F., Dolzhnikov D.S., Talapin D.V., Engel G.S. (2014) Persistent interexcitonic quantum coherence in CdSe quantum dots, *J. Phys. Chem. Lett.* **5**, 196. https://doi.org/10.1021/jz402336t.
[157] Cassette E., Pensack R.D., Mahler B., Scholes G.D. (2015) Room-temperature exciton coherence and dephasing in two-dimensional nanostructures, *Nat. Commun.* **6**, 6086.
[158] Dong S., Trivedi D., Chakrabortty S., Kobayashi T., Chan Y., Prezhdo O.V., Loh Z.-H. (2015) Observation of an excitonic quantum coherence in CdSe nanocrystals, *Nano Lett.* **15**, 6875. https://doi.org/10.1021/acs.nanolett.5b02786.
[159] Turner D.B., Hassan Y., Scholes G.D. (2012) Exciton superposition states in CdSe nanocrystals measured using broadband two-dimensional electronic spectroscopy, *Nano Lett.* **12**, 880. https://doi.org/10.1021/nl2039502.
[160] Pelzer K.M., Griffin G.B., Gray S.K., Engel G.S. Inhomogeneous dephasing masks coherence lifetimes in ensemble measurements, *J. Chem. Phys.* **136**, 164508. https://doi.org/10.1063/1.4704591.
[161] Kobayashi Y., Chuang C.-H., Burda C., Scholes G.D. (2014) Exploring ultrafast electronic processes of quasi-type II nanocrystals by two-dimensional electronic spectroscopy. *J. Phys. Chem. C* **118**, 16255. https://doi.org/10.1021/jp504559s.
[162] Seiler H., Palato S., Sonnichsen C., Baker H., Kambhampati P. (2018) Seeing multiexcitons through sample inhomogeneity: band-edge biexciton structure in CdSe nanocrystals revealed by two-dimensional electronic spectroscopy, *Nano Lett.* **18**, 2999. https://doi.org/10.1021/acs.nanolett.8b00470.
[163] Griffin G.B., Ithurria S., Dolzhnikov D.S., Linkin A., Talapin D.V., Engel G.S. (2013) Two-dimensional electronic spectroscopy of CdSe nanoparticles at very low pulse power, *J. Chem. Phys.* **138**, 14705. https://doi.org/10.1063/1.4772465.

[164] Awschalom D.D., Hanson R., Wrachtrup J., Zhou B.B. (2018) Quantum technologies with optically interfaced solid-state spins, *Nat. Photonics* **12**, 516. https://doi.org/10.1038/s41566-018-0232-2.

[165] Zhong T., Goldner P. (2019) Emerging rare-earth doped material platforms for quantum nanophotonics, *Nanophotonics* **8**, 2003. https://doi.org/10.1515/nanoph-2019-0185.

[166] Kagan C.R., Murray C.B. (2015) Charge transport in strongly coupled quantum dot solids, *Nat. Nanotechnol.* **10**, 1013. https://doi.org/10.1038/nnano.2015.247.

[167] Artemyev M.V., Woggon U., Jaschinski H., Gurinovich L.I., Gaponenko S.V. (2000) Spectroscopic study of electronic states in an ensemble of close-packed CdSe nanocrystals, *J. Phys. Chem. B* **104**, 11617. https://doi.org/10.1021/jp002085w.

[168] Mićić O.I., Ahrenkiel S.P., Nozik A.J. (2001) Synthesis of extremely small InP quantum dots and electronic coupling in their disordered solid films, *Appl. Phys. Lett.* **78**, 4022. https://doi.org/10.1063/1.1379990.

[169] Collini E., Gattuso H., Levine R.D., Remacle F. (2021) Ultrafast fs coherent excitonic dynamics in CdSe quantum dots assemblies addressed and probed by 2D electronic spectroscopy, *J. Chem. Phys.* **154**, 14301. https://doi.org/10.1063/5.0031420.

[170] Kühn O., Mančal T., Pullerits T. (2020) Interpreting fluorescence detected two-dimensional electronic spectroscopy, *J. Phys. Chem. Lett.* **11**, 838. https://doi.org/10.1021/acs.jpclett.9b03851.

[171] Goetz S., Li D., Kolb V., Pflaum J., Brixner T. (2018) Coherent two-dimensional fluorescence micro-spectroscopy, *Opt. Express* **26**, 3915. https://doi.org/10.1364/OE.26.003915.

[172] Bakulin A.A., Silva C., Vella E. (2016) Ultrafast spectroscopy with photocurrent detection: watching excitonic optoelectronic systems at work, *J. Phys. Chem. Lett.* **7**, 250. https://doi.org/10.1021/acs.jpclett.5b01955.

Chapter 9

Nonlinear Optical Imaging at the Nanoscale

Sophie Brasselet*

Aix-Marseille Université, CNRS, Centrale Marseille, Institut Fresnel,
F-13013 Marseille, France

Nonlinear optical frequency mixing of short (∼ps–100 fs) pulses offers today tremendous possibilities for imaging, in particular in biological media. It provides the possibility to access, at hundreds of micrometers deep into tissues, a new understanding on tissue morphology at a resolution of a few hundreds of nanometers, based on the intrinsic responses from protein and lipid assemblies. Explorations cover fundamental cell and tissue biology as well as biomedical optics, towards applications for clinics. This lecture covers fundamentals and latest advances in the field of nonlinear imaging, based on multiphoton fluorescence, coherent frequency generation (second and third harmonic generation) as well as frequency mixing, in particular coherent Raman scattering, which is able to detect specifically molecular vibrations based on a resonant four wave mixing process. We will address the current challenges faced by nonlinear imaging; first, how to use light polarization to gain new information on real-time molecular organizations at the nanoscale; second, how to overcome the detrimental effect of light scattering in complex media such as biological tissues.

9.1 Introduction

Optical microscopy is an extraordinary tool for the investigation of phenomena that occur at the sub-micrometric scale in molecular, biological, synthetized or

*sophie.brasselet@fresnel.fr

DOI: 10.1051/978-2-7598-2719-0.c009

nano-fabricated samples. Microscopy imaging has considerably evolved this past decade to answer more and more complex questions addressed by biologists and physicists of nanoscience. It is today possible to locate specific biomolecules in a cell or a tissue, *in vitro* or *in vivo*, to follow their interaction with neighbour molecules and their environment on spatial scales down to nanometers, and to relate this information to their biological function. Microscopy imaging for biology has in particular benefited from an important development of molecular and inorganic fluorescent nanoprobes, which provides the possibility to chemically label a protein or a lipid in order to follow its behaviour by optical imaging. These probes bring great flexibility in terms of label targeting, variable excitation and emission wavelengths, and sensitivity to various properties of their local environment such as pH or cell membrane potential. Imaging techniques are also under perpetual development and benefit from ingenious inventions that are intended to improve both spatial and time resolutions. These techniques are able today to bring local information with a spatial resolution of submicrometric size and temporal scales down to nanoseconds using time-resolved measurements. While one-photon fluorescence microscopy is a standard tool for bio-imaging, nonlinear contrasts have progressively emerged as interesting alternatives for many reasons. Nonlinear excitations involve in particular near-infrared excitation wavelengths, which are less affected by scattering in tissues and therefore allow a deeper penetration of imaging in thick samples. Owing to the nonlinear nature of the excitation in these regimes, intrinsic spatial resolution (typically 300 nm lateral) can be achieved with reduced out-of-plane photobleaching and phototoxic effects. While two-photon excitation fluorescence (2PF) microscopes were developed in the early nineties for biological samples, the first integration of the coherent nonlinear process of second-harmonic generation (SHG) into an optical microscope was introduced in the seventies to visualize crystalline structures. Technological evolutions on lasers have later allowed higher order nonlinear optics which involves weaker efficiencies. Third-order nonlinear coherent processes such as third-Harmonic generation (THG), coherent anti-Stokes Raman scattering (CARS), and its nonresonant counterpart four-wave mixing (FWM), are also now currently introduced into biological imaging. These processes, described in figure 9.1a,b and more in detail in section 9.2, target different biomolecular structures because of their own specificities:

- Two-photon excitation fluorescence (2PF) is an incoherent optical contrast of endogenous proteins of cells and tissues, synthesized fluorescent labels attached to proteins, antibodies, or embedded as lipid probes in cell membranes[1].
- SHG is a specific structural contrast for non-centro-symmetric molecular structures, applied for instance to the measurement of membrane potential using SHG active molecular lipid labels[2], endogenous structural proteins such as collagen type I[3], acto-myosin, and tubulin, which are present in cells, tendons, muscle fibres or other types of tissue[4].
- THG is an interface-sensitive contrast[5], applied to dense-structure imaging such as in lipid bodies and other cellular structures[6].
- CARS is a chemically specific contrast applied to vibrational mode imaging in biomolecular structures such as aliphatic C–H stretching vibration of lipids[7,8].

- FWM is a non-chemically specific contrast, applied for the visualization of molecular density and visible in non-resonant CARS microscopy[9].

An example of a multimodal microscopy imaging approach combining several of these optical processes is shown in figure 9.1c.

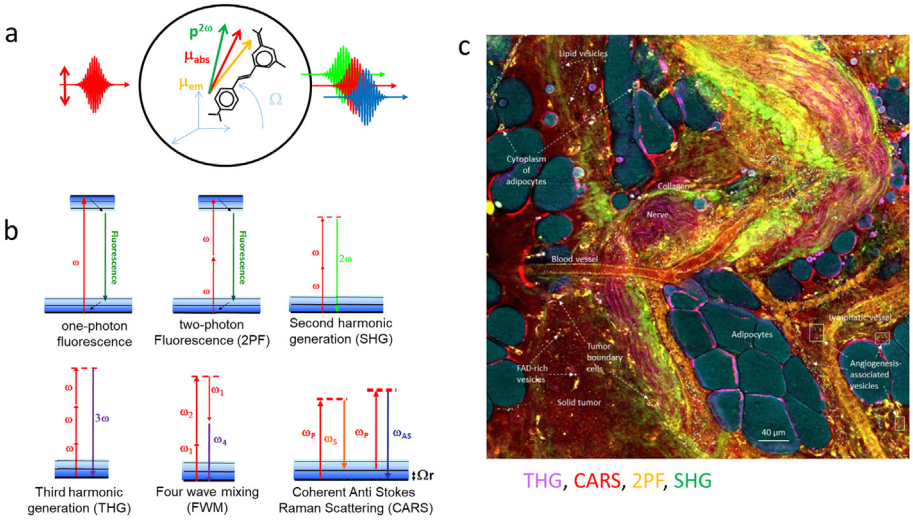

FIG. 9.1 – (a) Schematic drawing of a molecule excited by different frequencies. The radiation from the molecule originates either from an emission transition dipole moment (fluorescence), or from a nonlinear induced dipole moment (coherent second-order nonlinear optical process). (b) Energy diagram scheme of the different contrasts addressed in this lecture: one- and two-photon excited fluorescence (2PF) and the nonlinear coherent processes SHG, FWM, THG, and CARS. (c) Co-registered multi-modality image of a mammary tumor from a carcinogen-injected rat. The image (1140 × 1140 pixels with 0.5 μm pixel size) was collected by label-free nonlinear microscopy with multiple pseudo-colour contrasts: magenta-THG; red-CARS (lipids); yellow-2PF; green-SHG. Various structures in the tumour microenvironment are visible. From[10].

Among the light matter interactions processes of interest for imaging listed above, coherent nonlinear processes belong to a specific category. First, nonlinear interactions do not necessitate absorption by the involved molecules. This makes this type of interaction very different from fluorescence: it does not require the attachment of fluorophores adapted to the incident wavelength, thus avoiding a chemical or biomolecular intrusion in the sample which can potentially affect the biological function of the proteins under study. The price to pay for the use of such processes is their low efficiency. In contrast to linear optical interactions which can be very efficient, nonlinear optical processes exhibit efficiencies that decrease as the order of the nonlinear interaction increases. The use of pulsed lasers has been determining to circumvent this efficiency issue. Concentrating large amounts of energy within short (ps-fs) pulses has permitted to reveal nonlinear interactions even

in inefficient molecular assemblies, which have brought a considerable step forward in imaging, up to the clinics for intraoperative visualization of tumour tissues[10,11].

Another interesting feature of nonlinear optical interactions is their capability to be highly polarization dependent: the use of light polarization is able to bring one more advantage to nonlinear optical microscopy. Polarization defines a preferential direction for its interaction with bound electrons in matter, which play an important role in nonlinear optical interactions. This preferential interaction offers to optical microscopy the possibility to bring extra information on the investigated samples. Once an excitation polarization can be controlled, or a detection polarization can be measured, one can use this degree of freedom to probe locally, in a sample, directions in which electrons move preferentially. In molecules or dielectric crystals, these directions correspond to building blocks of the molecular/atomic structure, while in metallic particles, they correspond to preferential modes of excitation of free electrons that relate to their plasmonic modes.

Since nonlinear microscopy is specifically used for the investigation of biological tissues, it is important to consider limitations that occur in this context. The main issue in the use of near infra-red pulsed beams is **the degradation of the focus in time and space, which occurs when imaging deep into biological tissues and quickly degrades the nonlinear efficiency**. A large amount of research is dedicated today in the investigation of solutions to circumvent this problem, from smooth wavefront corrections in conditions that only deform this focus, to complex corrections that takes advantage of random paths undergone by the optical propagation in scattering media.

In this lecture, we overview different coherent nonlinear optical processes currently used in optical imaging based on pulsed laser excitations, in addition to multiphoton fluorescence (section 9.2). We will describe in particular the specificity of nonlinear optical interactions in a microscopy optical configuration. In addition, we will focus on how light polarization can be used in nonlinear optical microscopy to inform about molecular orientational organization or structural properties of nano-objects (section 9.3). Lastly, we will describe current research directions aiming at exploiting wavefront correction to control the spatio-temporal profile of pulse excitations in complex samples such as biological tissues (section 9.4).

9.2 Principles of Nonlinear Optical Microscopy

Nonlinear optics has been introduced in microscopy imaging since the late 90s due to its unique capacities for in-depth imaging in complex biological media where visible light is absorbed or scattered[1,12,13]. We describe here the essential optical processes behind nonlinear microscopy.

9.2.1 One- and Two-Photon Fluorescence Microscopy

Single molecule fluorescence response. Before describing coherent multi-photon excitation processes, we first give the basics of fluorescence microscopy, which is

today the most widely used tool for in vivo imaging in cells and tissues. Fluorescence is based on the emission of light by molecules used as labels (fluorophores) for specific proteins of interest, by the way of synthetic chemical labelling or genetic modifications using fluorescent proteins. Since fluorescence provides a sensitivity down to the single molecule level, it is also able to tackle problems related to protein–protein interactions at specific locations in cells, bringing important elements to the understanding of fundamental biological questions.

Fluorescence is generated from successive steps of an absorption process and an emission process, separated by the needed time (generally $1 - 10$ ns) for the molecule to de-excite from its excited state down to its ground state (figure 9.1b). The nature of this process makes it fundamentally incoherent: photons emitted at each de-excitation step do not have any phase relation between them, as photons emitted by each single molecules excited by the same laser light.

The one-photon fluorescence intensity from a single molecule (unit ph/s) can be summarized as a product between an absorption rate (unit ph/s) and an emission probability:

$$I^{\mathrm{1PF}} = P_{\mathrm{abs}}^{1-P} \cdot P_{\mathrm{em}} \tag{9.1}$$

where P_{abs}^{1-P} is the one-photon absorption rate and P_{em} the probability of emitting a photon through radiative de-excitation. In principle, the two steps occur at different times t and t', within the time scale of the fluorescence lifetime τ_f, the fluorescence intensity of a single molecule is thus written[14]:

$$I^{\mathrm{1PF}}(t, t') \propto P_{\mathrm{abs}}^{1-P}(t) \cdot P_{\mathrm{em}}(t') \cdot e^{-(t-t')/\tau_f} \tag{9.2}$$

In what follows, for the sake of simplification, we will suppose that the molecule has not changed in orientation between its excitation and emission steps; however, this refinement can be included to account for rotational diffusion.

The absorption rate from a single molecule between its ground state $|0\rangle$ to its excited state $|1\rangle$ can be written[15]:

$$P_{\mathrm{abs}}^{1-P} \propto |\boldsymbol{\mu}_{\mathrm{abs}} \cdot \boldsymbol{E}|^2 = \sum_{IJ} \mu_{01}^I \mu_{01}^J E_I^\omega E_J^\omega \tag{9.3}$$

with $\boldsymbol{E}$ (bold letters mean vectors) the electric field of the electromagnetic incident wave, $\boldsymbol{\mu}_{\mathrm{abs}}$ the absorption dipole of the molecule, which is related to its transition moment $\boldsymbol{\mu}_{01}$ from the ground to the excited state. In this equation, the vector components are expressed projected on directions (I, J) of the sample frame. We see that the 1-P excitation efficiency is governed by a tensorial second-rank term similar to a first-order absorption tensor α with $\alpha_{IJ} = \mu_{01}^I \mu_{01}^J$. More precisely, it corresponds to the imaginary part (*e.g.* absorption contribution) of the first order susceptibility α of the molecule:

$$P_{\mathrm{abs}}^{1-P} \propto \mathrm{Im}(\alpha(\omega;\omega)) \cdot \boldsymbol{E} \otimes \boldsymbol{E}^* \tag{9.4}$$

$\otimes$ is the tensorial product with $(A \otimes B)_{IJ} = A_I B_J$ and $\cdot$ is the contraction product between tensors, similar to a scalar product. In this expression, the term $\mathrm{Im}(\alpha(\omega;\omega))$

is also proportional to the absorption cross section σ_{abs} (unit cm^2) of the molecule, therefore another writing of equation (9.4) is:

$$P_{\text{abs}}^{1-P} = \sigma_{\text{abs}} \cdot I^{\omega} \tag{9.5}$$

where I^{ω} is the incident intensity (unit W/cm^2 or ph/s/cm^2).

The emission probability named $P_{\text{em},I}$ along a polarization direction I, is the result of the radiation from the emission dipole (which physically corresponds to the transition dipole moment from the lowest excited state to the ground state). It contains the quantum efficiency of radiation of a photon for each radiation step (called quantum yield), plus collection factors of the optical system:

$$P_{\text{em},I} \propto |\boldsymbol{E}_{\text{em}} \cdot \boldsymbol{I}|^2 \tag{9.6}$$

For a molecule which orientation is $\boldsymbol{\Omega}$ in the sample frame, the emitted fluorescence far field $\boldsymbol{E}_{\text{em}}$ is the field radiated by the emission dipole $\boldsymbol{\mu}_{\text{em}}(\boldsymbol{\Omega})$, which writes in the propagation direction $\boldsymbol{k}$**:**

$$\boldsymbol{E}_{\text{em}}(\boldsymbol{\Omega}, \boldsymbol{k}) \propto (\boldsymbol{k} \times \boldsymbol{\mu}_{\text{em}}) \times \boldsymbol{k} = \boldsymbol{\mu}_{\mathbf{em}}^{\perp}(\boldsymbol{\Omega}) \tag{9.7}$$

where $\times$ is the vectorial product and $\boldsymbol{\mu}_{\mathbf{em}}^{\perp}(\boldsymbol{\Omega})$ is the projection of the emission dipole on the direction perpendicular to $\boldsymbol{k}$.

In the paraxial approximation assuming planar illumination/collected waves, which is reasonable for low collection numerical apertures (NA) only, the $\boldsymbol{k}$ vector is considered to be close to the optical axis and the field can be simplified into a longitudinal-propagating field: $\boldsymbol{E}_{\text{em}} \propto \boldsymbol{\mu}_{\text{em}}$. It results in a very simple form for the one-photon fluorescence intensity:

$$I^{\text{1PF}} \propto |\boldsymbol{\mu}_{\text{abs}}(\boldsymbol{\Omega}) \cdot \boldsymbol{E}|^2 |\boldsymbol{\mu}_{\text{em}}(\boldsymbol{\Omega}) \cdot \boldsymbol{I}|^2 \tag{9.8}$$

How many photons can we get from the 1PF of a single molecule? Typically, absorption cross sections from single molecules are of the order of $\sigma_{\text{abs}} \sim 3 \times 10^{-16} \text{cm}^2$[16]. The fluorescence intensity expressed in equation (9.8) is overall:

$$I^{\text{1PF}} = C \cdot Q_F \cdot \sigma_{\text{abs}} \cdot I^{\omega} \tag{9.9}$$

which accounts for the collection factor of the optical detection C, and the fluorescence quantum yield Q_F, which quantifies the amount of fluorescence decay rates that lead to emission. Assuming a continuous excitation of averaged power $\langle P \rangle$, with photon energy $h\nu$, focussed on an area A, the signals writes:

$$I^{\text{1PF}} = C \cdot Q_F \cdot \frac{\langle P \rangle}{h\nu} \cdot \frac{\sigma_{\text{abs}}}{A} \tag{9.10}$$

Typical average powers at the focus in 1PF experiments, are of the order of tens of μW over an area of 1 μm^2. Considering a typical collection factor of $C \sim 2 - 10\%$, and $Q_F \sim 0.5 - 0.9$, leads to signals of $N_{\text{1PF}} \sim 6000 - 10\,000\,\text{ph/s}$, which is much above the dark noise of single photon detectors (at best about 50 ph/s). It is

therefore quite easy to detect the signal from a single molecule with a sensitive detector. This explains the important recent progresses made in the field of single molecule detection and single-molecule-based super-resolution imaging.

In two-photon fluorescence (2PF), the transition to the excited state is performed by the quasi-simultaneous absorption of two photons through an intermediate non-resonant, short-lived ($10^{-18} - 10^{-15}$ s) state (figure 9.1b). Developments in quantum mechanics by Maria Göppert-Mayer, in 1931, have shown at a very early stage that photons of 'low' energy together can be used in a step process to excite high energy excitation levels in a multi-photon excitation. She predicted that this event can take place with two photons interacting with a molecule nearly simultaneously. The two-photon absorption rate for a transition between states $|0\rangle$ and $|1\rangle$ involves all other $|n\rangle$ states and can be written[13]:

$$P_{\text{abs}}^{2-P} \propto |\boldsymbol{\mu}_{\text{abs}} \cdot \boldsymbol{E}|^4 = \sum_n \sum_{IJKL} \mu_{0n}^I \mu_{n1}^J \mu_{1n}^K \mu_{n0}^L E_I^{\omega *} E_J^{\omega} E_K^{\omega} E_L^{\omega *} \tag{9.11}$$

Here, a dominating excitation state is supposed, with transition dipole $\boldsymbol{\mu}_{\text{abs}}$. We see that the 2–P excitation efficiency is governed by a tensorial fourth-rank term similar to a third-order nonlinear absorption tensor γ with $\gamma_{IJKL} = \mu_{0n}^I \mu_{n1}^J \mu_{1n}^K \mu_{n0}^L$. It corresponds more precisely to the imaginary part (*e.g.* absorption contribution) of the third-order susceptibility γ of the molecule:

$$P_{\text{abs}}^{2-P} \propto \text{Im}(\gamma(\omega; \omega, \omega, -\omega)) \cdot \boldsymbol{E}^* \otimes \boldsymbol{E} \otimes \boldsymbol{E} \otimes \boldsymbol{E}^* \tag{9.12}$$

This absorption rate can be written similarly as above,

$$P_{\text{abs}}^{2-P} = \sigma_{\text{abs}}^{(2)} \cdot \left| \langle E^2 \rangle \right|^2 \tag{9.13}$$

with $\sigma_{\text{abs}}^{(2)}$ *being* the two-photon absorption cross section and $\langle\,\rangle$ the time average.

Fluorescence is then generated similarly as for a 1PF emission. The 2PF fluorescence intensity from a single molecule (unit ph/s) can be summarized as a product between an absorption rate (unit ph/s) and an emission probability, which writes in the planar waves approximation:

$$I^{2PF} = P_{\text{abs}}^{2-P} \cdot P_{\text{em}} \propto |\boldsymbol{\mu}_{\text{abs}}(\boldsymbol{\Omega}) \cdot \boldsymbol{E}|^4 |\boldsymbol{\mu}_{\text{em}}(\boldsymbol{\Omega}) \cdot \boldsymbol{I}|^2 \tag{9.14}$$

How many photons can we get from the 2PF of a single molecule? Moving to 2PF is more delicate than 1PF, since 2–P absorption cross sections are much lower with typically $\sigma_{\text{abs}}^{(2)} \sim (10 - 1000) \times 10^{-50}\,\text{cm}^4\text{s/ph}$ (the unit of this cross section is explained by the mean squared intensity dependence of the absorption probability). In a two-photon excitation process, the resulting emission efficiency will be, for a continuous excitation of average power $\langle P \rangle$:

$$I^{2\text{PF}} = C \cdot Q_F \cdot \sigma_{\text{abs}}^{(2)} \cdot \left| \langle E^2 \rangle \right|^2 = C \cdot Q_F \cdot \sigma_{\text{abs}}^{(2)} \cdot \left(\frac{\langle P \rangle}{h\nu} \cdot \frac{1}{A} \right)^2 \tag{9.15}$$

Considering an incident power of 10 mW and a focus surface of 1 μm^2 (which corresponds to an intensity of $10^{24}\,\frac{\text{ph}}{\text{s}}/\text{cm}^2$), it leads to $N_{2\text{PF}} \sim 0.6\,\text{ph/s}$, which is not detectable above the dark noise of single photon detectors. Using a pulse laser, however, permits to concentrate a larger number of photons in a shorter time. Rewriting the averaged 2PF signal in a pulsed regime[1]:

$$I^{2\text{PF}} = C \cdot Q_F \cdot g \cdot \sigma^{(2)}_{\text{abs}} \cdot \left(\frac{\langle P \rangle}{h\nu} \cdot \frac{1}{A}\right)^2 \tag{9.16}$$

with

$$g = \frac{\langle I^2 \rangle}{\langle I \rangle^2} = \frac{g_p}{f \cdot \tau} \tag{9.17}$$

with f the repetition rate of the pulsed laser, τ its time width and g_p a factor depending on the shape of the laser pulse, equal to 0.66 for Gaussian pulses. Using pulsed lasers considerably increases the efficiency of two-photon absorption processes, with a gain provided by the $\frac{1}{f.\tau}$ enhancement factor of about 10^5 for values generally used in oscillators ($f = 80\,\text{MHz}, \tau = 100\,\text{fs}$). It is therefore possible to provide high sensitivity 2PF signals down to single molecules, thanks to the use of pulsed lasers.

From one molecule to a density of molecules. In microscopy, we do not usually observe one molecule but a collection of them in the focal excitation volume V, with a molecular density N. Since fluorescence is an incoherent process, the molecule's radiations are uncorrelated in phase, in time, and space. The resulting intensity is the sum of all the intensities from individual molecules of positions $\boldsymbol{r}$ and orientations $\boldsymbol{\Omega} = (\theta, \varphi, \psi)$ (defined by their Euler set of angles). We consider that these orientations are distributed within an orientational distribution function $f(\boldsymbol{\Omega})$, normalized such as $\int f(\boldsymbol{\Omega})\, d\boldsymbol{\Omega} = 1$. The probability to find a molecule between angles $\boldsymbol{\Omega}$ and $\boldsymbol{\Omega} + d\boldsymbol{\Omega}$ is thus $N(\boldsymbol{\Omega})\, d\boldsymbol{\Omega} = Nf(\boldsymbol{\Omega})\, d\boldsymbol{\Omega}$ and the total intensity of 2PF fluorescence (similar equations can be found for 1PF) writes, along the polarizer direction I:

$$I_I^{2\text{PF}} = N\left\langle \int_{NA} \int_V \int_{\boldsymbol{\Omega}} |\boldsymbol{\mu}_{\text{abs}}(\boldsymbol{\Omega}, \boldsymbol{r}) \cdot \boldsymbol{E}(\boldsymbol{r})|^4 |\boldsymbol{E}_{\text{em}}(\boldsymbol{\Omega}, \boldsymbol{k}, \boldsymbol{r}) \cdot \boldsymbol{I}|^2 f(\boldsymbol{\Omega})\, d\boldsymbol{\Omega}\, d\boldsymbol{r}\, d\boldsymbol{k} \right\rangle \tag{9.18}$$

- $\int_{NA}$ means that the $\boldsymbol{k}$ dependence is integrated over the whole collection numerical aperture NA of the microscope objective. At high NA collection, propagation directions can be highly tilted and therefore polarization directions are mixed. This leads to a mixture of measured polarization states and the emission rate is a combination of all polarizations measured in all three directions of space, with weights that depend on the NA[17].
- $\int_{\text{V}}$ means that the intensities are summed over all molecules potentially positioned at different positions $\boldsymbol{r}$ within the focal volume.

- $\int_\Omega$ means an integration over all molecular orientations, with $\int d\Omega = \int\int\int \sin\theta\, d\theta\, d\varphi\, d\psi$.
- $\langle\,\rangle$ means that the intensity is averaged in time within the integration time of the detector, over all molecular position/orientation fluctuations.

Considering a homogeneous medium, the planar wave approximation leads to:

$$I_I^{\mathrm{2PF}} = N \int |\boldsymbol{\mu}_{\mathrm{abs}}(\Omega)\cdot\boldsymbol{E}|^4 |\boldsymbol{\mu}_{\mathrm{em}}(\Omega)\cdot\boldsymbol{I}|^2 f(\Omega)\, d\Omega \tag{9.19}$$

which is proportional to N times the signal of a single molecule. Due to its incoherent nature, the fluorescence signal thus increases linearly with the molecular density in the focal volume of a microscope.

9.2.2 Second-Order Coherent Nonlinear Microscopy

Nonlinear coherent optical processes originate from induced dipoles as a consequence of higher order interactions of light with matter[18]. Unlike fluorescence, the nonlinear induced dipole from a given molecule exhibits a determined phase relation with both the incident excitation field and the other molecules.

Single molecule SHG response. One of the first known processes in nonlinear optics is second harmonic generation (SHG), which results from the excitation of a system at the fundamental optical frequency ω, into a scattering at the double frequency 2ω[18]. Since the SHG radiation originates rather from a scattering process, there is no need to excite the molecule to a real excited level, and the optical process can therefore be non-resonant (figure 9.1b). For symmetry reasons and invariance upon point groups symmetry transformation[18], this process requires the molecule to be non-centro-symmetric (*e.g.* without any centre of symmetry), and therefore occurs only in specific structures. The SHG signal can be written from the radiation of the molecular nonlinear induced dipole $\boldsymbol{p}^{\mathrm{SHG}}$:

$$\boldsymbol{p}^{\mathrm{SHG}} \propto \beta(2\omega;\omega,\omega) : \boldsymbol{E}^{\omega}\boldsymbol{E}^{\omega} \tag{9.20}$$

where ":" is the contracted tensorial product operator, and β is the molecular hyperpolarizability. This second-order tensor has coefficients in the molecular frame β_{ijk}, which are directly related to the symmetry of the molecule. For instance, for a molecule whose conjugated electrons are strongly delocalized along the 1D z direction, β_{zzz} is dominant over all other coefficients. As in fluorescence, the molecular origin of this polarizability is the coupling between transition dipole moments, with, for a 2-level 1D molecule reads[18]:

$$\beta_{zzz}(2\omega;\omega,\omega) = \frac{3\mu_{01}^z\left(\mu_{11}^z-\mu_{00}^z\right)\mu_{01}^z}{2(\hbar\omega_0)^2}\cdot\frac{\omega_0^4}{\left(\omega_0^2-4\omega^2\right)\left(\omega_0^2-\omega^2\right)} \tag{9.21}$$

with $\hbar$ the reduced Planck's constant and ω_0 the frequency of the resonance of the $(0-1)$ transition. For more complex symmetries, the number of components of the β tensor (up to 27) is governed by the molecular symmetry. Far from resonances

however, due to Kleinman symmetry, the tensor components are invariant under cyclic permutation of the indices, which reduces the number of components[18].

The nonlinear induced dipole of equation (9.20) writes, along the I polarization direction for a molecule defined by an orientation $\mathbf{\Omega} = (\theta, \varphi, \psi)$ (Euler set of angles):

$$p_I^{\mathrm{SHG}}(\mathbf{\Omega}) = \sum_{JK} \beta_{IJK}(\mathbf{\Omega}) E_J^{\omega} E_K^{\omega} \tag{9.22}$$

with (I, J, K) being the macroscopic axes related to the sample. $\beta_{IJK}(\mathbf{\Omega})$ is related to the molecular β_{ijk} tensor by a simple transformation expression in the form of a rotation, from one frame to the other[19]:

$$\beta_{IJK}(\mathbf{\Omega}) = \sum_{ijk} \beta_{ijk} (\boldsymbol{i}\cdot\boldsymbol{I})(\boldsymbol{j}\cdot\boldsymbol{J})(\boldsymbol{k}\cdot\boldsymbol{K})(\mathbf{\Omega}) \tag{9.23}$$

with $(\boldsymbol{k}\cdot\boldsymbol{K})(\mathbf{\Omega})$ the vectorial projection of $\boldsymbol{k}$ (microscopic axis) on $\boldsymbol{K}$ (macroscopic axis).

Finally, the radiating SHG field from this single molecule dipole, in the wave-vector direction $\boldsymbol{k}$ writes:

$$\boldsymbol{E}^{\mathrm{SHG}}(\mathbf{\Omega}, \boldsymbol{k}) \propto \left(\boldsymbol{k} \times \boldsymbol{p}^{\mathrm{SHG}}\right) \times \boldsymbol{k} \tag{9.24}$$

Efficiency cross sections of second harmonic generation can be deduced similarly to a linear scattering cross section, based on the scattered power by the microscopic dipole $\boldsymbol{p}^{\mathrm{SHG}}$

$$P_{\mathrm{scat}}^{\mathrm{SHG}} \propto \sigma_{\mathrm{SHG}} \cdot I^2 \tag{9.25}$$

Of course, the corresponding *SHG* cross section σ_{SHG} depends on the nonlinear susceptibility of the single molecule. Its expression is given in[20] as:

$$\sigma_{\mathrm{SHG}} = \frac{4 n_{2\omega} \hbar \omega^5}{3\pi n_\omega^2 \varepsilon_0^3 c^5} |\beta|^2 \tag{9.26}$$

with $n_{2\omega}, n_\omega$ the refractive index at $2\omega, \omega$. This cross section is much less efficient than for 2PF: σ_{SHG} $10^{-53}\mathrm{cm}^4\mathrm{s/ph}$, which leads to about 0.01 ph/s of signal from a single molecule radiating a SHG signal. It is thus impossible to observe a single molecule SHG signal in such conditions, even in a pulsed laser regime.

From one molecule to the SHG response of a collection of molecules. In contrast to the incoherent fluorescence process, the macroscopic SHG signal results from the coherent addition of nonlinear molecular induced dipoles in the focal volume, *i.e.* in the focal spot of the objective. The macroscopic signal is the sum of all molecular dipoles over the volume V and the angular distribution $f(\mathbf{\Omega})$ explored by the molecules. In a homogeneous medium of molecular density N, the intensity projected along the polarizer direction I is:

$$I_I^{\mathrm{SHG}} = \left| N \int_{NA} \int_V \int_\Omega E_I^{\mathrm{SHG}}(\mathbf{\Omega}, \boldsymbol{r}, \boldsymbol{k}) f(\mathbf{\Omega})\, d\mathbf{\Omega}\, d\boldsymbol{r}\, d\boldsymbol{k} \right|^2 \tag{9.27}$$

with E_I^{SHG} the component of the SHG radiated field along the I polarization direction. Using similar approximations as in fluorescence, the far field radiation is the squared modulus of a macroscopic nonlinear dipole:

$$P_I^{\mathrm{SHG}} = N \int_{\Omega} p_I^{\mathrm{SHG}} f(\mathbf{\Omega})\, d\mathbf{\Omega} \tag{9.28}$$

Therefore, using the macroscopic expression $\boldsymbol{P}^{\mathrm{SHG}} = \chi^{(2)}(2\omega;\omega,\omega) : \boldsymbol{E}^{\omega}\boldsymbol{E}^{\omega}$,

$$I_I^{\mathrm{SHG}} = \left|P_I^{\mathrm{SHG}}\right|^2 = \left|\sum_{JK} \chi_{IJK}^{(2)} E_J^{\omega} E_K^{\omega}\right|^2 \tag{9.29}$$

with the resulting macroscopic susceptibility $\chi^{(2)}$ (unit: m/V) being the result of a summation of all microscopic susceptibilities over the orientational distribution present within the excited volume:

$$\chi_{IJK}^{(2)} = N \int_{\Omega} \beta_{IJK}(\mathbf{\Omega}) f(\mathbf{\Omega})\, d\mathbf{\Omega} \tag{9.30}$$

Similarly as for the microscopic hyperpolarizability β at the molecular scale, the $\chi^{(2)}$ susceptibility tensor carries information on the symmetry of the macroscopic medium, encompassing both the symmetry of β and of the distribution $f(\mathbf{\Omega})$.

Contrary to fluorescence, from equations (9.28) and (9.29), the SHG intensity of a molecular density N thus depends on N^2:

$$I_I^{\mathrm{SHG}} = N^2 \cdot C \cdot \sigma_{\mathrm{SHG}} \cdot I^2 \tag{9.31}$$

This squared dependence of a SHG signal with respect to the molecular density explains the high efficiency of SHG nonlinear microscopy, despite the lower cross sections involved. In a molecular crystal (which is a very dense object), the interaction volume in microscopy contains typically about $10^6 - 10^8$ molecules. With an incident intensity of about $10^{24}\,\frac{\mathrm{ph}}{\mathrm{s}}/\mathrm{cm}^2$, as used above in fluorescence, signals much higher than the dark noise of photon counters can be obtained for nano-objects of 10–100 nm diameter size[21].

In biological tissues, coherent SHG occurs in organized non-centro-symmetric structures such as tissues rich in collagen I[22], skeletal muscles[12], and microtubules[23]. SHG imaging is today exploited as a functional contrast for the diagnosis of pathological effects[24], aging[25], or the understanding of the mechanics of conjunctive tissues whose stiffness strongly depends on collagen content and structure[26,27].

9.2.3 Practical Aspects of Nonlinear Microscopy

Formation of an image. In optical microscopy, the observable size of objects in a sample is intrinsically limited by optical resolution. The focus of a microscope is not a single point as we could imagine from ray optics propagation, it is rather a spot whose size is defined by the wave nature of light propagation, in particular due to

light diffraction occurring at the border of lenses present in the microscope objective. The focus spot is the result of an interference pattern from all fields diffracted by lens apertures, with a diameter d defined, in linear optics, by[28]:

$$d \cong \frac{1.22\lambda}{2NA} \tag{9.32}$$

where NA is the numerical aperture of the objective, such as $NA = n.\sin\Theta$ with n the immersion medium refractive index and Θ the semi-aperture angle of the objective lens in the object space.

The point spread function (PSF) of the microscope is defined as the image of a point source. Its size is generally governed not only by optical diffraction but also by optical aberrations that originate at high apertures and large fields and further deform and enlarge a focus spot.

Nonlinear microscopy (figure 9.2a) relies generally on an excitation from a pulsed laser (typically a Ti:Sapphire laser), delivering 100–300 fs pulses at a rate of 80 MHz, with a tunable incident wavelength ranging from $\sim$690 nm to $\sim$1000 nm and an average power up to a few hundred mW. The laser beam is reflected by a dichroic mirror and focused on the sample by a microscope objective of large numerical aperture ranging from 0.6 to 1.2. The use of a large numerical aperture provides the advantage of a small optical resolution (typically 300 nm lateral) and a high collection factor if the signal is detected in the epi direction (reflection). For transmission detection, a second lens is required. The laser is generally raster-scanned across the sample using galvanometric mirrors. The signal is sent towards detectors (photomultipliers) on which the back-focal plane of the objective is imaged. The resulting image is reconstructed from the intensity recorded at each pixel.

Nonlinear cross sections are extremely small, thus a few factors are essential for a sufficiently high signal-to-noise ratios: (1) spatial focussing to reach high intensities, (2) raster-scanning to reduce sample damage focussing, (3) the use of pulsed lasers to increase the number of excitation photons per unit time, as described above. While raster-scanning of a focus is the most used modality, recent developments in nonlinear fluorescence imaging have, however, developed other geometries to more rapidly image a whole plane, using light sheets produced by shaped beams[29].

Optical resolution and sectioning. The considerable advantage of two-photon excitation in contrast to one-photon excitation is the squared intensity dependence of the outcoming signal. This nonlinear dependence drops down very fast when going out of the focus plane, in contrast with 1PF which is affected by a larger out-of-focus background. Typically in microscopy in a biological tissue, thousands of molecules are excited within the excitation volume of a two-photon microscope. This volume can be deduced from the squared dependence on the incident intensity, leading to a dependence $V_{2\mathrm{PF}} \propto \lambda^3/NA^4$ (in contrast to $V_{1\mathrm{PF}} \propto \lambda^3/NA^3$)[1]. This means that a 2PF/SHG excitation volume, even though the incident wavelength used is longer, is typically $\sqrt{2}$ times smaller than a 1PF excitation volume, in addition to a strong advantage of natural depth sectioning from the nonlinear dependence on the incident intensity[13].

Spatial considerations. In principle, the total SHG field calculation of equation (9.27) needs to account for the fact that the fields emitted from individual

dipoles are spread within the focal volume, with distances between them. Since SHG is a coherent process, phase shifts between emitting dipoles have to be accounted for. Note also that at this stage, we have not considered any particular phase matching conditions. The different molecules present in the focal volume generate fields that interfere in the far field propagation through the microscope. We will determine the conditions for obtaining constructive interferences (*e.g.* a detectable intensity), when a set of non-linear molecules are distributed in a volume depth of characteristic size L. In the case of nonlinear microscopy L is of the order of the wavelength (up to a few wavelengths), it is therefore not necessary to take into account the coupling between fundamental and harmonic waves in the nonlinear propagation, in contrast to propagation in thick crystals. The SHG signal detected at a position $(\boldsymbol{r})$ is the sum of all fields radiated by all nonlinear dipoles positioned at distances $\boldsymbol{r}_n$ from the origin, with orientation $\boldsymbol{\Omega}_n$ (figure 9.2b). Each molecule sees the incident field $\boldsymbol{E} = \boldsymbol{E}_0 \exp(-i\omega t + i\boldsymbol{k}_\omega \cdot \boldsymbol{r})$ where $\boldsymbol{k}_\omega$ is the incident wavevector at the ω frequency. Adding coherently all fields radiated at 2ω leads to a total intensity:

$$I^{\mathrm{SHG}} \propto |\beta : \boldsymbol{E}_0 \boldsymbol{E}_0|^2 \sum_{n,n'} \exp(i(2\boldsymbol{k}_\omega - \boldsymbol{k}_{2\omega}) \cdot (\boldsymbol{r}_n - \boldsymbol{r}_{n'})) \tag{9.33}$$

with $\boldsymbol{k}_{2\omega} = n_{2\omega} . \frac{2\omega}{c} . \boldsymbol{u}, \boldsymbol{u}$ being the unit vector along the 2ω propagation direction. In this expression, $\boldsymbol{\Delta k} = 2\boldsymbol{k}_\omega - \boldsymbol{k}_{2\omega}$ appears as the important factor defining a phase mismatch, which needs to be compared to the focal volume explored by all dimensions $\boldsymbol{\Delta r} = \boldsymbol{r}_n - \boldsymbol{r}_{n'}$. This phase mismatch is due to the fact that dipoles radiate from different positions. Since the refractive index depends on frequency, $\boldsymbol{\Delta k} \neq 0$ and the intensity above will be vanishing if $\Delta k \cdot L > \pi$. This allows defining a coherence length as $L_c = \frac{\pi}{\Delta k}$. L_c is the sample propagation length required to be imaged in microscopy without attenuation of the signal. L_c is different depending on the geometry. In the transmission direction in planar wave illumination conditions:

$$L_{c,fwd} = \frac{\pi}{\Delta k_{fwd}} = \frac{\lambda}{4(n_{2\omega} - n_\omega)} \tag{9.34}$$

Biological samples have typical indices close to water with $n_\omega = 1.329$ at 800 nm $n_{2\omega} = 1.344$ at 400 nm. This leads to $L_{c,fwd} = 13\,\mu m$. In focussed conditions we have to include the Gouy phase shift that adds a π phase shift over a distance of 2λ, hence an additional number $\pi/2\lambda$ to Δk. This leads to $L_{c,fwd}\ \lambda$ which says that in transmission, propagation build-up of SHG can occur over about a wavelength depth. In epi reflection, however, the relative direction of $\boldsymbol{k}_{2\omega}$ is changed into its opposite and $\Delta k_{\mathrm{epi}} = 2k_\omega + k_{2\omega} + \pi/2\lambda$. This leads to:

$$L_{c,\mathrm{epi}} = \frac{\pi}{\Delta k_{\mathrm{epi}}} \sim \frac{\lambda}{8n_\omega + 1} \sim \frac{\lambda}{12} \tag{9.35}$$

Epi SHG direction is thus sensitive to only nanometric sizes objects[30]. This effect is illustrated in figure 9.2c. Note that in biological tissues, however, the signal is often obtained from back scattered light of transmission SHG, therefore multiple sizes of objects can be observed in this situation[31].

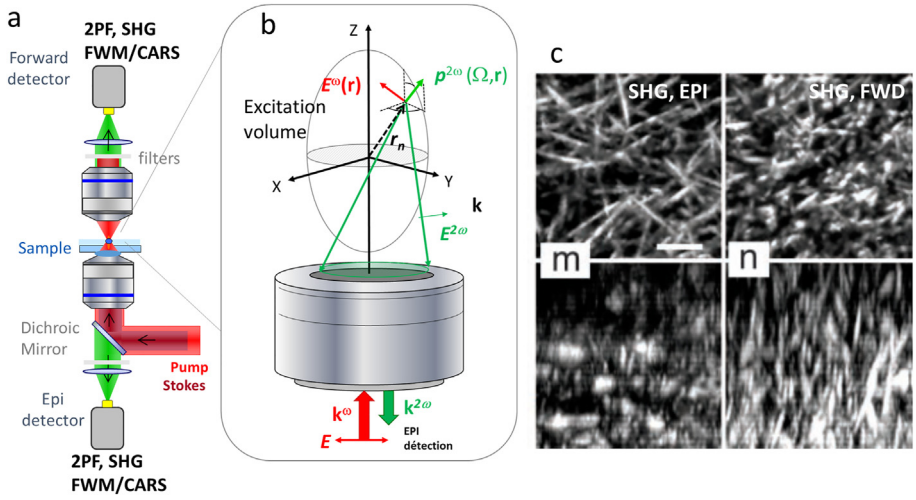

FIG. 9.2 – (a) Experimental layout of a scanning nonlinear optical microscope. (b) schematic drawing of the interaction at the molecular level, with consequent epi and forward directions imaging in SHG. Below: (m) Backward-directed SHG image of a 10 μm-thick collagen gel (Upper, lateral projection; Lower, axial projection; scale bar, 5 μm). (n) Forward-directed SHG from the same collagen gel. From[30].

Time considerations. In the calculations above, we suppose that the field is almost monochromatic, *e.g.* not large enough to affect the determination of the signal by its spectral expansion. In the case of a short pulse, *e.g.* spectrally broad pulse, the spectral phase of the pulse can have a crucial influence on the build-up of the nonlinear excitation signal. Suppose a pulse of amplitude input time profile $E(t) = E_0 \exp(-i\omega_0 t + i\varphi(t))$ which Fourier transform is denoted $E(\omega) = |E(\omega)|e^{i\phi(\omega)}$. A two-photon excitation process induces multiple possible pathways to reach its final step, which can be viewed as intra-pulse interferences that provide a coherent control tool. While a modification of the incident spectral phase $\phi(\omega)$ does not affect a one-photon excitation process which is only dependent on its amplitude squared at a single frequency $|E(\omega)|^2$, a nonlinear excitation provides such intra-pulse interferences. A two-photon excitation process for instance leads to a new excitation profile[1]:

$$I^{\mathrm{2PF}} \propto \int \sigma^{(2)}_{\mathrm{abs}}(2\omega) \cdot \left| \int E(\omega - \Delta) E(\omega + \Delta) d\Delta \right|^2 d\omega \tag{9.36}$$

The two-photon excitation term $\mathrm{Exc}^{(2)}(\omega) = \left| \int E(\omega - \Delta) E(\omega + \Delta) d\Delta \right|^2$ writes:

$$\mathrm{Exc}^{(2)}(\omega) = \int |E(\omega - \Delta)||E(\omega + \Delta)| e^{i[\phi(\omega - \Delta) + \phi(\omega + \Delta)]} d\Delta \tag{9.37}$$

Showing that the 2–P transition probability is governed by the spectral phase of the incident field. This two-photon excitation term is spectrally tunable depending on the spectral phase of the incident field. In particular, while an antisymmetric phase has no effect on this transition probability, a local antisymmetric point in the spectral phase function leads to a maximum two-photon excitation[32]. This effect has been used to optimize the two-photon absorption of fluorescent proteins[33] and provide coherent control of molecular excitations[32]. In order to optimize this function over the whole excitation spectrum of a transition, a flat-phase transform limited pulse will be the most efficient profile[34].

Similarly as for 2PF, the SHG intensity from a pulsed excitation writes:

$$I^{\mathrm{SHG}}(2\omega) \propto \left| \int \chi^{(2)}(2\omega; \omega - \Delta, \omega + \Delta) \cdot E(\omega - \Delta) E(\omega + \Delta)\, d\Delta \right|^2 \tag{9.38}$$

The SHG intensity is now dependent not only on the spectral phase of the incident beam, but also on the spectral content of the nonlinear susceptibility. This function is particularly frequency-sensitive when close to resonances[34].

9.2.4 Third-Harmonic Generation and Four-Wave Mixing

Section 9.4 can be written for higher order effects, and in particular third-harmonic generation (THG) and four-wave mixing (FWM), processes that involve an even order of electronic interactions (figure 9.1b), which provide a signal in media of whatever symmetries. However, because of this higher order, the spatial coherence becomes a crucial factor, and not all media will provide contrasted images by use of third-order nonlinear optical processes. In the case of pure THG, the signal is even more restricted, since it vanishes in homogeneous media and appears only at interfaces[5]. Both phenomena are based on a fourth rank tensor:

$$\chi^{(3)}_{IJKL} = N \int_{\Omega} \gamma_{IJKL}(\Omega) f(\Omega)\, d\Omega \tag{9.39}$$

with γ the third-order molecular susceptibility and N the molecular density. THG and FWM can be expressed from their respective nonlinear induced dipoles at different radiating frequencies:

$$\boldsymbol{P}^{THG}(3\omega) = \chi^{(3)}(3\omega; \omega, \omega, \omega) : \boldsymbol{E}^{\omega}\boldsymbol{E}^{\omega}\boldsymbol{E}^{\omega}$$

$$\boldsymbol{P}^{FWM}(\omega_4) = \chi^{(3)}(\omega_4; \omega_1, \omega_2, -\omega_3) : \boldsymbol{E}^{\omega_1}\boldsymbol{E}^{\omega_2}\boldsymbol{E}^{\omega_3 *} \tag{9.40}$$

with $\omega_4 = \omega_1 + \omega_2 - \omega_3$.

In biological tissues, coherent THG has been mainly applied to visualize strong index mismatch-interfaces such as the ones from lipid structures[35], and FWM to image tissue morphologies[36].

9.2.5 Coherent Anti-Stokes Raman Scattering and Stimulated Raman Scattering

CARS is a particular case of FWM that involves an intermediate resonance corresponding to a vibrational level (figure 9.1b). In CARS, the molecule is excited by two optical frequencies, the pump beam at frequency ω_p, and Stokes at frequency ω_S. This excitation, when falling in resonance with a vibration transition $\mathbf{\Omega}_R$ at the frequency difference $\omega_p - \omega_S = \mathbf{\Omega}_R$, induces a coherent build-up of the molecular vibrations that makes it much more sensitive than a Raman process, due to its coherent nature[8]. The resulting microscopic induced dipole at the anti-Stokes detected frequency $\omega_{AS} = 2\omega_p - \omega_S$ is:

$$\boldsymbol{P}^{\mathrm{CARS}}(\omega_{AS}) = \chi^{(3)}\left(\omega_{AS}; \omega_p, \omega_p, -\omega_S\right) : \boldsymbol{E}^{\omega_p}\boldsymbol{E}^{\omega_p}\boldsymbol{E}^{\omega_S *} \tag{9.41}$$

The specificity of the CARS process is to exhibit, for specific frequencies ω_S, a resonant contribution when $\delta\omega = \omega_p - \omega_S = \mathbf{\Omega}_R$ corresponds to a vibrational energy of the molecule. The advantage of this technique is to be able to address optically, with near-IR lasers, Raman-like vibrational levels of low frequencies with high efficiency. The involved third-order nonlinear tensor approaching a vibrational resonance by tuning ω_S can be written as:

$$\gamma(\delta\omega) = \gamma^{NR} + \gamma^{R}(\delta\omega) \tag{9.42}$$

where γ^{NR} is a nonresonant FWM susceptibility and $\gamma^{R}(\delta\omega)$ is an additional resonant contribution with:

$$\gamma^{R}(\delta\omega) = \frac{a}{(\delta\omega - \mathbf{\Omega}_R) + i\mathbf{\Gamma}} \tag{9.43}$$

where a is the oscillator strength of the vibration and $\mathbf{\Gamma}$ the line width of the Raman resonance corresponding to the $\mathbf{\Omega}_R$ vibrational energy.

A CARS tensor out of resonance possesses 21 nonvanishing components $\chi^{(3)}_{IJKL}$, through index permutations: either intrinsically due to the CARS interaction (in particular the degeneracy in the ω_p frequency), or due to Kleinman symmetry. In non-isotropic samples, the non-resonant CARS third-order nonlinear susceptibility tensor exhibits a complex structure characteristics of the symmetry of the studied medium. The structure of the CARS tensor close to resonances is, however, more complex and requires specific investigations in both the resonant and non-resonant regimes. CARS imaging, in addition to having the advantages of coherent nonlinear imaging abilities, is the only nonlinear interaction that can target specifically known chemical bonds in a medium, making it a chemically sensitive contrast[37] which offers very rich possibilities, including cancer diagnosis[10].

9.3 Polarized Nonlinear Microscopy

Being able to report high level of detail in the structural molecular organization using optical microscopy is one of the prevailing goals in the field of functional imaging in biology, material sciences and molecular physics. Polarized optical

microscopy is becoming a powerful tool to address molecular orientational distributions in the focal volume of a microscope. Here, we investigate the nature of polarization resolved nonlinear fluorescence and coherent signals (figure 9.3a), and their respective capacity to disentangle molecular orientational information in the focal volume of a microscope.

9.3.1 Molecular Order

Molecular order is the angular extent explored by molecular and atomic directions within the focal volume of a microscope. If molecules undergo angular fluctuations at a time faster than the integration time of the detector, molecular order encompasses also those angular fluctuations. As a result, molecular order contains two contributions, a 'structural' contribution corresponding to how molecules are aligned on average over the integration time scale, and a 'time fluctuation' contribution coming from temporal disorder. Lipid membranes are, for instance, fluid-like but preserve a tight ordering of molecules with important morphological nanometric-scale modifications in case of pathologies, as for instance in the lipid layers which surround axons to form their protective myelin sheath (figure 9.3b)[38]. Other examples can be found in the cytoskeleton of the cell (as actin represented in figure 9.3c) as well as the extracellular matrix of tissues, where the organization of filaments in collagen and elastin has a large role in their mechanical properties.

To encompass both structural order and fluctuations, molecular angular distributions are modelled by an angular function of given shape $f(\mathbf{\Omega})$ where $(\mathbf{\Omega})$ defines molecular orientation in the sample frame (see section 9.2). The angular aperture of this distribution is called molecular order.

We will assume that optical interactions take place with light polarizations lying in the sample plane (X, Y), which is an approximation that holds at reasonable ($<$1.2) numerical apertures. Therefore they will involve primarily the φ in-plane orientation variable of the molecules. We define an effective molecular distribution as a φ-dependent function $p(\varphi)$, which is related to $f(\mathbf{\Omega})$ in a way specific to each optical interaction process[39], as described in the next sections. It is convenient to decompose a molecular angular distribution in circular functions of given symmetry orders (figure 9.3d)[19]:

$$p(\varphi) = S_0\left[1 + \sum_{n=1}^{\infty} S_n \cos(n(\varphi - \rho_n))\right] \tag{9.44}$$

where the parameters S_n denote symmetry order contributions of order n in the molecular distributions, and the angle ρ_n refers to the orientations of these symmetry orders in the sample plane (figure 9.3). The S_n coefficients give specific contributions of molecular order: S_0 determines its isotropic contribution, S_1 and S_2 define its anisotropy, and higher orders S_n define more precisely the shape of this function. Each of the symmetry order S_n has a specific orientation ρ_n, allowing to define functions of very general shape, including those which do not possess a cylindrical symmetry axis[40].

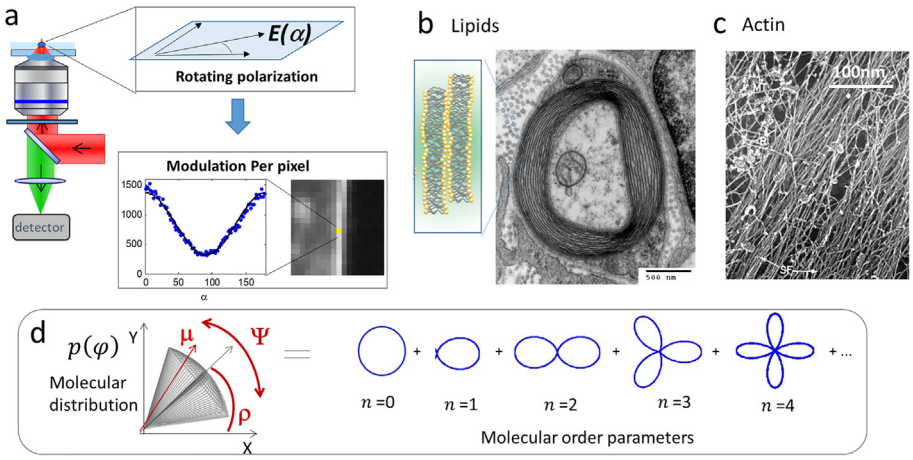

FIG. 9.3 – (a) Principle of polarization-resolved microscopy. The incident linear polarization is rotated in the sample plane, and the nonlinear emitted signal resulting modulation recorded for every pixel of the image. (b) Example of lipid membrane organization in a tight and packed way in the myelin sheath around axons (Electron microscopy image - from[41]). (c) Electron microscopy image showing both packed and disordered organization of actin in a cell (from[42]). (d) Symmetry order decomposition of a molecular angular distribution function in the sample plane (of mean orientation ρ and angular aperture Ψ), where circular functions are represented up to the order $n = 4$.

In what follows, we will use this symmetry order decomposition as a read-out of an angular distribution function such as measured by polarized optical microscopy (figure 9.3a). We will show in particular that an optical interaction (fluorescence, nonlinear optics) is capable of measuring only a limited quantity of symmetry orders in a molecular distribution function.

9.3.2 Polarized Two-Photon Fluorescence Microscopy

The goal of polarization-resolved fluorescence is to extract information on $p(\varphi)$ from the measurements of several polarization angles $\boldsymbol{E}(\alpha)$. We suppose here that the $E(\alpha) = (\cos\alpha, \sin\alpha, 0)$ field components rotate in the sample plane (in reality tight focussing induces a longitudinal contribution, which contribution can be neglected, however, in many cases). Renaming the in-plane projection of the dipole $\mu_{\text{abs}}(\varphi) = (\cos\varphi, \sin\varphi, 0)$ such as $\mu_{\text{abs}}(\theta, \varphi) = \mu_{\text{abs}}(\varphi).\sin\theta$ in the absorption probability of equation (9.3), the 1PF signal can be simplified into[19]:

$$I^{\text{1PF}}(\alpha) \propto N \int |\mu_{\text{abs}}(\varphi) \cdot E(\alpha)|^2 \cdot p(\varphi)\, d\varphi \tag{9.45}$$

with the in-plane integral distribution $p(\varphi) = \int f(\theta, \varphi).\sin^3\theta\, d\theta$. This expression shows that when rotating the incident polarization field, the detected fluorescence

signal will be maximized when the field is parallel to the absorption dipoles. The contrast of modulation obtained is a signature of the molecular order, from highly organized (high modulation) to completely random (no modulation).

Since the α dependence of this expression does not exceed a power of two in $(\cos, \sin)$ functions, the fluorescence intensity can be written in a more convenient measurable form[43]:

$$I^{1\mathrm{PF}}(\alpha) \propto a_0 + a_2 \cos 2\alpha + b_2 \sin 2\alpha \tag{9.46}$$

This circular decomposition contains harmonic coefficients of the polarization response (a_0, a_2, b_2) that can be directly measured: $a_0 = \int I^{1\mathrm{PF}}(\alpha) d\alpha$ is the total intensity, and the other coefficients are deduced from $a_2 = 2 \int I^{1\mathrm{PF}}(\alpha).\cos 2\alpha d\alpha / a_0$ and $b_2 = 2 \int I^{1\mathrm{PF}}(\alpha).\sin 2\alpha d\alpha / a_0$. These orders can be assembled into an amplitude (I_2) and orientation (φ_2):

$$I_2 = \sqrt{a_2^2 + b_2^2},\ \varphi_2 = \frac{1}{2}\arctan\frac{b_2}{a_2} \tag{9.47}$$

Ultimately, (I_2, φ_2) can be related to the $p(\varphi)$ function. Since the intensity polarization dependence does not surpass the order two in α, the readable part of the $p(\varphi)$ function will be limited to the order two as well, therefore the only measurable part of $p(\varphi)$ is:

$$p(\varphi) = S_0[1 + S_2 \cos(2(\varphi - \rho_2)] \tag{9.48}$$

A direct calculation of the intensity expression in equation (9.45) and its circular coefficients (a_0, a_2, b_2) combined in equation (9.47) leads to:

$$I_2 = \frac{2}{3} S_2,\ \varphi_2 = \rho_2 \tag{9.49}$$

which permits to measure the (S_2, ρ_2) parameters that characterize the molecular angular distribution. The number of parameters that can be retrieved is limited by the fact that the optical interaction takes place at the power two of the electric field of the incident light. Interpreting the (S_2, ρ_2) parameters in terms of angular characteristics of a molecular distribution function gives a more physical picture of the organization behaviour of a sample. The fact that only one symmetry parameter can be measured using 1PF prevents, however, from measuring detailed information on the shape of this angular distribution, apart from its angular width. Assume for instance, a cone distribution of molecules $f(\mathbf{\Omega})$ of aperture ψ, lying in the sample plane with an orientation ρ with respect to the direction X (figure 9.3d), then $p(\varphi) = \int f(\theta, \varphi).\sin^3\theta d\theta$ and $S_2 = 2 \int p(\varphi).\cos 2\varphi d\varphi$ lead to a direct relation between the coefficients $(S_2,\ \rho_2)$ and the molecular distribution angles (ψ, ρ)[19]:

$$S_2 = \frac{\sin\psi}{\psi},\ \rho_2 = \rho \tag{9.50}$$

While 1PF gives access to a limited amount of information on the symmetry decomposition of a molecular distribution, accessing higher orders can be made possible by an increase of the power at which light-matter interaction occurs. In the case of two-photon absorption, the 2PF intensity writes[13,19,43]:

$$I^{2\mathrm{PF}}(\alpha) \propto \int |\boldsymbol{\mu}_{\mathrm{abs}}(\varphi) \cdot \boldsymbol{E}(\alpha)|^4 \cdot p(\varphi)\, d\varphi \tag{9.51}$$

with $p(\varphi) = \int f(\theta, \varphi).\sin^5\theta d\theta$ for a $\boldsymbol{E}$ field polarized in the sample plane. The fluorescence intensity can thus be decomposed in circular functions, similarly as for 1PF:

$$I^{2\mathrm{PF}}(\alpha) \propto a_0 + I_2 \cos\, 2(\alpha - \varphi_2) + I_4 \cos\, 4(\alpha - \varphi_4) \tag{9.52}$$

where amplitudes (I_2, I_4) and orientations (φ_2, φ_4) can be deduced from circular projections[40]. As for 1PF, this decomposition can be directly related to the symmetry orders of the $p(\varphi)$ function, this time decomposed over higher orders:

$$p(\varphi) = S_0[1 + S_2 \cos\,(2(\varphi - \rho_2) + S_4 \cos\,(4(\varphi - \rho_4)] \tag{9.53}$$

A direct calculation of the integral function leads to:

$$S_2 = \frac{3}{2} I_2,\ S_4 = 6 I_4$$

$$\text{and } \rho_2 = \rho_4 = \rho = \varphi_2 = \varphi_4 [\mathrm{modulo}\pi/2] \tag{9.54}$$

for a cylindrical symmetry distribution of in plane orientation ρ.

A higher number of coefficients of $p(\varphi)$ can thus be directly deduced from a 2PF polarization modulation measurement, as compared to 1PF, which provides a richer amount of information (on both aperture and shape) since both second and fourth orders of symmetry are now accessible.

Experimentally, polarized microscopy consists in retrieving polarization-dependent modulations of the recorded fluorescent/nonlinear signal, upon the variation of an incoming rotating polarization. The excitation focal spot is scanned over the sample by galvanometric mirrors, allowing a typical image rate of 1 image/second (for about 100 μm × 100 μm field of views). The polarization is rotated by a rotation motor in which a half wave plate is mounted (figure 9.3a). The number of polarization angles to record is a minimum of four, but generally higher to allow for a larger number of photons to be recorded, which governs the precision of the measurement. In each pixel of the recorded stack of images, a modulated signal is recorded (figure 9.3a), which is interpreted in terms of order parameters. These can be for instance a cone aperture and mean direction (ψ, ρ) that are then encoded in an image. Note that recently, other schemes have been developed which rather rotate the incident polarization very fast using electro-optic modulators, while the measured modulation is demodulated using a lock-in detector or during the scan of the image[45,46].

Polarization resolved 2PF has shown various responses in cell membranes depending on the order present in the lipids (figure 9.4). The extraction of readable $p(\varphi)$ coefficients resembles more or less sharp distributions depending on the membrane nature (figure 9.4c). This information can be translated into physical interpretation such as interaction potentials between lipids. When modelling different types of distributions, for instance Gaussian or Cone-like of various angular aperture, it is visible that they strongly differ in (S_2, S_4) values, thus allowing to discriminate them (figure 9.4d). This provides insights into local membrane order properties[14,44,47,48], lipid phases[14,44,47,49] but also local morphological changes due to cell interactions in signalling processes[50–52].

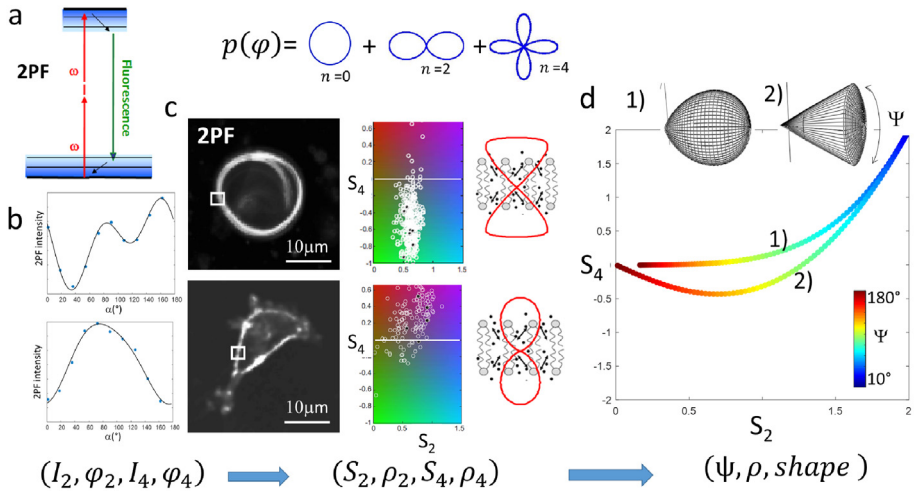

FIG. 9.4 – Polarized 2PF microscopy. (a) Principle of 2PF emission. (b) Examples of polarization resolved 2PF signals in cell membranes, revealing a high fourth-order response of the intensity (upper graph) and a high second-order response (lower graph). (c) Those responses come from two types of samples (square region), a multilamellar vesicle (upper image) and a COS 7 cell plasma membrane (lower image), both labelled with the lipid probe di-8-ANEPPQ. Reporting the measured pixels in a (S_2, S_4) graph shows very different behaviours. The schematic drawing of the membrane shows the retrieved $p(\varphi)$ function, which is smoother in the lower graph case because of the negligible fourth order. (c) These responses can be compared to models for which (S_2, S_4) are retrieved for various aperture angles ψ. The measurement of S_4 permits to discriminate between (1) smooth (Gaussian) and (2) sharp (Cone) distribution functions. Case (1) applies to plasma membranes, while case (2) applies to multi-lamellar vesicles. Adapted from[40].

9.3.3 Polarized Second Harmonic Generation

In this section, we derive the polarization response obtained in SHG imaging (figure 9.5). As seen in section 9.2 the SHG intensity comes from the radiation of a macroscopic dipole of the form:

$$I^{\mathrm{SHG}}(\alpha) \propto |\boldsymbol{P}_{\mathrm{SHG}}|^2 = \left|\chi^{(2)} : \boldsymbol{E}(\alpha)\boldsymbol{E}(\alpha)\right|^2 \tag{9.55}$$

From its fourth power dependence in $\boldsymbol{E}(\alpha)$, this intensity can thus be decomposed, similarly as for fluorescence, in contributions of different harmonics in α:

$$I^{\mathrm{SHG}}(\alpha) \propto a_0 + I_2 \cos 2(\alpha - \varphi_2) + I_4 \cos 4(\alpha - \varphi_4) \tag{9.56}$$

The $(a_0, I_2, \ldots.)$ coefficients are directly related to the macroscopic tensor $\chi^{(2)}$ the tensorial form of which carries information on the way molecules are organized. This tensor can be built up from the coherent addition of individual 1D dipoles, tensor components of which are non-vanishing only in one direction $\boldsymbol{e}$ (typically the red arrows in figure 9.5b). This assumption is valid under non resonant conditions[39,53]. Similarly as above for fluorescence, the goal is thus to determine the angular distribution of the elementary dipoles $\boldsymbol{e}$ (θ, φ) whose orientation is (θ, φ) in the macroscopic frame (we ignore here the third Euler angle for simplicity). The macroscopic tensor components are thus written:

$$\chi^{(2)}_{IJK} = N|\beta| \int (\boldsymbol{I}.\boldsymbol{e})(\boldsymbol{J}.\boldsymbol{e})(\boldsymbol{K}.\boldsymbol{e})(\theta, \varphi) f(\theta, \varphi) \sin\theta d\theta d\varphi \tag{9.57}$$

with $(I, J, K) = (X, Y)$ the macroscopic in-plane directions of the sample plane and $(\boldsymbol{I}.\boldsymbol{e})$ the scalar projection of $\boldsymbol{I}$ on $\boldsymbol{e}$. $|\beta|$ is the norm of the β tensor. Due to the θ dependence of the scalar projection functions, the macroscopic tensor can be directly related to a 2D distribution function of φ:

$$\chi^{(2)}_{IJK} = N|\beta| \int (\boldsymbol{I}.\boldsymbol{e})(\boldsymbol{J}.\boldsymbol{e})(\boldsymbol{K}.\boldsymbol{e})_{2D}(\varphi) p(\varphi) d\varphi \tag{9.58}$$

which is directly related to the distribution function $p(\varphi)$ mentioned in section 9.3.1. Here however, the power to which (cos, sin) functions appear is $n = 3$, so the only retrievable coefficients of the function $p(\varphi)$ are:

$$p(\varphi) = S_0[1 + S_1 \cos((\varphi - \rho_1) + S_3 \cos(3(\varphi - \rho_3)] \tag{9.59}$$

Not surprisingly, the only accessible order parameters are of odd symmetry, which is expected in SHG that is only active in non-centrosymmetric structures[18,19]. The relation between the $(a_0, I_2, \ldots.)$ intensity Fourier components and the $(S_1, S_3, \rho_1, \rho_3)$ distribution function coefficients can be found by a direct calculation which leads to, for a cylindrical symmetry distribution of in-plane orientation ρ[39]:

$$I_2 = \frac{4\left(S_1^2 + S_1 S_3\right)}{\left(5S_1^2 + S_3^2\right)},\ I_4 = \frac{2(S_1 S_3)}{\left(5S_1^2 + S_3^2\right)}$$

$$\rho_1 = \rho_3 = \rho = \varphi_2 = \varphi_4[\pi/2] \tag{9.60}$$

Visibly, the relation between the intensity coefficients and distribution coefficients is more complex than in fluorescence, due to a nonlinear dependence that originates from the nonlinear coherent nature of the optical process. Nevertheless, it is possible to resolve the inverse problem and retrieve molecular order information

from polarization resolved SHG[39], together with possible estimation strategies and precision that has been intensively studied[54,55]. The determination of (S_1, S_3) coefficients, complementary to 2PF, permits deducing rich information on odd orders of a molecular distribution.

The polarized nature of SHG has been in particular broadly investigated in collagen, where it has been found that peptide bounds, forming a conserved helicoidal structure (figure 9.5b), could be at the origin of individual induced dipoles[3,56]. This non centro-symmetric arrangement leads to strong SHG signals. When analysed in polarization, strong negative third-order S_3 values are found in individual collagen fibers (figure 9.5c,d)[25,39]. A comparison of retrieved (S_1, S_3) with possible models shows that those values are in strong agreement with a distribution of nonlinear dipoles at the surface of a cone, rather than inside a filled distribution (figure 9.5d). In deep tissues, this distribution is essentially broadened and filled in a more complex distribution, which requires also accounting for polarization distortions occurring from scattering and birefringence[57,58]. Nevertheless, polarized SHG microscopy has shown the possibility to reveal changes of organization in tissues upon mechanical modifications[59,60].

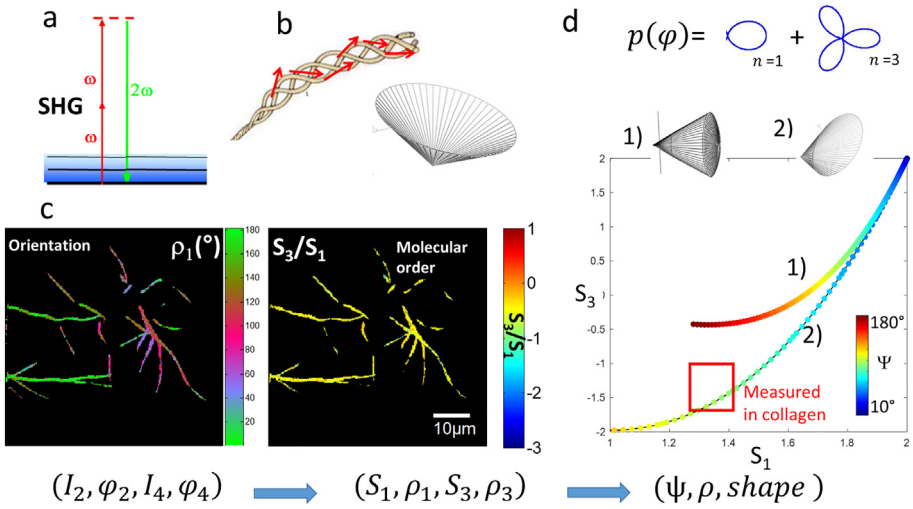

FIG. 9.5 – Polarization resolved SHG microscopy. (a) Principle of SHG emission. (b) collagen individual fibrils are expected to lead to a distribution of nonlinear induced dipoles along a cone surface. (c) P-SHG image of collagen fibers deposited on a glass coverslip. The polarization SHG data are treated to retrieve the mean orientation or the fibers (left image) and their (S_1, S_3) values, the ratio of which is depicted (right image). (d) Polarization SHG filters out only odd orders of the molecular distribution, represented here schematically. Models of two different dipole distributions (1) filled cone of angular aperture $s\psi$ and (2) cone surface, showing that the measurement of (S_1, S_3) can discriminate for these two distributions in some cases. The curves represent (S_1, S_3) values for these distributions, at various angular aperture ψ. Measured values in individual collagen fibers are in closer agreement with a cone surface, of aperture of about $\psi \simeq 50°$.

9.3.4 Polarized FWM and CARS

As seen in section 9.2, the FWM/CARS intensity comes from the radiation of a macroscopic dipole of the form:

$$I^{\mathrm{THG,FWM,CARS}}(\alpha) \propto |\boldsymbol{P}_{\mathrm{SHG}}|^2 = \left|\chi^{(3)} : \boldsymbol{E}(\alpha)\boldsymbol{E}(\alpha)\boldsymbol{E}(\alpha)\right|^2 \tag{9.61}$$

Assuming that all incident polarizations rotate with the same polarization angle, the measured intensity is a sixth power dependence in $\boldsymbol{E}(\alpha)$, which can thus be decomposed in contributions of different harmonics in α[35,45,61,62]:

$$I_{\mathrm{THG,FWM,CARS}}(\alpha) \propto a_0 + I_2 \cos 2(\alpha - \varphi_2) + I_4 \cos 4(\alpha - \varphi_4) + I_6 \cos 6(\alpha - \varphi_6) \tag{9.62}$$

The relation between the (I_n, φ_n) coefficients and the molecular orientation information comes from the nature of the underlying nonlinear tensor. Knowing the symmetry of the individual molecules (structure of the γ_{ijkl} tensor) can therefore lead to a model that permits to retrieve partially $f(\boldsymbol{\Omega})$ and molecular order information, as done recently on lipids in tissues *via* THG (figure 9.6a–c)[35].

In CARS, the obtained modulation has a maximum contrast when the vibration bonds oscillate in the same direction, a signature of a high molecular order. The nature of the response is, however, more complex since the γ_{ijkl} tensor originates from two different contributions, resonant and non-resonant. Supposing that the resonant contribution is predominant, the microscopic tensor can be considered being representative of the direction of the molecular bonds directions e, with γ_{eeee} dominating over the other components[62]:

$$\chi^{(3)}_{IJKL} = N|\gamma| \int (\boldsymbol{I}.\boldsymbol{e})(\boldsymbol{J}.\boldsymbol{e})(\boldsymbol{K}.\boldsymbol{e})(\boldsymbol{L}.\boldsymbol{e})_{2D}(\varphi)p(\varphi)\,d\varphi \tag{9.63}$$

The relevant $p(\varphi)$ contributions are therefore different from the ones appearing in SHG, since now even symmetries are read:

$$p(\varphi) = S_0[1 + S_2 \cos((\varphi - \rho_2) + S_4 \cos(4(\varphi - \rho_4)] \tag{9.64}$$

Injecting this tensorial form into the polarization sensitive intensity leads to a complex nonlinear relation between the (I_n, φ_n) coefficients and the (S_n, ρ_n) molecular order signatures. This makes the retrieval of the parameters complex involving optimization procedures. Nevertheless, a recent work has permitted to simply relate coefficients through the study of the function[63] $\sqrt{I_{\mathrm{CARS}}(\alpha)} = a_0 + I_2 \cos 2(\alpha - \varphi_2) + I_4 \cos 4(\alpha - \varphi_4) + ..$, where a direct relationship can be found which is identical to the one found in 2PF above. Note that when the non-resonant background, intrinsic to CARS, is not negligible, the interpretation of polarized signals leads generally to overestimated order parameters[63].

Using polarization resolved CARS, high molecular organization has been evidenced in water molecules between phospholipid layers[64], CN bonds of liquid crystals[65], and CH bonds of polyglucan chains in cellulose[66]. Monitoring the CH_2 vibrational stretching bond in lipids has shown a considerable level of information

on lipid order within artificial multilayers, where the measured modulation was used to retrieve quantitative information on sub-diffraction molecular orientational order behaviours, in particular, its mean orientation and angular distribution shape[67]. Lipid order imaging by polarization-resolved CARS has also been applied to myelin (figure 9.6d,e), which forms dense lipid multilayers around axons in fixed tissues in mouse brains[68] and sciatic nerves[69], as well as in the spinal cords of mice[62,70,71]. Being able to monitor the lipid order without the need of fluorescent labels ultimately brings new knowledge on lipid packing properties (figure 9.6e), which is critical for the structural integrity of myelin in the central and peripheral nervous systems, with consequences in neuro-pathologies[62,72].

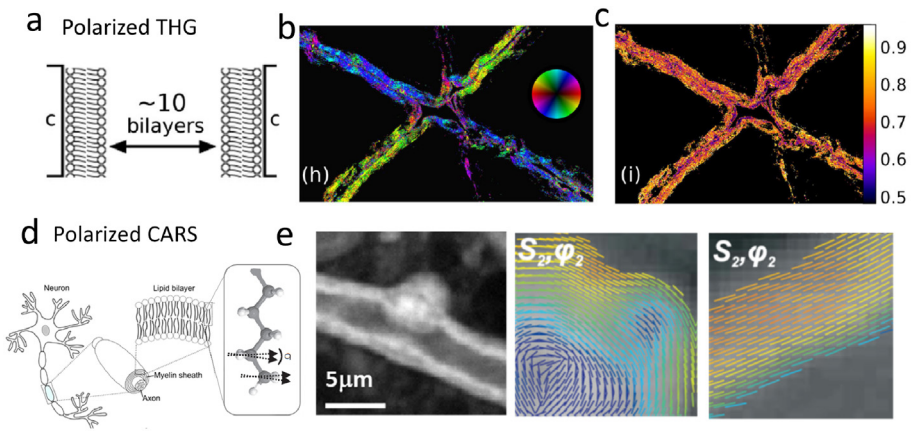

FIG. 9.6 – (a) Within the skin stratum corneum, stacked lipid bilayers do exist between the dead corneocytes (labeled "c"). Vertically oriented folds extending tens of microns deep into the epidermis provide an optimal geometry for P-THG imaging. (b) Lipid orientation deduced from P-THG images of a human skin biopsy approximately 25 μm from the skin. (c) modulation obtained in the same image, providing information on the lipid ordering within the interfaces. A strong modulation is observed exclusively from ordered phases and not from other structures. From[35]. (d) Schematics of a neuron and its myelin sheath made of lipid multilayers used in P-CARS imaging. (e) Left: CARS image of myelin in a fixed spinal cord. Middle and right: deduced lipid organization measured from P-CARS modulations, in different regions of the myelin sheath. Sticks at each pixel of the image represent the complete information on the mean orientation of the lipid distribution (stick orientation) and its molecular order (stick color). From[62].

9.3.5 Sub-Diffraction Vectorial Imaging in Metal Nanostructures

SHG imaging has not been employed for biological imaging alone, it also provides an interesting contrast for the investigation of nanomaterials and crystals down to the nanometric size[73–75].

Metal nanostructures are important elements for the design of optical functions in nano-optics, which is the core of the field of nano-plasmonics. The optical properties of metal nanostructures are not only highly dependent on the excitation polarization, which has a consequence on their spectral scattering properties[76], but also on the spatial and vectorial extent of the local fields they support[77,78]. Recent works have shown that performing polarization sensitive SHG in a scanned image can reveal important information on nonlinear vectorial information occurring at the nanoscale in metal nanostructures[77]. In figure 9.7, isolated gold nanoparticles of 150 nm size and various shapes have been scanned in SHG microscopy, leading to images that resemble the point spread function (PSF) of the nonlinear microscope, *e.g.* with a resolution of about 250 nm. Resolving the SHG polarization response of each pixel for pixel sizes well below the diffraction limit (here 40 nm size per pixel) reveals very different images depending on the nanostructure shape. In figure 9.7b, (I_2, φ_2) images of the recorded polarization SHG signal reveal indeed directions of sticks (φ_2) that mainly follow the symmetry of the particle itself, while intense polarization modulation amplitudes (I_2) appear only in certain parts of the images, in particular for the four-arm particle. These images result from a nonlinear coupling at the overlap between the nanoparticle and the excitation diffraction-limited spot at this particular pixel position, which explains their larger spatial expansion as compared to the intensity image. The (I_2, φ_2) maps reveal information of the orientational organization of nonlinear induced dipoles within each location of the incident focal spot. In particles larger than 100 nm, the SHG signal is dominated by their surface contribution[79], which is normal to the surface contour, and by the presence of a localized confined field at the resonant excitation, which explains the resemblance of the polarized SHG patterns with the particles' shape themselves, even though their size is below the diffraction limit size.

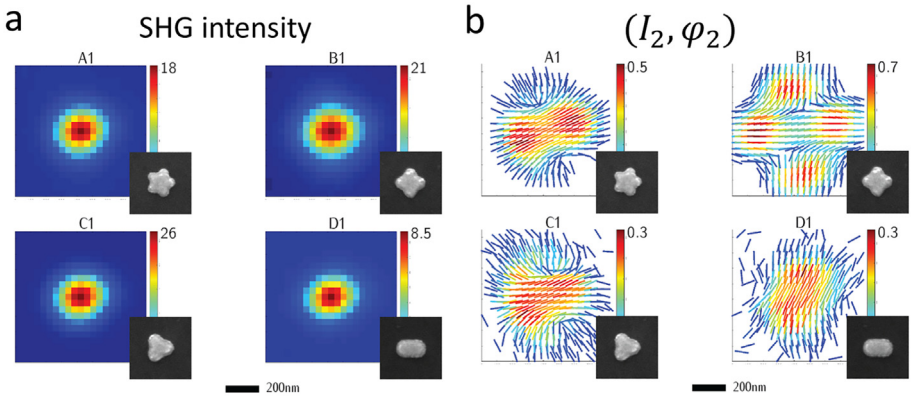

FIG. 9.7 – Polarization SHG responses in metal nanoparticles. (a) Pure intensity SHG images of gold nanoparticles of 150 nm size (TEM and optical SHG images are at the same scale), excited at 800 nm. (b) (I_2, φ_2) map (encoding I_2 in stick colours and φ_2 in the stick orientation) of the particles shown in (a). The 5-arm structure is not sufficiently resolved to show its shape by polarized SHG. The nano-rod structure evidences a transverse resonance. All images are produced using a 40 nm pixel size. Adapted from[77].

9.4 In Depth Nonlinear Microscopy in Complex Media

9.4.1 Nonlinear Microscopy in the Presence of Aberrations: Adaptive Optics

Imaging deep into biological tissues is inherently affected by the refractive index heterogeneities of the medium, which provoke a deformation of the incoming beam's spatial phase (the optical wavefront), resulting in a deformed focus (called Point Spread Function, PSF), which quickly distorts and blurs the image. When these perturbations occur at shallow depths, they can be modelled by optical aberrations and classified into different types such as astigmatism and spherical aberrations, such as Zernike polynomials of different orders.

To correct for such aberrations, researchers in optical microscopy have developed a methodology called adaptive optics (AO) inspired from astronomy, a field which has a long standing experience in correcting star images distorted by the atmosphere turbulences. AO is based on the real-time measurement of an optical signal (fluorescence for instance) in a sample, from an object considered as a guide star, whose signal is to be improved by an iterative change of the incident optical wavefront. While in astronomy, it is possible to use real or artificial stars to effectively measure the emission wavefront and possibly reverse it to correct for the incident distortions (phase conjugation), isolated point-like "guide stars" in biological samples are not always guaranteed. It is nevertheless possible to create them artificially with embedded fluorescent beads[80] or from intrinsic two-photon fluorescence emission from the sample within a small volume[81]. Different approaches exist, either directly measuring the emitted wavefront (using a wavefront sensor) and reverse it on the incident beam to provide a direct correction[80], or *via* an indirect wavefront sensing in which the measured signal is iteratively improved based on a metric (generally the measured emission brightness or contrast)[82]. To modify the incident wavefront iteratively and finally use an optimized one, deformable mirrors are used such as liquid crystal spatial light modulators (SLM) or deformable mirrors (DM). These modulators adjust the distorted wavefront to decrease the PSF to the diffraction-limit. Optical aberrations are then corrected and the performance of the imaging system can be optimized. AO techniques have improved the quality of fluorescence microscopy over the last decade[83–85], allowing to correct both aberrations from optical elements and from weak changes of the medium's refractive index. They have for instance permitted to reveal the neuronal network of a mouse cortex with sub-micrometric resolution down to a depth of 450 μm[86]. Usually in a biological tissue such as the mouse brain, it is necessary to use a large number of Zernike modes (up to 10–100), which increases with depth.

9.4.2 Nonlinear Microscopy in Scattering Media

When going deeper into biological samples, light scattering predominates and surpasses smooth optical aberrations, making adaptive optics to fail to sufficiently correct the PSF deformation, since a much larger number of wavefront modes needs

to be manipulated. In this scattering regime, the medium seen by the optical incoming focussed beam is now made of a very large number of scatterers acting as obstacles which ultimately deviate the light propagation direction and mix together a considerable number of different wave-vectors. We suppose here that the medium does not absorb light. The physical mechanism occurring that affects light propagation is primarily Mie scattering. The scale of interest is called the scattering mean free path L_s, which is the average distance between two scattering events. When the thickness (depth) of the medium is below L_s, the optical propagation regime is called the ballistic regime. Well above this thickness, it is called the multiple scattering regime[87]. An important quantity in light propagation in scattering media is the distance at which light loses its main incident direction, the transport mean free path L_t. When the size of the scatterers is well above the wavelength, light is scattered forward; however, if the scatterer size decreases, the radiation becomes more isotropic. An averaged quantity to express this loss of directionality is called the anisotropy factor g, defined as the average cosine of the emission angle θ of scattered radiation, $g = \langle \cos \rangle \theta$. $g \sim 0$ in 'isotropic scattering' media, while $g \sim 1$ in 'forward scattering' media. The scale of interest to express the loss of directionality of wave propagation is the transport mean free path L_t, related to L_s *via* the relation:

$$L_t = \frac{L_s}{1-g} \tag{9.65}$$

In biological tissues, $g \sim 0.9$ and $L_s \sim 100\,\mu\text{m}$ which leads to $L_t \sim 1\,\text{mm}$.

Above L_t in depth, optical waves cannot be described by Maxwell's equations and other tools are used such as the radiative transfer equation, which neglects the wave nature of light but rather studies its intensity.

In this regime, light scattering randomizes the optical propagation paths in such a way that the optical wavefront is not anymore resembling a focus, but rather a random light interference pattern named speckle[88](figure 9.8a). This speckle is made out of the interference between a very large number of modes of propagation, which depends on the size of the illuminated area A and on the wavelength of the incident light λ:

$$N_{\text{modes}} = \frac{A}{\lambda^2} \tag{9.66}$$

The spatial fluctuations present in a speckle pattern are well defined in statistics, and exhibit dark and bright grains of characteristic size proportional to λ[88]. Similarly to a random amplitude, a speckle is also random in the polarization state, each grain exhibiting its own polarization state.

Speckle patterns, while spatially random, are nevertheless deterministic (as long as the scattering medium is stable) and linearly depend on the incident fields, with variations occurring when changing the incoming light incidence for instance. A speckle can therefore be coherently manipulated by adjusting the phase front of the incident light, leading to a possible active control despite the large number of modes to handle. Active wavefront shaping (WS) of light consists in manipulating the phase front of light using a very large number of modes (generally coming from

SLMs with $\sim 10^3$–10^6 pixels) in order to coherently manipulate a speckle at the exit of a scattering medium, even if this number of modes stays lower than the ones present in the medium.

Wavefront-Shaping (figure 9.8a) has emerged as a promising tool to control scattered light over the last ten years[89,90] in order to deterministically modify a beam at the exit of a scattering medium. The first experimental demonstration was performed in 2007[91], in which the authors manipulated a continuous wave (CW) through a thick layer of white paint. A feedback control was used between the intensity at a target position and the spatial shape of the incident light modulated by a Spatial Light Modulator (SLM) to put back in phase a large number of paths interfering at this specific point. This work, similar to an extreme adaptive optics iteration, has later opened many other initiatives to manipulate light behind a scattering medium[90]. Among them, a more deterministic approach consisted in measuring experimentally the relation between incoming and outcoming fields, in order to use an inverse operation to create any wanted outcoming pattern or to focus light[92]. This matrix relation is particularly interesting to investigate the effect of a non-monochromatic beam (*e.g.* a pulsed beam) in a scattering medium propagation. This approach assumes a linear scattering process, resulting in a matrix relation between incoming and outcoming fields from the medium[90]:

$$E_{\text{out}} = S \cdot E_{\text{in}} \tag{9.67}$$

S is called the Scattering Matrix, and contains both transmission and reflexion components of the fields propagating inside the medium. The experimentally accessible contribution of S is the Transmission Matrix (TM) component, measured by controlling a number of N modes in the incoming side E_{in} while measuring M modes in the outcoming side E_{out} *via* the M pixels of a CCD camera. The TM matrix T leads to:

$$E_{\text{out}}^{\text{CCD}} = T \cdot E_{\text{in}}^{\text{SLM}} \tag{9.68}$$

In[92], the authors demonstrated how to easily measure the TM by self-reference interferometry through the scattering medium (white paint) illuminated by a CW monochromatic source, using N phase-stepped modes created in the SLM, for which one part of the area stayed non-modulated. This experiment, very similar to phase-shifting holography, allows for the measurement of the phase pattern of the unknown field at the exit of the scattering medium. The authors then exploited the TM to refocus light through the medium under monochromatic conditions. This refocussing operation requires the use of an adequate inverse of the T operator that avoids sensitivity to noise and the fact that only phases can be controlled. This is done *via* the transpose conjugate operator $T^{\dagger}$:

$$E_{\text{in}}^{\text{SLM}} = T^{\dagger} \cdot E_{\text{out}}^{\text{target}} \tag{9.69}$$

The reversal operation above is appropriate in the monochromatic regime where the TM matrix is well defined. The need to use optical pulses in the context of nonlinear optics makes WS more challenging since both space and time need to be controlled to retrieve a focussed, short pulse at the exit of the medium. Indeed, a short

pulse is likely to be largely distorted in time through the optical propagation, with no guaranty that WS provides a temporal control of the pulse while controlling its spatial properties. Similarly, propagation through a scattering medium is likely to distort the spectral phase of the pulse, since the medium responds differently to each spectral component of the incident pulse. In addition to a spatial speckle-like pattern, an ultra-short pulse becomes therefore a complex spatio-temporal speckle field different in every point, resulting in a temporally broadened pulse[89]. Experimentally, a 100 fs pulse centred around 800 nm passing through a 100 μm thick medium made of ZnO nanoparticles gives a light confinement time τ_m of about 10 ps[93]. In thick (mm) biological media where almost no ballistic light is present, it is expected that the time profile of such a pulse would be broadened up to 10–100 times compared to the initial duration.

This quantity can be related to its spectral counterpart. Considering that a speckle pattern gets decorrelated when tuning the wavelength of the incident light, one can define a characteristic spectral width $\delta\lambda_m$[88] inversely proportional to τ_m. An ultrashort pulse of spectral width $\delta\lambda_L$ will therefore be spectrally distorted if $\delta\lambda_L > \delta\lambda_m$. Similarly in the time domain, an ultrashort pulse of time width $\delta\tau_L$ will be temporally elongated if $\delta\tau_L < \tau_m$. The number of spectral or temporal speckle grains (or modes) N_λ that can be manipulated within the bandwidth of the pulse is:

$$N_\lambda = \frac{\delta\lambda_L}{\delta\lambda_m} = \frac{\tau_m}{\delta\tau_L} \tag{9.70}$$

N_λ denotes the number of uncorrelated 'spectral grains/modes' that are present within the spectral bandwidth of the pulse. It also corresponds to the number of uncorrelated 'temporal spectral grains' found in a time interval of duration τ_m. If the pulse propagating in the medium is much shorter than τ_m, the resulting speckle is the incoherent superposition of N_λ uncorrelated speckles, and is therefore of much lower contrast than 1. Wavefront shaping experiments would become, in such a situation, much less efficient than in a monochromatic regime since WS can coherently manipulate only modes which spectral width is smaller than $\delta\lambda_m$. In the diffusive regime (layer of paint), this width can be very narrow ($\sim$nm)[94]. Temporal control of an ultrashort pulse of light, of large spectral bandwidth, has been intensively investigated[89]. Different approaches were proposed to perform spatio-temporal focusing by exploiting only the spatial degrees of freedom of a single SLM. It consists in focusing light in a single spatial speckle grain, while ensuring that the temporal profile in this specific position has the same ultrashort duration than the input pulse. Spatio-temporal focusing was performed using methods such as feedback-based algorithms based on either a nonlinear optical process[95,96] (figure 9.8b), which naturally selects modes based on a nonlinear mechanism that is active for focussed, short pulses, or a time-gated signal[97]. Another approach consisted in measuring both the amplitude and phase of the spatio-spectral speckle field by quantifying spectral distortions of a speckle using pulse shaping approaches[98]. The Fourier transform of the spatio-spectral complex electric field along the frequency axis provides in this case a reconstruction of the spatio-temporal speckle.

More recently, researchers have shown that it is possible to manipulate the spatio-temporal speckle by the use of WS and only one spatial SLM. Spectral

diversity of the scattering medium prevents the use of a monochromatic TM to control an ultrashort pulse of light. They measured the multi-spectral TM of a medium, made of a stack of monochromatic TMs for all the spectral components of the output pulse[93,99]. This allowed to focus different spectral components in different spatial positions, using the scattering medium as a controllable dispersive element. Focusing all the spectral components in the same output spatial position with accurate spectral phase control enabled deterministic control of the output pulse time profile. With this tool not only a focus can be formed at a given position with a short pulse time profile, but also the medium can be used as a pulse shaper, since a scattering medium couples both spectral and spatial degrees of freedom. Similarly, the authors could perform a stack of time-gated TMs to build up a time-resolved TM in a scattering medium, enabling spatio-temporal focusing. Both approaches permitted to focus the output pulse almost back to its initial duration. These methods permit to enhance a non-linear process at the output of the scattering medium, where the low power per speckle grain inherently limits such interactions. Other approaches have used a direct self-reference 'broadband' TM matrix measurement. In such configuration, it has been shown that a strong nonlinear SHG signal can be recovered after refocussing[100], accompanied by a natural polarization recovery thanks to the intrinsic selection propagation paths in the medium[101]. At last, thanks to the manipulation of spectrally correlated TMs, the recovering of a nonlinear frequency mixing signal was permitted through a thick scattering medium[102] in a CARS configuration, thanks to the coherent manipulation of the TMs even for two distant frequencies.

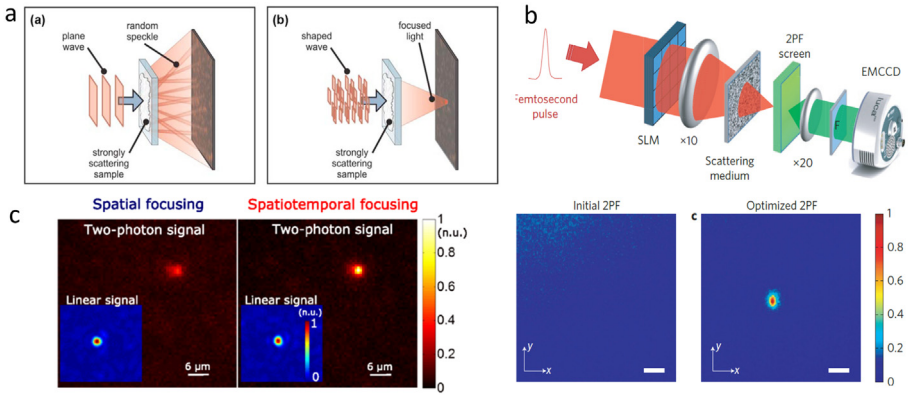

FIG. 9.8 – (a) Spatial wavefront shaping to refocus light behind a scattering medium in a monochromatic continuous regime. From[91]. (b) Spatio-temporal focusing by optimizing 2PF. A SLM controls the incident wavefront, optimizing the 2PF at a selected point imaged by a camera. The temporal focussing is ensured by the nonlinear signal imaged[96]. (c) Spatio-temporal focusing using a Multispectral Transmission Matrix, using a 110 fs laser and a strongly scattering medium (thin layer of ZnO nanoparticles, placed in front of a 2PF-active sample). Comparison of 2PF/linear signals for spatial (monochromatic phase conjugation, left) and spatiotemporal focusing (right). From[93].

9.5 Conclusions

In this lecture, we have described the important aspects and specificities of nonlinear imaging, polarized nonlinear imaging and nonlinear imaging through and in complex media. Challenges remain in the field to accommodate the complexity of biological media and make nonlinear imaging adapt to new challenges in biology, nanosciences and eventually biomedical optics. Among them, the speed of imaging needs to reach a real-time capability, and scattering needs to be circumvented to reach higher depth through a fast modality. Recent advances in the field of spatial and spectral shaping, for instance, using spectral focussing[103] or new microscopy geometries such as light sheet imaging[29], are promising routes towards these goals.

Acknowledgements

The author thanks all students and colleagues who contributed to the results mentioned in this lecture: J Duboisset, P. Gasecka (SHG, CARS, 2PF); C. Rendon-Barraza, N. Kumar Balla (SHG in metal nanoparticles); M. Hofer, H. B. De Aguiar, S. Gigan (polarization in scattering media).

References

[1] Zipfel W.R., Williams R.M., Webb W.W. (2003) Nonlinear magic: Multiphoton microscopy in the biosciences, *Nat. Biotechnol.* **21**(11), 1369. https://doi.org/10.1038/nbt899.

[2] Moreaux L., Pons T., Dambrin V., Blanchard-Desce M., Mertz J. (2003) Electro-optic response of second-harmonic generation membrane potential sensors, *Opt. Lett.* **28**(8), 625. https://doi.org/10.1364/ol.28.000625.

[3] Deniset-Besseau A., Duboisset J., Benichou E., Hache F., Brevet P.-F., Schanne-Klein M.-C. (2009) Measurement of the second-order hyperpolarizability of the collagen triple helix and determination of its physical origin, *J. Phys. Chem. B* **113**(40), 13437. https://doi.org/10.1021/jp9046837.

[4] Guo Y., Ho P.P., Savage H., Harris D., Sacks P., Schantz S., Liu F., Zhadin N., Alfano R.R. (1997) Second-harmonic tomography of tissues, *Opt. Lett.* **22**(17), 1323. https://doi.org/10.1364/ol.22.001323.

[5] Oron D., Yelin D., Tal E., Raz S., Fachima R., Silberberg Y. (2004) Depth-resolved structural imaging by third-harmonic generation microscopy, *J. Struct. Biol.* **147**(1), 3. https://doi.org/10.1016/S1047-8477(03)00125-4.

[6] Débarre D., Supatto W., Pena A.M., Fabre A., Tordjmann T., Combettes L., Schanne-Klein M.C., Beaurepaire E. (2006) Imaging lipid bodies in cells and tissues using third-harmonic generation microscopy, *Nat. Methods* **3**(1), 47. https://doi.org/10.1038/nmeth813.

[7] Cheng J.X., Jia Y.K., Zheng G., Xie X.S. (2002) Laser-scanning coherent anti-Stokes Raman scattering microscopy and applications to cell biology, *Biophys. J.* **83**(1), 502. https://doi.org/10.1016/S0006-3495(02)75186-2.

[8] Zumbusch A., Holtom G.R., Xie X.S. (1999) Three-dimensional vibrational imaging by coherent anti-Stokes Raman scattering, *Phys. Rev. Lett.* **82**(20), 4142. https://doi.org/10.1103/PhysRevLett.82.4142.

[9] Akimov D., Chatzipapadopoulos S., Meyer T., Tarcea N., Dietzek B., Schmitt M., Popp J. (2009) Different contrast information obtained from CARS and nonresonant FWM images, *J. Raman Spectrosc.* **40**(8), 941. https://doi.org/10.1002/jrs.2205.

[10] Tu H., Liu Y., Marjanovic M., Chaney E.J., You S., Zhao Y., Boppart S.A. (2017) Concurrence of extracellular vesicle enrichment and metabolic switch visualized label-free in the tumor microenvironment, *Sci. Adv.* **3**(1). https://doi.org/10.1126/sciadv.1600675.

[11] Sun Y., You S., Tu H., Spillman D.R., Chaney E.J., Marjanovic M., Li J., Barkalifa R., Wang J., Higham A.M., Luckey N.N., Cradock K.A., George Liu Z., Boppart S.A. (2018) Intraoperative visualization of the tumor microenvironment and quantification of extracellular vesicles by label-free nonlinear imaging, *Sci. Adv.* **4**(12), eaau5603. https://doi.org/10.1126/sciadv.aau5603.

[12] Campagnola P.J., Millard A.C., Terasaki M., Hoppe P.E., Malone C.J., Mohler W.A. (2002) Three-dimensional high-resolution second-harmonic generation imaging of endogenous structural proteins in biological tissues, *Biophys. J.* **82**(1 Pt 1), 493. https://doi.org/10.1016/S0006-3495(02)75414-3.

[13] Denk W., Strickler J.H., Webb W.W. (1990) Two-photon laser scanning fluorescence microscopy, *Science (New York, N.Y.)* **248**(4951), 73. http://www.ncbi.nlm.nih.gov/pubmed/2321027.

[14] Florine-Casteel K. (1990) Phospholipid order in gel- and fluid-phase cell-size liposomes measured by digitized video fluorescence polarization microscopy, *Biophys. J.* **57**(6), 1199. https://doi.org/10.1016/S0006-3495(90)82639-4.

[15] Forkey J.N., Quinlan M.E., Goldman Y.E. (2000) Protein structural dynamics by single-molecule fluorescence polarization, *Prog. Biophys. Mol. Biol.* **74**, 1.

[16] Moerner W.E. (2002) A dozen years of single-molecule spectroscopy in physics, chemistry, and biophysics, *Journal of Physical Chemistry B*. American Chemical Society, Vol. 106, Issue 5, pp. 910–927. https://doi.org/10.1021/jp012992g.

[17] Axelrod D. (1989) Chapter 12 Fluorescence polarization microscopy, *Methods Cell Biol.* **30**, 333. https://doi.org/10.1016/S0091-679X(08)60985-1.

[18] Boyd R.W. (2008) *Nonlinear optics*. Academic Press.

[19] Brasselet S. (2011) Polarization-resolved nonlinear microscopy: Application to structural molecular and biological imaging, *Adv. Opt. Photonics* **3**(3), 205. https://doi.org/10.1364/AOP.3.000205.

[20] Moreaux L., Sandre O., Blanchard-Desce M., Mertz J. (2000) Membrane imaging by simultaneous second-harmonic generation and two-photon microscopy, *Opt. Lett.* **25**(5), 320. https://doi.org/10.1364/ol.25.000320.

[21] Delahaye E., Sandeau N., Tao Y., Brasselet S., Clement R. (2009) Synthesis and second harmonic generation microscopy of nonlinear optical efficient hybrid nanoparticles embedded in polymer films. Evidence for intra- and internanoparticles orientational synergy, *J. Phys. Chem. C* **113**(21). https://doi.org/10.1021/jp8104985.

[22] Freund I., Deutsch M., Sprecher A. (1986) Connective tissue polarity. Optical second-harmonic microscopy, crossed-beam summation, and small-angle scattering in rat-tail tendon, *Biophys. J.* **50**(4), 693. https://doi.org/10.1016/S0006-3495(86)83510-X.

[23] Kwan A.C., Dombeck D.A., Webb W.W. (2008) Polarized microtubule arrays in apical dendrites and axons, *Proc. Nat. Acad. Sci. U.S.A.* **105**(32), 11370. https://doi.org/10.1073/pnas.0805199105.

[24] Strupler M., Hernest M., Fligny C., Martin J.-L., Tharaux P.-L., Schanne-Klein M.-C. (2008) Second harmonic microscopy to quantify renal interstitial fibrosis and arterial remodeling, *J. Biomed. Opt.* **13**(5), 054041. https://doi.org/10.1117/1.2981830.

[25] Aït-Belkacem D., Guilbert M., Roche M., Duboisset J., Ferrand P., Sockalingum G., Jeannesson P., Brasselet S. (2012) Microscopic structural study of collagen aging in isolated fibrils using polarized second harmonic generation, *J. Biomed. Opt.* **17**(8). https://doi.org/10.1117/1.JBO.17.8.080506.

[26] Gusachenko I., Tran V., Houssen Y.G., Allain J.-M., Schanne-Klein M.-C. (2012) Polarization-resolved second-harmonic generation in tendon upon mechanical stretching, *Biophys. J.* **102**(9), 2220. https://doi.org/10.1016/j.bpj.2012.03.068.

[27] Mansfield J.C., Winlove C.P., Moger J., Matcher S.J. (2008) Collagen fiber arrangement in normal and diseased cartilage studied by polarization sensitive nonlinear microscopy, *J. Biomed. Opt.* **13**(4), 044020. https://doi.org/10.1117/1.2950318.

[28] Born M., Wolf E., Bhatia A.B., Clemmow P.C., Gabor D., Stokes A.R., Taylor A.M., Wayman P.A., Wilcock W.L. (1999) *Principles of optics*. Cambridge University Press. https://doi.org/10.1017/cbo9781139644181.

[29] Maioli V., Boniface A., Mahou P., Ortas J.F., Abdeladim L., Beaurepaire E., Supatto W. (2020) Fast in vivo multiphoton light-sheet microscopy with optimal pulse frequency, *Biomed. Opt. Exp.* **11**(10), 6012. https://doi.org/10.1364/boe.400113.

[30] Zipfel W.R., Williams R.M., Christiet R., Nikitin A.Y., Hyman B.T., Webb W.W. (2003) Live tissue intrinsic emission microscopy using multiphoton-excited native fluorescence and second harmonic generation, *Proc. Nat. Acad. Sci. U.S.A.* **100**(12), 7075. https://doi.org/10.1073/pnas.0832308100.

[31] Débarre D., Olivier N., Beaurepaire E. (2007) Signal epidetection in third-harmonic generation microscopy of turbid media, *Opt. Exp.* **15**(14), 8913. https://doi.org/10.1364/oe.15.008913.

[32] Lozovoy V.V., Pastirk I., Walowicz K.A., Dantus M. (2003) Multiphoton intrapulse interference. II. Control of two- and three-photon laser induced fluorescence with shaped pulses, *J. Chem. Phys.* **118**(7), 3187. https://doi.org/10.1063/1.1531620.

[33] Drobizhev M., Makarov N.S., Tillo S.E., Hughes T.E., Rebane A. (2011) Two-photon absorption properties of fluorescent proteins, *Nature Methods*. Nature Publishing Group, Vol. 8, Issue 5, pp. 393–399. https://doi.org/10.1038/nmeth.1596.

[34] Silberberg Y. (2009) Quantum coherent control for nonlinear spectroscopy and microscopy, *Ann. Rev. Phys. Chem.* **60**(1), 277. https://doi.org/10.1146/annurev.physchem.040808.090427.

[35] Zimmerley M., Mahou P., Débarre D., Schanne-Klein M.-C., Beaurepaire E. (2013) Probing ordered lipid assemblies with polarized third-harmonic-generation microscopy, *Phys. Rev. X* **3**(1), 011002. https://doi.org/10.1103/PhysRevX.3.011002.

[36] Munhoz F., Rigneault H., Brasselet S. (2012) Polarization-resolved four-wave mixing microscopy for structural imaging in thick tissues, *J. Opt. Soc. Am. B: Opt. Phys.* **29**(6). https://doi.org/10.1364/JOSAB.29.001541.

[37] Cheng J.-X., Xie X.S. (2015) Vibrational spectroscopic imaging of living systems: An emerging platform for biology and medicine, *Science (New York, N.Y.)* **350**(6264), aaa8870. https://doi.org/10.1126/science.aaa8870.

[38] Aggarwal S., Yurlova L., Simons M. (2011) Central nervous system myelin: Structure, synthesis and assembly, *Trends Cell Biol.* **21**(10), 585. https://doi.org/10.1016/j.tcb.2011.06.004.

[39] Duboisset J., Aït-Belkacem D., Roche M., Rigneault H., Brasselet S. (2012) Generic model of the molecular orientational distribution probed by polarization-resolved second-harmonic generation, *Phys. Rev. A – At. Mol. Opt. Phys.* **85**(4). https://doi.org/10.1103/PhysRevA.85.043829.

[40] Ferrand P., Gasecka P., Kress A., Wang X., Bioud F.-Z., Duboisset J., Brasselet S. (2014) Ultimate use of two-photon fluorescence microscopy to map orientational behavior of fluorophores, *Biophys. J.* **106**(11). https://doi.org/10.1016/j.bpj.2014.04.011.

[41] Mi S., Lee X., Hu Y., Ji B., Shao Z., Yang W., Huang G., Walus L., Rhodes K., Gong B.J., Miller R.H., Pepinsky R.B. (2011) Death receptor 6 negatively regulates oligodendrocyte survival, maturation and myelination, *Nat. Med.* **17**(7), 816. https://doi.org/10.1038/nm.2373.

[42] Powell K. (2005) What the cytoskeleton really looks like, *J. Cell Biol.* **170**(7), 1019. https://doi.org/10.1083/jcb1707fta2.

[43] Kress A., Wang X., Ranchon H., Savatier J., Rigneault H., Ferrand P., Brasselet S. (2013) Mapping the local organization of cell membranes using excitation-polarization-resolved confocal fluorescence microscopy, *Biophys. J.* **105**(1). https://doi.org/10.1016/j.bpj.2013.05.043.

[44] Gasecka A., Han T.-J., Favard C., Cho B.R., Brasselet S. (2009) Quantitative imaging of molecular order in lipid membranes using two-photon fluorescence polarimetry, *Biophys. J.* **97**(10). https://doi.org/10.1016/j.bpj.2009.08.052.

[45] Hofer M., Balla N.K., Brasselet S. (2017) High-speed polarization-resolved coherent Raman scattering imaging, *Optica* **4**(7). https://doi.org/10.1364/OPTICA.4.000795.

[46] Morizet J., Ducourthial G., Supatto W., Boutillon A., Legouis R., Schanne-Klein M.-C., Stringari C., Beaurepaire E. (2019) High-speed polarization-resolved third-harmonic microscopy, *Optica* **6**(3), 385. https://doi.org/10.1364/optica.6.000385.

[47] Axelrod D. (1979) Carbocyanine dye orientation in red cell membrane studied by microscopic fluorescence polarization, *Biophys. J.* **26**(3), 557. https://doi.org/10.1016/S0006-3495(79)85271-6.

[48] Benninger R.K.P., Önfelt B., Neil M.A.A., Davis D.M., French P.M.W. (2005) Fluorescence imaging of two-photon linear dichroism: Cholesterol depletion disrupts molecular orientation in cell membranes, *Biophys. J.* **88**(1), 609. https://doi.org/10.1529/biophysj.104.050096.

[49] Haluska C.K., Schröder A.P., Didier P., Heissler D., Duportail G., Mély Y., Marques C.M. (2008) Combining fluorescence lifetime and polarization microscopy to discriminate phase separated domains in giant unilamellar vesicles, *Biophys. J.* **95**(12), 5737. https://doi.org/10.1529/biophysj.108.131490.

[50] Benninger R.K.P., Vanherberghen B., Young S., Taner S.B., Culley F.J., Schnyder T., Neil M.A.A., Wüstner D., French P.M.W., Davis D.M., Önfelt B. (2009) Live cell linear dichroism imaging reveals extensive membrane ruffling within the docking structure of natural killer cell immune synapses, *Biophys. J.* **96**(2), L13. https://doi.org/10.1016/j.bpj.2008.10.005.

[51] Chouaki-Benmansour N., Ruminski K., Sartre A.-M., Phelipot M.-C., Salles A., Bergot E., Wu A., Chicanne G., Fallet M., Brustlein S., Billaudeau C., Formisano A., Mailfert S., Payrastre B., Marguet D., Brasselet S., Hamon Y., He H.-T. (2018) Phosphoinositides regulate the TCR/CD3 complex membrane dynamics and activation, *Sci. Rep.* **8**(1), 4966. https://doi.org/10.1038/s41598-018-23109-8.

[52] Lazar J., Bondar A., Timr S., Firestein S.J. (2011) Two-photon polarization microscopy reveals protein structure and function, *Nat. Methods* **8**(8), 684. https://doi.org/10.1038/nmeth.1643.

[53] Davis R.P., Moad A.J., Goeken G.S., Wampler R.D., Simpson G.J. (2008) *Selection rules and symmetry relations for four-wave mixing measurements of uniaxial assemblies*. https://doi.org/10.1021/JP709961K.

[54] Réfrégier P., Roche M., Brasselet S. (2011) Precision analysis in polarization-resolved second harmonic generation microscopy, *Opt. Lett.* https://doi.org/10.1364/OL.36.002149.

[55] Réfrégier P., Roche M., Duboisset J., Brasselet S. (2012) Precision increase with two orthogonal analyzers in polarization-resolved second-harmonic generation microscopy, *Opt. Lett.* **37**(20), 4173.

[56] Bancelin S., Aimé C., Gusachenko I., Kowalczuk L., Latour G., Coradin T., Schanne-Klein M.-C. (2014) Determination of collagen fibril size *via* absolute measurements of second-harmonic generation signals, *Nat. Commun.* **5**(1), 4920. https://doi.org/10.1038/ncomms5920.

[57] Ait-Belkacem D., Gasecka A., Munhoz F., Brustlein S., Brasselet S. (2010) Influence of birefringence on polarization resolved nonlinear microscopy and collagen SHG structural imaging, *Opt. Exp.* **18**(14). https://doi.org/10.1364/OE.18.14859.

[58] Gusachenko I., Latour G., Schanne-Klein M.-C. (2010) Polarization-resolved Second Harmonic microscopy in anisotropic thick tissues, *Opt. Exp.* **18**(18), 19339. https://doi.org/10.1364/OE.18.019339.

[59] Bancelin S., Lynch B., Bonod-Bidaud C., Dokládal P., Ruggiero F., Allain J.M., Schanne-Klein M.C. (2019) Combination of traction assays and multiphoton imaging to quantify skin biomechanics, *Methods in Molecular Biology*. Humana Press Inc., Vol. 1944, pp. 145–155. https://doi.org/10.1007/978-1-4939-9095-5_11.

[60] Mansfield J.C., Mandalia V., Toms A., Peter Winlove C., Brasselet S. (2019) Collagen reorganization in cartilage under strain probed by polarization sensitive second harmonic generation microscopy, *J. R. Soc. Interface* **16**(150). https://doi.org/10.1098/rsif.2018.0611.
[61] Bioud F.-Z., Gasecka P., Ferrand P., Rigneault H., Duboisset J., Brasselet S. (2014) Structure of molecular packing probed by polarization-resolved nonlinear four-wave mixing and coherent anti-Stokes Raman-scattering microscopy, *Phys. Rev. A – At. Mol. Opt. Phys.* **89**(1). https://doi.org/10.1103/PhysRevA.89.013836.
[62] Gasecka P., Jaouen A., Bioud F.-Z., de Aguiar H.B., Duboisset J., Ferrand P., Rigneault H., Balla N.K., Debarbieux F., Brasselet S. (2017) Lipid order degradation in autoimmune demyelination probed by polarized coherent Raman microscopy, *Biophys. J.* **113**(7), 1520. https://doi.org/10.1016/j.bpj.2017.07.033.
[63] Duboisset J., Berto P., Gasecka P., Bioud F.Z., Ferrand P., Rigneault H., Brasselet S. (2015) Molecular orientational order probed by coherent anti-Stokes Raman scattering (CARS) and stimulated Raman scattering (SRS) microscopy: A spectral comparative study, *J. Phys. Chem. B* **119**(7), 3242. https://doi.org/10.1021/jp5113813.
[64] Cheng J.X., Pautot S., Weitz D.A., Xie X.S. (2003) Ordering of water molecules between phospholipid bilayers visualized by coherent anti-Stokes Raman scattering microscopy, *Proc. Nat. Acad. Sci. U.S.A.* **100**(17), 9826. https://doi.org/10.1073/pnas.1732202100.
[65] Kachynski A.V., Kuzmin A.N., Prasad P.N., Smalyukh I.I. (2007) Coherent anti-Stokes Raman scattering polarized microscopy of three-dimensional director structures in liquid crystals, *Appl. Phys. Lett.* **91**(15), 151905. https://doi.org/10.1063/1.2800887.
[66] Zimmerley M., Younger R., Valenton T., Oertel D.C., Ward J.L., Potma E.O. (2010) Molecular orientation in dry and hydrated cellulose fibers: A coherent anti-Stokes Raman scattering microscopy study, *J. Phys. Chem. B* **114**(31), 10200. https://doi.org/10.1021/jp103216j.
[67] Wurpel G.W.H., Rinia H.A., Muller M. (2005) Imaging orientational order and lipid density in multilamellar vesicles with multiplex CARS microscopy, *J. Microsc.* **218**(1), 37. https://doi.org/10.1111/j.1365-2818.2005.01462.x.
[68] Fu Y., Huff T.B., Wang H.-W., Wang H., Cheng J.-X. (2008) Ex vivo and in vivo imaging of myelin fibers in mouse brain by coherent anti-Stokes Raman scattering microscopy, *Opt. Exp.* **16**(24), 19396. https://doi.org/10.1364/oe.16.019396.
[69] de Vito G., Cappello V., Tonazzini I., Cecchini M., Piazza V. (2017) RP-CARS reveals molecular spatial order anomalies in myelin of an animal model of Krabbe disease, *J. Biophotonics* **10**(3), 385. https://doi.org/10.1002/jbio.201500305.
[70] Fu Y., Frederick T.J., Huff T.B., Goings G.E., Miller S.D., Cheng J.-X. (2011) Paranodal myelin retraction in relapsing experimental autoimmune encephalomyelitis visualized by coherent anti-Stokes Raman scattering microscopy, *J. Biomed. Opt.* **16**(10), 106006. https://doi.org/10.1117/1.3638180.
[71] Imitola J., Côté D., Rasmussen S., Xie X.S., Liu Y., Chitnis T., Sidman R.L., Lin C.P., Khoury S.J. (2011) Multimodal coherent anti-Stokes Raman scattering microscopy reveals microglia-associated myelin and axonal dysfunction in multiple sclerosis-like lesions in mice, *J. Biomed. Opt.* **16**(2), 021109. https://doi.org/10.1117/1.3533312.
[72] Turcotte R., Rutledge D.J., Bélanger E., Dill D., Macklin W.B., Côté D.C. (2016) Intravital assessment of myelin molecular order with polarimetric multiphoton microscopy, *Sci. Rep.* **6** (1), 31685. https://doi.org/10.1038/srep31685.
[73] Brasselet S., Le Floc'h V., Treussart F., Roch J.-F., Zyss J., Botzung-Appert E., Ibanez A. (2004) In situ diagnostics of the crystalline nature of single organic nanocrystals by nonlinear microscopy, *Phys. Rev. Lett.* **92**(20).
[74] Kim E., Steinbrück A., Buscaglia M.T., Buscaglia V., Pertsch T., Grange R. (2013) Second-harmonic generation of single $BaTiO_3$ nanoparticles down to 22 nm diameter, *ACS Nano*. https://doi.org/10.1021/nn401198g.
[75] Zielinski M., Oron D., Chauvat D., Zyss J. (2009) Second-harmonic generation from a single core/shell quantum dot, *Small* **5**(24), 2835. https://doi.org/10.1002/smll.200900399.

[76] Dopf K., Moosmann C., Kettlitz S.W., Schwab P.M., Ilin K., Siegel M., Lemmer U., Eisler H.-J. (2015) Coupled T-shaped optical antennas with two resonances localized in a common nanogap, *ACS Photonics* **2**(11), 1644. https://doi.org/10.1021/acsphotonics.5b00446.
[77] Kumar Balla N., Rendón-Barraza C., Hoang L.M., Karpinski P., Bermúdez-Ureña E., Brasselet S. (2017) Polarized nonlinear nanoscopy of metal nanostructures, *ACS Photonics* **4** (2). https://doi.org/10.1021/acsphotonics.6b00635.
[78] Shen H., Nguyen N., Gachet D., Maillard V., Toury T., Brasselet S. (2013) Nanoscale optical properties of metal nanoparticles probed by Second Harmonic Generation microscopy, *Opt. Exp.* **21**(10). https://doi.org/10.1364/OE.21.012318.
[79] Bachelier G., Russier-Antoine I., Benichou E., Jonin C., Brevet P.-F. (2008) Multipolar second-harmonic generation in noble metal nanoparticles, *J. Opt. Soc. Am. B* **25**(6), 955. https://doi.org/10.1364/JOSAB.25.000955.
[80] Azucena O., Crest J., Kotadia S., Sullivan W., Tao X., Reinig M., Gavel D., Olivier S., Kubby J. (2011) Adaptive optics wide-field microscopy using direct wavefront sensing, *Opt. Lett.* **36**(6), 825. https://doi.org/10.1364/ol.36.000825.
[81] Wang K., Milkie D.E., Saxena A., Engerer P., Misgeld T., Bronner M.E., Mumm J., Betzig E. (2014) Rapid adaptive optical recovery of optimal resolution over large volumes, *Nature Methods*. Nature Publishing Group, Vol. 11, Issue 6, pp. 625–628. https://doi.org/10.1038/nmeth.2925.
[82] Débarre D., Botcherby E.J., Watanabe T., Srinivas S., Booth M.J., Wilson T. (2009) Image-based adaptive optics for two-photon microscopy, *Opt. Lett.* **34**(16), 2495. https://doi.org/10.1364/ol.34.002495.
[83] Booth M.J. (2014) Adaptive optical microscopy: The ongoing quest for a perfect image, *Light: Sci. App.* **3**(4), e165. https://doi.org/10.1038/lsa.2014.46.
[84] Ji N. (2017) Adaptive optical fluorescence microscopy, *Nature Methods*. Nature Publishing Group, Vol. 14, Issue 4, pp. 374–380. https://doi.org/10.1038/nmeth.4218.
[85] Katz O., Small E., Guan Y., Silberberg Y. (2014) Noninvasive nonlinear focusing and imaging through strongly scattering turbid layers, *Optica* **1**(3), 170. https://doi.org/10.1364/OPTICA.1.000170.
[86] Ji N., Sato T.R., Betzig E. (2012) Characterization and adaptive optical correction of aberrations during in vivo imaging in the mouse cortex, *Proc. Nat. Acad. Sci. U.S.A.* **109**(1), 22. https://doi.org/10.1073/pnas.1109202108.
[87] Ntziachristos V. (2010) Going deeper than microscopy: The optical imaging frontier in biology, *Nat. Methods* **7**(8), 603. https://doi.org/10.1038/nmeth.1483.
[88] Goodman J.W. (2007) *Speckle phenomena in optics : Theory and applications*. Roberts & Co.
[89] Mosk A.P., Lagendijk A., Lerosey G., Fink M. (2012) Controlling waves in space and time for imaging and focusing in complex media, *Nat. Photonics* **6**(5), 283. https://doi.org/10.1038/nphoton.2012.88.
[90] Rotter S., Gigan S. (2017) Light fields in complex media: Mesoscopic scattering meets wave control, *Rev. Mod. Phys.* **89**(1), 015005. https://doi.org/10.1103/RevModPhys.89.015005.
[91] Vellekoop I.M., Mosk A.P. (2007) Focusing coherent light through opaque strongly scattering media, *Opt. Lett.* **32**(16), 2309. https://doi.org/10.1364/OL.32.002309.
[92] Popoff S.M., Lerosey G., Carminati R., Fink M., Boccara A.C., Gigan S. (2010) Measuring the transmission matrix in optics: An approach to the study and control of light propagation in disordered media, *Phys. Rev. Lett.* **104**(10), 100601. https://doi.org/10.1103/PhysRevLett.104.100601.
[93] Mounaix M., Andreoli D., Defienne H., Volpe G., Katz O., Grésillon S., Gigan S. (2016) Spatiotemporal coherent control of light through a multiple scattering medium with the multispectral transmission matrix, *Phys. Rev. Lett.* **116**(25), 253901. https://doi.org/10.1103/PhysRevLett.116.253901.
[94] van Beijnum F., van Putten E.G., Lagendijk A., Mosk A.P. (2011) Frequency bandwidth of light focused through turbid media, *Opt. Lett.* **36**(3), 373. https://doi.org/10.1364/OL.36.000373.

[95] Aulbach J., Gjonaj B., Johnson P., Lagendijk A. (2012) Spatiotemporal focusing in opaque scattering media by wave front shaping with nonlinear feedback, *Opt. Exp.* **20**(28), 29237. https://doi.org/10.1364/OE.20.029237.

[96] Katz O., Small E., Bromberg Y., Silberberg Y. (2011) Focusing and compression of ultrashort pulses through scattering media, *Nat. Photonics* **5**(6), 372. https://doi.org/10.1038/nphoton.2011.72.

[97] Aulbach J., Gjonaj B., Johnson P.M., Mosk A.P., Lagendijk A. (2011) Control of light transmission through opaque scattering media in space and time, *Phys. Rev. Lett.* **106**(10), 103901. https://doi.org/10.1103/PhysRevLett.106.103901.

[98] McCabe D.J., Tajalli A., Austin D.R., Bondareff P., Walmsley I.A., Gigan S., Chatel B. (2011) Spatio-temporal focusing of an ultrafast pulse through a multiply scattering medium, *Nat. Commun.* **2**(1), 447. https://doi.org/10.1038/ncomms1434.

[99] Andreoli D., Volpe G., Popoff S., Katz O., Grésillon S., Gigan S. (2015) Deterministic control of broadband light through a multiply scattering medium *via* the multispectral transmission matrix, *Sci. Rep.* **5**(1), 10347. https://doi.org/10.1038/srep10347.

[100] De Aguiar H.B., Gigan S., Brasselet S. (2016) Enhanced nonlinear imaging through scattering media using transmission-matrix-based wave-front shaping, *Phys. Rev. A*. https://doi.org/10.1103/PhysRevA.94.043830.

[101] De Aguiar H.B., Gigan S., Brasselet S. (2017) Polarization recovery through scattering media, *Sci. Adv.* **3**(9). https://doi.org/10.1126/sciadv.1600743.

[102] Hofer M., Shivkumar S., El Waly B., Brasselet S. (2020) Coherent anti-Stokes Raman scattering through thick biological tissues by single-wavefront shaping, *Phys. Rev. Appl.* **14** (2). https://doi.org/10.1103/PhysRevApplied.14.024019.

[103] Accanto N., Chen I.W., Ronzitti E., Molinier C., Tourain C., Papagiakoumou E., Emiliani V. (2019) Multiplexed temporally focused light shaping through a gradient index lens for precise in-depth optogenetic photostimulation, *Sci. Rep.* **9**(1), 1. https://doi.org/10.1038/s41598-019-43933-w.